3-D LARGE EDDY SIMULATION FOR JET AEROACOUSTICS

A Thesis

Submitted to the Faculty

of

Purdue University

by

Ali Uzun

In Partial Fulfillment of the

Requirements for the Degree

of

Doctor of Philosophy

December 2003

To my family...

ACKNOWLEDGMENTS

I am grateful to my advisors Dr. Anastasios Lyrintzis and Dr. Gregory Blaisdell for giving me the opportunity to work on this interesting research project. I have greatly enjoyed working with both of them. I thank Dr. Marc Williams and Dr. Steven Frankel for serving on my thesis committee and for their valuable comments and suggestions. Sincere thanks also go to Dr. Christophe Bogey at École Centrale de Lyon who provided answers to many questions and shared results from his jet simulations. Loren Garrison provided assistance while comparing numerical jet noise predictions with experimental measurements. My colleagues and friends Charles (aka Chuck) Wright, Phoi-Tack (aka Charlie) Lew, Loren Garrison, and Brent Robbins provided a fun and stimulating environment during my stay at Purdue. My family members in Cyprus also deserve special acknowledgment for their endless love and support.

This work was sponsored by the Indiana 21st Century Research & Technology Fund. A portion of the computing time was provided by the National Computational Science Alliance under the grant CTS010032N on the SGI Origin 2000 computer systems located at the University of Illinois at Urbana-Champaign. This research was also supported in part by National Science Foundation cooperative agreement ACI-9619020 through computing resources provided by the National Partnership for Advanced Computational Infrastructure at the San Diego Supercomputer Center. Computations of the very expensive Lighthill volume integrals were performed on the National Science Foundation Terascale Computing System at the Pittsburgh Supercomputing Center. The access provided to me by Indiana University to its IBM-SP3 Research Computer for this research is also gratefully acknowledged. Some of the preliminary computations in this research were done on the IBM-SP3 computer of Purdue University.

TABLE OF CONTENTS

Page

LIST OF TABLES

LIST OF FIGURES

Figure Page

Figure Page

Figure Page

Figure Page

Figure Page

Figure Page

Figure Page

Figure Page

Figure Page

Figure Page

NOMENCLATURE

Roman Symbols

C_{sgs}	Subgrid-scale model constant in the original Smagorinsky model
C_I	Compressibility correction constant in the subgrid-scale model
c	Speed of sound
D_j	Jet nozzle diameter
$E(k)$	Turbulent kinetic energy spectrum
$E_f(f)$	Power spectral density of velocity fluctuations
$\mathbf{e}_\phi$	Unit vector in the ϕ direction of the spherical coordinate system
$\mathbf{e}_r$	Unit vector in the r direction of the spherical coordinate system
$\mathbf{e}_\theta$	Unit vector in the θ direction of the spherical coordinate system
e_t	Total energy
f	Arbitrary variable; frequency
$\overline{f}$	Large scale component of variable f
f_{sg}	Subgrid-scale component of variable f
$\mathbf{F}, \mathbf{G}, \mathbf{H}$	Inviscid flux vectors in the Navier-Stokes equations
$\mathbf{F_v}, \mathbf{G_v}, \mathbf{H_v}$	Viscous flux vectors in the Navier-Stokes equations
$G(\vec{\mathbf{x}}, \vec{\mathbf{x}}', \Delta)$	Filter function

J	Jacobian of the coordinate transformation from physical to computational domain
k	Wavenumber
k_x	Axial wavenumber
L_r	Reference length
M	Mach number
M_j	Mach number at jet nozzle exit
M_r	Reference Mach number
N	Number of grid points along a given spatial direction
p	Pressure
Pr	Prandtl number
Pr_t	Turbulent Prandtl number
$\mathbf{q}, \mathbf{Q}$	Vector of conservative flow variables
Q_i	Subgrid-scale heat flux vector
q_i	Resolved heat flux vector
$\mathbf{q}^{'}, \mathbf{RHS}(\mathbf{q}; t)$	Right-hand side of the governing equations
Q_i	Subgrid-scale heat flux vector
$\mathbf{Q_{target}}$	Target solution in the sponge zone
$\tilde{\mathbf{q}}, \hat{\mathbf{q}}$	Intermediate values of $\mathbf{q}$ during the 4-stage Runge-Kutta time integration scheme
Re	Reynolds number

Re_D	Reynolds number based on jet diameter
Re_ω	Reynolds number based on vorticity thickness
r_o	Jet nozzle radius
$r_{1/2}$	Half velocity radius
r	Radial direction in cylindrical coordinates
S	Control surface
$\tilde{S}_{ij}$	Favre-filtered strain rate tensor
$\tilde{S}_M$	Magnitude of the Favre-filtered strain rate tensor
St	Strouhal number
t	Time
t_n	Time step n
T	Temperature
T_r	Reference temperature
T_{ij}	Lighthill stress tensor
T_{ij}^m	Mean component of T_{ij}
T_{ij}^l	Component of T_{ij} linear in velocity fluctuations
T_{ij}^n	Component of T_{ij} non-linear in velocity fluctuations
T_{ij}^s	Entropy component of T_{ij}
$\tilde{U}, \tilde{V}, \tilde{W}$	Contravariant velocity components
U_c	Jet centerline velocity as a function of streamwise distance

U_o	Jet centerline velocity at nozzle exit
U_r	Reference velocity
$\bar{\mathbf{u}} = (\bar{u}, \bar{v}, \bar{w})$	Mean velocity vector
u	Velocity component in the x direction of Cartesian coordinates
(u, v, w)	Velocity vector in Cartesian coordinates
u_i	Alternate notation for (u, v, w)
v	Velocity component in the y direction of Cartesian coordinates
v_r	Velocity component in the radial (r) direction of cylindrical coordinates
v_θ	Velocity component in the azimuthal (θ) direction of cylindrical coordinates
v_x	Velocity component in the axial (x) direction of cylindrical coordinates
V	Integration volume
V_g	Acoustic group velocity
w	Velocity component in the z direction of Cartesian coordinates
(x, y, z)	Cartesian coordinates
x	Streamwise direction in both Cartesian and cylindrical coordinates
y	Transverse direction in Cartesian coordinates
z	Transverse direction in Cartesian coordinates
x_i or $\vec{x}$	Alternate notation for (x, y, z)

Greek Symbols

α_f	Filtering parameter of the tri-diagonal filter
α	Parameter that controls the strength of the vortex ring forcing
$\overline{\phi}_i$	Spatially filtered variable at grid point i
$\chi(x)$	Parameter that controls the strength of the sponge zone damping term
Δ	Local grid spacing or eddy viscosity length scale
δ_{ij}	Kronecker delta
δ_ω	Vorticity thickness of shear layer
$\hat{\Delta}$	Test filter width
Δt	Time increment
$\Delta\xi$	Uniform grid spacing along the ξ direction in the computational domain
γ	Ratio of the specific heats of air
$\Lambda_1, \Lambda_2, \Lambda_3, \Lambda_4, \Lambda_5$	Amplitudes of characteristic waves
μ	Molecular viscosity
μ_r	Reference viscosity
ν	Kinematic viscosity
ρ	Density
ρ_r	Reference density
Ψ_{ij}	Resolved shear stress tensor

σ_{ij}	Normalized Reynolds stress components
$\sigma_{xx} = \frac{\langle v_x{}' v_x{}' \rangle}{U_c^2}$	Normalized Reynolds normal stress in the axial (x) direction of cylindrical coordinates
$\sigma_{rr} = \frac{\langle v_r{}' v_r{}' \rangle}{U_c^2}$	Normalized Reynolds normal stress in the radial (r) direction of cylindrical coordinates
$\sigma_{\theta\theta} = \frac{\langle v_\theta{}' v_\theta{}' \rangle}{U_c^2}$	Normalized Reynolds normal stress in the azimuthal (θ) direction of cylindrical coordinates
$\sigma_{rx} = \frac{\langle v_r{}' v_x{}' \rangle}{U_c^2}$	Normalized Reynolds shear stress in cylindrical coordinates
τ	Retarded time
τ_{ij}	Subgrid-scale stress tensor
θ	Azimuthal direction in cylindrical coordinates; angle from downstream jet axis
(ξ, η, ζ)	Generalized curvilinear coordinates

Other Symbols

$(\,)_i{}'$	Spatial or time derivative at grid point i
$(\,)_\eta$	Spatial derivative along the η direction
$(\,)_\xi$	Spatial derivative along the ξ direction
$(\,)_\zeta$	Spatial derivative along the ζ direction
$(\,)^*$	Dimensional quantity
$\bar{(\,)}$	Mean quantity
$\overline{(\,)}$	Spatially filtered quantity
$\tilde{(\,)}$	Favre averaged quantity

$(\,)'$	Perturbation from mean value; acoustic variable
$(\,)_\infty$	Ambient flow value
$(\,)_o$	Flow value at jet centerline on the nozzle exit
$\widehat{(\,)}$	Test filtered quantity
$\langle\,\rangle$	Time averaging operator
$\frac{\partial}{\partial x}, \frac{\partial}{\partial y}, \frac{\partial}{\partial z}$	Partial spatial derivative operators in Cartesian coordinates
$\frac{\partial}{\partial \xi}, \frac{\partial}{\partial \eta}, \frac{\partial}{\partial \zeta}$	Partial spatial derivative operators in computational domain
$\frac{\partial}{\partial t}$	Partial time derivative operator

Abbreviations

CAA	Computational Aeroacoustics
DNS	Direct Numerical Simulation
DSM	Dynamic Smagorinsky Model
FWH	Ffowcs Williams - Hawkings
LES	Large Eddy Simulation
OASPL	Overall Sound Pressure Level
RANS	Reynolds Averaged Navier-Stokes
RHS	Right-Hand Side of the Navier-Stokes Equations
rms	Root Mean Square
SGS	Subgrid-Scale
SPL	Sound Pressure Level

ABSTRACT

Uzun, Ali. Ph.D., Purdue University, December, 2003. 3-D Large Eddy Simulation for Jet Aeroacoustics. Major Professors: Anastasios S. Lyrintzis and Gregory A. Blaisdell.

Future design of aircraft engines with low jet noise emissions undoubtedly needs a better understanding of noise generation in turbulent jets. Such an understanding, on the other hand, demands very reliable prediction tools. This study is therefore focused on developing a Computational Aeroacoustics (CAA) methodology that couples the near field unsteady flow field data computed by a 3-D Large Eddy Simulation (LES) code with various integral acoustic formulations for the far field noise prediction of turbulent jets. Turbulent jet simulations were performed at various Reynolds numbers. Comparisons of jet mean flow, turbulence statistics as well as jet aeroacoustics results with experimental data of jets at similar flow conditions were done and reasonable agreement was observed. The actual jet nozzle geometry was not included in the present simulations in order to keep the computational cost at manageable levels, therefore the jet shear layers downstream of the nozzle exit were modelled in an *ad hoc* fashion. As also observed by other researchers, the results obtained in the simulations were seen to be somewhat sensitive to the way the inflow forcing was done. The study of the effects of the eddy-viscosity based Smagorinsky subgrid-scale (SGS) model on noise predictions shows that the Smagorinsky model suppresses the resolved scale high-frequency noise. Simulations with filtering only suggest that treating the spatial filter as an implicit SGS model might be a good alternative. To our best knowledge, Lighthill's acoustic analogy was applied to a reasonably high Reynolds number jet for the first time in this study. A database greater than 1 Terabytes (TB) in size was post-processed using 1160 processors in parallel on a modern supercomputing platform for this purpose. It is expected that

the current CAA methodology will yield better jet noise predictions when improved SGS models for both turbulence and high-frequency noise are incorporated into the LES code and when the computing technology reaches a level where including the jet nozzle geometry in the simulations will not be so computationally prohibitive.

1. INTRODUCTION

1.1 Motivation

Jet noise remains as one of the most complicated and difficult problems in aeroacoustics because the details of noise generation mechanisms by the complex turbulence phenomena in a jet are still not well understood. Thus, there is a need for more research that will lead to improved jet noise prediction methodologies and further understanding of the jet noise generation mechanisms which will eventually aid in the design process of aircraft engines with low jet noise emissions.

With the recent improvements in the processing speed of computers, the application of Direct Numerical Simulation (DNS) and Large Eddy Simulation (LES) to jet noise prediction methodologies is becoming more feasible. Although there has been numerous experimental studies of jet noise to date, the experiments provide only a limited amount of information and the ultimate understanding of jet noise generation mechanisms will most likely be possible through numerical simulations since the computations can literally provide any type of information needed for the analysis of jet noise generation mechanisms. The first DNS of a turbulent jet was done for a Reynolds number 2,000, supersonic jet at Mach 1.92 by Freund *et al.* [1]. The computed overall sound pressure levels were compared with experimental data and found to be in good agreement with jets at similar convective Mach numbers. Freund [2] also simulated a Reynolds number 3,600, Mach 0.9 turbulent jet using 25.6 million grid points, matching the parameters of the experimental jet studied by Stromberg *et al.* [3]. Excellent agreement with the experimental data was obtained for both the mean flow field and the radiated sound. Such results clearly show the attractiveness of DNS to the jet noise problem. However, due to the wide range of length and time scales present in turbulent flows, DNS is still restricted to low-Reynolds-number

flows and relatively simple geometries. DNS of high-Reynolds-number jet flows of practical interest would necessitate tremendous resolution requirements that are far beyond the reach of the capability of even the fastest supercomputers available today.

Therefore, turbulence still has to be modelled in some way to do simulations for problems of practical interest. LES, with lower computational cost, is an attractive alternative to DNS. In an LES, the large scales are directly resolved and the effect of the small scales or the subgrid scales on the large scales are modelled. The large scales are generally much more energetic than the small ones and are directly affected by the boundary conditions. The small scales, however, are usually much weaker and they tend to have more or less a universal character. Hence, it makes sense to directly simulate the more energetic large scales and model the effect of the small scales. LES methods are capable of simulating flows at higher Reynolds numbers and many successful LES computations for different types of flows have been performed to date. Since noise generation is an inherently unsteady process, LES will probably be the most powerful computational tool to be used in jet noise research in the foreseeable future since it is the only way, other than DNS, to obtain time-accurate unsteady data. Although the application of Reynolds Averaged Navier Stokes (RANS) methods to jet noise prediction is also subject of ongoing research [4–8], RANS methods heavily rely on turbulence models to model all relevant scales of turbulence. Moreover, such methods try to predict the noise using the mean flow properties provided by a RANS solver. Since noise generation is a multi-scale problem that involves a wide range of length and time scales, it appears the success of RANS-based prediction methods will remain limited unless very good turbulence models capable of accurately modelling a wide range of turbulence scales are developed and implemented into existing RANS solvers.

It is now widely accepted among the jet noise research community that the low frequency noise generated by the jet flow is associated with the large scale turbulent motions with length scales on the order of the jet diameter, whereas the high frequency noise is related to the finer scales of turbulence. Moreover, the large scales

are known to be strongly affected by the jet nozzle geometry. So although LES seems to be very suitable for directly computing the low frequency jet noise and a portion of the higher frequencies, some ingenuity is still needed so as to estimate the noise from the unresolved higher frequencies generated by the very fine turbulent scales not resolved by the LES grid. Such an estimation necessitates subgrid-scale noise models that will somehow extrapolate the information contained in the scales well-resolved by the LES to predict the high frequency noise. Although there has been some preliminary efforts in this area [9], [10], [11], [12], [13], a satisfactory SGS noise model is yet to be developed.

At this point, it seems appropriate to give an overview of the application of LES to jet noise prediction. Although the overview given here is not a comprehensive list of all the jet noise LES computations done to date, it certainly includes a review of the state-of-the-art computations that are believed to be the most successful application of LES to jet noise prediction. One of the first attempts in using LES as a tool for jet noise prediction was carried out by Mankbadi *et al.* [14]. They employed a high-order numerical scheme to perform LES of a supersonic jet flow to capture the time-dependent flow structure and applied Lighthill's theory [15] to calculate the far field noise. Lyrintzis and Mankbadi [16] used LES in combination with Kirchhoff's method for jet noise prediction. LES has been used together with Kirchhoff's method [17] for the noise prediction of a Mach 2.0 jet also by Gamet and Estivalezes [18] as well as for a Mach 1.2 jet with Mach 0.2 coflow by Choi *et al.* [19] with encouraging results obtained in both studies. Zhao *et al.* [20] did LES for a Mach 0.9, Reynolds number 3,600 jet obtaining mean flow results that compared well with Freund's DNS and experimental data. Their overall sound pressure levels for this test case were in good agreement with experiments as well. They also studied the far field noise from a Mach 0.4, Reynolds number 5,000 jet. They compared Kirchhoff's method results with the directly computed sound and observed good agreement. Morris *et al.* [21–25] simulated high speed round jet flows using the Nonlinear Disturbance Equations (NLDE). In their NLDE method, the instantaneous

quantities are decomposed into a time-independent mean component, a large-scale perturbation and a small-scale perturbation. The mean quantities are obtained using a traditional Reynolds Averaged Navier-Stokes (RANS) method. As in LES, they resolved the large-scale fluctuations directly and used a subgrid-scale model for the small-scale fluctuations in their unsteady calculations. They also analyzed the noise from a supersonic elliptic jet in another study [26]. Chyczewski and Long [27] conducted a supersonic rectangular jet flow simulation and also did far field noise predictions with a Kirchhoff method. Boersma and Lele [28] did LES for a Mach 0.9 jet at Reynolds numbers of 3,600 and 36,000 without any noise predictions. Bogey *et al.* [29] simulated a Reynolds number 65,000, Mach 0.9 jet using LES and obtained very good mean flow results, turbulent intensities as well as sound levels and directivity. Constantinescu and Lele [30] did simulations for a Mach 0.9 jet at Reynolds numbers of 3,600 and 72,000. They directly calculated the near field noise using LES. Their mean flow parameters and turbulence statistics were in good agreement with experimental data and results from other simulations. The peak of the near field noise spectra was also captured accurately in their calculations. DeBonis and Scott [31] simulated a Reynolds number 1.2 million, Mach 1.4 jet using 1.5 million grid points but they did not do any noise predictions. Bodony and Lele [32] studied a Mach 0.9, Reynolds number 72,000 jet using 5.9 million grid points in an LES and experimented with the inlet conditions. They showed the important role of the inlet conditions in the far field noise of the jet. More recently, Bogey and Bailly's LES [33] for a Mach 0.9 round jet at Reynolds number, $Re_D = 400,000$ using 12.5 and 16.6 million grid points produced mean flow and sound field results that are in good agreement with the experimental measurements available in the literature. They also studied the effect of the various inflow conditions on the jet flow field as well as on the jet noise in another recent study [34]. Their study once again revealed the importance of inflow conditions in jet noise LES. Moreover, they brought up the issue of the effects of the eddy viscosity based Smagorinsky SGS model on the jet noise in yet another recent study [35]. They showed that the high-frequency portion

of the noise spectra was significantly suppressed by the eddy viscosity. The recent jet noise computations of Bogey and Bailly [33], [34], [35] are perhaps the most successful LES calculations done for reasonably high Reynolds number jets at the time of this writing. In this study, we will repeat some of the test cases studied by Bogey and Bailly [34], [35] and make comparisons with their results as part of the validation of our CAA methodology.

In general, the LES results in the literature to date are encouraging and show the potential promise of LES application to jet noise prediction. Except for the studies of Choi *et al.* [19] and DeBonis and Scott [31] which are not well-resolved LES calculations, and the recent studies of Bogey and Bailly [33], [34], [35], the highest Reynolds numbers reached in the LES simulations so far are still below those of practical interest. The cut-off frequency of the noise spectra in the LES computations is dictated by the grid resolution, hence only a portion of the noise spectra was computed in the LES computations to date. Moreover, none of the LES studies in the literature so far have predicted the high-frequency noise associated with the unresolved fine scales due to the lack of an SGS noise model. Well-resolved LES calculations of jets at higher Reynolds numbers close enough to practical values of interest would be very helpful for evaluating the suitability of LES to such problems as well as for analyzing the broad-band noise spectrum and possibly looking into the mechanisms of jet noise generation at such Reynolds numbers.

1.2 Objectives of the Present Study

With this motivation behind the current study given, we now present the two main objectives of this research:

1. *Development and validation of a versatile 3-D LES code for turbulent jet simulations.* A high-order accurate 3-D compressible LES code utilizing a robust dynamic subgrid-scale (SGS) model has been developed to simulate high speed jet flows with high subsonic Mach numbers. Generalized curvilinear coordinates

are used, so the code can be easily adapted for calculations in several applications with complicated geometries. Since the sound field is several orders of magnitude smaller than the aerodynamic field, we make use of high-order accurate non-dissipative compact schemes which satisfy the strict requirements of CAA. Implicit spatial filtering is employed to remove the high-frequency oscillations resulting from unresolved scales and mesh non-uniformities. Non-reflecting boundary conditions are imposed on the boundaries of the domain to let outgoing disturbances exit the domain without spurious reflection. A sponge zone that is attached downstream of the physical domain damps out the disturbances before they reach the outflow boundary. Initial simulations were performed with the constant-coefficient Smagorinsky SGS model. However, the results were found to be sensitive to the choice of the Smagorinsky constant. The latest version of the LES code has the dynamic SGS model implemented. As will be shown in the results section, an LES with the dynamic SGS model for a compressible round jet at Reynolds number 100,000 produced mean flow results in excellent agreement with experimental observations. The code also has the capability to turn off the SGS model and treat the spatial filter as an implicit SGS model. This type of LES with filtering only, were also done and the results were compared against the LES done with the dynamic Smagorinsky SGS model. The compressible LES solver developed herein can be further modified to study supersonic jets in the future.

2. *Accurate prediction of the far field noise.* Even though sound is generated by a nonlinear process, the sound field itself is known to be linear and irrotational. This implies that instead of solving the full nonlinear flow equations out in the far field for sound propagation, one can use Lighthill's acoustic analogy [15] or surface integral acoustic methods such as Kirchhoff's method [17] and the Ffowcs Williams - Hawkings (FWH) method [36], [37]. In this study, we couple the near field data directly provided by LES with Kirchhoff's and Ffowcs Williams - Hawkings methods as well as with Lighthill's acoustic analogy for

computing the noise propagation to the far field. Overall sound pressure levels in the far field as well acoustic pressure spectra are presented. Results are also compared with experimental as well as computational data available in the literature.

It should be noted at this point that the Ffowcs Williams - Hawkings method and Kirchhoff's method cannot be used with incompressible CFD data. For low speeds (i.e., incompressible flow) and a stationary impermeable surface, the Ffowcs Williams - Hawkings equation reduces to Curle's integral [38]. Since the LES code developed in this study is a compressible solver, the flow field data provided by the code are compatible with the standard Ffowcs Williams - Hawkings and Kirchhoff formulations.

The compressible LES code and the integral acoustics codes developed in this study form the core of a CAA methodology for jet noise prediction. Using these tools, we will attempt state-of-the-art well-resolved LES computations for jet flows with Reynolds numbers as high as 400,000. As will be shown in the results section, the cut-off non-dimensional frequency (Strouhal number) in the subsequent noise computations will be as high as 4.0. Such a cut-off frequency, to our best knowledge, is greater than the cut-off frequencies captured in all other jet noise LES computations for similar Reynolds numbers available in the literature to date. It is expected that the coupling of the present CAA methodology with a future SGS model for high-frequency noise from unresolved scales will be a powerful jet noise prediction tool.

1.3 Organization of the Thesis

This thesis is organized as follows. Governing equations as well as various numerical techniques implemented in our LES code are described in Chapter 2. The formulation of the surface integral acoustics methods are also given in this chapter. Chapter 3 shows the results of 2-D planar mixing layer simulations that were carried

out to test the various numerical algorithms prior to the 3-D jet simulations. Results and discussion of the initial 3-D round jet simulations are presented in Chapter 4. Chapter 5 includes the mean flow and aeroacoustics results of a Reynolds number 100,000 jet simulation performed with the dynamic Smagorinsky model. Chapter 6 compares the results of the Reynolds number 400,000 jet simulations done with and without an explicit SGS model. It also provides a study of surface integral acoustics methods and compares Kirchhoff's method and the Ffowcs Williams - Hawkings method results for various control surfaces surrounding the jet flow. Chapter 7 gives a description of Lighthill's acoustic analogy and presents the details of the far field noise computations using Lighthill's acoustic analogy. Comparison of Lighthill's acoustic analogy results with the results obtained using the Ffowcs Williams - Hawkings method as well as with some experimental far field noise spectra are also made in this chapter. Concluding remarks as well as future work proposals are given in Chapter 8.

Parts of this work were published as conference or journal papers listed as References [39–43].

2. SIMULATION TECHNIQUES

2.1 Governing Equations

Large Eddy Simulation (LES) can be thought of as a compromise between Direct Numerical Simulation (DNS) and the Reynolds Averaged Navier-Stokes (RANS) equations. In a DNS, all the relevant scales of turbulence have to be directly computed whereas in a RANS calculation, all the relevant scales of turbulence need to be modelled. In an LES, the flowfield is decomposed into a large-scale or resolved-scale component ($\overline{f}$) and a small-scale or subgrid-scale component (f_{sg}),

$$f = \overline{f} + f_{sg}. \tag{2.1}$$

The large-scale component is obtained by filtering the entire domain using a grid filter function, G as follows

$$\overline{f}(\vec{\mathbf{x}}) = \int_V G(\vec{\mathbf{x}}, \vec{\mathbf{x}}', \Delta) f(\vec{\mathbf{x}}')\, d\vec{\mathbf{x}}'. \tag{2.2}$$

The filtering operation removes the small-scale or the subgrid-scale turbulence from the Navier-Stokes equations. The resulting governing equations are then solved directly for the large-scale turbulent motions while the subgrid-scales are computed using a subgrid-scale model, such as the classical Smagorinsky model [44] or the more sophisticated dynamic Smagorinsky models proposed by Germano *et al.* [45] and Moin *et al.* [46].

For compressible flows, the large-scale component is written in terms of a Favre-filtered variable

$$\tilde{f} = \frac{\overline{\rho f}}{\overline{\rho}}. \tag{2.3}$$

The Favre-filtered unsteady, compressible, non-dimensionalized Navier-Stokes equations formulated in conservative form are solved in this study. The dimensional variables are non-dimensionalized as follows

$$\rho = \frac{\rho^*}{\rho_r} \qquad u_i = \frac{{u_i}^*}{U_r} \qquad p = \frac{p^*}{\rho_r {U_r}^2} \qquad t = \frac{t^* U_r}{L_r} \qquad x_i = \frac{{x_i}^*}{L_r}. \tag{2.4}$$

The continuity equation is expressed as

$$\frac{\partial \overline{\rho}}{\partial t} + \frac{\partial \overline{\rho} \tilde{u}_i}{\partial x_i} = 0. \tag{2.5}$$

The momentum equation is expressed as

$$\frac{\partial \overline{\rho} \tilde{u}_i}{\partial t} + \frac{\partial \overline{\rho} \tilde{u}_i \tilde{u}_j}{\partial x_j} + \frac{\partial \overline{p}}{\partial x_i} - \frac{\partial}{\partial x_j}(\Psi_{ij} - \tau_{ij}) = 0, \tag{2.6}$$

where the resolved shear stress tensor is given by

$$\Psi_{ij} = \frac{2\tilde{\mu}}{Re}\big(\tilde{S}_{ij} - \frac{1}{3}\tilde{S}_{kk}\delta_{ij}\big), \tag{2.7}$$

with the Favre-filtered strain rate tensor defined as

$$\tilde{S}_{ij} = \frac{1}{2}\left(\frac{\partial \tilde{u}_j}{\partial x_i} + \frac{\partial \tilde{u}_i}{\partial x_j}\right). \tag{2.8}$$

The subgrid-scale stress tensor is given by

$$\tau_{ij} = \overline{\rho}(\widetilde{u_i u_j} - \tilde{u}_i \tilde{u}_j), \tag{2.9}$$

and is modelled as

$$\tau_{ij} = -2C_{sgs}\overline{\rho}\Delta^2 \tilde{S}_M\big(\tilde{S}_{ij} - \frac{1}{3}\tilde{S}_{kk}\delta_{ij}\big) + \frac{2}{3}C_I \overline{\rho}\Delta^2 \tilde{S}_M^2 \delta_{ij}, \tag{2.10}$$

where

$$\tilde{S}_M = \big(2\tilde{S}_{ij}\tilde{S}_{ij}\big)^{1/2}, \tag{2.11}$$

and C_{sgs}, C_I are the model coefficients, and Δ is the filter width or the eddy viscosity length scale. In the subgrid-scale stress equation, the first term on the right hand side is the original incompressible term in Smagorinsky's model [44], and the second term is the compressible correction proposed by Yoshizawa [47].

Finally, the energy equation is expressed as

$$\frac{\partial \overline{e}_t}{\partial t} + \frac{\partial \tilde{u}_i(\overline{e}_t + \overline{p})}{\partial x_i} - \frac{\partial}{\partial x_i}\tilde{u}_j(\Psi_{ij} - \tau_{ij}) + \frac{\partial}{\partial x_i}(q_i + Q_i) = 0, \tag{2.12}$$

where the total energy is defined as

$$\overline{e}_t = \frac{1}{2}\overline{\rho}\tilde{u}_i\tilde{u}_i + \frac{\overline{p}}{\gamma - 1}. \tag{2.13}$$

The resolved heat flux is

$$q_i = -\left[\frac{\tilde{\mu}}{(\gamma - 1){M_r}^2 RePr}\right]\frac{\partial \tilde{T}}{\partial x_i}. \tag{2.14}$$

The subgrid-scale heat flux is given by

$$Q_i = \overline{\rho}(\widetilde{u_i T} - \tilde{u}_i\tilde{T}), \tag{2.15}$$

and is modelled as

$$Q_i = \frac{-C_{sgs}\rho\Delta^2\tilde{S}_M}{Pr_t}\frac{\partial \tilde{T}}{\partial x_i}. \tag{2.16}$$

The ideal gas relation

$$\overline{p} = \frac{\overline{\rho}\tilde{T}}{\gamma {M_r}^2}, \tag{2.17}$$

and Sutherland's law for the molecular viscosity, $\tilde{\mu}$

$$\frac{\tilde{\mu}}{\mu_r} = \left(\frac{\tilde{T}}{T_r}\right)^{3/2}\frac{T_r + S}{\tilde{T} + S} \tag{2.18}$$

are also used in these equations with the Sutherland constant, S chosen as $110K$ while the reference temperature, T_r and reference viscosity, μ_r are chosen as the jet centerline temperature and viscosity, respectively.

The three coefficients for the subgrid-scale models are C_{sgs}, C_I and the turbulent Prandtl number, Pr_t. In the standard Smagorinsky model with compressibility corrections, these coefficients are set to some constants based on previous studies. It is also possible to represent these coefficients as functions of space and time, and compute them dynamically as part of the flowfield simulation [45, 46].

Both the standard constant-coefficient Smagorinsky [44] as well as the dynamic Smagorinsky model for compressible flows proposed by Moin *et al.* [46] have been

implemented into the LES code. The main idea in the dynamic model is to compute the model coefficients as functions of space and time by making use of the information contained within the smallest resolved scales of motion. The coefficient C_{sgs} is evaluated using the following relation

$$C_{sgs} = -\frac{(L_{ij} - \frac{1}{3}L_{kk})M_{ij}}{2M_{ij}M_{ij}}, \tag{2.19}$$

where

$$L_{ij} = \widehat{\overline{\rho}\tilde{u}_i\tilde{u}_j} - \frac{1}{\hat{\rho}}\widehat{\overline{\rho}\tilde{u}_i}\widehat{\overline{\rho}\tilde{u}_j}, \tag{2.20}$$

$$M_{ij} = \hat{\overline{\rho}}\widehat{\tilde{S}_M}\left(\hat{\Delta}/\Delta\right)^2\left(\widehat{\tilde{S}_{ij}} - \frac{1}{3}\widehat{\tilde{S}_{kk}}\delta_{ij}\right) - \widehat{N_{ij}}, \tag{2.21}$$

$$N_{ij} = \overline{\rho}\tilde{S}_M\left(\tilde{S}_{ij} - \frac{1}{3}\tilde{S}_{kk}\delta_{ij}\right), \tag{2.22}$$

and $\widehat{\ }$ represents the test filtering operation.

For the dynamic model, a fifteen-point explicit filter developed by Bogey and Bailly [48] is used as the test filter. Details of this test filter are given in section 2.2.3. The ratio of the test filter width to the grid spacing, $(\hat{\Delta}/\Delta)$ is taken as 2. The usual practice in LES calculations is to average certain dynamically computed quantities over statistically homogeneous directions and then use these averaged quantities to compute the model coefficients. This is an *ad hoc* procedure that is used to remove very sharp fluctuations in the dynamic model coefficients and to stabilize the model. Obviously, such an approach is not useful for turbulent flows for which there is no homogeneous direction. In our implementation, the dynamically computed model coefficients are locally averaged in space using a second-order three-point filter along all spatial directions in order to avoid the sharp fluctuations in the model coefficient. No negative model coefficients are allowed. The upper limit for the model coefficients is set to 0.5. This procedure works reasonably well for the jet flows we are studying. The LES code which dynamically computes the Smagorinsky constant requires approximately 50% more computing time relative to the LES code which employs the constant-coefficient SGS model. Dynamic evaluation of the compressibility correction coefficient and the turbulent Prandtl number require test

filtering of some additional quantities. To keep the additional cost of the dynamic model at an acceptable level, the compressibility correction coefficient, C_I and the turbulent Prandtl number, Pr_t are not computed dynamically in this study and are set to constant values instead.

In order to do direct numerical simulations using these Favre-filtered equations, all spatially filtered variables can be replaced by their unfiltered forms and the subgrid-scale stress tensor and the subgrid-scale heat flux terms are simply set to zero.

The equations given so far are formulated in Cartesian coordinates. For problems involving complex geometries, the form of the governing equations in generalized curvilinear coordinates should be used. Extension of the equations from Cartesian coordinates to generalized curvilinear coordinates can be expressed as

$$\frac{1}{J}\frac{\partial \mathbf{Q}}{\partial t} + \frac{\partial}{\partial \xi}\left(\frac{\mathbf{F}-\mathbf{F_v}}{J}\right) + \frac{\partial}{\partial \eta}\left(\frac{\mathbf{G}-\mathbf{G_v}}{J}\right) + \frac{\partial}{\partial \zeta}\left(\frac{\mathbf{H}-\mathbf{H_v}}{J}\right) = 0, \tag{2.23}$$

where t is the time, ξ, η, and ζ are the generalized curvilinear coordinates of the computational space, and J is the Jacobian of the coordinate transformation from the physical domain to the computational domain and can evaluated as follows

$$J = \frac{1}{x_\xi\left(y_\eta z_\zeta - y_\zeta z_\eta\right) - x_\eta\left(y_\xi z_\zeta - y_\zeta z_\xi\right) + x_\zeta\left(y_\xi z_\eta - y_\eta z_\xi\right)}. \tag{2.24}$$

$\mathbf{Q}$ is the vector of conservative flow variables, $\mathbf{F}$, $\mathbf{G}$, and $\mathbf{H}$ are the inviscid flux vectors, $\mathbf{F_v}$, $\mathbf{G_v}$, and $\mathbf{H_v}$ are the viscous flux vectors defined as follows

$$\mathbf{Q} = \begin{bmatrix} \overline{\rho} \\ \overline{\rho}\tilde{u} \\ \overline{\rho}\tilde{v} \\ \overline{\rho}\tilde{w} \\ \overline{e}_t \end{bmatrix} \quad \mathbf{F} = \begin{bmatrix} \overline{\rho}\tilde{U} \\ \overline{\rho}\tilde{u}\tilde{U} + \xi_x\overline{p} \\ \overline{\rho}\tilde{v}\tilde{U} + \xi_y\overline{p} \\ \overline{\rho}\tilde{w}\tilde{U} + \xi_z\overline{p} \\ (\overline{e}_t + \overline{p})\tilde{U} \end{bmatrix} \quad \mathbf{G} = \begin{bmatrix} \overline{\rho}\tilde{V} \\ \overline{\rho}\tilde{u}\tilde{V} + \eta_x\overline{p} \\ \overline{\rho}\tilde{v}\tilde{V} + \eta_y\overline{p} \\ \overline{\rho}\tilde{w}\tilde{V} + \eta_z\overline{p} \\ (\overline{e}_t + \overline{p})\tilde{V} \end{bmatrix} \quad \mathbf{H} = \begin{bmatrix} \overline{\rho}\tilde{W} \\ \overline{\rho}\tilde{u}\tilde{W} + \zeta_x\overline{p} \\ \overline{\rho}\tilde{v}\tilde{W} + \zeta_y\overline{p} \\ \overline{\rho}\tilde{w}\tilde{W} + \zeta_z\overline{p} \\ (\overline{e}_t + \overline{p})\tilde{W} \end{bmatrix}, \tag{2.25}$$

$$\mathbf{F_v} = \begin{bmatrix} F_{v1} \\ F_{v2} \\ F_{v3} \\ F_{v4} \\ F_{v5} \end{bmatrix} \quad \mathbf{G_v} = \begin{bmatrix} G_{v1} \\ G_{v2} \\ G_{v3} \\ G_{v4} \\ G_{v5} \end{bmatrix} \quad \mathbf{H_v} = \begin{bmatrix} H_{v1} \\ H_{v2} \\ H_{v3} \\ H_{v4} \\ H_{v5} \end{bmatrix}, \tag{2.26}$$

$$\begin{bmatrix} F_{v1} \\ F_{v2} \\ F_{v3} \\ F_{v4} \\ F_{v5} \end{bmatrix} = \begin{bmatrix} 0 \\ \xi_x(\Psi_{xx} - \tau_{xx}) + \xi_y(\Psi_{xy} - \tau_{xy}) + \xi_z(\Psi_{xz} - \tau_{xz}) \\ \xi_x(\Psi_{xy} - \tau_{xy}) + \xi_y(\Psi_{yy} - \tau_{yy}) + \xi_z(\Psi_{yz} - \tau_{yz}) \\ \xi_x(\Psi_{xz} - \tau_{xz}) + \xi_y(\Psi_{yz} - \tau_{yz}) + \xi_z(\Psi_{zz} - \tau_{zz}) \\ \tilde{u}F_{v2} + \tilde{v}F_{v3} + \tilde{w}F_{v4} - \xi_x(q_x + Q_x) - \xi_y(q_y + Q_y) - \xi_z(q_z + Q_z) \end{bmatrix}, \tag{2.27}$$

$$\begin{bmatrix} G_{v1} \\ G_{v2} \\ G_{v3} \\ G_{v4} \\ G_{v5} \end{bmatrix} = \begin{bmatrix} 0 \\ \eta_x(\Psi_{xx} - \tau_{xx}) + \eta_y(\Psi_{xy} - \tau_{xy}) + \eta_z(\Psi_{xz} - \tau_{xz}) \\ \eta_x(\Psi_{xy} - \tau_{xy}) + \eta_y(\Psi_{yy} - \tau_{yy}) + \eta_z(\Psi_{yz} - \tau_{yz}) \\ \eta_x(\Psi_{xz} - \tau_{xz}) + \eta_y(\Psi_{yz} - \tau_{yz}) + \eta_z(\Psi_{zz} - \tau_{zz}) \\ \tilde{u}G_{v2} + \tilde{v}G_{v3} + \tilde{w}G_{v4} - \eta_x(q_x + Q_x) - \eta_y(q_y + Q_y) - \eta_z(q_z + Q_z) \end{bmatrix}, \tag{2.28}$$

$$\begin{bmatrix} H_{v1} \\ H_{v2} \\ H_{v3} \\ H_{v4} \\ H_{v5} \end{bmatrix} = \begin{bmatrix} 0 \\ \zeta_x(\Psi_{xx} - \tau_{xx}) + \zeta_y(\Psi_{xy} - \tau_{xy}) + \zeta_z(\Psi_{xz} - \tau_{xz}) \\ \zeta_x(\Psi_{xy} - \tau_{xy}) + \zeta_y(\Psi_{yy} - \tau_{yy}) + \zeta_z(\Psi_{yz} - \tau_{yz}) \\ \zeta_x(\Psi_{xz} - \tau_{xz}) + \zeta_y(\Psi_{yz} - \tau_{yz}) + \zeta_z(\Psi_{zz} - \tau_{zz}) \\ \tilde{u}H_{v2} + \tilde{v}H_{v3} + \tilde{w}H_{v4} - \zeta_x(q_x + Q_x) - \zeta_y(q_y + Q_y) - \zeta_z(q_z + Q_z) \end{bmatrix}, \tag{2.29}$$

where ξ_x, ξ_y, ξ_z, η_x, η_y, η_z, ζ_x, ζ_y, ζ_z are the transformation metrics. Since the governing equations written in strong-conservation form are used in this study, we pay special attention to the evaluation of metrics. In order to ensure metric cancellation on general 3-D curvilinear grids when high-order spatial discretization schemes

are employed, we use the following "conservative" form of evaluating the metric expressions [49]

$$\begin{aligned} \xi_x/J &= \left(y_\eta z\right)_\zeta - \left(y_\zeta z\right)_\eta, \\ \eta_x/J &= \left(y_\zeta z\right)_\xi - \left(y_\xi z\right)_\zeta, \\ \zeta_x/J &= \left(y_\xi z\right)_\eta - \left(y_\eta z\right)_\xi, \end{aligned} \tag{2.30}$$

$$\begin{aligned} \xi_y/J &= \left(z_\eta x\right)_\zeta - \left(z_\zeta x\right)_\eta, \\ \eta_y/J &= \left(z_\zeta x\right)_\xi - \left(z_\xi x\right)_\zeta, \\ \zeta_y/J &= \left(z_\xi x\right)_\eta - \left(z_\eta x\right)_\xi, \end{aligned} \tag{2.31}$$

$$\begin{aligned} \xi_z/J &= \left(x_\eta y\right)_\zeta - \left(x_\zeta y\right)_\eta, \\ \eta_z/J &= \left(x_\zeta y\right)_\xi - \left(x_\xi y\right)_\zeta, \\ \zeta_z/J &= \left(x_\xi y\right)_\eta - \left(x_\eta y\right)_\xi. \end{aligned} \tag{2.32}$$

$\tilde{U}$, $\tilde{V}$, $\tilde{W}$ are given by

$$\tilde{U} = \xi_x\tilde{u} + \xi_y\tilde{v} + \xi_z\tilde{w}, \tag{2.33}$$

$$\tilde{V} = \eta_x\tilde{u} + \eta_y\tilde{v} + \eta_z\tilde{w}, \tag{2.34}$$

$$\tilde{W} = \zeta_x\tilde{u} + \zeta_y\tilde{v} + \zeta_z\tilde{w}. \tag{2.35}$$

The grid filter width, Δ is taken as

$$\Delta = \left(\frac{1}{J}\right)^{1/3}. \tag{2.36}$$

2.2 Numerical Methods

In this section, the numerical methods that are used for spatial and temporal discretization of the governing equations as well as the boundary conditions and implicit spatial filtering techniques will be introduced.

2.2.1 Spatial Discretization

We first transform a given non-uniformly spaced curvilinear computational grid in the physical space to a uniform grid in the computational space and solve the discretized governing equations on the uniform grid. To compute the spatial derivatives at interior grid points away from the boundaries, we employ the following non-dissipative sixth-order compact scheme of Lele [50]

$$\frac{1}{3}f'_{i-1} + f'_i + \frac{1}{3}f'_{i+1} = \frac{7}{9\Delta\xi}\big(f_{i+1} - f_{i-1}\big) + \frac{1}{36\Delta\xi}\big(f_{i+2} - f_{i-2}\big), \tag{2.37}$$

where f'_i is the approximation of the first derivative of f at point i along the ξ direction, f_i denotes the value of f at grid point i, and $\Delta\xi$ is the uniform grid spacing in the ξ direction. For the left boundary at $i = 1$ and the right boundary at $i = N$, we apply the following third-order one-sided compact scheme equations, respectively

$$f'_1 + 2f'_2 = \frac{1}{2\Delta\xi}\big(-5f_1 + 4f_2 + f_3\big), \tag{2.38}$$

$$f'_N + 2f'_{N-1} = \frac{1}{2\Delta\xi}\big(5f_N - 4f_{N-1} - f_{N-2}\big). \tag{2.39}$$

For the points at $i = 2$ and $i = N - 1$ next to the boundaries, we use the following fourth-order central compact scheme formulations, respectively

$$\frac{1}{4}f'_1 + f'_2 + \frac{1}{4}f'_3 = \frac{3}{4\Delta\xi}\big(f_3 - f_1\big), \tag{2.40}$$

$$\frac{1}{4}f'_{N-2} + f'_{N-1} + \frac{1}{4}f'_N = \frac{3}{4\Delta\xi}\big(f_N - f_{N-2}\big). \tag{2.41}$$

2.2.2 Spatial Filtering

Spatial filtering is sometimes used as a means of suppressing unwanted numerical instabilities that can arise from the boundary conditions, unresolved scales and mesh non-uniformities. In our study, we considered two different filters. We initially used the following fourth-order compact filter developed by Lele [50]

$$\begin{aligned}\alpha_2\overline{f}_{i-2} + \alpha_1\overline{f}_{i-1} + \overline{f}_i + \alpha_1\overline{f}_{i+1} + \alpha_2\overline{f}_{i+2} = a_1 f_i + a_2(f_{i+1} + f_{i-1}) \\ + a_3(f_{i+2} + f_{i-2}) + a_4(f_{i+3} + f_{i-3}),\end{aligned} \tag{2.42}$$

where f_i and $\overline{f}_i$ represent the solution variable and the spatially filtered solution variable at point i, respectively and the coefficients are given by

$$\begin{gathered}\alpha_1 = 0.652247 \quad \alpha_2 = 0.170293, \\ a_1 = \frac{2+3\alpha_1}{4} \quad a_2 = \frac{9+16\alpha_1+10\alpha_2}{32}, \\ a_3 = \frac{\alpha_1+4\alpha_2}{8} \quad a_4 = \frac{6\alpha_2-1}{32}.\end{gathered} \tag{2.43}$$

The application of this filter results in a penta-diagonal system of equations. The filter transfer function of this filter is plotted in figure 2.1. It was determined by Zhao [51] that filtering at and near the boundaries is not necessary and therefore, this filter is used on grid points $i = 5$ through $i = N-4$ where N is the total number of grid points along the grid line.

The second filter we considered is the following sixth-order tri-diagonal filter used by Visbal and Gaitonde [49]

$$\alpha_f \overline{f}_{i-1} + \overline{f}_i + \alpha_f \overline{f}_{i+1} = \sum_{n=0}^{3} \frac{a_n}{2} \left(f_{i+n} + f_{i-n} \right), \tag{2.44}$$

where

$$a_0 = \frac{11}{16} + \frac{5\alpha_f}{8} \quad a_1 = \frac{15}{32} + \frac{17\alpha_f}{16} \quad a_2 = \frac{-3}{16} + \frac{3\alpha_f}{8} \quad a_3 = \frac{1}{32} - \frac{\alpha_f}{16}. \tag{2.45}$$

The parameter α_f must satisfy the inequality $-0.5 < \alpha_f < 0.5$. A less dissipative filter is obtained with higher values of α_f within the given range. With $\alpha_f = 0.5$, there is no filtering effect. This filter was used in various simulations with α_f set to values of 0.49, 0.47, and 0.45. Filter transfer functions of this filter for these three α_f values are shown in figure 2.1. Since this filter has a 7-point right-hand side stencil, it obviously cannot be used at near-boundary points. Instead, the following sixth-order equation with a one-sided right-hand side stencil is used at grid points near the left boundary point $i = 1$ [49]

$$\alpha_f \overline{f}_{i-1} + \overline{f}_i + \alpha_f \overline{f}_{i+1} = \sum_{n=1}^{7} a_{n,i} f_n \qquad i = 2, 3, \tag{2.46}$$

with

$$a_{1,2} = \frac{1}{64} + \frac{31\alpha_f}{32} \quad a_{2,2} = \frac{29}{32} + \frac{3\alpha_f}{16} \quad a_{3,2} = \frac{15}{64} + \frac{17\alpha_f}{32},$$
$$a_{4,2} = \frac{-5}{16} + \frac{5\alpha_f}{8} \quad a_{5,2} = \frac{15}{64} - \frac{15\alpha_f}{32} \quad a_{6,2} = \frac{-3}{32} + \frac{3\alpha_f}{16}, \tag{2.47}$$
$$a_{7,2} = \frac{1}{64} - \frac{\alpha_f}{32},$$

and

$$a_{1,3} = \frac{-1}{64} + \frac{\alpha_f}{32} \quad a_{2,3} = \frac{3}{32} + \frac{13\alpha_f}{16} \quad a_{3,3} = \frac{49}{64} + \frac{15\alpha_f}{32},$$
$$a_{4,3} = \frac{5}{16} + \frac{3\alpha_f}{8} \quad a_{5,3} = \frac{-15}{64} + \frac{15\alpha_f}{32} \quad a_{6,3} = \frac{3}{32} - \frac{3\alpha_f}{16}, \tag{2.48}$$
$$a_{7,3} = \frac{-1}{64} + \frac{\alpha_f}{32}.$$

For the points near the right boundary point $i = N$, we apply a similar formulation

$$\alpha_f \overline{f}_{i-1} + \overline{f}_i + \alpha_f \overline{f}_{i+1} = \sum_{n=0}^{6} a_{N-n,i} f_{N-n} \qquad i = N-2, N-1, \tag{2.49}$$

where

$$a_{N-n,i} = a_{n+1,N-i+1} \qquad i = N-2, N-1 \qquad n = 0, 6. \tag{2.50}$$

The boundary points, $i = 1$ and $i = N$ are left unfiltered.

The spatial filtering operation is carried out in the uniformly spaced computational domain. The conservative flow variables are filtered in all spatial directions at the end of every time step. In DNS calculations, filtering is typically used to maintain numerical stability. The filter eliminates all the scales that cannot be resolved by the finite difference scheme. Hence, in LES calculations, the filter is treated as the grid filter.

2.2.3 Test Filtering

During the dynamic computation of the subgrid-scale model coefficients, test filtering is needed in order to extract the necessary information contained within the

smallest resolved scales of motion. For test filtering, the following 15-point explicit filter developed by Bogey and Bailly [48] is employed

$$\widehat{f_i} = \sum_{n=0}^{7} d_n (f_{i-n} + f_{i+n}), \tag{2.51}$$

where f_i and $\widehat{f_i}$ represent the quantity and the test filtered quantity at point i, respectively and the coefficients d_n are given by

$$\begin{gathered} d_0 = 0.25 \quad d_1 = 0.30834723 \quad d_2 = 0, \\ d_3 = -0.07876835 \quad d_4 = 0 \quad d_5 = 0.02617123, \\ d_6 = 0 \quad d_7 = -0.00575011. \end{gathered} \tag{2.52}$$

The filter transfer function of this filter is shown in figure 2.1. The test filtering operation is carried out in the uniformly spaced computational domain.

2.2.4 Time Integration

The standard fourth-order explicit Runge-Kutta scheme is used for time advancement. The governing equations can be expressed in the following form

$$\frac{\partial \mathbf{q}}{\partial t} = \mathbf{RHS}(\mathbf{q}; t), \tag{2.53}$$

where $\mathbf{q}$ is the vector of the conservative variables. Following Mitchell *et al.* [52], the first step of the Runge-Kutta time advancement scheme is an Euler predictor

$$\begin{aligned} \mathbf{q}^{'} &= \mathbf{RHS}(\mathbf{q}^n; t_n) \\ \tilde{\mathbf{q}} &= \mathbf{q}^n + \frac{\Delta t}{2}\mathbf{q}^{'} \\ \hat{\mathbf{q}} &= \mathbf{q}^n + \frac{\Delta t}{6}\mathbf{q}^{'}, \end{aligned} \tag{2.54}$$

followed by an Euler corrector

$$\mathbf{q}^{'} = \mathbf{RHS}\left(\tilde{\mathbf{q}}; t_n + \frac{\Delta t}{2}\right)$$

$$\tilde{\mathbf{q}} = \mathbf{q}^n + \frac{\Delta t}{2}\mathbf{q}^{'}$$
$$\hat{\mathbf{q}} = \hat{\mathbf{q}} + \frac{\Delta t}{3}\mathbf{q}^{'}, \tag{2.55}$$

followed by a leapfrog predictor

$$\mathbf{q}^{'} = \mathbf{RHS}\left(\tilde{\mathbf{q}}; t_n + \frac{\Delta t}{2}\right)$$
$$\tilde{\mathbf{q}} = \mathbf{q}^n + \Delta t\mathbf{q}^{'}$$
$$\hat{\mathbf{q}} = \hat{\mathbf{q}} + \frac{\Delta t}{3}\mathbf{q}^{'}, \tag{2.56}$$

and concluded by a Milne corrector as follows

$$\mathbf{q}^{'} = \mathbf{RHS}(\tilde{\mathbf{q}}; t_n + \Delta t)$$
$$\mathbf{q}^{n+1} = \hat{\mathbf{q}} + \frac{\Delta t}{6}\mathbf{q}^{'}. \tag{2.57}$$

This time integration scheme requires 2 temporary arrays, $\tilde{\mathbf{q}}$, $\hat{\mathbf{q}}$ and the solution vector at time step n, $\mathbf{q}^n$ to be stored.

2.2.5 Boundary Conditions and Inflow Forcing

Several boundary conditions were used throughout the course of this study. We initially employed Thompson's non-reflecting boundary conditions [53, 54] on all boundaries of the domain except for the inflow boundary. The form of Thompson's non-reflecting boundary conditions in curvilinear coordinates that were formulated by Jiang *et al.* [55] were used in the Reynolds number $3,600$ jet and and some of the Reynolds number $36,000$ jet calculations. However, during our 3-D turbulent round jet simulations at a Reynolds number of $36,000$, we discovered that Thompson's boundary conditions actually did not provide the correct entrainment flow physics on the boundaries of a Cartesian grid. The ambient fluid that is entrained by a round jet should be coming in radially towards the jet centerline along the boundaries of the Cartesian grid. However, it was found that with Thompson's boundary conditions, the entrained fluid came in at almost normal angles pretty much everywhere along

the boundaries except at the corners. Hence, we decided to abandon Thompson's boundary conditions completely and switch to the boundary conditions of Tam and Dong [56] instead. The original two-dimensional boundary conditions of Tam and Dong were recently extended to 3-D by Bogey and Bailly [57]. The following radiation boundary conditions formulated in spherical coordinates are applied on the lateral boundaries of the computational domain illustrated in figure 2.2

$$\frac{1}{V_g}\frac{\partial}{\partial t}\begin{pmatrix}\rho\\ u\\ v\\ w\\ p\end{pmatrix}+\left(\frac{\partial}{\partial r}+\frac{1}{r}\right)\begin{pmatrix}\rho-\bar{\rho}\\ u-\bar{u}\\ v-\bar{v}\\ w-\bar{w}\\ p-\bar{p}\end{pmatrix}=0, \tag{2.58}$$

where ρ, u, v, w, p are the local primitive flow variables on the boundary, $\bar{\rho}$, $\bar{u}$, $\bar{v}$, $\bar{w}$, $\bar{p}$ are the local mean flow properties, V_g is the so-called acoustic group velocity defined as

$$V_g=(\bar{\mathbf{u}}+\bar{\mathbf{c}})\cdot\mathbf{e}_r=\bar{\mathbf{u}}\cdot\mathbf{e}_r+\sqrt{\bar{c}^2-(\bar{\mathbf{u}}\cdot\mathbf{e}_\theta)^2-(\bar{\mathbf{u}}\cdot\mathbf{e}_\phi)^2}, \tag{2.59}$$

$\bar{\mathbf{c}}$ is the local mean sound velocity vector and $|\bar{\mathbf{c}}|=\bar{c}$. $\mathbf{e}_r$, $\mathbf{e}_\theta$, $\mathbf{e}_\phi$ respectively denote the unit vectors in r, θ and ϕ directions of the spherical coordinate system shown in figure 2.3. These unit vectors can be expressed in terms of Cartesian coordinates as

$$\begin{aligned}\mathbf{e}_r&=(\sin\theta\cos\phi,\sin\theta\sin\phi,\cos\theta),\\ \mathbf{e}_\theta&=(\cos\theta\cos\phi,\cos\theta\sin\phi,-\sin\theta),\\ \mathbf{e}_\phi&=(-\sin\phi,\cos\phi,0).\end{aligned} \tag{2.60}$$

The acoustic group velocity is actually the same as the wave propagation speed, and is equal to the projection of the vector sum of the local mean sound velocity and local mean flow velocity onto the sound propagation direction. It is assumed that in the far field, the outgoing acoustic disturbances are propagating in the radial direction relative to the acoustic source.

The local mean flow variables as well as their spatial derivatives are calculated during the simulation. The position vector, r is computed as

$$r = \sqrt{(x - x_{source})^2 + (y - y_{source})^2 + (z - z_{source})^2}, \tag{2.61}$$

where x, y, z are the coordinates of the boundary point, and x_{source}, y_{source}, z_{source} are the coordinates of the acoustic source location. In jet flow computations, the source location is usually chosen as the end of the potential core of the jet. The derivative along the r direction is expressed in terms of the derivatives in the Cartesian coordinate system as follows

$$\frac{\partial}{\partial r} = \nabla \cdot \mathbf{e}_r = \sin\theta\cos\phi\frac{\partial}{\partial x} + \sin\theta\sin\phi\frac{\partial}{\partial y} + \cos\theta\frac{\partial}{\partial z}, \tag{2.62}$$

where ∇ is the gradient operator in the Cartesian coordinate system.

Tam and Dong's radiation boundary conditions are formulated for boundaries to which only acoustic disturbances are reaching. The lateral boundaries of figure 2.2 are therefore suitable for the application of these boundary conditions. However, radiation boundary conditions cannot be applied on the outflow boundary of figure 2.2 since there are entropy and vorticity waves in addition to the acoustic waves crossing this boundary. Instead, Tam and Dong's outflow boundary conditions are imposed on the outflow boundary as follows

$$\begin{aligned}
\frac{\partial \rho}{\partial t} + \bar{\mathbf{u}}\cdot\nabla(\rho - \bar{\rho}) &= \frac{1}{\bar{c}^2}\left(\frac{\partial p}{\partial t} + \bar{\mathbf{u}}\cdot\nabla(p - \bar{p})\right), \\
\frac{\partial u}{\partial t} + \bar{\mathbf{u}}\cdot\nabla(u - \bar{u}) &= -\frac{1}{\bar{\rho}}\frac{\partial(p - \bar{p})}{\partial x}, \\
\frac{\partial v}{\partial t} + \bar{\mathbf{u}}\cdot\nabla(v - \bar{v}) &= -\frac{1}{\bar{\rho}}\frac{\partial(p - \bar{p})}{\partial y}, \\
\frac{\partial w}{\partial t} + \bar{\mathbf{u}}\cdot\nabla(w - \bar{w}) &= -\frac{1}{\bar{\rho}}\frac{\partial(p - \bar{p})}{\partial z}, \\
\frac{1}{V_g}\frac{\partial p}{\partial t} + \frac{\partial(p - \bar{p})}{\partial r} + \frac{(p - \bar{p})}{r} &= 0.
\end{aligned} \tag{2.63}$$

Since the actual nozzle geometry is not included in the present calculations, we initially thought that the inflow boundary should be responsible for generating

disturbances that trigger the growth of instabilities in the flowfield in addition to allowing the outgoing acoustic waves to leave the domain. For the inflow boundary conditions, we initially applied a procedure based on characteristics [51]. In this procedure, it should first be noted that the right-hand side of the Navier-Stokes equations or the time derivative of the conservative variables, i.e.,

$$\frac{\partial \mathbf{Q}}{\partial t} = RHS, \tag{2.64}$$

involves computing the spatial derivatives of the fluxes. Since compact finite differences are used, the flux derivatives are computed at all boundary points as well as interior points. Now, consider the inflow boundary located at $x = 0$ in figure 2.2. The $+x$ direction corresponds to the streamwise direction. For all boundaries except for the inflow boundary, the right hand sides are overwritten by the time derivatives obtained by applying Thompson's non-reflecting or Tam and Dong's boundary conditions. Then, all the points are time advanced. Using the new solution on the inflow boundary, we estimate the amplitude of the outgoing acoustic wave that propagates in the $-x$ direction as follows

$$\Lambda_5 = (p_c - \bar{p}) - \bar{\rho}\bar{c}(u_c - \bar{u}), \tag{2.65}$$

where p_c and u_c are the pressure and streamwise velocity on the inflow boundary, respectively, that are obtained from the time integration. In the above equation, $\bar{p}$, $\bar{\rho}$, $\bar{u}$, $\bar{c}$ are the local mean values of pressure, density, streamwise velocity and speed of sound, respectively. Once Λ_5 is estimated, the incoming acoustic wave that propagates in the $+x$ direction is calculated from

$$\Lambda_1 = \Lambda_5 + 2\bar{\rho}\bar{c}(u_f - \bar{u}), \tag{2.66}$$

where u_f is the forced streamwise velocity on the inflow boundary. Details on u_f are given in Chapter 4. Then, using Λ_1 and Λ_5, we calculate the pressure fluctuation on the boundary as follows

$$p' = \frac{1}{2}(\Lambda_1 + \Lambda_5). \tag{2.67}$$

Finally, the density fluctuation is computed using the amplitude of the entropy wave, Λ_2 and p'

$$\rho' = \frac{1}{\bar{c}^2}(p' - \Lambda_2). \tag{2.68}$$

The amplitude of the entropy wave Λ_2 is usually set to zero. p' and ρ' are then added to $\bar{p}$ and $\bar{\rho}$ to get the pressure and density on the inflow boundary.

Velocity fluctuations on the two transverse velocity components can also be imposed. These fluctuations determine the amplitude of the two incoming vorticity waves

$$\Lambda_3 = \bar{\rho}\bar{c}v', \tag{2.69}$$

$$\Lambda_4 = \bar{\rho}\bar{c}w', \tag{2.70}$$

where v', w' are the velocity fluctuations applied on the mean y and z velocities, respectively. Details on v' and w' are given in Chapter 4. For jet flow computations, the mean transverse velocities on the inflow boundary are set to zero.

Simulations of Reynolds number $3,600$ and $36,000$ jets were done using these inflow boundary conditions. During these simulations, it was realized that the implementation of the inflow boundary conditions in the above described form were resulting in reflections of the upstream propagating acoustic waves from the inflow boundary. Furthermore, the forcing procedure applied on the inflow boundary was found to generate some artificial noise which contaminated the natural sound field of the jet. Acoustic wave reflections as well as excessive artificial noise were not acceptable and consequently the inflow boundary conditions described above were completely abandoned. In the new inflow boundary implementation, we decided to apply Tam and Dong's 3-D radiation boundary conditions [57] on the inflow boundary of the computational domain as illustrated in figure 2.4 which summarizes how the boundary conditions are handled in the latest version of the LES code. In this figure, vorticity magnitude contours are shown within the jet while divergence of velocity contours are shown in the outer part of the computational domain. The new implementation of the inflow boundary conditions was found to be truly non-

reflecting since the new inflow boundary conditions let the outgoing acoustic waves exit the inflow boundary without spurious reflection back into the domain.

We also decided to modify the inflow forcing technique since the previous inflow forcing procedure was found to be generating some spurious noise. In the new inflow forcing, randomized velocity perturbations in the form of a vortex ring are added into the jet shear layers at a short distance downstream of the inflow boundary in order to excite the 3-D instabilities in the jet and cause the potential core of the jet to break up at a reasonable distance downstream of the inflow boundary. This forcing procedure has been adapted from Bogey *et al.* [58]. A vortex ring whose radius is equal to the initial jet radius, r_o is considered in this type of forcing. The vortex ring has a mean axial and radial velocity distribution which can be computed using the analytical expressions given in Bogey *et al.* [58], but it has no azimuthal velocity. The mean axial and radial velocity components of the vortex ring of radius of r_o are respectively given as

$$U_{x_{ring}} = 2\frac{r_o}{r}\frac{r - r_o}{\Delta_o}\exp\left(-\ln(2)\left(\frac{\Delta(x,y)}{\Delta_o}\right)^2\right), \tag{2.71}$$

$$U_{r_{ring}} = -2\frac{r_o}{r}\frac{x - x_o}{\Delta_o}\exp\left(-\ln(2)\left(\frac{\Delta(x,y)}{\Delta_o}\right)^2\right), \tag{2.72}$$

for $r = \sqrt{y^2 + z^2} \neq 0$, where Δ_o is the minimum grid spacing in the jet shear layer, $\Delta(x,y)^2 = (x - x_o)^2 + (r - r_o)^2$, x_o is the streamwise location of the center of the vortex ring and is usually chosen as $x_o = r_o$. There are certain number of azimuthal modes involved in the forcing. The amplitude and phase of each forcing mode are randomly picked within a specified range of values by using a random number generator. The parameter α controls the strength of the perturbations. Streamwise and radial velocity perturbations are added onto the local velocity components as follows

$$v_x = v_x + \alpha U_{x_{ring}} U_o \sum_{n=0}^{n_{modes}} \epsilon_n \cos(n\Theta + \varphi_n), \tag{2.73}$$

$$v_r = v_r + \alpha U_{r_{ring}} U_o \sum_{n=0}^{n_{modes}} \epsilon_n \cos(n\Theta + \varphi_n), \tag{2.74}$$

where $\Theta = \arctan(y/z)$, ϵ_n and φ_n are randomly generated numbers that satisfy $-1 < \epsilon_n < 1$ and $0 < \varphi_n < 2\pi$, respectively. Due to the circular nature of the vortex ring, the velocity perturbations given above are formulated in cylindrical coordinates. However, one can easily convert these fluctuations to the Cartesian coordinate system. The total number of forcing modes, $n_{modes} + 1$, is usually chosen as 10 or more. Combining the basic vortex ring's mean velocity distribution with the azimuthal forcing modes produces randomized axial and radial velocity disturbances in the form of a vortex ring which are added into the initial jet shear layers. The reader is referred to Reference [58] for more details. The vortex ring forcing described here is approximately solenoidal and therefore quiet. The simulations of Reynolds number $100,000$ and $400,000$ jets were performed using the new inflow boundary conditions and the new inflow forcing technique. Details of the number of modes and the α parameter used in these simulations are given in Chapters 5 and 6.

2.2.6 Sponge Zone

It is known that numerical reflections usually arise from the outflow boundaries which strong vortices convecting downstream must pass through in order to leave the domain. Such unwanted reflections, if left untreated, will propagate upstream and contaminate the acoustic field. They can even cause the computations to blow up. To avoid such problems, we use the sponge zone method proposed by Colonius *et al.* [59]. This approach has been shown to be quite effective in minimizing reflections from the outflow boundary. In this method, a sponge zone is attached downstream of the physical domain as shown in figures 2.2 and 2.4. We apply grid stretching together with explicit filtering or artificial damping along the streamwise direction in this exit zone to dissipate the vortices present in the flowfield before they hit the outflow boundary. In our initial simulations, we employed second-order filtering and used Thompson's non-reflecting boundary conditions without any modification at the end of the sponge zone. Use of the second-order explicit filtering

together with Thompson's boundary conditions were observed to be stable. However, when we implemented Tam and Dong's outflow boundary conditions and kept the same second-order explicit filtering in the sponge zone, numerical instabilities were observed on the outflow boundary. These instabilities are believed to be due to the interaction of the second-order explicit filtering and Tam and Dong's outflow boundary conditions. Therefore, we decided to switch to artificial damping instead of explicit filtering in the sponge zone. The combination of artificial damping and Tam and Dong's outflow boundary conditions was found to be stable and did not cause any further problems. The turbulent flow field in the sponge zone is forced towards a smooth solution through the use of a damping term which is added to the right hand side of the governing equations as follows

$$\frac{\partial \mathbf{Q}}{\partial t} = RHS - \chi(x)(\mathbf{Q} - \mathbf{Q_{target}}). \tag{2.75}$$

In the above equation,

$$\chi(x) = \chi_{max}\left(\frac{x - x_{phy}}{x_{max} - x_{phy}}\right)^3, \tag{2.76}$$

where x is the streamwise location, x_{phy} is the streamwise coordinate of the end of the physical portion of the domain, x_{max} is the streamwise coordinate of the end of the sponge zone, $\mathbf{Q}$ is the vector of conservative variables, $\mathbf{Q_{target}}$ is the target solution in the sponge zone, and $\chi(x)$ controls the strength of the damping term with the value of χ_{max} usually chosen around 1.0. In jet simulations, the target solution is usually specified as the self-similar solution of an isothermal incompressible round jet.

2.3 LES Code Parallelization

Both the compact scheme and the implicit spatial filter are non-local since they require the solution of a linear system of equations along the grid lines. Consequently, one needs all of the data points along a given grid line in order to compute the derivatives and filter the solution along that spatial direction. Because of this

requirement, the transposition strategy depicted in figure 2.5 was chosen for code parallelization. Initially, the grid is partitioned along the z direction only as shown in the top configuration and each block is assigned to a processor. In this configuration, one can compute the derivatives and do filtering along the x and y directions in each block independently from all other blocks. However, in order to apply the compact scheme and the filter along the z direction, a data transposition is needed for the re-alignment of the blocks as shown in the bottom configuration. Only then, the processors can apply the compact scheme and the filter along the z direction. Once the computations along the z direction are finished, then another transposition back to the initial configuration has to be done in order to send the newly computed information back to the original configuration for further use.

The Fortran 90 programming language has been used for code development. Optimized LAPACK (Linear Algebra Package) subroutines are employed to solve the linear systems of equations which arise during the application of the compact differencing scheme as well as the implicit spatial filter. As will be evident shortly, great care has been taken to minimize cache misses and optimize the code performance as much as possible. The conservative formulation of the governing Navier-Stokes equations are chosen for discretization in order to minimize the number of spatial differencing operations. In addition, advanced compiler optimization flags are used during code compilation in order to further improve our code performance. The standard MPI (Message Passing Interface) library routines have been used in the code parallelization. The code has restarting capability, so a simulation can be run in many stages.

To evaluate the performance of the latest version of our code, we did test runs on a $470 \times 160 \times 160$-node computational grid using 20, 40, 80, and 160 processors on the *Lemieux* cluster at the Pittsburgh Supercomputing Center. Approximately 16 GB of memory was needed for the test runs on the given grid, hence we were unable to test the code performance on fewer than 20 processors since the total amount of memory available would be insufficient in such cases.

We assumed a speedup value of 1 for the 20-processor run and then computed our speedups relative to the 20-processor run. Figure 2.6 shows the parallel performance of our code on *Lemieux*. As can be observed from the plot, the code scales very well and super-linear speedups have been obtained when the code is run on 80 or more processors. The code is memory intensive and each processor works on a smaller set of memory as the number of partitions are increased. The excellent performance is due to the fact that with more processors the problem data handled by any one processor fits better in cache memory, so fewer cache misses happen and each processor executes faster than the single processor could. These observations provide us with the proof for the excellent performance of our LES code on the *Lemieux* cluster.

We also did some test runs by increasing the grid size in proportion to the number of processors. In other words, the overall grid size was adjusted as the number of processors increased so that the memory per processor remained constant and every processor did the same amount of work in all test runs. This test was performed on an IBM-SP3 machine using 20, 40, 80 and 160 processors in parallel. Every processor worked on 300,800 grid points during the test runs. We now define an efficiency parameter (with respect to the 20-processor test run) as the run time with 20 processors divided by the run time with N processors. Figure 2.7 shows how the efficiency varies as the number of processors increases. The efficiency is equal to 1 when the number of processors is equal to 20. Then, it starts to drop gradually as the number of processors increases. As the number of processors reaches 160, we get an efficiency of about 76% which is quite satisfactory. Hence, we see that the parallel code has a good efficiency when it is run on a large number of processors.

2.4 Surface Integral Acoustics Methods

Far field noise computations are done by coupling the time accurate near field flow field data provided by the LES code with surface integral acoustics methods

[60], [61] such as Kirchhoff's method and the Ffowcs Williams - Hawkings method. A description of these methods will be given in this section.

2.4.1 Kirchhoff's Method

In Kirchhoff's method, it is assumed that the following linear, homogeneous wave equation

$$\frac{1}{c_\infty^2}\frac{\partial^2 p'}{\partial t^2} - \frac{\partial^2 p'}{\partial x_i \partial x_i} = 0, \tag{2.77}$$

is valid for the acoustic pressure variable, p', in the entire region outside of a closed and bounded smooth surface, S.

For a stationary surface, Kirchhoff's formula is the following integral representation of the solution to the linear, homogeneous wave equation

$$4\pi p'(\vec{x},t) = \int_S \frac{1}{r}\left[\frac{1}{c_\infty}\dot{p}'\cos\vartheta - \frac{\partial p'}{\partial n}\right]_{ret} dS + \int_S \frac{[p'\cos\vartheta]_{ret}}{r^2} dS. \tag{2.78}$$

Here, $(\vec{x},t)$ are the observer coordinates and time, r is the distance from the source on the surface to the observer, ϑ is the source emission angle such that $\cos\vartheta = \mathbf{r}\cdot\mathbf{n}$ where $\mathbf{n}$ is the control surface unit normal vector and $\mathbf{r}$ is the unit vector in the radiation direction. The dot over a variable indicates a time derivative. The surface integrals are evaluated over the control surface S, and subscript ret indicates evaluation of the integrands at the emission (retarded) time, $\tau = t - r/c_\infty$.

Since Kirchhoff's method is based on the linear wave equation, it works well for aeroacoustic predictions when the control surface is placed in a region of the flow field where the linear wave equation is valid. However, this might not be possible for some cases. Additional nonlinearities such as quadrupoles can be added outside the control surface [62]. Kirchhoff's method has also been applied for open surfaces [63] and can be extended to include mean flow refraction effects [64].

2.4.2 Ffowcs Williams - Hawkings Method

The Ffowcs Williams - Hawkings formulation for a stationary permeable control surface, S is given as follows

$$p'(\vec{x},\ t) = p'_T(\vec{x},\ t) + p'_L(\vec{x},\ t) + p'_Q(\vec{x},\ t), \tag{2.79}$$

where

$$4\pi p'_T(\vec{x},\ t) = \int_S \left[\frac{\rho_\infty \dot{U}_n}{r}\right]_{ret} dS, \tag{2.80}$$

$$4\pi p'_L(\vec{x},\ t) = \frac{1}{c_\infty} \int_S \left[\frac{\dot{L}_r}{r}\right]_{ret} dS + \int_S \left[\frac{L_r}{r^2}\right]_{ret} dS, \tag{2.81}$$

and

$$U_i = \frac{\rho u_i}{\rho_\infty}, \tag{2.82}$$

$$L_i = p'\delta_{ij}n_j + \rho u_i u_n. \tag{2.83}$$

$(\vec{x}, t)$ are the observer coordinates and time, r is the distance from the source on the surface to the observer, subscript ∞ implies ambient conditions, and c_∞ is the ambient sound speed. The dot over a variable indicates a time derivative, a subscript r or n indicates a dot product of the vector with the unit vector in the radiation direction $\mathbf{r}$ or the unit vector in the surface normal direction $\mathbf{n}$, respectively. The surface integrals are over the control surface S, and the subscript ret indicates evaluation of the integrands at the emission time, $\tau = t - r/c_\infty$. The quadrupole noise pressure $p'_Q(\vec{x},\ t)$ denotes the quadrupole sources outside the control surface and consists of a volume integral. This term has been neglected in this study.

The Ffowcs Williams - Hawkings formulation is based on the conservation laws of fluid mechanics rather than the wave equation. Brentner and Farassat [65] showed that if the quadrupole term is neglected outside the control surface, the Ffowcs Williams - Hawkings solution is less sensitive than Kirchhoff's method to the placement of integration surface in the non-linear flow region. They also showed that the Ffowcs Williams - Hawkings formulation is equivalent to the Kirchhoff formulation when the integration surface is located in the linear wave propagation region.

2.4.3 Numerical Implementation of Surface Integral Acoustics Methods

Since the LES code runs on generalized curvilinear grids, the control surface on which time accurate flow data are gathered is divided into many 2-D quadrilateral elements. The flow quantities needed by the surface integral methods are stored at the quadrilateral element centers. There are 2 main stages involved in both Kirchhoff's method and the Ffowcs Williams - Hawkings method. In the first stage, a pre-processor program reads in the flow variables gathered on the control surface and computes the time derivatives of some quantities needed by these surface integral acoustics methods. The 6^{th}-order accurate compact scheme is applied along the temporal direction in order to compute the time derivatives. For Kirchhoff's method, only the time derivative of acoustic pressure is needed. For the Ffowcs Williams - Hawkings method, the time derivatives of U_n , L_1 , L_2 , and L_3 are needed (see the Ffowcs Williams - Hawkings formulation for these quantities). The time derivatives at every point in the time history are computed only once and stored in data files along with other quantities of interest for the two methods. Stage 1 takes place only once no matter how many observer points there are. The flow quantities that are stored for Kirchhoff's method are p', $\dot{p}'$, $\frac{\partial p'}{\partial n}$, whereas the flow quantities that are stored for the Ffowcs Williams - Hawkings method are $\rho_\infty \dot{U}_n$, L_1, L_2, L_3, $\dot{L}_1$, $\dot{L}_2$, $\dot{L}_3$.

In the second stage, the data produced in stage 1 are read in and the surface integrals are carried out to compute the far field noise. The surface integrals are performed in a discrete sense by adding up the contributions from every quadrilateral element on the surface. The run time of the second stage is almost the same for the two surface integral acoustics methods. This is because all time derivatives have already been computed in the first stage and stored along with other quantities of interest which are directly needed in the surface integrals. The second stage does the linear interpolation of the quantities produced in stage 1 to retarded times depending on the distance between the source and the observer. It then divides or multiplies the new values at the retarded times by some quantities that depend on

the observer location relative to the source (such as r or r^2, etc.) and finally adds up the contributions from all surface elements to calculate the acoustic pressure history.

The second stage is fully parallelized, hence the control surface is divided into many partitions and the surface integrals are carried out in parallel. In the second stage, the ratio of the memory needed for the Ffowcs Williams - Hawkings method to that needed for Kirchhoff's method is 7/3. The total run time of stage 2 depends on the total number of observer points. Run times of the acoustics codes will be given when aeroacoustics results are presented in Chapters 5, 6, and 7.

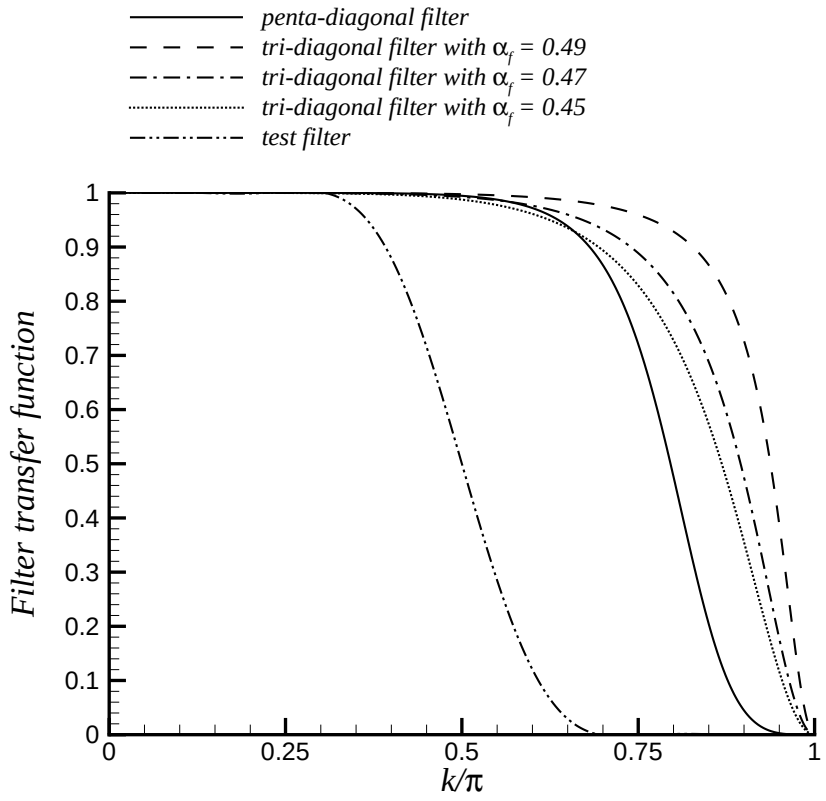

Figure 2.1. Transfer functions of various filters used in this study.

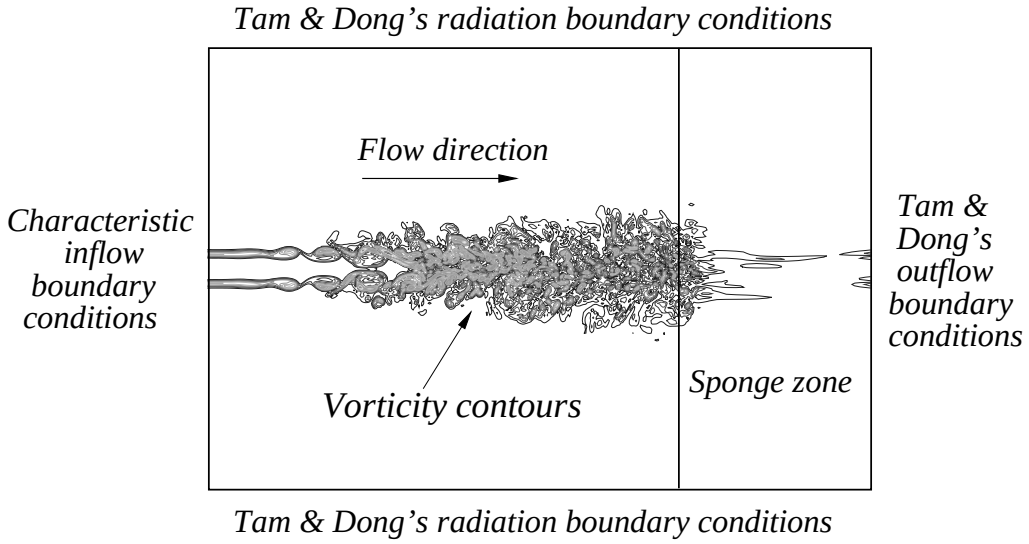

Figure 2.2. Schematic of the boundary conditions used in the initial simulations.

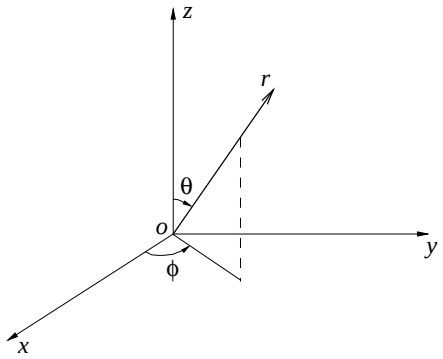

Figure 2.3. Spherical coordinate system used in the 3-D radiation and outflow boundary conditions.

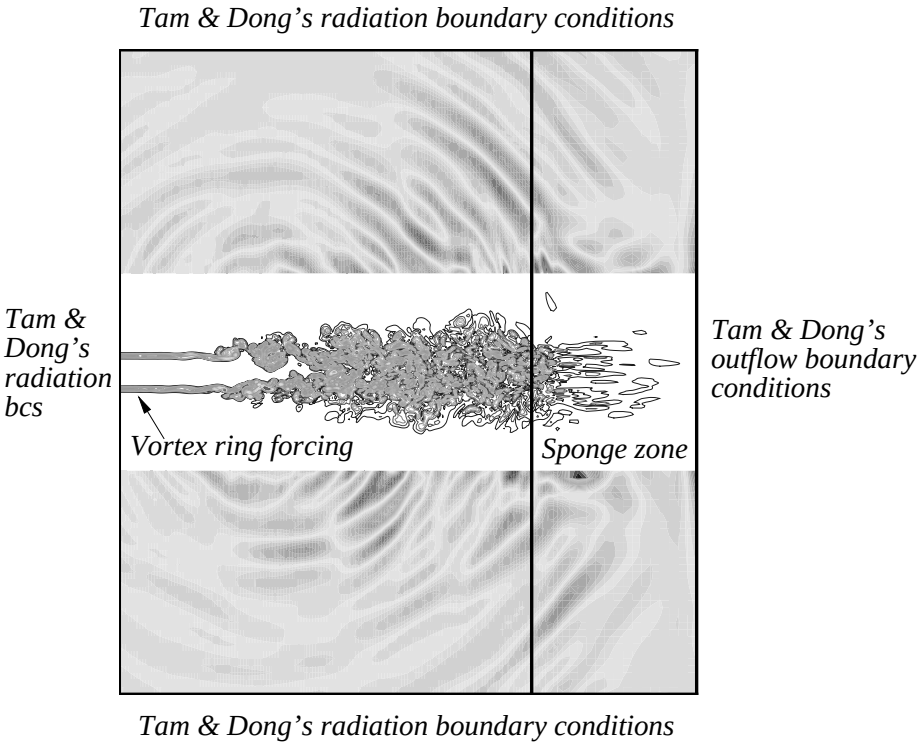

Figure 2.4. Schematic of the boundary conditions used in the latest version of the LES code.

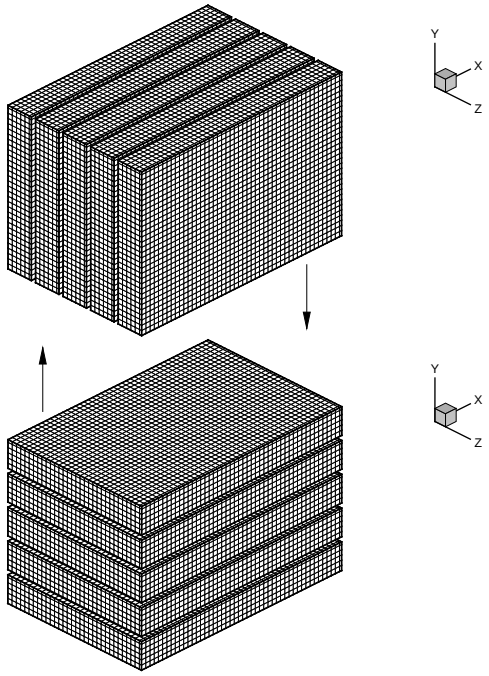

Figure 2.5. Transposition scheme used in parallel computing.

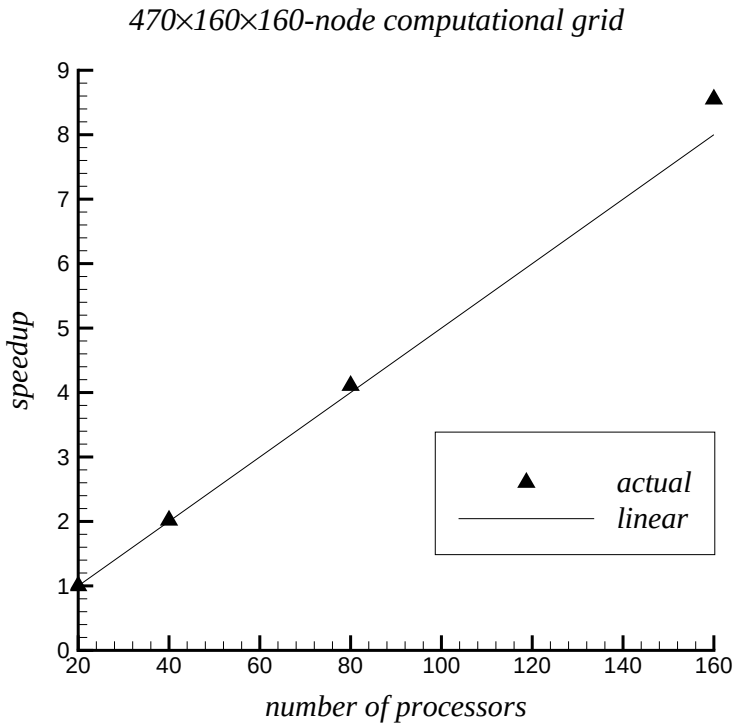

Figure 2.6. Parallel code speedup on the Compaq Alphaserver Cluster (*Lemieux*) at the Pittsburgh Supercomputing Center.

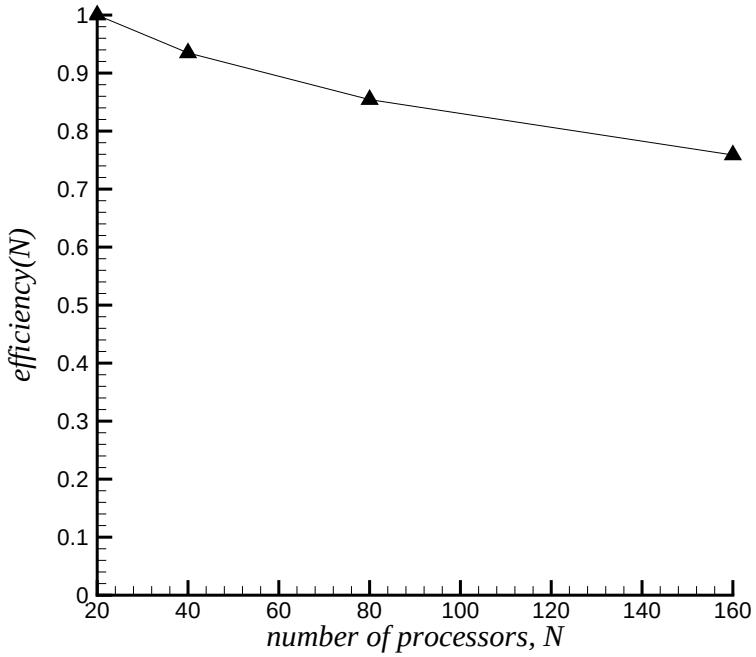

Figure 2.7. Parallel code efficiency on an IBM-SP3 machine.

3. 2-D MIXING LAYER SIMULATIONS

Our eventual aim in this work is to do turbulence simulations of fully turbulent three-dimensional jets which are an important class of free-shear flows. Mixing layers are another class of free-shear flows that are commonly studied. Before going to full three-dimensional turbulent jet simulations, we decided to test our simulation techniques in a two-dimensional free-shear flow. Therefore, we first examined the planar mixing layer problem. Planar shear layers have been studied experimentally by Wygnanski and Fiedler [66], Spencer and Jones [67] as well as Bell and Mehta [68], and computationally by Rogers and Moser [69], Stanley and Sarkar [70], and Bogey [71], among others. We did a DNS calculation for a mixing layer at a relatively low Reynolds number, as well as a LES calculation for a mixing layer at a higher Reynolds number and compared some of our results with available experimental and computational results in the literature.

3.1 Test Case 1 - DNS at a Reynolds Number of 720

In the first 2-D test case, we will perform a DNS calculation for a mixing layer. The following hyperbolic tangent inflow profile is given for the mean streamwise velocity

$$\bar{u}(y) = \frac{U_1 + U_2}{2} + \frac{U_2 - U_1}{2} \tanh\left(\frac{2y}{\delta_\omega(0)}\right), \tag{3.1}$$

and for the mean transverse velocity, we simply take

$$\bar{v}(y) = 0. \tag{3.2}$$

U_1 and U_2 are the velocities of the low-speed and high-speed streams, respectively, and $\delta_\omega(0)$ is the initial vorticity thickness, which is defined as

$$\delta_\omega(0) = \frac{U_2 - U_1}{\left|\frac{\partial U}{\partial y}\right|_{max}}. \tag{3.3}$$

The convection velocity is

$$U_c = \frac{U_1 + U_2}{2} = 0.375 c_\infty, \tag{3.4}$$

and the relative convective Mach number is

$$M_c = \frac{U_2 - U_1}{2 c_\infty} = 0.125, \tag{3.5}$$

where c_∞ is the ambient speed of sound. The Reynolds number based on the initial vorticity thickness and the velocity difference across the mixing layer is equal to

$$Re = \frac{(U_2 - U_1)\delta_\omega(0)}{\nu} = 720. \tag{3.6}$$

This test case is the same as the one studied by Stanley and Sarkar [70]. The computational grid used in our simulation is shown in figure 3.1. The domain extends to about $350\delta_\omega(0)$ in the streamwise x-direction and from $-300\delta_\omega(0)$ to $300\delta_\omega(0)$ in the transverse y-direction. The grid has 576 points along both directions. The minimum grid spacing in the y-direction is about $0.16\delta_\omega(0)$ around the centerline. Exponential grid stretching is applied in the transverse direction such that the maximum spacing around the upper and lower boundaries is about $3\delta_\omega(0)$. In the x-direction, the physical region extends up to about $x = 200\delta_\omega(0)$ and the region after $x = 200\delta_\omega(0)$ is the sponge region. In the physical region, the grid spacing in the x-direction is uniform and about $0.40\delta_\omega(0)$. In the sponge region, the grid is stretched using the grid-stretching function proposed by Colonius *et al.* [59]. The first 500 points in the x-direction are in the physical region and the remaining 76 points form the sponge region. In the simulation done by Stanley and Sarkar [70], a 375×99-node grid was used with a domain size of about $143\delta_\omega(0)$ in the x-direction and about $38\delta_\omega(0)$ in the y-direction. They kept the grid spacing in the x-direction constant at $0.38\delta_\omega(0)$. Their minimum grid spacing in the y-direction was about $0.19\delta_\omega(0)$ around the centerline. They also applied stretching in the y-direction using the grid stretching functions utilized by Colonius *et al.* [59] to form the sponge zone.

In order to simulate a naturally developing mixing layer, we apply the following random perturbation on the transverse velocity on the inflow boundary

$$v(y) = \epsilon\alpha U_c \exp\left(-\frac{y^2}{\Delta {y_0}^2}\right), \tag{3.7}$$

where ϵ is a random number between -1 and 1, $\alpha = 0.0045$, and Δy_0 is the minimum grid spacing in the y-direction. This kind of random perturbation was used by Bogey [71] to simulate a naturally developing mixing layer at a Reynolds number of $5,333$. We will also study the test case of Bogey [71] in the next part using LES with the same random forcing method.

Figure 3.2 shows the instantaneous vorticity contours for the naturally developing mixing layer. Occasional vortex pairing was observed in the domain at various locations during the simulation. Unlike a mixing layer forced at discrete frequencies, the position of the vortex pairing is not fixed at a certain location in a naturally developing mixing layer.

After the initial transients exited the domain, the code was run for 35,000 time steps and the flow statistics were gathered during this time interval. An acoustic wave travelling at the ambient sound speed travels a distance equal to about 16 times the domain length in the streamwise direction during this interval. Figure 3.3 plots the scaled mean streamwise velocity profiles at five stations. The scaled velocity is given by

$$f(\xi) = \frac{\bar{U} - U_c}{U_2 - U_1}, \tag{3.8}$$

where $\bar{U}$ is the time averaged streamwise velocity component, and

$$\xi = \frac{y - \bar{y}(x)}{\delta(x)}, \tag{3.9}$$

$$\delta(x) = y_{0.9}(x) - y_{0.1}(x), \tag{3.10}$$

$$\bar{y}(x) = \frac{1}{2}[y_{0.9}(x) + y_{0.1}(x)]. \tag{3.11}$$

$y_{0.1}(x)$ is the y location where

$$U = U_1 + 0.1(U_2 - U_1), \tag{3.12}$$

and, similarly, $y_{0.9}(x)$ is the y location where

$$U = U_1 + 0.9(U_2 - U_1). \tag{3.13}$$

Pope [72] shows that the following error-function

$$f(\xi) = \frac{1}{2}\,\mathrm{erf}\left(\frac{\xi}{0.5518}\right), \tag{3.14}$$

is a good fit to the experimental data of Champagne *et al.* [73]. Hence, the error function profile is also included in figure 3.3 for comparison. As can be seen from this plot, the scaled velocity profiles show a good degree of self-similarity. The agreement with the error-function is also very good.

Figure 3.4 shows how the vorticity thickness grows for the naturally developing mixing layer. From the plot it can be seen that initially there is a region of slow growth till about $x = 50\delta_\omega(0)$ and then there is a nearly linear growth downstream. A similar observation was also reported by Stanley and Sarkar [70]. Shown also in the plot is the linear fit to the data in the region for $x > 50\delta_\omega(0)$. The slope of the line is about 0.050. Using this value, we can calculate the growth rate as follows

$$\frac{1}{\eta}\frac{\partial \delta_\omega(x)}{\partial x} = 0.15, \tag{3.15}$$

since

$$\eta = \frac{U_2 - U_1}{U_2 + U_1} = \frac{1}{3}. \tag{3.16}$$

This value agrees well with the experimentally obtained growth rate of 0.16 observed by Spencer and Jones [67] as well as the computational result of 0.15 by Stanley and Sarkar [70].

Figures 3.5, 3.6, and 3.7 show the normalized Reynolds stress profiles at various downstream locations. The normalized Reynolds stresses are defined as

$$\sigma_{xx} = \frac{\langle u'u' \rangle}{(U_2 - U_1)^2} \quad \sigma_{yy} = \frac{\langle v'v' \rangle}{(U_2 - U_1)^2} \quad \sigma_{xy} = \frac{\langle u'v' \rangle}{(U_2 - U_1)^2}, \tag{3.17}$$

where $\langle\ \rangle$ denotes time-averaging. The σ_{xx} and σ_{yy} profiles are observed to collapse well in the far downstream region and hence exhibit self-similarity. The σ_{xy} profile

also shows a similar trend; however, there seems be a noticeable difference between the profiles at $x = 160\delta_\omega(0)$ and $x = 190\delta_\omega(0)$. The reason for this is unknown but it is believed to be related to the statistical sample size. A bigger statistical sample collected over a larger number of time steps would probably eliminate this discrepancy. The peak values for σ_{xx}, σ_{yy}, and σ_{xy} in the far downstream region are approximately 0.048, 0.078 and 0.012, respectively.

3.2 Test Case 2 - LES at a Reynolds Number of 5,333

In the second test case, we are doing an LES calculation for a mixing layer at a higher Reynolds number. The Reynolds number based on the initial vorticity thickness and the velocity difference across the layer is

$$Re = \frac{(U_2 - U_1)\delta_\omega(0)}{\nu} = 5,333. \tag{3.18}$$

The relative convective Mach number is

$$M_c = \frac{U_2 - U_1}{2c_\infty} = 0.074. \tag{3.19}$$

The convection velocity is

$$U_c = \frac{U_1 + U_2}{2} = 0.222c_\infty, \tag{3.20}$$

and

$$\eta = \frac{U_2 - U_1}{U_2 + U_1} = \frac{1}{3}. \tag{3.21}$$

The hyperbolic tangent profile that was specified for the inflow velocity in the first test case is also used here. We again simulate a naturally developing mixing layer in this computation by adding random perturbations to the transverse velocity component on the inflow profile. This test case is same as the one studied by Bogey [71] using LES. The grid we used in this test case is similar to the one used in the DNS test case and is depicted in figure 3.8. The grid extends to about $400\delta_\omega(0)$ in the streamwise x-direction and from $-300\delta_\omega(0)$ to $300\delta_\omega(0)$ in the transverse y-direction. The grid has 720 points along the streamwise direction and 576 points

along the transverse direction. The minimum grid spacing in the y-direction is about $0.16\delta_\omega(0)$ around the centerline. Again, exponential grid stretching is applied in the transverse direction such that the maximum spacing around the upper and lower boundaries is about $3\delta_\omega(0)$. In the x-direction, the physical region extends up to about $x = 250\delta_\omega(0)$. In the physical region, the grid spacing in the x-direction is uniform and about $0.40\delta_\omega(0)$. The first 625 points in the x-direction are in the physical region and the remaining 95 points form the sponge region. For comparison, the grid of Bogey [71] consists of 601×281 points. His domain extends up to about $x = 350\delta_\omega(0)$ in the streamwise direction and from $y = -90\delta_\omega(0)$ to $y = 90\delta_\omega(0)$ in the transverse direction. His minimum grid spacing in the y-direction around the centerline is $0.16\delta_\omega(0)$. He also applied grid stretching toward the upper and lower boundaries. In the x-direction, he kept the spacing constant at $0.32\delta_\omega(0)$ until $x = 150\delta_\omega(0)$ where the sponge zone starts. He used the last 100 points along the x-direction form the sponge zone.

For subgrid-scale modelling in this simulation, we used the Smagorinsky model with $C_{sgs} = 0.18^2 = 0.0324$, $C_I = 0.00575$ and the turbulent Prandtl number, $Pr_t = 0.9$. Bogey [71] also used the Smagorinsky model with the same C_{sgs} value but he did not include the compressibility correction term. Since the convective Mach number is very low in this test case, compressibility effects are not expected to be significant in this simulation.

The instantaneous vorticity contours are shown in figure 3.9. As it has been observed earlier in the low Reynolds number DNS, occasional vortex pairing also happened at various locations in the domain during this simulation.

After the initial transients got out of the computational domain, we ran an additional 50,000 time steps to obtain the statistical data. During this time interval, an acoustic wave travelling at ambient sound speed travelled a distance that is equal to about 17 times the domain length in the streamwise direction. The scaled mean streamwise velocity profiles at five stations are plotted in figure 3.10. The velocity

profiles are again observed to collapse well and there is good agreement with the error function defined previously.

The vorticity thickness growth for the naturally developing mixing layer is shown in figure 3.11. A linear fit to the data in the region for $x > 60\delta_\omega(0)$ is also plotted. The slope of the line is about 0.053. Using this value, the growth rate is calculated as

$$\frac{1}{\eta}\frac{\partial \delta_\omega(x)}{\partial x} = 0.16, \tag{3.22}$$

which is in good agreement with our DNS result in the first test case as well as some other researchers' results mentioned previously.

Finally, the Reynolds stress profiles at various downstream locations obtained in this simulation are plotted in figures 3.12, 3.13, and 3.14. The peak values for σ_{xx}, σ_{yy}, and σ_{xy} in the far downstream region are approximately 0.058, 0.090 and 0.017, respectively. The σ_{xx} and σ_{yy} profiles collapse well in the far downstream region and exhibit self-similarity. The σ_{xy} profile shows a discrepancy similar to that observed in the DNS calculation; there is a noticeable difference between the profiles at $x = 180\delta_\omega(0)$ and $x = 210\delta_\omega(0)$.

Table 3.1 compares some of our results obtained in both test cases to available experimental and computational data in the literature. From the comparison, we see that the mixing layer growth rates obtained in our simulations compare well with other results; however, the peak Reynolds stresses seem to be overpredicted compared to experiments. A similar observation can be done with the two-dimensional simulation results of Stanley and Sarkar [70] as well as those of Bogey [71]. The inability of the 2-D simulations to predict Reynolds stresses accurately is not very surprising since the energy dissipation mechanism in a 2-D simulation is not expected to be the same as the case in a 3-D simulation or a physical experiment. In a 2-D calculation, there is obviously no energy transfer to the third dimension. Furthermore, the 3-D features of a turbulent flow such as the 3-D breakdown of large scale structures into fine scale turbulence and the vortex stretching mechanisms are also absent in the 2-D calculations.

In conclusion, it can be summarized that the 2-D simulations done in this study were capable of getting the mean streamwise velocity profiles as well as the vorticity thickness growth rates fairly accurately although the predicted peak Reynolds stresses were inaccurate. One normally should not use 2-D turbulence simulation results for a mixing layer problem if accurate prediction of the Reynolds stresses is considered to be an important issue.

After testing the basic numerical methods in the 2-D LES code and getting reasonable results, our next step was the extension of the 2-D code to 3-D. The following chapters in this thesis will present the turbulence simulations done with the 3-D LES code and the subsequent noise computations using various integral acoustics methods.

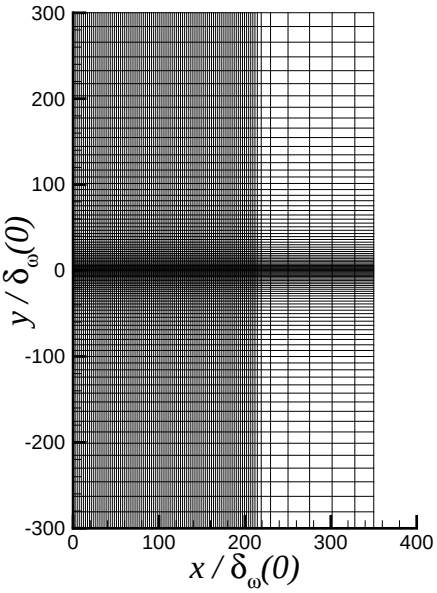

Figure 3.1. Computational grid used in the DNS. (Every 6^{th} node is shown.)

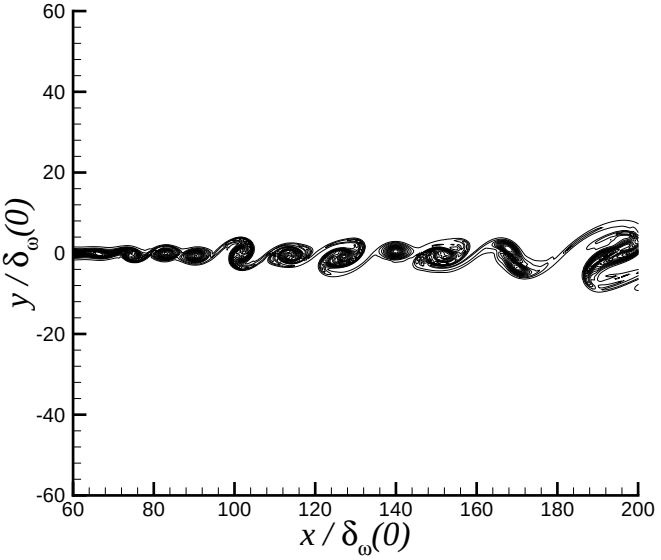

Figure 3.2. Instantaneous vorticity contours in a naturally developing mixing layer. ($Re_\omega = 720$)

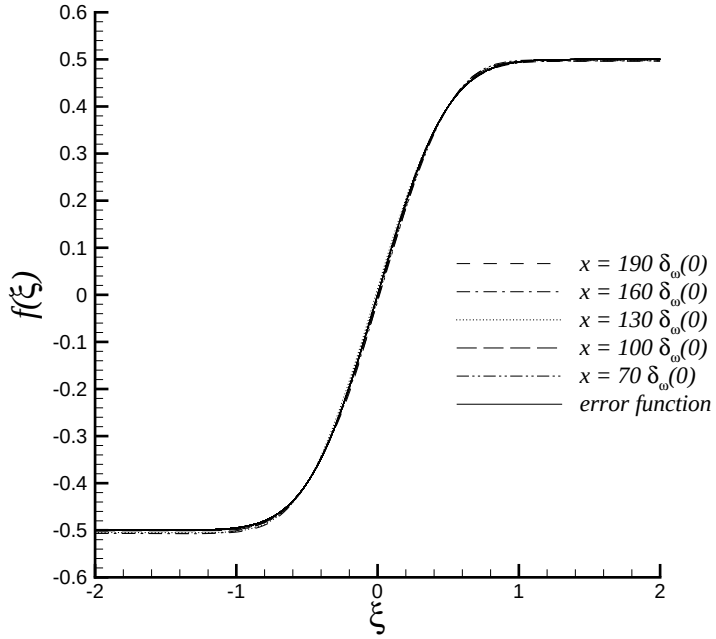

Figure 3.3. Scaled velocity profiles. Error-function profile also shown.

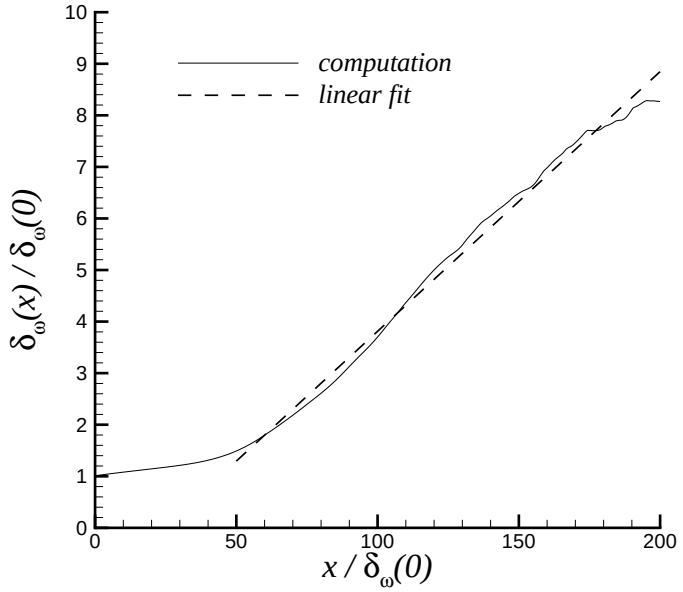

Figure 3.4. Vorticity thickness growth in the mixing layer.

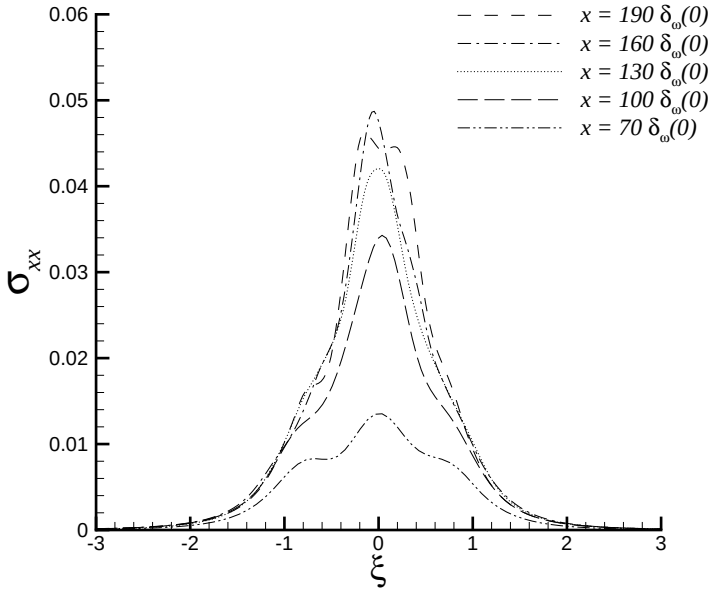

Figure 3.5. Normalized Reynolds normal stress σ_{xx} profiles.

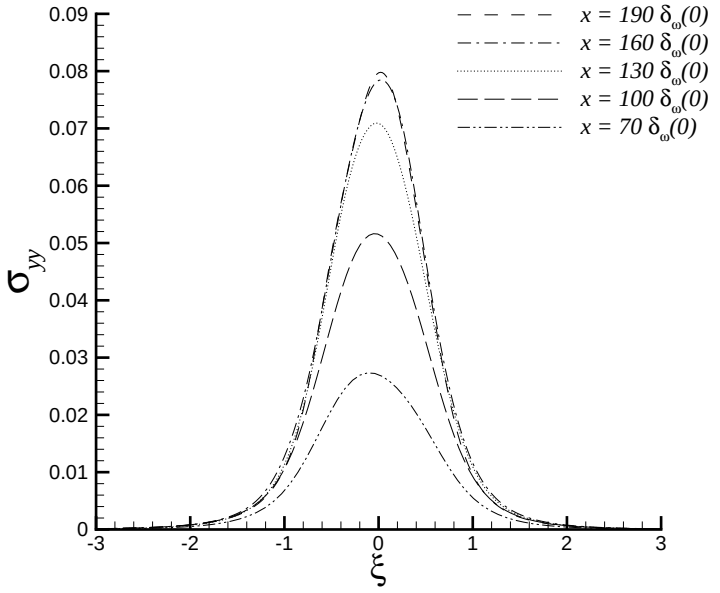

Figure 3.6. Normalized Reynolds normal stress σ_{yy} profiles.

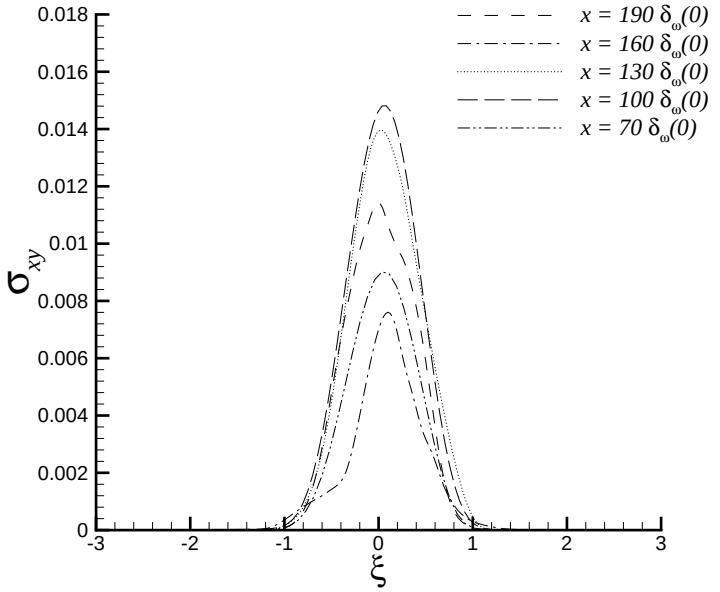

Figure 3.7. Normalized Reynolds shear stress σ_{xy} profiles.

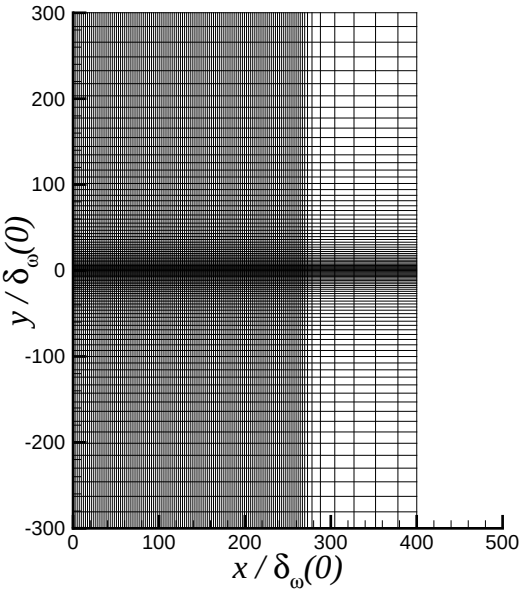

Figure 3.8. Computational grid used in the LES. (Every 6^{th} node is shown.)

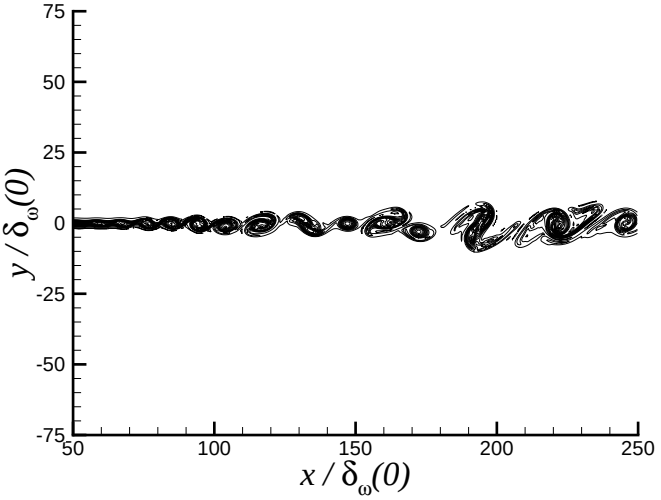

Figure 3.9. Instantaneous vorticity contours in a naturally developing mixing layer. ($Re_\omega = 5,333$)

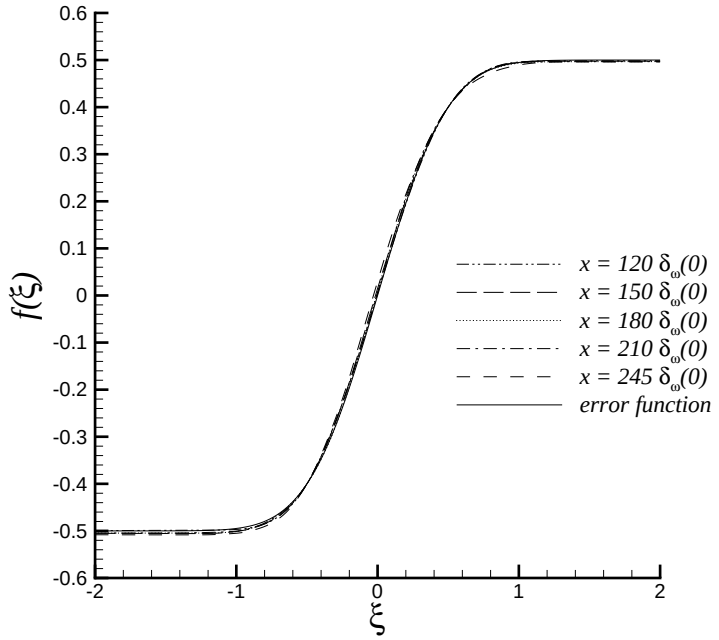

Figure 3.10. Scaled velocity profiles. Error-function profile also shown.

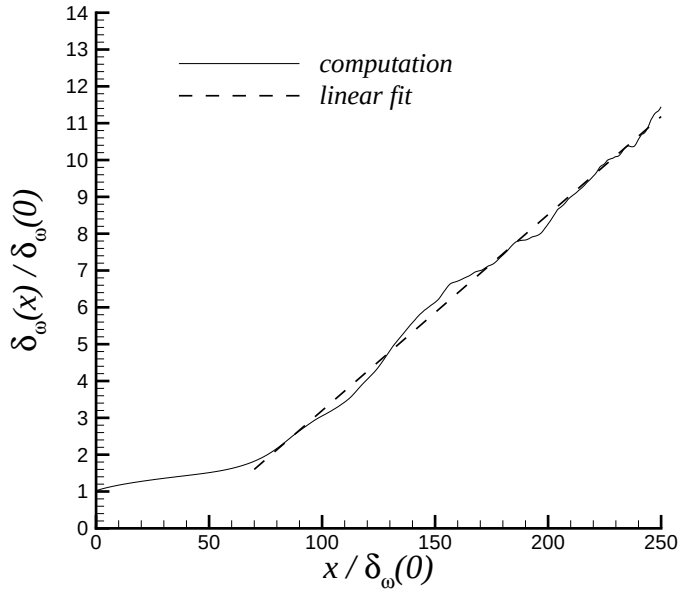

Figure 3.11. Vorticity thickness growth in the mixing layer.

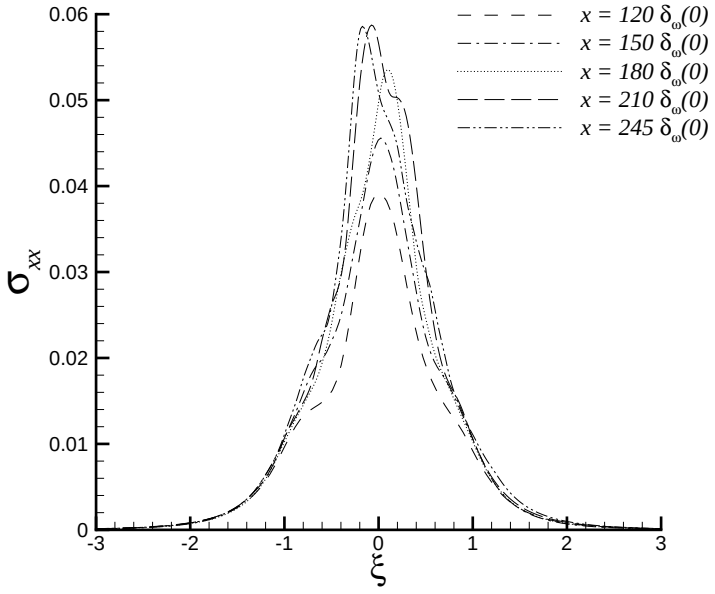

Figure 3.12. Normalized Reynolds normal stress σ_{xx} profiles.

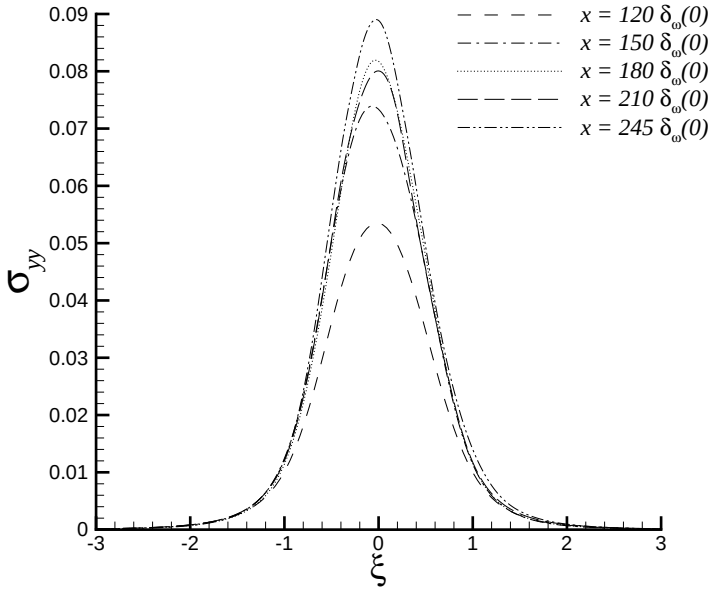

Figure 3.13. Normalized Reynolds normal stress σ_{yy} profiles.

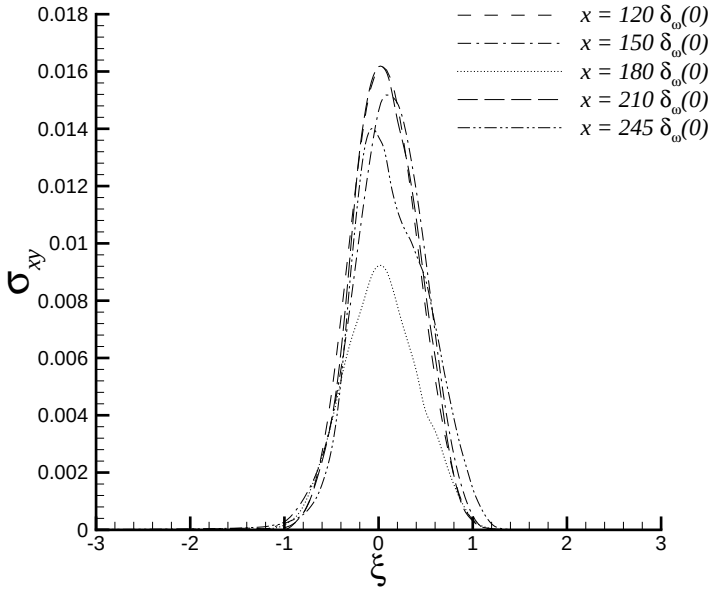

Figure 3.14. Normalized Reynolds shear stress σ_{xy} profiles.

Table 3.1. Comparison of the normalized peak Reynolds stresses and growth rates with available experimental and computational data.

Re_ω	σ_{xx}	σ_{yy}	σ_{xy}	$\frac{1}{\eta}\frac{\partial \delta_\omega(x)}{\partial x}$	Reference
-	0.031	0.019	0.009	0.19	Wygnanski and Fiedler's experiment [66]
-	0.036	0.014	0.013	0.16	Spencer and Jones' experiment [67]
1,800	0.032	0.020	0.010	0.163	Bell and Mehta's experiment [68]
3,200	0.026	0.017	0.010	0.13	Rogers and Moser's 3-D DNS [69]
720	0.040	0.084	0.023	0.15	Stanley and Sarkar's 2-D DNS [70]
5,333	0.040	0.068	0.020	0.18	Bogey's 2-D LES [71]
720	0.048	0.078	0.012	0.15	Our 2-D DNS
5,333	0.058	0.090	0.017	0.16	Our 2-D LES

4. INITIAL 3-D ROUND JET SIMULATIONS WITH THE CONSTANT-COEFFICIENT SMAGORINSKY MODEL

4.1 Estimation of the Kolmogorov Length Scale

Due to a wide range of length scales existing in turbulent flows, the computational grids that are used for 3-D DNS and LES calculations have to provide sufficient grid resolution throughout the turbulent flow that is being simulated and especially in critical regions where the local length scales are expected to be very small. In a DNS, if the grid resolution is not enough, numerical instabilities will occur due to the unresolved scales and consequently, the simulation will and should eventually blow up. In an LES, the effect of the unresolved scales on the resolved scales is represented through the subgrid-scale (SGS) model and the dissipation provided by the SGS model provides stability for the numerical computations. Hence, relatively coarse grids can be employed in LES calculations. However, one still needs to know what length scales are resolved with a given grid in a LES. Therefore, in order to have an idea about the range of turbulent length scales that will be present in the flow that is being simulated and generate computational grids that will allow sufficient resolution in the simulations, it is well worth doing a Kolmogorov length scale analysis using available experimental and/or DNS data for the problem under consideration. In this section, the Kolmogorov length scale estimation will be presented for a 3-D turbulent round jet using experimental data.

The Kolmogorov length scale, which is the characteristic length scale of the smallest eddies present in a turbulent flow, is defined as

$$\eta = \left(\frac{\nu^3}{\epsilon}\right)^{\frac{1}{4}}, \tag{4.1}$$

where ν is the kinematic viscosity and ϵ is the dissipation.

We can define a local Reynolds number based on jet centerline velocity and half-radius as follows

$$Re_c(x) = \frac{U_c(x) r_{1/2}(x)}{\nu}, \tag{4.2}$$

where $U_c(x)$ is the mean jet centerline velocity and $r_{1/2}(x)$ is the jet half-radius at which the mean streamwise velocity is one-half of $U_c(x)$. Using this equation, we can express ν as

$$\nu = \frac{U_c(x) r_{1/2}(x)}{Re_c(x)}. \tag{4.3}$$

As mentioned by Pope [72], the experimental data of Hussein *et al.* [74] confirms that the non-dimensional dissipation

$$\hat{\epsilon} = \epsilon \left(\frac{{U_c}^3}{r_{1/2}} \right)^{-1}, \tag{4.4}$$

that is illustrated in figure 4.1, is self-similar and independent of the Reynolds number in the fully developed turbulent region of the jet. From this equation, we get

$$\epsilon = \hat{\epsilon} \left(\frac{{U_c}^3}{r_{1/2}} \right). \tag{4.5}$$

Now, substituting for ν and ϵ into the Kolmogorov length scale equation, we obtain the following relation

$$\frac{\eta}{r_{1/2}} = {Re_c}^{-3/4}\ \hat{\epsilon}^{-1/4}. \tag{4.6}$$

From experimental measurements, it is known that for the round jet,

$$U_c(x) = U_o\ \frac{B}{(x - x_o)/D_j} \qquad r_{1/2}(x) = S(x - x_o), \tag{4.7}$$

where $B = 5.8$, $S = 0.094$ (from [72]), D_j is the jet diameter, x is the streamwise distance, and x_o is the so-called virtual origin of the jet.

Therefore,

$$Re_c(x) = \frac{U_c(x) r_{1/2}(x)}{\nu} = \frac{U_o}{\nu}\ \frac{B}{(x - x_o)/d}\ S(x - x_o) = \frac{U_o d}{\nu}\ B\ S = Re_D\ B\ S, \tag{4.8}$$

where Re_D is the Reynolds number based on the jet diameter and nozzle exit conditions. From the above equation, we see that the local Reynolds number is a constant

and independent of the streamwise distance x in the fully turbulent region. Using this result and recalling that $\hat{\epsilon}$ is self-similar and independent of the Reynolds number, it can be concluded from equation 4.6 that at a given Re_D, the non-dimensional Kolmogorov length scale profile in the fully developed turbulent region of the 3-D round jet is simply self-similar.

The non-dimensional Kolmogorov length scale profile for a Reynolds number, Re_D of $3,600$ is shown in figure 4.2. As can be observed from the plot, the smallest turbulent length scale occurs on the jet centerline. The local length scales get larger as one moves away from the jet centerline along the radial direction.

The analysis done in this section will be utilized to determine what length scales are resolved with the grids used in our numerical simulations.

4.2 Test Case 1 - LES at a Reynolds Number of 3,600

The first 3-D LES test case we considered is a turbulent round jet at a Mach number of 0.9. The Reynolds number of the jet is

$$Re_D = \frac{\rho_o U_o D_j}{\mu_o} = 3,600, \tag{4.9}$$

where ρ_o, U_o, μ_o are the jet centerline density, velocity and viscosity at the nozzle exit, respectively and D_j is the jet diameter. This is the same test case studied by Freund [2] in his DNS.

The stretched Cartesian grid used in this simulation consisted of $340 \times 128 \times 128$ points in the x, y, and z directions, respectively. Figures 4.3 and 4.4 illustrate the $x-y$ and $y-z$ sections of our grid. The domain extends $60r_o$ in the streamwise direction and from $-15r_o$ to $15r_o$ in the transverse y and z directions, where r_o is the jet radius. In the x direction, the physical region ends at $x = 45r_o$. The region from $x = 45r_o$ to $x = 60r_o$ is the sponge region that is used to dissipate the fluctuations present in the flow field before they reach the outflow boundary. The minimum grid spacing in the y and z directions is about $0.05r_o$ around the jet centerline. Exponential grid stretching is applied along the transverse directions such

that the maximum spacing around the external boundaries is about $0.66r_o$. In the physical region of the grid, the spacing along the streamwise direction is uniform and about $0.15r_o$. In the sponge region, the grid is stretched using the grid-stretching function proposed by Colonius *et al.* [59]. The first 300 points in the x direction are in the physical region and the remaining 40 points form the sponge zone. The maximum streamwise spacing at the end of the sponge zone is about $1r_o$. In the DNS done by Freund [2], a $640 \times 250 \times 160$-node cylindrical grid was used with a domain size of about $50r_o$ in the streamwise direction and about $20r_o$ in the radial direction. The physical portion of his computational domain extended $33r_o$ in the streamwise direction and $8r_o$ in the radial direction. In Freund's grid, the physical portion of the domain was surrounded by an absorbing buffer zone in all directions. The grid was highly stretched and dissipative terms were added to the equations in his buffer zone. Freund's grid was compressed radially with a minimum radial spacing of $0.018r_o$ around the centerline, and axially with minimum axial spacing of $0.049r_o$ at around the axial position $x = 20r_o$. His grid spacing changed by less than 1% per grid point. The azimuthal grid spacing was, of course, kept uniform.

For the inflow forcing, we used a method similar to that used by Freund [2] to add random perturbations to the streamwise component of velocity on the inflow boundary. The following velocity profile was specified on the inflow boundary

$$u(r) = \frac{1}{2}U_o \left[1 - \tanh\left[b(\theta, t)\left(\frac{r}{r_o} - \frac{r_o}{r}\right)\right]\right], \tag{4.10}$$

where r_o is the jet radius, U_o is the mean jet centerline velocity on the inflow boundary, and b is the shear layer thickness parameter with a mean value of 3.125. Larger values of this parameter correspond to thinner shear layers. Freund [2] used a value of 12.5 for this parameter since his fine grid enabled such thin shear layer resolutions. It should be noted here that since a Cartesian grid is used in this simulation, the shear layer resolution is not the same at all azimuthal locations. However, the average number of grid points in the initial jet shear layer is about 8 which has been found to be sufficient to accurately resolve the shear layer in this simulation. The shear layer thickness parameter was varied along the azimuthal direction θ and in

Table 4.1. Parameters used for inflow forcing.

Parameter	Δ per time step	min.	max.
A	0.0001	0.01	0.07
St	0.003	0.1	0.7
ϕ	0.003	-	-
ψ	0.003	-	-

time t in order to add small-amplitude random perturbations and excite the instabilities in the jet. We used the following *ad hoc* modelling for $b(\theta, t)$, similar to that used by Freund [2]

$$b(\theta, t) = 3.125 + \sum_{m=0}^{2} \sum_{n=0}^{1} A_{nm} \cos\left(\frac{St_{nm} U_o}{2r_o} + \phi_{nm}\right) \cos(m\theta + \psi_{nm}), \tag{4.11}$$

where the parameters with the nm subscript were slowly varied in a random manner during the simulation. At each time step, a random-number generator was used to determine the 1-in-20 chance that the variation would change from positive (indicating an increase) to negative (indicating a decrease) or vice versa and each of the randomly varying parameters were either increased or decreased by a small amount accordingly. The limits on the variation of the parameters used for inflow forcing as well as the increments used per time step are given in table 4.1.

Following Morris *et al.* [21], we chose the Smagorinsky constant as $C_{sgs} = 0.012$, and the compressibility correction constant as $C_I = 0.0066$ in our simulation. The turbulent Prandtl number was chosen as $Pr_t = 0.7$.

For the mean density profile on the inflow boundary, we applied the following distribution used by Freund [75]

$$\bar{\rho} = (\rho_o - \rho_\infty)\frac{\bar{u}}{U_o} + \rho_\infty, \tag{4.12}$$

where $\bar{u}/U_o$ is the mean streamwise velocity on the inflow boundary normalized by the jet centerline velocity, ρ_o is the density at the jet centerline, ρ_∞ is the freestream

density, and $\rho_o/\rho_\infty = 0.86$. The mean pressure distribution on the inflow boundary was kept uniform and equal to the jet centerline pressure.

The mean profiles on the inflow boundary were specified initially in the entire domain and the simulation was started from these uniform initial conditions. We used 128 processors on an SGI Origin 2000 computer of the National Computational Science Alliance (NCSA) at the University of Illinois, Urbana-Champaign in our simulation. We ran a total of 65,000 time steps during which an acoustic wave propagating at the ambient sound speed travelled a distance of 36 times the domain length in the streamwise direction. The initial transients exited the domain over the first 15,000 time steps. We then collected the flow statistics over the 50,000 time steps. The simulation was performed in the 128-processor dedicated queue and required a total run time of about 3.5 days to complete.

The solution was filtered using a 4^{th}-order accurate penta-diagonal filter in each spatial dimension at the end of every time step. Thompson's non-reflecting boundary conditions were used on the side boundaries of the domain as well as on the outflow boundary at the end of the sponge zone. Special characteristic boundary conditions were applied on the inflow boundary.

Figure 4.5 shows the instantaneous contours of vorticity magnitude on the $x-z$ plane. After the initial region of laminar flow, the transition process starts and the jet eventually becomes fully turbulent. Since this is a low Reynolds number jet and the initial shear layer of the jet is relatively thick, the potential core of the jet is relatively long and does not break up until after $x = 20r_o$. This potential core is longer than the potential core length of $14r_o$ obtained in Freund's DNS [2] as well as in the experiment of Stromberg *et al.* [3].

In figure 4.6, we plot the streamwise variation of the inverse of the mean centerline velocity normalized by the jet inflow velocity. After transition to turbulence, we get a linear growth. The slope of the line can be used to compute the jet decay coefficient and our value is around 4.55. Experimental values of the jet decay coefficient are in between 5.4 and 6.1. Our underpredicted value was initially believed to be related

to the amplitude of the forcing that we used to excite the 3-D instabilities in the flow. However, it was later realized that the forcing amplitude should only affect the transition to turbulence and determine the location where the potential core of the jet breaks up and, therefore, it should not have any effect on the jet decay coefficient [76]. Furthermore, during our high Reynolds number simulations that are presented in the next section, we discovered that Thompson's non-reflecting boundary conditions actually did not provide the correct entrainment physics on the boundaries of a Cartesian grid. Since we are dealing with a round jet problem, the ambient fluid that is entrained by the jet should be coming in radially towards the jet centerline along the boundaries of the $y - z$ section of the grid that was previously shown in figure 4.4. However, it was found that with Thompson's boundary conditions, the entrained fluid came in at almost normal angles pretty much everywhere along the boundaries except at the corners. Clearly, this is not physical. Therefore, the lack of the correct entrainment physics in the current simulation might be partially responsible for the low value of the jet decay coefficient. The simulations done for the high Reynolds number jet in the next section using Tam and Dong's boundary conditions instead of Thompson's boundary conditions produce jet decay coefficient values closer to the experimental data. It will also be shown in the next section that the value of the Smagorinsky coefficient used in the subgrid-scale modelling also has an influence on the jet decay coefficient as well as the jet spreading rate. Going back to the results of the current test case, we see that the growth of the half-velocity radius, illustrated in figure 4.7, also shows a linear growth in the turbulent region of the jet, consistent with experimental observations. The slope of the linear line which is defined as the jet spreading rate, is about 0.116. Experimental values for the jet spreading rate range from 0.086 to 0.096. It is known that the jet spreading rate decreases with increasing jet decay coefficient. Therefore, our overpredicted value of the jet spreading rate is closely related to the low value of our jet decay coefficient.

Mean streamwise velocity profiles at two downstream locations are plotted in figure 4.8 and compared with the experimental data of Hussein *et al.* [74] for an

incompressible jet at $Re_D = 95,500$ as well as that of Panchapakesan and Lumley [77] for an incompressible jet at $Re_D = 11,000$. From this figure, it can be observed that the profiles of our compressible jet at the two downstream locations collapse onto each other fairly well and exhibit self-similarity which is consistent with experimental observations. Our results are also in very good agreement with the experimental profiles of incompressible jets. We also compared our Reynolds stresses with the available experimental data of Hussein *et al.* [74] and Panchapakesan and Lumley [77]. The normalized Reynolds stresses in cylindrical coordinates are defined as follows

$$\sigma_{xx} = \frac{\langle v_x{}' v_x{}' \rangle}{U_c^2} \quad \sigma_{rr} = \frac{\langle v_r{}' v_r{}' \rangle}{U_c^2} \quad \sigma_{\theta\theta} = \frac{\langle v_\theta{}' v_\theta{}' \rangle}{U_c^2} \quad \sigma_{rx} = \frac{\langle v_r{}' v_x{}' \rangle}{U_c^2}, \tag{4.13}$$

where $v_x{}'$, $v_r{}'$, $v_\theta{}'$ are the axial, radial and azimuthal components of the fluctuating velocity, respectively, U_c is the mean jet centerline velocity at a given axial location, and $\langle\ \rangle$ denotes time-averaging. In order to compare our Reynolds stresses with the experimental data, we transformed our Reynolds stresses from the Cartesian coordinate system to the cylindrical coordinate system. The transformation process was trivial and the details of it will be skipped here. Figures 4.9, 4.10, 4.11, 4.12 plot our computed Reynolds stresses and compare them with the experimental data. From these plots, we see that our Reynolds stress profiles also exhibit self-similarity, consistent with experimental evidence, and our data are again in fairly good agreement with experiment.

Finally, we looked at the length scales resolved in our simulation. Using the Kolmogorov length scale estimation that was presented earlier, we plotted the ratio of our grid spacings to the local Kolmogorov length scales along the transverse and streamwise directions in figures 4.13 and 4.14. It should be noted that in our Kolmogorov length scale estimation, we made use of the fact that the non-dimensional dissipation profile is self-similar and independent of the Reynolds number in the fully turbulent region of the jet. However, in the region immediately downstream of the end of potential core, which is around $x = 20r_o$ in this simulation, the non-dimensional dissipation profile may not be quite self-similar yet and hence our analysis may not

be very accurate in this region. Nevertheless, we believe our analysis should be fairly accurate in the far downstream portion of the jet. Keeping this in mind, we see that in the region $x > 25r_o$, our coarsest grid resolution along the transverse y direction was slightly larger than 6 times the local Kolmogorov length scale. Our coarsest resolution in the streamwise direction was about 13 times the local Kolmogorov length scale for $x > 25r_o$. Analyzing the grid used by Freund [2] in his DNS, we also see that his coarsest grid resolution was about 4 times the Kolmogorov scale. As one moves further downstream, the Kolmogorov length scales get larger and better resolution is obtained with our grid.

4.3 Test Case 2 - LES at a Reynolds Number of 36,000

For our second test case, we studied a turbulent round jet at a Reynolds number of $36,000$. The stretched Cartesian grid used in this test case had $350 \times 128 \times 128$ points in the x, y, and z directions respectively. Figure 4.15 plots the $x - y$ section of the grid. The domain extends to about $45r_o$ in the streamwise direction and from $-15r_o$ to $15r_o$ in the transverse y and z directions, where r_o is the jet radius. In the x direction, the physical region ends at around $x = 32r_o$. The grid spacing along the x direction in the physical portion of the grid is uniform and about $0.10r_o$, which is equal to two-thirds of the constant streamwise spacing in the previous grid that was used for the low Reynolds number test case. The transverse grid point distribution in the current grid was kept the same as in the previous grid. There are about 8 grid points in the initial jet shear layer.

For the inflow forcing in this test case, we applied the same kind of forcing used by Constantinescu and Lele [30] in their LES calculations. In this forcing, time-harmonic fluctuations are imposed on the mean streamwise velocity on the inflow boundary as follows

$$u(r) = \frac{1}{2}U_o \left[1 - \tanh\left[b\left(\frac{r}{r_o} - \frac{r_o}{r}\right)\right]\right](1 + \alpha \sin(2\pi St\ t)), \tag{4.14}$$

where the Strouhal number, $St = 2r_o f/U_o$ is 0.9, r_o is the jet radius, U_o is the mean jet centerline velocity on the inflow boundary, f is the frequency of the perturbations, $b = 3.125$ is the shear layer thickness parameter, and the amplitude of the sinusoidal oscillations, α is 0.005. Randomly generated perturbations are applied on the azimuthal velocity component using the following equation

$$v_\theta{}'(r,\theta) = 0.025U_o\,\epsilon \exp\left(-3\left(1-\frac{r}{r_o}\right)^2\right), \tag{4.15}$$

where ϵ is a random number between -0.5 and 0.5. The mean azimuthal velocity on the inflow boundary is zero. No perturbation is applied on the radial velocity component. The exponential function in the above equation localizes the perturbations within the shear layer region only.

As explained below, we did several runs in this test case. For all the simulations presented in this section, we used 128 processors on Indiana University's IBM-SP3 research computer. Each run required about 3 days to complete. For every simulation, we ran a total of 50,000 time steps during which an acoustic wave travelling at the ambient sound speed moved a distance of about 37 times the domain length in the streamwise direction. The initial transients exited the domain over the first 10,000 time steps. We then collected the flow statistics over the 40,000 time steps. Although a value of $C_{sgs} = 0.012$ was used for our low Reynolds number jet simulation, the Smagorinsky coefficient at this higher Reynolds number was chosen as $C_{sgs} = 0.018$ in an *ad hoc* manner. As the Reynolds number is increased, the dissipative length scales are hardly resolved on relatively coarse grids, hence all the dissipation has to come from the SGS model. Using the Kolmogorov length scale analysis earlier, our coarsest grid resolution for this Reynolds number was seen to be between 50 and 60 times the local Kolmogorov length scale. Assuming that the upper limit of the dissipative length scales is 60 times the Kolmogorov length scale [72, 78], we see that we hardly resolved any of the dissipative length scales in portions of the flow where the local length scales were very small. We believe that a larger coefficient should represent the effect of the dissipative length scales on the large scales more accu-

rately at high Reynolds numbers on a relatively coarse grid. For comparison, Bogey *et al.* [29] used a larger constant of $C_{sgs} = 0.18^2 = 0.0324$ in their LES calculation for a jet at a Reynolds number of 65,000. We kept the compressibility correction constant at $C_I = 0.0066$, and the turbulent Prandtl number at $Pr_t = 0.7$, same as the values used in the low Reynolds number jet simulation.

As mentioned in the previous section, we discovered some entrainment flow problems with Thompson's boundary conditions during the runs done in this test case. Hence, starting from the current test case, we decided to employ Tam and Dong's boundary conditions in our future simulations.

Figure 4.16 shows the instantaneous contours of vorticity magnitude on the $x-z$ plane. We see that the potential core of the high Reynolds number jet breaks up earlier than that of the low Reynolds number jet. The potential core length of the Reynolds number 36,000 jet is about $14r_o$.

In order to study the effect of filtering on our results, we did a run using the 4^{th}-order accurate implicit penta-diagonal filter as well as another run using the 6^{th}-order accurate implicit tri-diagonal filter with $\alpha_f = 0.49$. The solution was filtered once in each spatial dimension at the end of every time step in both runs. Figures 4.17 through 4.23 summarize the mean flow results obtained with the 4^{th}-order accurate penta-diagonal filter whereas the figures 4.24 through 4.30 are the ones obtained with the 6^{th}-order accurate tri-diagonal filter. In general, the two sets of results do not seem to differ much although the Reynolds stress profiles obtained with the 6^{th}-order filter match the experimental profiles of Hussein *et al.* [74] slightly better. The jet decay coefficients obtained in both runs still seem a bit low relative to the experimental values. The jet spreading coefficient obtained with the 4^{th}-order accurate filter is just below the upper limit of the experimental values while the one obtained with the 6^{th}-order accurate filter is slightly larger. The mean streamwise velocity profiles as well as the Reynolds stress profiles in both cases compare fairly well with experiment.

We also investigated the effect of the Smagorinsky coefficient on the mean flow properties. We did a new run using $C_{sgs} = 0.019$ and the 6^{th}-order filter with $\alpha_f = 0.49$. The mean flow results for this simulation are plotted in figures 4.31 through 4.37. As can be seen from these results, a slightly larger Smagorinsky coefficient results in a jet decay coefficient of 5.76 which is within the range of experimental observations. The jet decay coefficient obtained with $C_{sgs} = 0.018$ was 5.0, a bit smaller than the lower limit of experimental data. The reason for this difference is believed to be the fact that with a higher SGS model coefficient, the jet loses more of its energy into dissipation and does not have as much energy left to spread out. Furthermore, with increasing jet decay coefficient, the jet spreading rate gets smaller. This is justified by the fact that a jet spreading rate of 0.106 is obtained with $C_{sgs} = 0.018$ while a value of 0.086 is obtained with $C_{sgs} = 0.019$. Hence, the jet decay coefficient as well as the jet spreading rate are directly affected by the SGS model constant. For a 5.56% increase in the model constant, the jet decay coefficient increases by 15.20% while the jet spreading rate decreases by 18.87%. Another interesting fact is that even though the simulation with $C_{sgs} = 0.019$ produced a jet decay coefficient and a jet spreading rate in good agreement with experiment, we see that the Reynolds stress profiles in this simulation have significantly changed relative to the ones obtained in the simulation done with $C_{sgs} = 0.018$. This must be due to the too dissipative nature of the Smagorinsky SGS model. A slight increase in the model coefficient provides more dissipation but at the same time it suppresses more of the turbulence and subsequently causes a significant change in the Reynolds stresses.

Finally, in order to see how much the filtering parameter α_f affects the mean flow results, we did a simulation using $\alpha_f = 0.45$ in our 6^{th}-order tri-diagonal filter with the Smagorinsky coefficient chosen as $C_{sgs} = 0.018$. Shown in figures 4.38 through 4.44 are the results obtained in this run. It is easily observed that the lower value of the filtering parameter qualitatively has the same effect as increasing the Smagorinsky coefficient. This makes sense since the lower values of α_f correspond

to a more dissipative filter. The dissipation coming from the filter at this value of α_f seems to be causing noticeable changes in the Reynolds stress profiles relative to the ones obtained using $\alpha_f = 0.49$ with $C_{sgs} = 0.018$.

In conclusion, we can summarize that the mean flow properties calculated in our simulations using the Smagorinsky SGS model seem reasonable when compared with the experimental data and provide us with valuable evidence towards the full validation of our 3-D LES code. The choice of the Smagorinsky SGS model constant, however, seems to be quite important to the mean flow properties. A lower value of the filtering parameter, α_f which is used in the 6^{th}-order accurate tri-diagonal filter, was found to have effects qualitatively similar to those caused by increasing the Smagorinsky constant. Furthermore, a slight change in the Smagorinsky model constant alters the Reynolds stress profiles quite significantly. Clearly, the Smagorinsky model was found to possess some undesirable features. In the next chapter, we will address the shortcomings of the Smagorinsky SGS model by replacing it with a dynamic SGS model in which the SGS model coefficients are computed dynamically as functions of space and time during the simulations. The dynamic model allows automatic adjustment of the model coefficients to their optimum values throughout the domain and yields a more accurate representation of the actual flow physics.

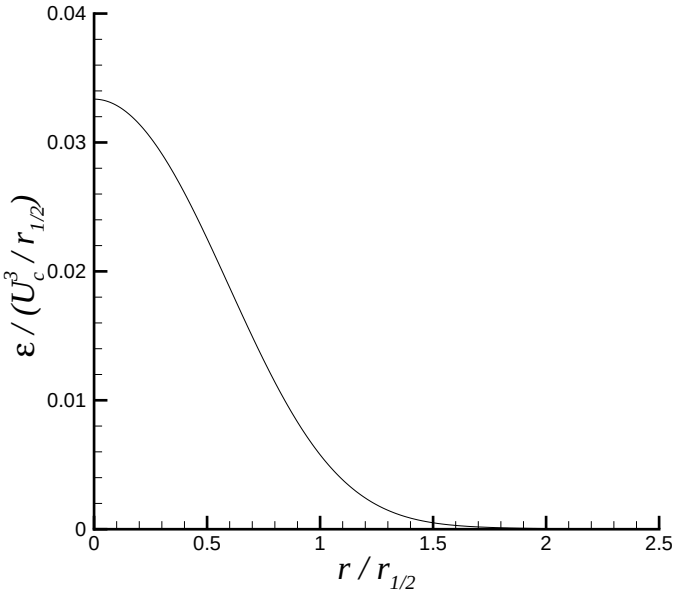

Figure 4.1. Non-dimensional dissipation profile provided by the experimental data of Hussein *et al.* [74].

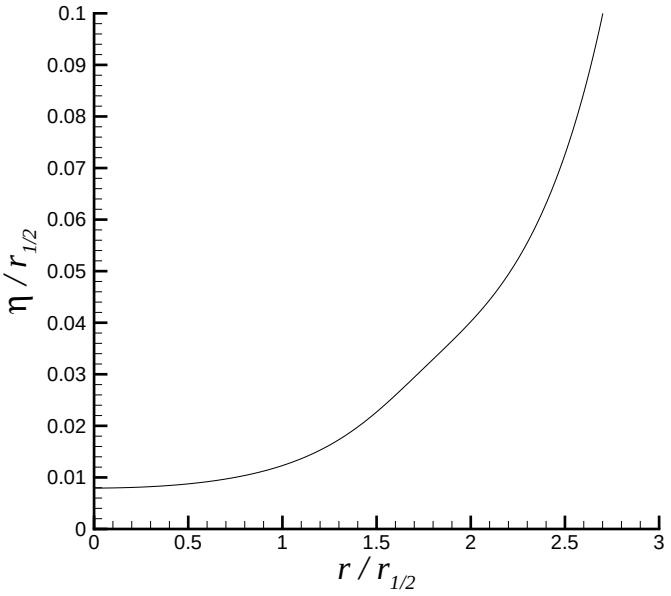

Figure 4.2. Non-dimensional Kolmogorov length scale profile for $Re_D = 3,600$.

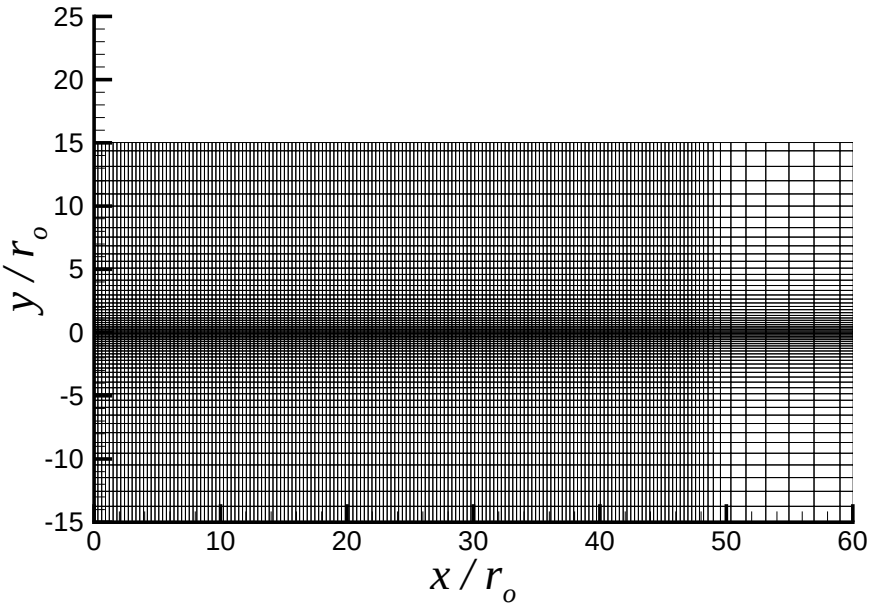

Figure 4.3. The $x - y$ section of the computational grid used in the $Re_D = 3,600$ simulation. (Every 2^{nd} node is shown.)

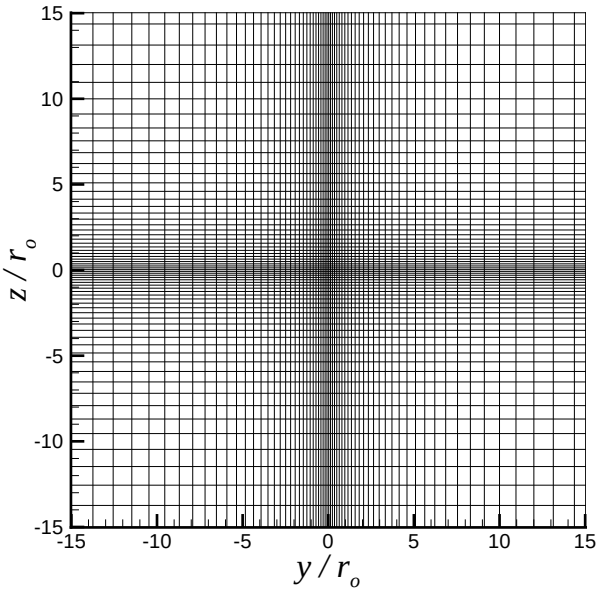

Figure 4.4. The $y - z$ section of the computational grid used in the $Re_D = 3,600$ simulation. (Every 2^{nd} node is shown.)

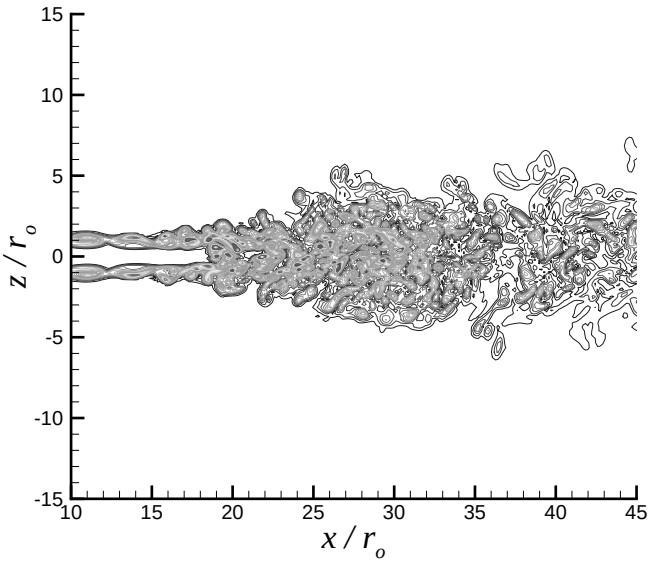

Figure 4.5. Instantaneous contours of vorticity magnitude on the $x - z$ plane at $y = 0$, $Re_D = 3,600$. 30 levels shown.

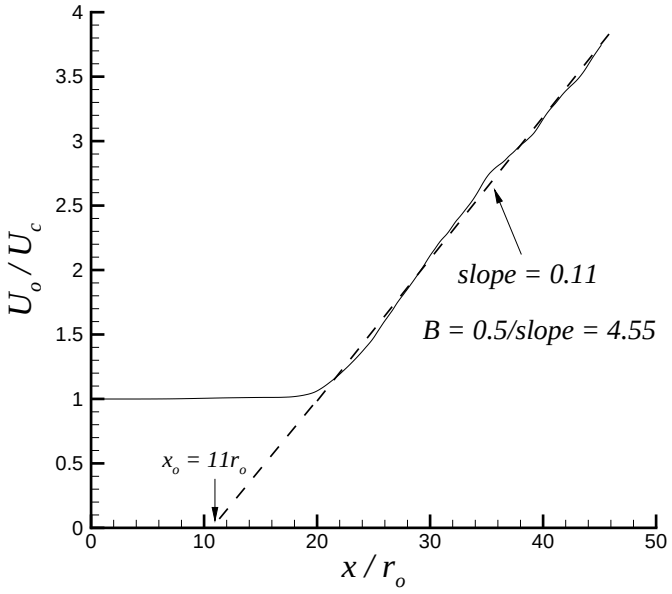

Figure 4.6. Inverse of the mean streamwise velocity on the centerline normalized by the jet inflow velocity, $Re_D = 3,600$.

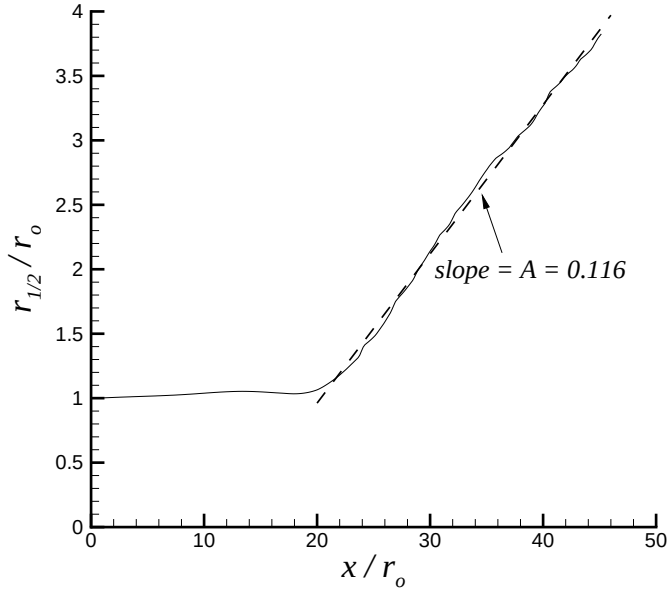

Figure 4.7. Half-velocity radius normalized by the jet radius, $Re_D = 3,600$.

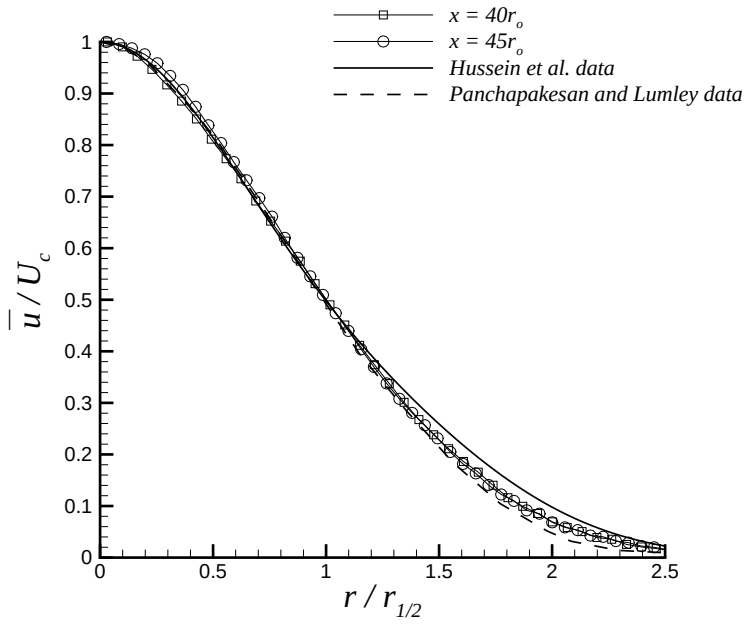

Figure 4.8. Normalized mean streamwise velocity profiles and comparison with experimental data, $Re_D = 3,600$.

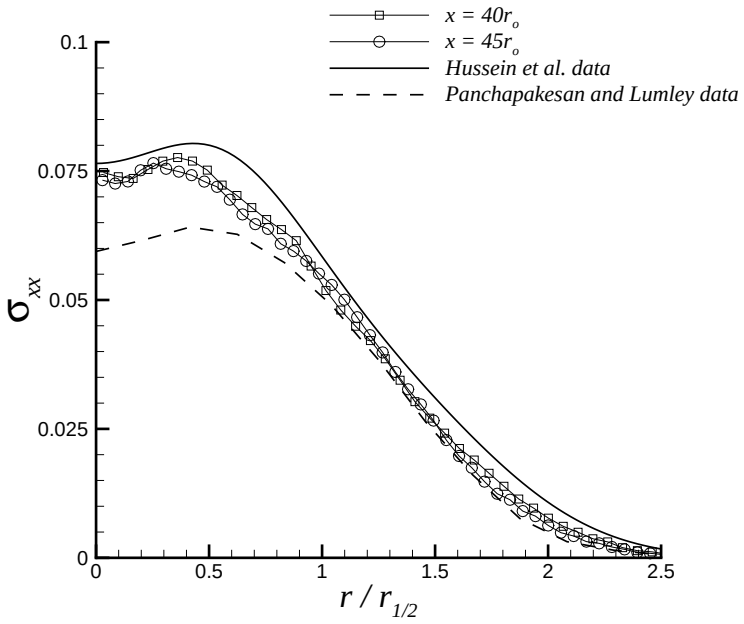

Figure 4.9. Normalized Reynolds normal stress σ_{xx} profiles and comparison with experimental data, $Re_D = 3,600$.

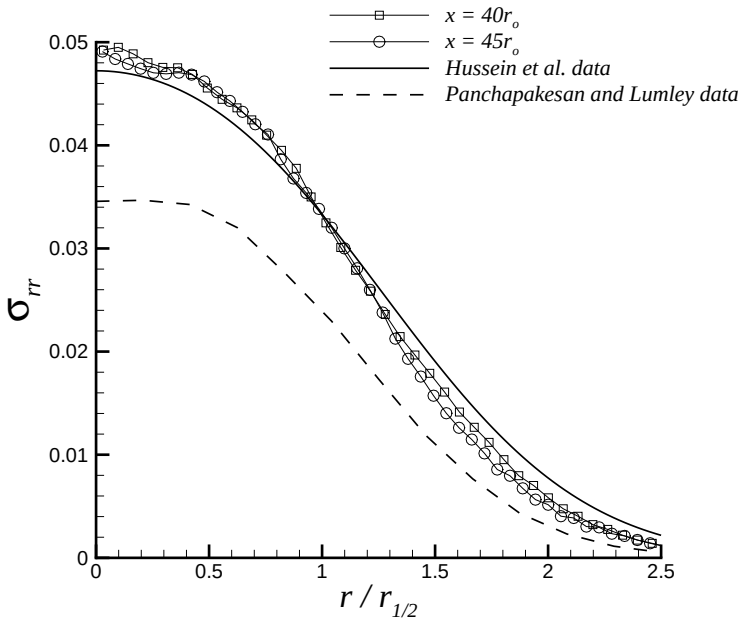

Figure 4.10. Normalized Reynolds normal stress σ_{rr} profiles and comparison with experimental data, $Re_D = 3,600$.

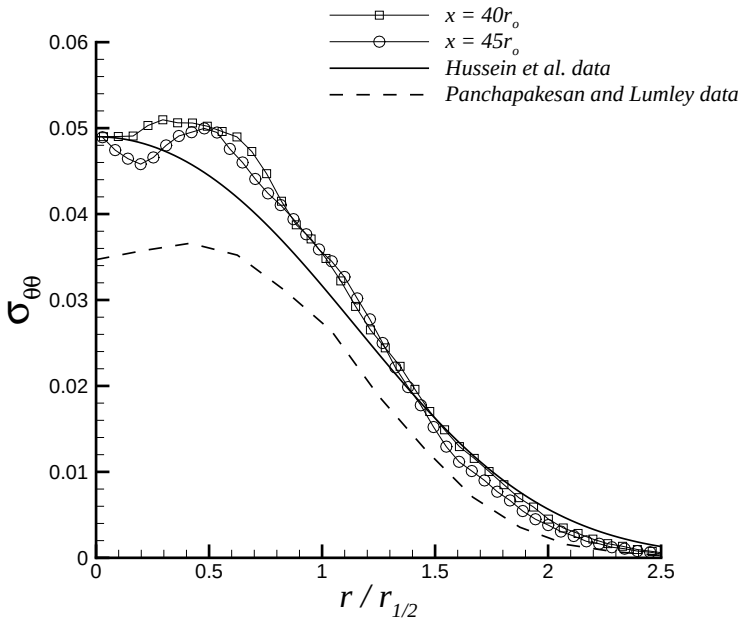

Figure 4.11. Normalized Reynolds normal stress $\sigma_{\theta\theta}$ profiles and comparison with experimental data, $Re_D = 3,600$.

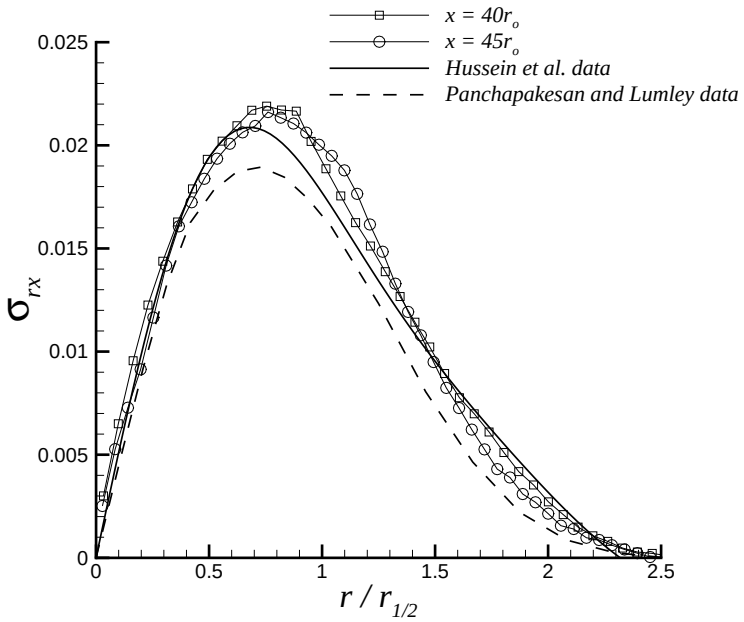

Figure 4.12. Normalized Reynolds shear stress σ_{rx} profiles and comparison with experimental data, $Re_D = 3,600$.

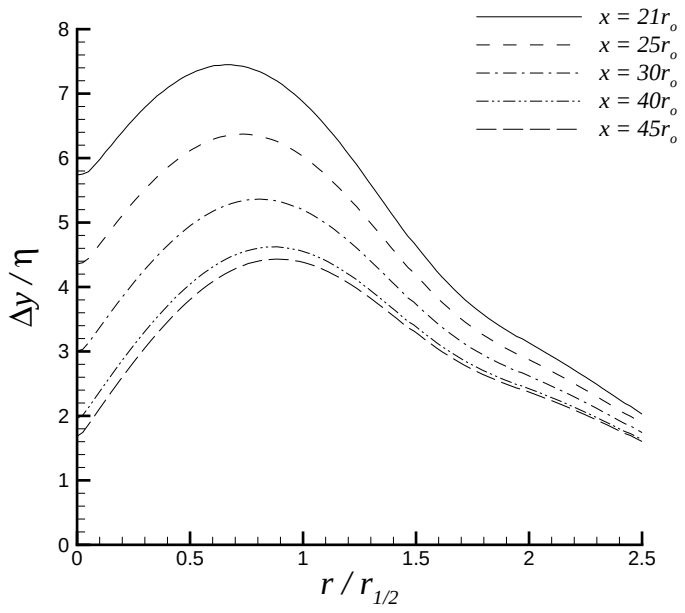

Figure 4.13. Ratio of the transverse grid spacing along the y direction to the local Kolmogorov length scale, $Re_D = 3,600$.

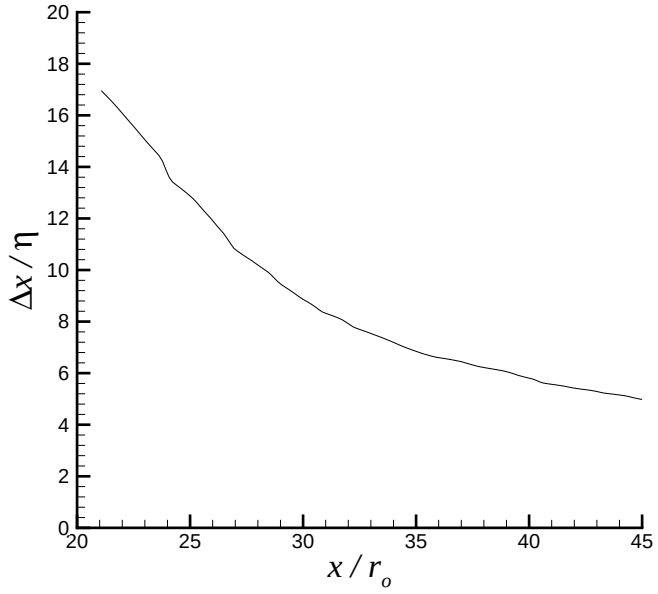

Figure 4.14. Ratio of the streamwise grid spacing along the jet centerline to the local Kolmogorov length scale, $Re_D = 3,600$.

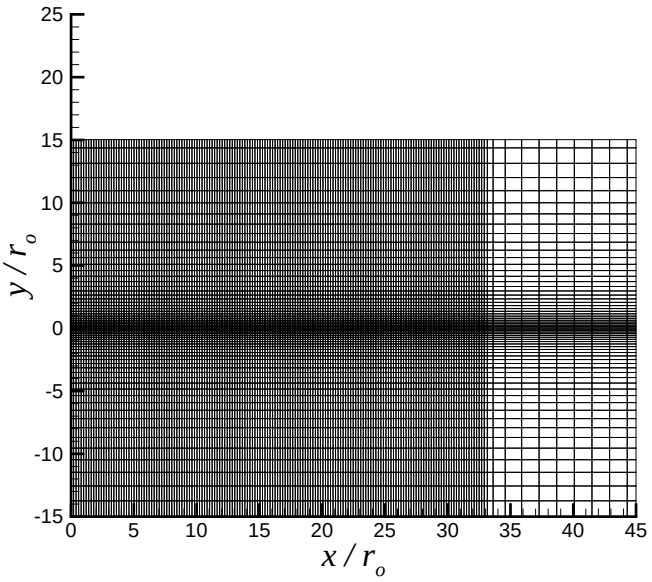

Figure 4.15. The $x-y$ section of the computational grid used in the $Re_D = 36,000$ simulation. (Every 2^{nd} node is shown.)

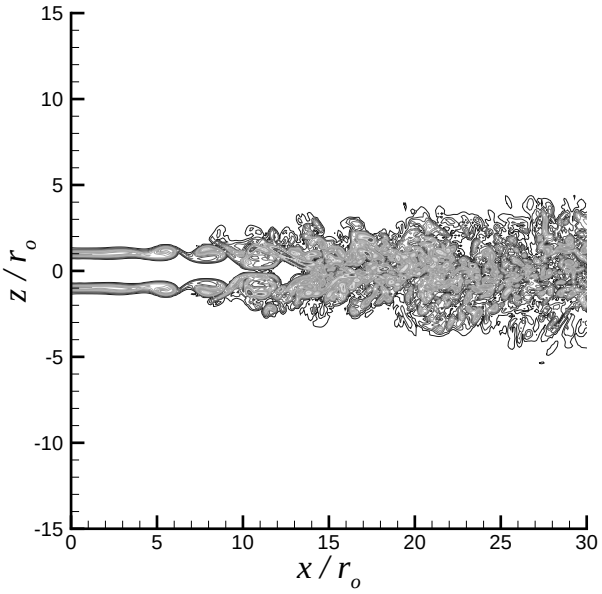

Figure 4.16. Instantaneous contours of vorticity magnitude on the $x-z$ plane at $y = 0$, $Re_D = 36,000$. 30 levels shown.

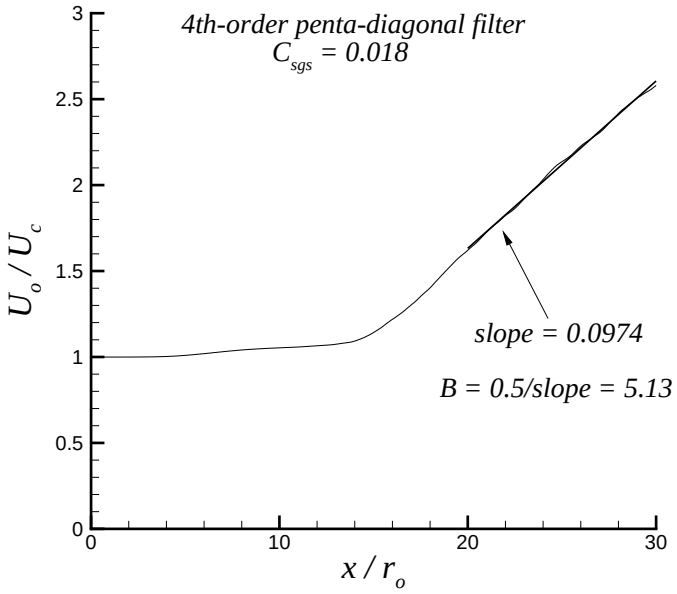

Figure 4.17. Inverse of the mean streamwise velocity on the centerline normalized by the jet inflow velocity, $Re_D = 36,000$, 4th-order accurate filter, $C_{sgs} = 0.018$.

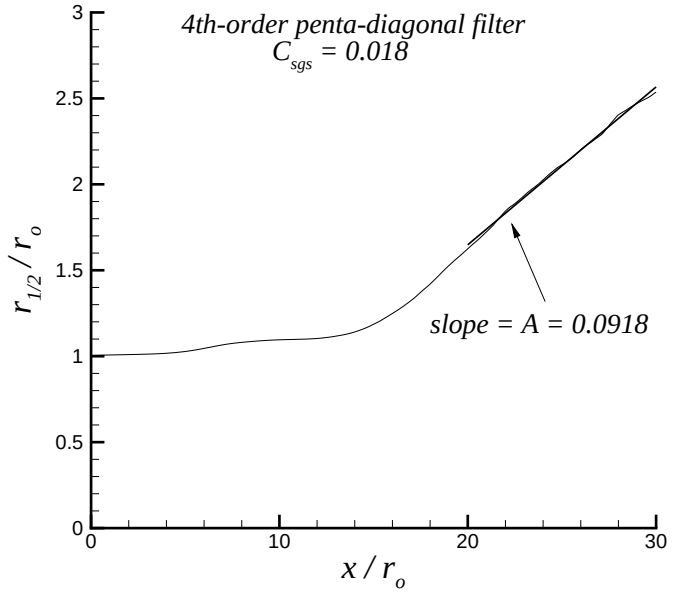

Figure 4.18. Half-velocity radius normalized by the jet radius, $Re_D = 36,000$, 4th-order accurate filter, $C_{sgs} = 0.018$.

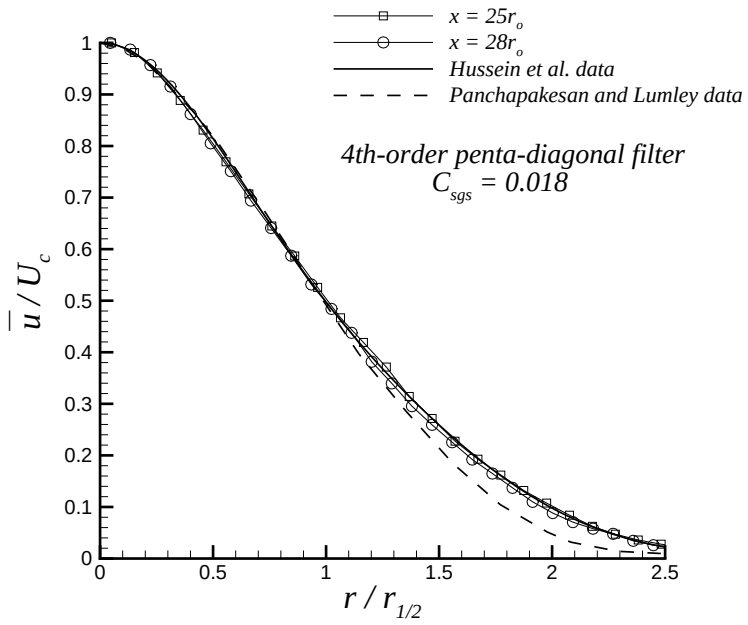

Figure 4.19. Normalized mean streamwise velocity profiles and comparison with experimental data, $Re_D = 36,000$, 4th-order accurate filter, $C_{sgs} = 0.018$.

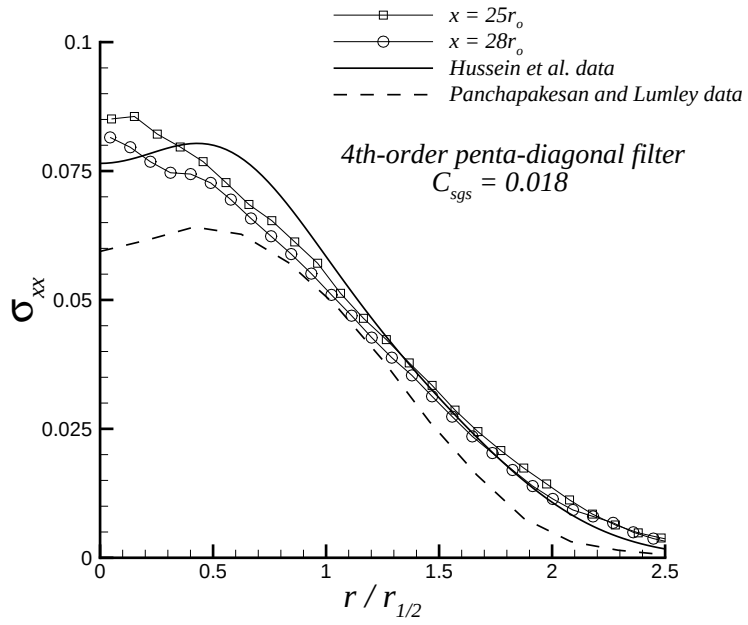

Figure 4.20. Normalized Reynolds normal stress σ_{xx} profiles and comparison with experimental data, $Re_D = 36,000$, 4th-order accurate filter, $C_{sgs} = 0.018$.

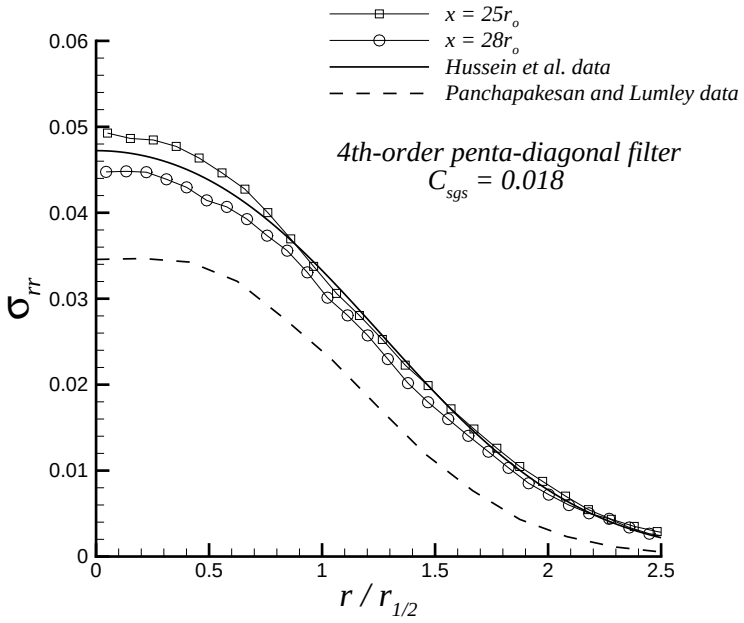

Figure 4.21. Normalized Reynolds normal stress σ_{rr} profiles and comparison with experimental data, $Re_D = 36,000$, 4th-order accurate filter, $C_{sgs} = 0.018$.

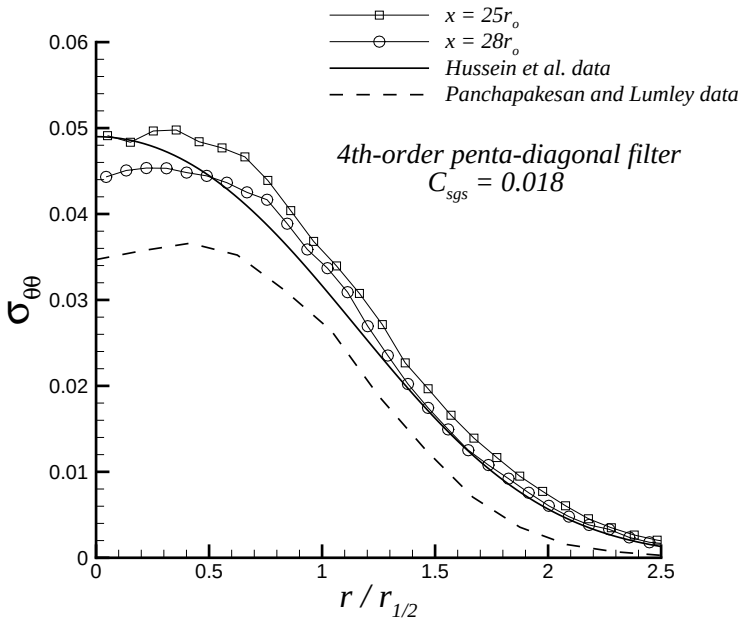

Figure 4.22. Normalized Reynolds normal stress $\sigma_{\theta\theta}$ profiles and comparison with experimental data, $Re_D = 36,000$, 4th-order accurate filter, $C_{sgs} = 0.018$.

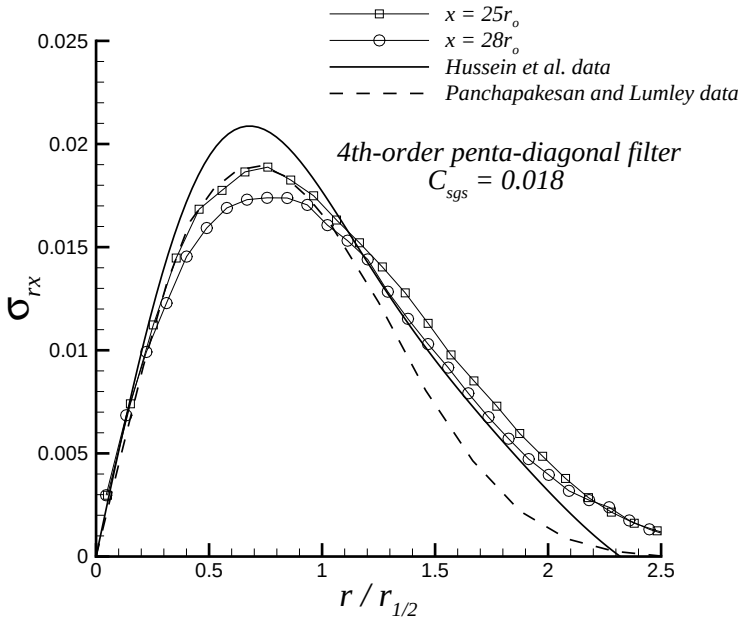

Figure 4.23. Normalized Reynolds shear stress σ_{rx} profiles and comparison with experimental data, $Re_D = 36,000$, 4th-order accurate filter, $C_{sgs} = 0.018$.

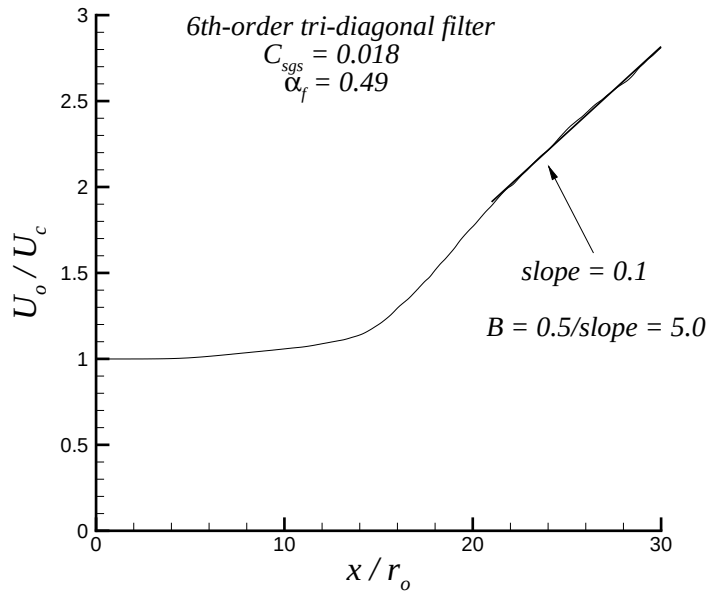

Figure 4.24. Inverse of the mean streamwise velocity on the centerline normalized by the jet inflow velocity, $Re_D = 36,000$, 6th-order accurate filter, $C_{sgs} = 0.018$, $\alpha_f = 0.49$.

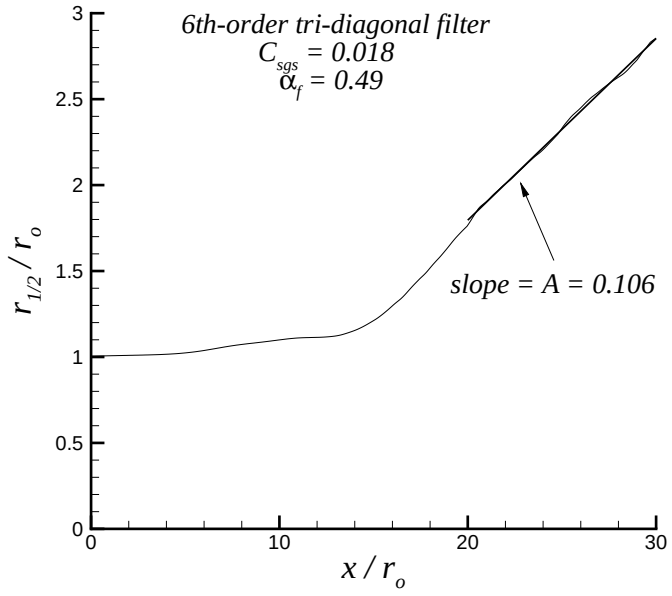

Figure 4.25. Half-velocity radius normalized by the jet radius, $Re_D = 36,000$, 6th-order accurate filter, $C_{sgs} = 0.018$, $\alpha_f = 0.49$.

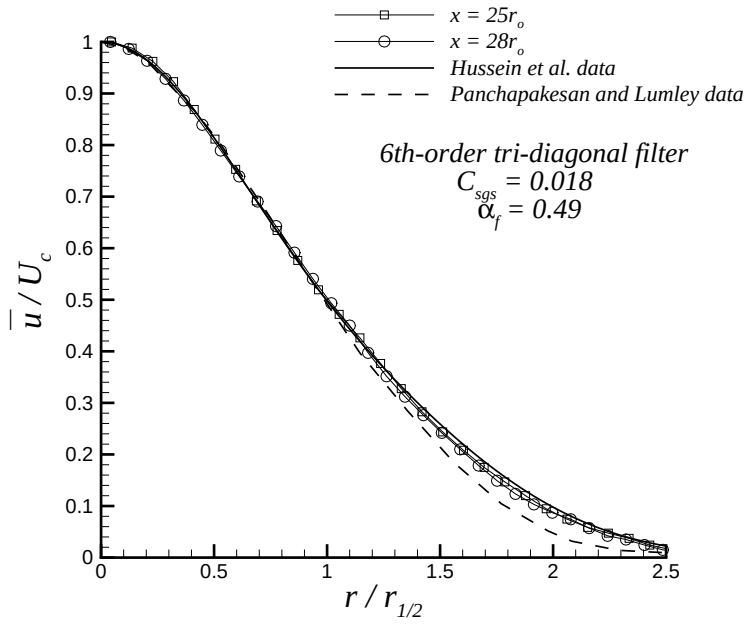

Figure 4.26. Normalized mean streamwise velocity profiles and comparison with experimental data, $Re_D = 36,000$, 6th-order accurate filter, $C_{sgs} = 0.018$, $\alpha_f = 0.49$.

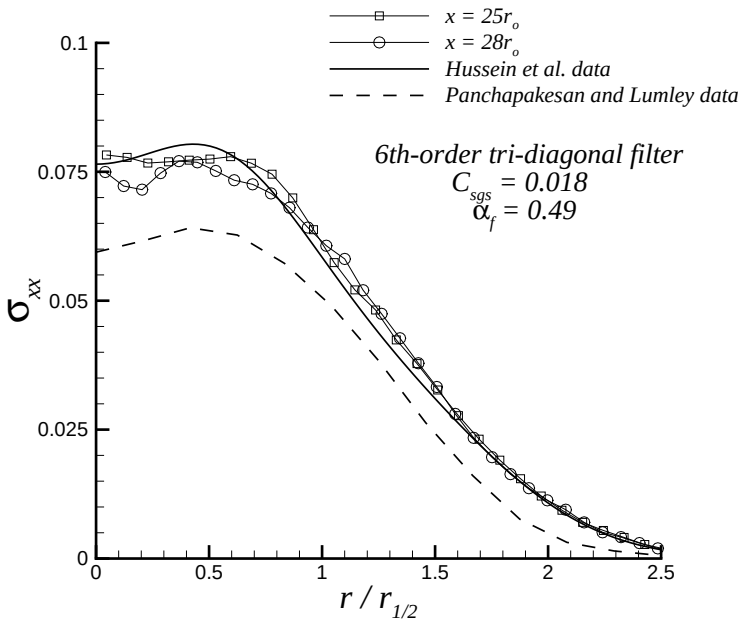

Figure 4.27. Normalized Reynolds normal stress σ_{xx} profiles and comparison with experimental data, $Re_D = 36,000$, 6th-order accurate filter, $C_{sgs} = 0.018$, $\alpha_f = 0.49$.

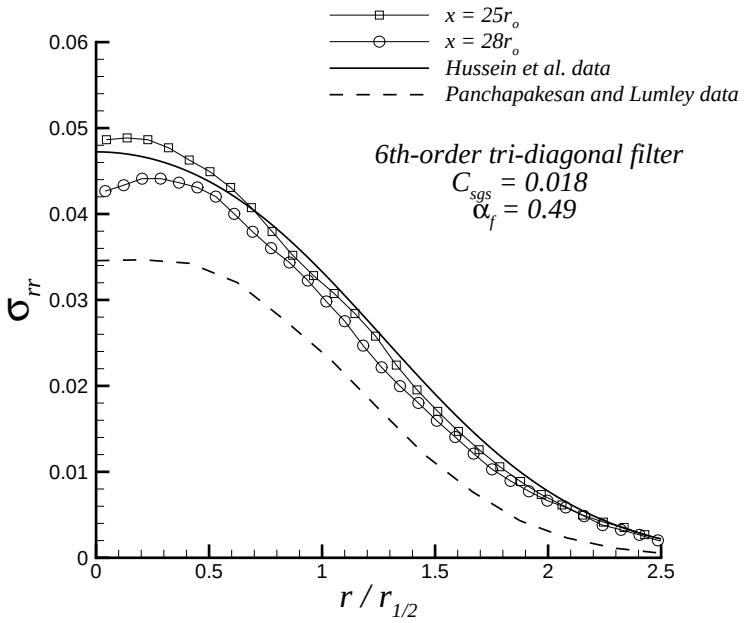

Figure 4.28. Normalized Reynolds normal stress σ_{rr} profiles and comparison with experimental data, $Re_D = 36,000$, 6th-order accurate filter, $C_{sgs} = 0.018$, $\alpha_f = 0.49$.

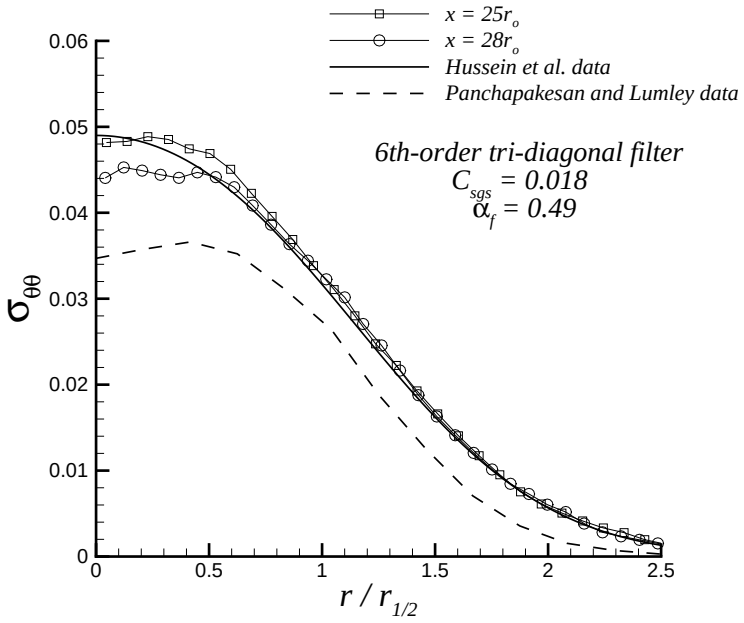

Figure 4.29. Normalized Reynolds normal stress $\sigma_{\theta\theta}$ profiles and comparison with experimental data, $Re_D = 36,000$, 6th-order accurate filter, $C_{sgs} = 0.018$, $\alpha_f = 0.49$.

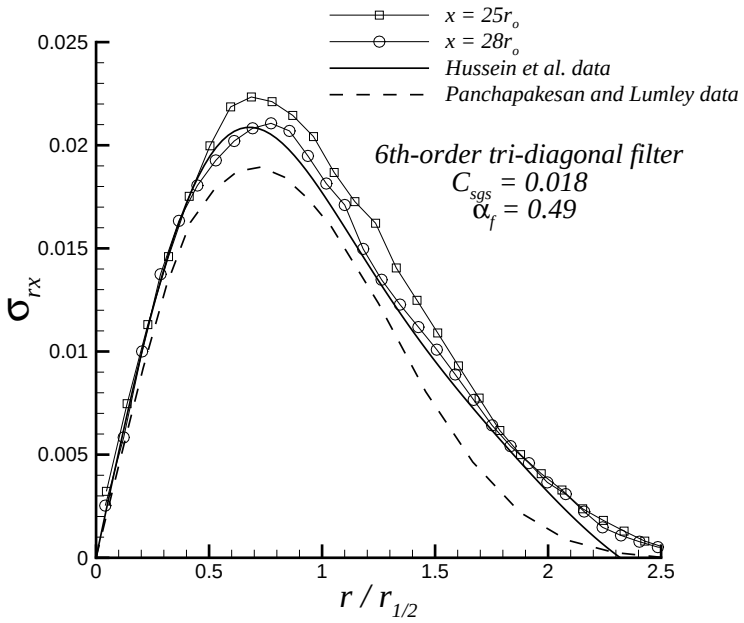

Figure 4.30. Normalized Reynolds shear stress σ_{rx} profiles and comparison with experimental data, $Re_D = 36,000$, 6th-order accurate filter, $C_{sgs} = 0.018$, $\alpha_f = 0.49$.

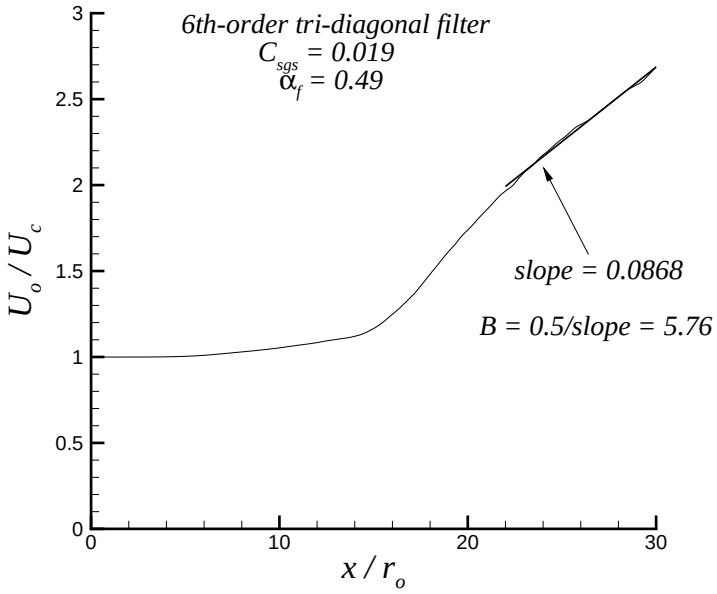

Figure 4.31. Inverse of the mean streamwise velocity on the centerline normalized by the jet inflow velocity, $Re_D = 36,000$, 6th-order accurate filter, $C_{sgs} = 0.019$, $\alpha_f = 0.49$.

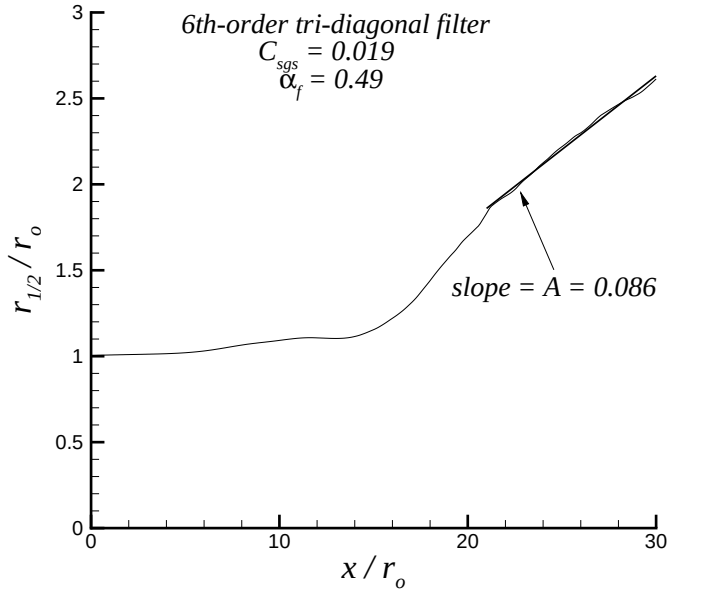

Figure 4.32. Half-velocity radius normalized by the jet radius, $Re_D = 36,000$, 6th-order accurate filter, $C_{sgs} = 0.019$, $\alpha_f = 0.49$.

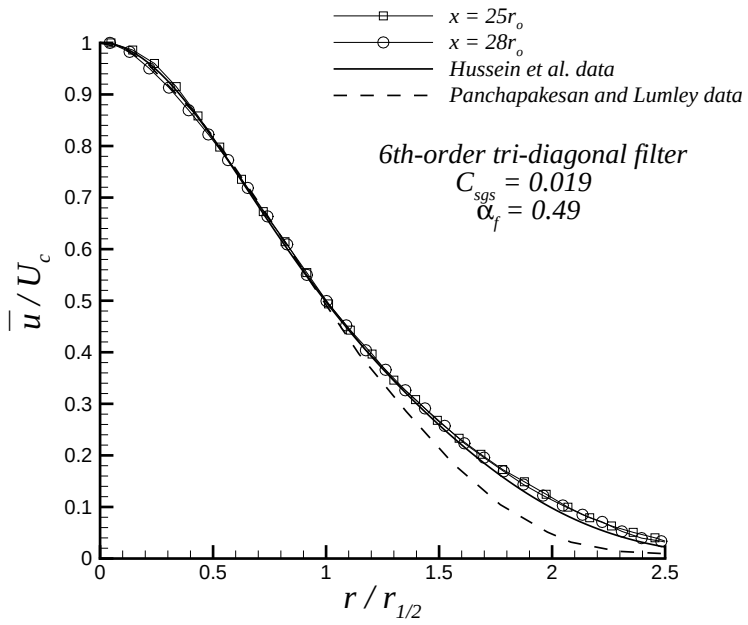

Figure 4.33. Normalized mean streamwise velocity profiles and comparison with experimental data, $Re_D = 36,000$, 6th-order accurate filter, $C_{sgs} = 0.019$, $\alpha_f = 0.49$.

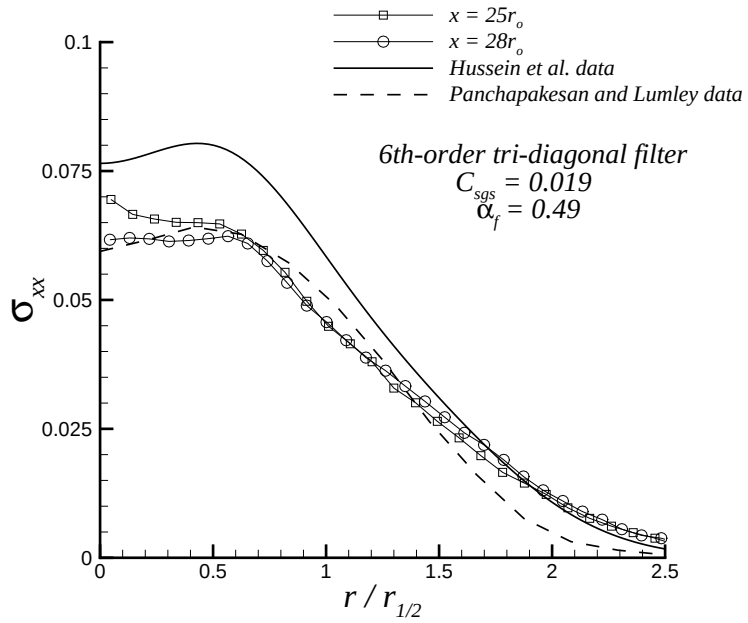

Figure 4.34. Normalized Reynolds normal stress σ_{xx} profiles and comparison with experimental data, $Re_D = 36,000$, 6th-order accurate filter, $C_{sgs} = 0.019$, $\alpha_f = 0.49$.

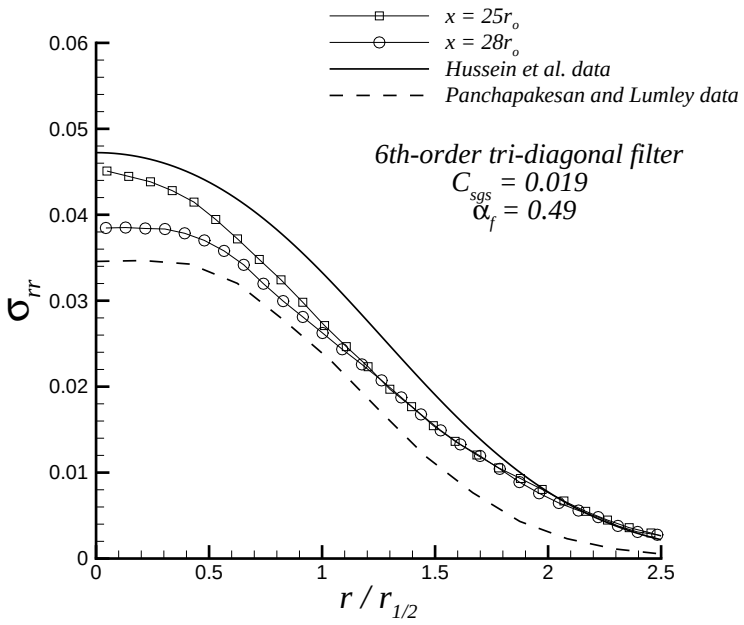

Figure 4.35. Normalized Reynolds normal stress σ_{rr} profiles and comparison with experimental data, $Re_D = 36,000$, 6th-order accurate filter, $C_{sgs} = 0.019$, $\alpha_f = 0.49$.

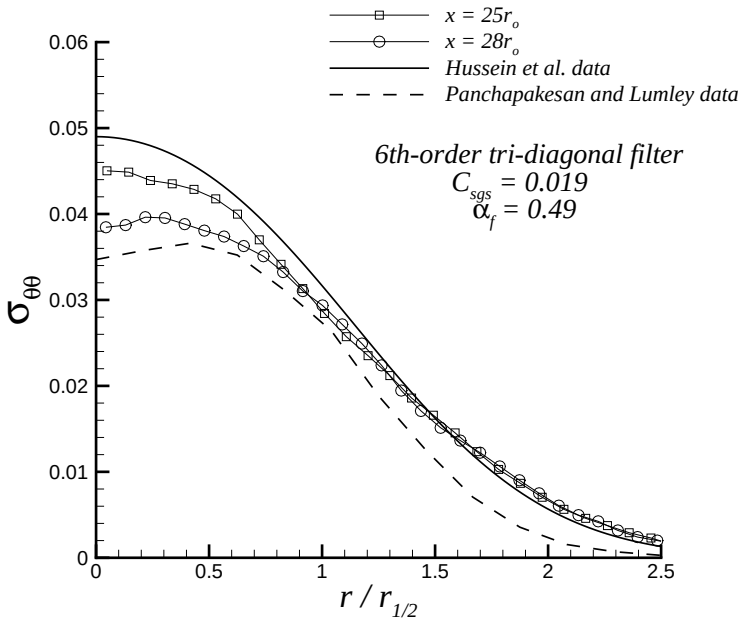

Figure 4.36. Normalized Reynolds normal stress $\sigma_{\theta\theta}$ profiles and comparison with experimental data, $Re_D = 36,000$, 6th-order accurate filter, $C_{sgs} = 0.019$, $\alpha_f = 0.49$.

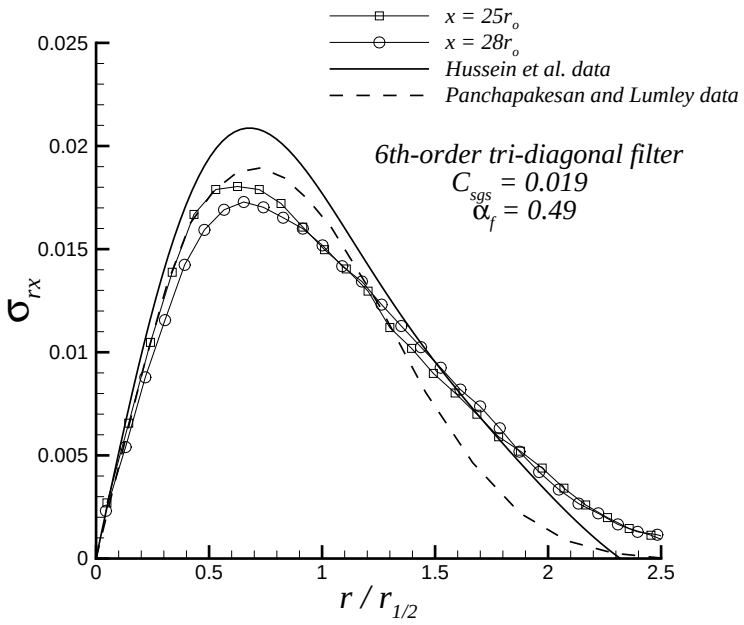

Figure 4.37. Normalized Reynolds shear stress σ_{rx} profiles and comparison with experimental data, $Re_D = 36,000$, 6th-order accurate filter, $C_{sgs} = 0.019$, $\alpha_f = 0.49$.

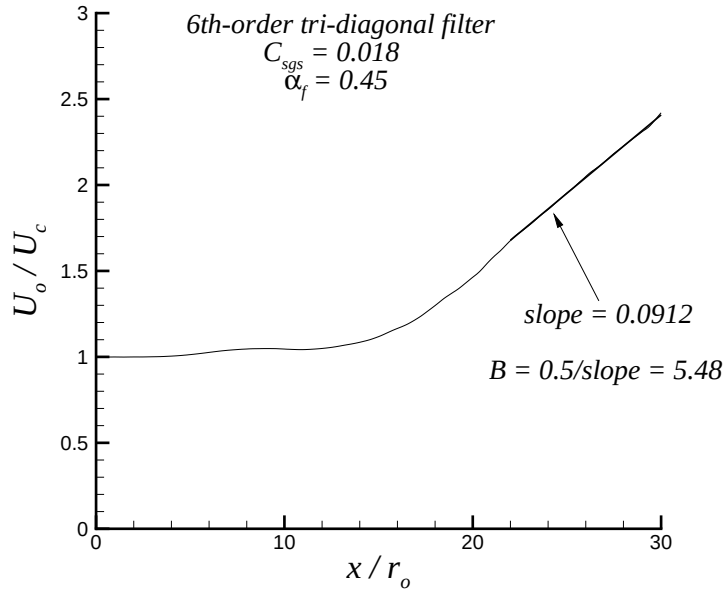

Figure 4.38. Inverse of the mean streamwise velocity on the centerline normalized by the jet inflow velocity, $Re_D = 36,000$, 6th-order accurate filter, $C_{sgs} = 0.018$, $\alpha_f = 0.45$.

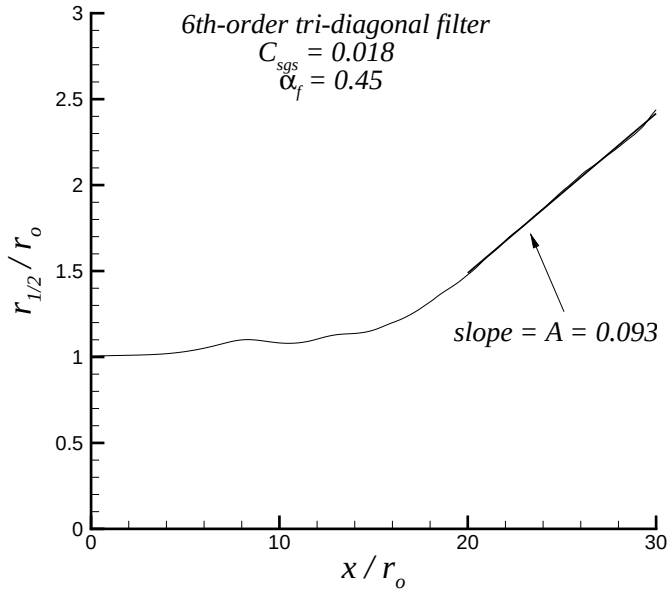

Figure 4.39. Half-velocity radius normalized by the jet radius, $Re_D = 36,000$, 6th-order accurate filter, $C_{sgs} = 0.018$, $\alpha_f = 0.45$.

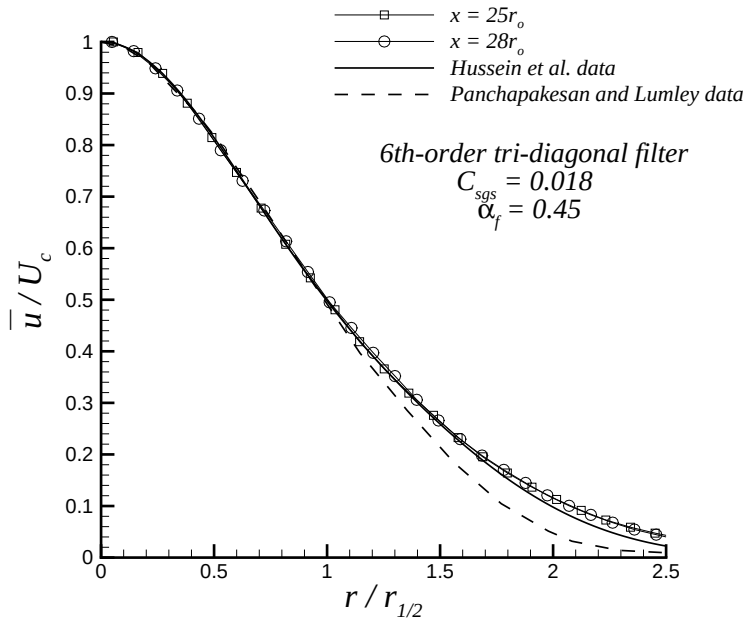

Figure 4.40. Normalized mean streamwise velocity profiles and comparison with experimental data, $Re_D = 36,000$, 6th-order accurate filter, $C_{sgs} = 0.018$, $\alpha_f = 0.45$.

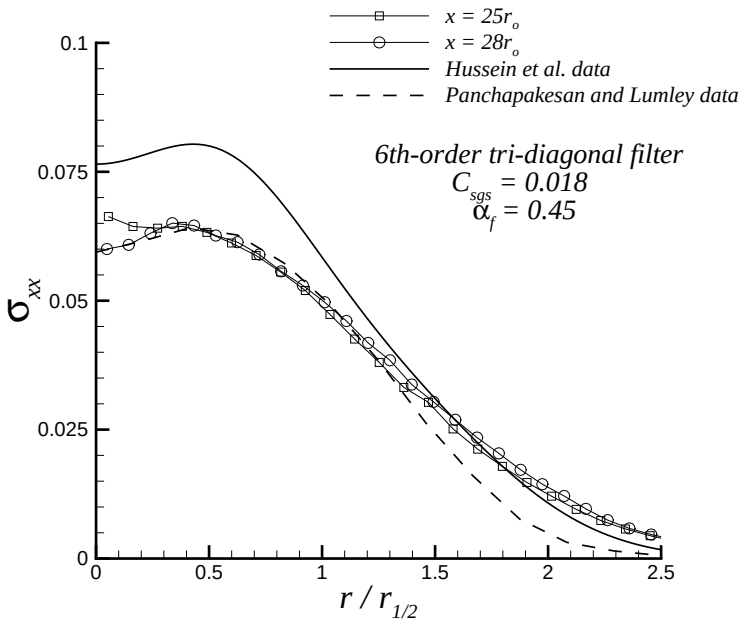

Figure 4.41. Normalized Reynolds normal stress σ_{xx} profiles and comparison with experimental data, $Re_D = 36,000$, 6th-order accurate filter, $C_{sgs} = 0.018$, $\alpha_f = 0.45$.

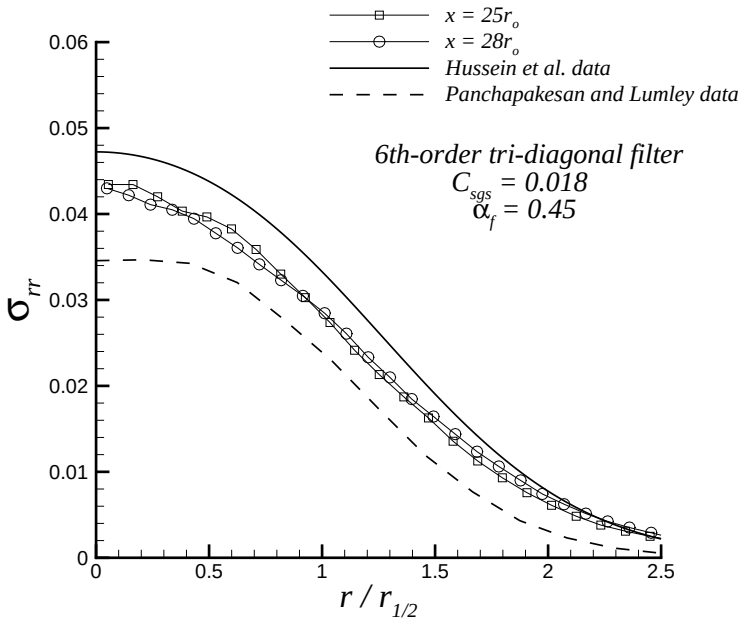

Figure 4.42. Normalized Reynolds normal stress σ_{rr} profiles and comparison with experimental data, $Re_D = 36,000$, 6th-order accurate filter, $C_{sgs} = 0.018$, $\alpha_f = 0.45$.

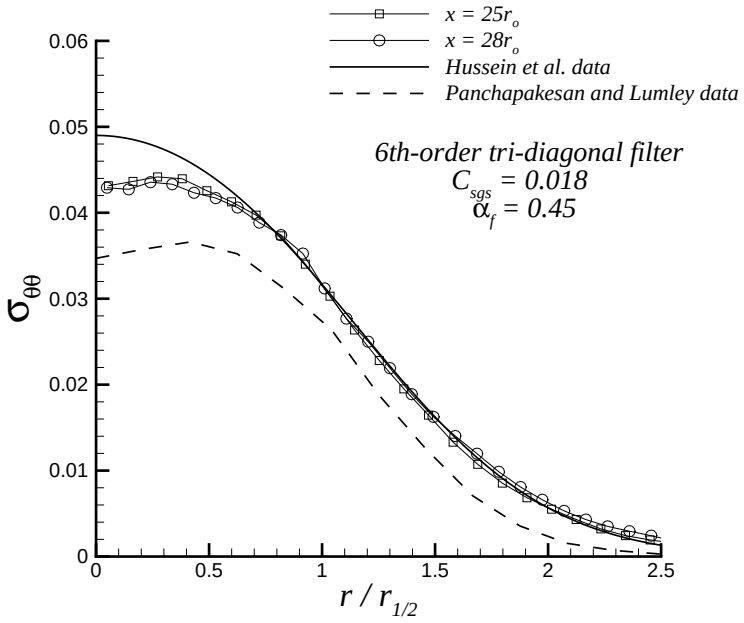

Figure 4.43. Normalized Reynolds normal stress $\sigma_{\theta\theta}$ profiles and comparison with experimental data, $Re_D = 36,000$, 6th-order accurate filter, $C_{sgs} = 0.018$, $\alpha_f = 0.45$.

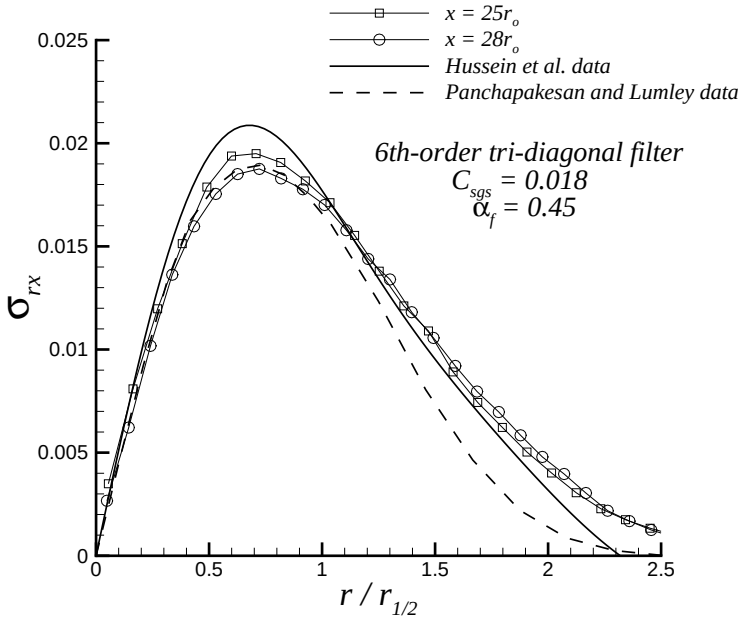

Figure 4.44. Normalized Reynolds shear stress σ_{rx} profiles and comparison with experimental data, $Re_D = 36,000$, 6th-order accurate filter, $C_{sgs} = 0.018$, $\alpha_f = 0.45$.

5. LES OF A REYNOLDS NUMBER 100,000 ROUND JET WITH THE DYNAMIC SMAGORINSKY MODEL AND JET AEROACOUSTICS

In this chapter, we will present both aerodynamics and aeroacoustics results from an LES performed with the dynamic SGS model for a turbulent isothermal round jet at a Mach number of 0.9, and Reynolds number $Re_D = \rho_o U_o D_j/\mu_o = 100,000$ where ρ_o, U_o, μ_o are the jet centerline density, velocity and viscosity at the nozzle exit, respectively and D_j is the jet diameter. The jet centerline temperature was chosen the same as the ambient temperature and set to $288K$. The turbulent Prandtl number was set to a constant value of 0.7, while the compressibility correction constant in the SGS model was set to 0.

A fully curvilinear grid consisting of approximately 12 million grid points was used in the simulation. The physical portion of the domain extended to $60r_o$ in the streamwise direction and from $-20r_o$ to $20r_o$ in the transverse y and z directions, where $r_o = D_j/2$ is the jet radius. The coarsest resolution in this simulation is estimated to be about 170 times the local Kolmogorov length scale. Figures 5.1 through 5.4 show how the grid is stretched in all three directions. Initially, the grid points are clustered around the shear layer of the jet in order to accurately resolve the shear layer. After the potential core of the jet breaks up, the grid is also stretched in the y and z directions in order to redistribute the grid points and achieve a more uniform distribution. The $y-z$ cross-section of the grid remains the same along the streamwise direction after a distance of $35r_o$. A total of 10 modes were used in the vortex ring forcing. The forcing parameter α was set to 0.01. The reader is referred to section 2.2.5 for the details of the vortex ring forcing. The tri-diagonal spatial

filter was used to filter the flow field using the parameter $\alpha_f = 0.47$. The following mean streamwise velocity profile was imposed on the inflow boundary

$$\bar{u}(r) = \frac{U_o}{2}\left[1 + \tanh\left[7.5\left(1 - \frac{r}{r_o}\right)\right]\right]. \tag{5.1}$$

This velocity profile is similar to the one used by Bogey and Bailly in their LES calculations [33], [34], [35]. It should be noted here that the given profile produces an initial jet shear layer that is thinner than those used in the previous lower Reynolds number jet simulations. We were able to afford a thinner jet shear layer in the current simulation since the grid used here has a finer resolution than those used in the previous lower Reynolds number jet simulations. There are about 14 grid points in the initial jet shear layer. The following Crocco-Buseman relation for an isothermal jet is specified for the density profile on the inflow boundary [33]

$$\bar{\rho}(r) = \rho_o\left(1 + \frac{\gamma - 1}{2}M_r^2\frac{\bar{u}(r)}{U_o}\left(1 - \frac{\bar{u}(r)}{U_o}\right)\right)^{-1}, \tag{5.2}$$

where $M_r = 0.9$.

5.1 Jet Mean Flow Field

It has been observed by Bogey and Bailly [33] that the jet spreading rate and the jet decay coefficient do not reach their asymptotic values if the computational domain size is kept relatively short. Furthermore, they found out that Reynolds stresses do not reach their self-similar state either in a relatively short domain. Our aim is to fully validate the dynamic model, so it is important that the asymptotic jet spreading rate and the centerline velocity decay rate as well as the self-similar state of Reynolds stresses are reached in the simulation. This will facilitate the comparison of our numerical results with the experimental jet data at similar flow conditions. Hence, we decided to choose a long domain length of $60r_o$ in the streamwise direction.

In our simulation, the initial transients exited the domain over the first 20,000 time steps. An ambient sound wave travels 8 times the domain length in the streamwise direction in 20,000 time steps. We then collected the flow statistics over 150,000

time steps. This sampling period corresponds to a time length in which an ambient sound wave travels about 60 times the domain length in the streamwise direction. A total of about 30 days of computing time was needed for this simulation on an IBM-SP3 machine using 160 processors in parallel. It should be noted that the mean flow convection speeds in the far downstream region are relatively low, hence the turbulence convects slowly in the far downstream region resulting in slowly converging statistics. As a result, we had to collect data over a period of 150,000 time steps to obtain reasonably converged statistics.

In figure 5.5, the one-dimensional spectrum of the streamwise velocity fluctuations at the $x = 20r_o$ location on the jet centerline is shown. The temporal spectrum of the streamwise velocity fluctuations at the given location was coupled with Taylor's hypothesis of frozen turbulence to compute this one-dimensional spectrum. In this hypothesis, the one-dimensional spectrum of the streamwise velocity fluctuations is calculated from the temporal streamwise velocity fluctuations as follows

$$E(k_x) = E_f(f)\frac{\bar{u}}{2\pi}, \tag{5.3}$$

where

$$k_x = f\frac{2\pi}{\bar{u}}, \tag{5.4}$$

is the axial wavenumber, f is the frequency and $E_f(f)$ is the power spectral density of the streamwise velocity fluctuations. As expected, the one-dimensional spectrum becomes almost flat as the axial wavenumber approaches zero. We also show the grid cutoff wavenumber corresponding to our grid resolution at the given axial location. The spectral energy at the grid cutoff wavenumber is about 2 orders of magnitude smaller than that at the lowest wavenumbers. Before the grid cutoff wavenumber, the spectrum exhibits a decay which is quite similar to Kolmogorov's $-5/3$ decay rate prediction in the inertial range of turbulence. This means that our grid resolution is fine enough to resolve a portion of the inertial range of wavenumbers at the given axial location.

For code validation, we first compared our jet's centerline decay rate in the far downstream region with the experiments of Zaman [79]. Zaman [79] did a series of experiments for initially compressible jets and examined the asymptotic jet centerline velocity decay and entrainment rates. He found out that the asymptotic jet centerline velocity decay rate decreased with increasing initial jet Mach number. In figure 5.6, we plot the streamwise variation of the inverse of the mean jet centerline velocity normalized by the jet inflow velocity. In the far downstream region, we see that the slope of the linear fit to the curve is 0.161. From the experiments of Zaman [79], the corresponding experimental slope for a Mach 0.9 jet is about 0.155 which is very close to our computed value. For incompressible jets, on the other hand, experimental values ranging from 0.165 to 0.185 have been previously reported in the literature [74], [77], [80].

The end of the potential core of our jet is at around $x = 11r_o$. Raman *et al.* [81] measured a potential core length of about $10r_o$ for jets with initially transient shear layers. Arakeri *et al.* [82] reported a value of about $14r_o$ for the potential core length of a Mach 0.9, Reynolds number 500,000 jet with initially transient shear layers. For high Reynolds number jets with initially turbulent shear layers, potential core lengths of about $14r_o$ have been measured by Raman *et al.* [81] and Lau *et al.* [83]. Our jet's potential core length compares favorably with these existing experimental measurements.

In figure 5.7, we show the streamwise variation of the mass flux, m, normalized by the mass flux through the jet nozzle, m_e. In the far downstream region, we again see a linear growth. This time the slope of the line is 0.267 showing very good agreement with the experimental value of 0.26 from Zaman [79]. The jet spreading rate, which is the slope of the half-velocity radius growth in the far downstream region depicted in figure 5.8, has been found to be 0.092 in our simulation. The half-velocity radius, $r_{1/2}$ at a given downstream location is defined as the radial location where the mean streamwise velocity is one half of the jet mean centerline velocity at that location. To the best of our knowledge, no experimental value has been reported from an

initially compressible jet in the literature for the jet spreading parameter. However, experimental values ranging from 0.086 to 0.096 have been previously found for incompressible jets. Hence, our computed value is within the experimental range observed for incompressible jets [74], [77], [80].

Properly scaled mean streamwise velocity profiles at three downstream locations are plotted in figure 5.9. The self-similarity coordinate is taken as $r/r_{1/2}$ where r is the radial location and $r_{1/2}$ is the half-velocity radius. The vertical axis of the figure is normalized by the mean jet centerline velocity. From this figure, it can be observed that the profiles of our jet at the three downstream locations collapse onto each other fairly well and exhibit self-similarity which is consistent with experimental observations. Our results are also in very good agreement with the experimental profiles of Hussein *et al.* [74] for an incompressible jet at $Re_D = 95,500$ as well as that of Panchapakesan and Lumley [77] for an incompressible jet at $Re_D = 11,000$. The convective Mach number of the jet flow is low in the far downstream region, hence the compressibility effects are negligible. Therefore, it is safe to compare our profiles in the far downstream region with incompressible experimental data.

We also compared our Reynolds stress profiles with the experimental profiles of Hussein *et al.* [74] and Panchapakesan and Lumley [77]. Figures 5.10 through 5.13 plot our properly scaled Reynolds stress profiles at five downstream locations and compare them with the two experiments. Again, the self-similarity coordinate is taken as $r/r_{1/2}$. The vertical axis of the figures is normalized by the square of the mean jet centerline velocity. The downstream locations are chosen at $x = 25r_o$, $x = 30r_o$, $x = 45r_o$, $x = 50r_o$, and $x = 55r_o$. As can be observed from the plots, the properly scaled profiles at $x = 45r_o$, $x = 50r_o$, and $x = 55r_o$ collapse onto each other exhibiting self-similarity. It is also clear that the self-similarity region of the Reynolds stresses is not reached at around $x = 25r_o$ or $x = 30r_o$ since the profiles at these two downstream locations are lower than those in the far downstream region. Overall, the agreement of the profiles at $x = 45r_o$, $x = 50r_o$, and $x = 55r_o$ with experiments is very good. It should be noted that our

Reynolds stresses computed by LES are based on filtered velocities, while the actual experimental profiles are based on unfiltered velocities. Hence, some differences should be expected between LES and experiments when the Reynolds stresses are compared. As can be seen from the figures, the Reynolds normal stress σ_{xx} profiles match the experiment of Panchapakesan and Lumley [77] better, while the other Reynolds stresses are in between the two experimental profiles. It should also be noted that the difference between the initial conditions imposed in our simulation and the actual initial conditions in experimental jets could be another possible reason for the differences between LES and experimental profiles. We have imposed randomized velocity fluctuations in the form of a vortex ring [58] in our simulation since the actual nozzle geometry was not included in the calculations. Furthermore, it can be argued that the experimental Reynolds stress profiles have been measured in the very far downstream region, usually at distances of 100 jet radii or more. It has also been observed experimentally that the different Reynolds stress components reach asymptotic self-similarity at different downstream locations, depending on initial conditions. The Reynolds number of the jet is also expected to have an influence on where exactly the self-similarity region is reached. The experiments of Wygnanski and Fiedler [66] suggest a distance of about 100 jet radii downstream of the jet nozzle for the start of the self-similarity region in high Reynolds number jets, while Freund's DNS for a Reynolds number 3,600 jet [2] shows the self-similarity region begins at around $x = 25r_o$ in a low Reynolds number jet. Since our domain length of 60 jet radii is still relatively short compared to experiments and the jet Reynolds number is relatively high, the normalized Reynolds normal stresses σ_{xx} may not have reached their true asymptotic values. If we did a new simulation using a domain longer than $60r_o$ in the streamwise direction, it is possible that the Reynolds normal stress σ_{xx} profiles in the far downstream region might shift upwards and come in between the two experiments. However, such a simulation would require even more grid points and many more time steps to run since the very slowly convecting mean

flow in the far downstream region would cause very slowly converging flow statistics. Hence such a simulation would not be very practical.

To summarize, the mean flow properties computed using the dynamic SGS model compared very well with the experimental data. Furthermore, the comparison of Reynolds stresses in the present simulation with experiments is found to be reasonable. These findings provide us with valuable evidence towards the validity of the numerical schemes as well as the dynamic subgrid-scale model used in our LES code.

5.2 Far Field Aeroacoustics

In this section, we will look at some far field aeroacoustics results obtained by coupling the near field LES data with a Ffowcs Williams-Hawkings code which has the capability to work on any general control surface geometry. We put a control surface around our jet as illustrated in figure 5.14 and we gathered flow field data on the control surface at every 10 time steps over a period of 23,000 time steps during our LES run. The control surface starts 1 jet radius downstream of the inflow boundary and extends to 60 jet radii along the streamwise direction. To investigate the effect of the streamwise length of the control surface on the far field noise predictions, we divided the control surface into 3 segments. As can be seen in figure 5.14, the first segment extends to $35r_o$ in the streamwise direction, while the second and third segments extend to $45r_o$ and $60r_o$, respectively. Hence, the total streamwise lengths of these 3 control surfaces are $34r_o$, $44r_o$ and $59r_o$. The total acoustic sampling period corresponds to a time scale in which an ambient sound wave travels about 9.4 times the domain length in the streamwise direction. Assuming at least 6 points per wavelength are needed to accurately resolve an acoustic wave, we see that the maximum frequency resolved with our grid spacing around the control surface corresponds to a Strouhal number of approximately 1.0. The Nyquist frequency, on the other hand, which is the maximum frequency that can be resolved with the time increment of our data sampling rate, corresponds to a Strouhal number of about 4.55. However,

we choose the maximum frequency that is based on spatial resolution as our cutoff frequency. The time increment used in the LES corresponds to a Strouhal number of about 45.45. Based on the data sampling rate, there are about 10 temporal points per period in the highest resolved frequency. Such a temporal resolution is adequate.

The acoustic pressure spectra computed using the data directly provided by LES at some arbitrary points in the near field of the jet were compared against the FWH predictions at the same near field observation points in order to validate the FWH code. Figures 5.15 and 5.16 show such comparisons at two near field points. As can be seen from the figures, the noise spectra predicted by the FWH method at these two observation points are almost identical to the noise spectra computed using the direct LES data. Excellent agreement was also obtained at the other near field observation points not shown here. These observations provide proof for the validity the FWH code.

We computed the overall sound pressure levels along an arc of radius $60r_o$ from the jet nozzle. The center of the arc is chosen as the jet nozzle exit and the angle θ is measured from the jet axis as illustrated in figure 5.17. We applied the Ffowcs Williams - Hawkings method to compute the acoustic pressure signal at 36 equally spaced azimuthal points on a full circle at a given θ location on the arc. θ values on the arc range from 25° to 90° with an increment of 5°. The far field noise calculations were performed using 60 processors in parallel on an IBM-SP3. The computation of the 2048-point time history of acoustic pressure at a given far field location took about 7 minutes of computing time. Hence, a total of 59 hours was needed to compute the acoustic pressure history at a total of 504 far field points. In order to confine spurious spectral contributions to low frequencies, we multiplied the pressure history at every azimuthal location by a windowing function similar to that used by Freund [2]. We ran the windowed pressure history through a 2048-point Fast Fourier Transform, and converted to polar notation to obtain the power spectral density at each frequency. We then averaged the acoustic pressure spectra over the equally spaced 36 azimuthal points and finally integrated the averaged spectrum to

Table 5.1. Some jet noise experiments with similar Mach numbers.

M	Re_D	Reference
0.9	540,000	Mollo-Christensen *et al.* [85]
0.88	500,000	Lush [86]
0.9	3,600	Stromberg *et al.* [3]
0.9	100,000	Our 3-D LES

compute the overall sound pressure level at the given θ location. Figure 5.18 shows our overall sound pressure levels computed along the arc and compares them with some experimental data. Table 5.1 summarizes the Mach numbers and Reynolds numbers of the experiments that we are doing comparisons with. It should be noted that the experimental jets were cold jets, whereas our jet is an isothermal jet. We also plot the SAE ARP 876C [84] database prediction for an isothermal Mach 0.9 jet. This database consists of actual engine jet noise measurements and can be used to predict overall sound pressure levels within a few dB at various jet operating conditions. The same database was also used to predict the overall sound pressure levels for a cold Mach 0.9 jet with a temperature ratio of $T_o/T_\infty = 0.86$ and the differences between the isothermal and cold jet predictions were found to be only 0.3 dB.

From the OASPL plot, we see that the control surface with streamwise length $59r_o$ predicts a continuous increase in OASPL values as the observation angle, θ drops towards the $\theta = 25^\circ$ limit. On the other hand, the control surface with streamwise length $44r_o$ predicts a drop-off in OASPL as θ decreases from 30° to 25°, whereas the control surface with streamwise length $34r_o$ gives a similar drop-off in OASPL as θ decreases from 40° to 25°. Compared to $59r_o$, the control surfaces with streamwise lengths $34r_o$ and $44r_o$ are relatively short. Hence, these 2 surfaces cannot effectively capture the acoustic waves travelling at the shallow angles and this explains the behavior of the predictions of these 2 control surfaces at observation

angles which are close to the jet axis. The OASPL prediction of the control surface with streamwise length $59r_o$ is, of course, the most accurate one and this prediction will be used from this point on to make comparisons with other data. From the OASPL plot, we also see that our jet is louder than the experimental jets of Lush [86] and Stromberg *et al.* [3] for all points along the arc. On the other hand, our prediction is within 1.5 dB of the measurements of Mollo-Christensen *et al.* [85]. We also see as much as 3 dB difference between our prediction and the SAE ARP 876C prediction at the downstream angles where $\theta < 40°$. The missing higher frequencies in the LES are expected to increase our OASPL predictions by a few more dB. The differences between the current predictions and experimental measurements are believed to be related to the inflow forcing employed in the simulation. Since the actual nozzle geometry is not included in the present computations, randomized velocity fluctuations in the form of a vortex ring have been imposed a short distance downstream of the inflow boundary in order to trigger the instabilities in the flow. This vortex ring forcing is the same type of forcing employed by Bogey and Bailly [58] in their LES calculations. In a recent study, Bogey and Bailly [34] took a close look at the effects of the inflow conditions on the jet flow and noise and they showed that the inflow forcing has a significant impact on the noise of the jet. We will also look at the effects of the inflow forcing on the jet noise in the next chapter and show that the far field noise is indeed dependent upon how the inflow forcing is done in the LES.

We should also mention here that in the LES done by Zhao *et al.* [20] for a Mach 0.9, Reynolds number 3,600 jet, the agreement between the overall sound pressure levels predicted by LES and the experiments was better than the agreement observed between our LES and the experiments. However, Zhao *et al.* [20] had used a relatively coarse mesh consisting of about 2 million grid points in their LES. They do not provide information about the cut-off frequency corresponding to their grid resolution. It is believed that the low cut-off frequency due to the relatively coarse mesh used in their LES is primarily responsible for the better agreement of their

overall sound pressure levels with the experiments. As the cut-off frequency gets higher, integration of the noise spectra over a wider resolved frequency range results in increased overall sound pressure levels.

Finally, we compare our acoustic pressure spectra at three observation locations with the recent results of Bogey and Bailly [33] for an isothermal round jet at a Reynolds number of 400,000. It should be noted here that Bogey and Bailly [33] computed the spectra in the near field of the jet only, using the data directly provided by LES. The first observation point of Bogey and Bailly [33] is located inside of our control surface while the other two are located outside, hence we can directly compute the near field spectra at the latter two points using the Ffowcs Williams - Hawkings method. On the other hand, in order to make a comparison at their first near field observation point which is located inside of our control surface, we first adjust our θ location along the far field arc at $R = 60r_o$ such that an acoustic ray drawn between the end of the potential core ($x = 11r_o$) and the θ location on the arc crosses their near field observation point. After we compute our far field spectrum at the corresponding θ location on the arc, we can then transfer the far field spectrum to the near field observation point using the r^{-1} decay assumption of acoustic waves. In this assumption, the acoustic wave amplitudes drop by a factor of 2 for every doubling of the distance from the source region. The source region is assumed to be compact and taken at the end of the potential core of the jet.

The acoustic pressure spectra are plotted as the sound pressure level (SPL) versus the Strouhal number which is defined as $St = fD_j/U_o$, where f is the frequency, D_j and U_o are the jet nozzle diameter and the jet centerline velocity on the inflow boundary, respectively. It should be mentioned here that since the computed spectra are noisy, the spectra that are shown are polynomial fits to the actual computed spectra. Figure 5.19 plots the spectrum at the $x = 29r_o$ and $r = 12r_o$ location over our resolved frequency range and compares it with the corresponding near field spectrum of Bogey and Bailly [33]. An acoustic ray that originates from the end of the potential core and passes through this near field observation point hits the far

field arc at around the $\theta = 25^\circ$ location. The far field spectrum at this θ location on the arc is also shown in the figure. The distance between the far field observation point and the end of the potential core is about $50.25r_o$, whereas the distance between the near field point and the end of the potential core is $21.63r_o$. The ratio of these two distances is about 2.32. A factor of 2.32 means about 7.32 dB/St difference according to the r^{-1} decay assumption of acoustic waves. Hence we shift our far field spectrum computed at $R = 60r_o$ and $\theta = 25^\circ$ upwards by 7.32 dB/St to get our near field spectrum at the first observation point of Bogey and Bailly [33]. We see that our spectrum has a peak at around $St = 0.25$ while that of Bogey and Bailly [33] is at $St = 0.3$. The peak of our spectrum has a sound pressure level (SPL) slightly higher than that of Bogey and Bailly [33]. We also see that after the peak, our spectrum decays somewhat faster than that of Bogey and Bailly [33]. Finally, from our spectrum, it is observed that there is a drop of about 15 dB/St in the sound pressure level from the peak Strouhal number of 0.25 to the grid cutoff Strouhal number of 1.0. Figures 5.20 and 5.21 show our near field spectra at the other two observation points, respectively and make comparisons with the spectra obtained by Bogey and Bailly [33]. The acoustic rays that originate from the end of the potential core and pass through these two near field observation points hit the far field arc at the $\theta = 50^\circ$ and $\theta = 80^\circ$ locations, respectively. We also show our far field spectra corresponding to these two near field observation points. From these figures, we see that our near and far field spectra basically have the same shape. Our spectra also become broad-band at these observation points demonstrating the fact that higher frequencies are becoming more dominant. It is also interesting to note that our spectra demonstrate a decay after they reach their peak, whereas the spectra of Bogey and Bailly [33] stay relatively flat after the peak.

One possible reason for the differences between our spectra and those of Bogey and Bailly [33] could be the different Reynolds numbers of the two simulations. It should also be reminded here that Bogey and Bailly [33] did not employ any SGS model in their LES. Instead, they treated the spatial filter used in their simulation

as the SGS model. In a recent study, Bogey and Bailly [35] also looked at the effect of SGS modelling on the computed jet noise. Their comparisons of acoustic pressure spectra obtained with and without an SGS model for a round jet at Reynolds number 400,000 are very similar to our observations in this study shown in the next chapter. These findings imply that the eddy viscosity associated with the SGS model is somehow affecting the well-resolved length scales of motion thereby resulting in a reduction of the amplitudes of the well-resolved acoustic waves. In the next chapter, we will look at the effects of the dynamic Smagorinsky model on the jet noise in more detail.

There is almost 10 dB/St difference between our near and far field spectra in figure 5.20. The distance between the far field point and the end of the potential core is about $53.60r_o$, whereas the distance between the near field point and the end of the potential core is $17.49r_o$. The ratio of these two distances is about 3. A factor of 3 means about 10 dB/St difference according to the r^{-1} decay assumption of acoustic waves. Similarly, the difference between our near and far field spectra in figure 5.21 is about 12 dB/St. In this case, the ratio of the far field observation point distance to the near field observation point distance is about 4 which also translates into 12 dB/St difference according to the r^{-1} decay assumption.

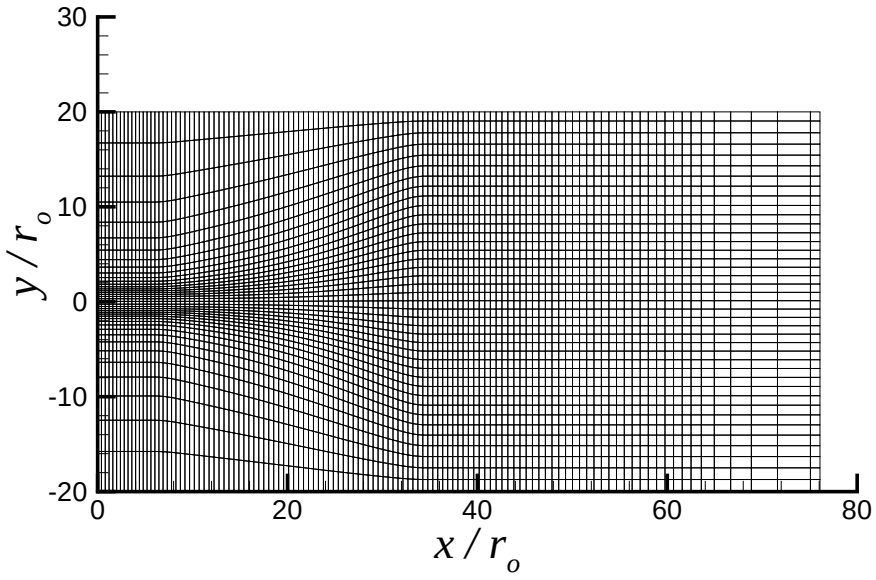

Figure 5.1. The $x - y$ cross-section of the grid on the $z = 0$ plane. (Every 4^{th} grid node is shown.)

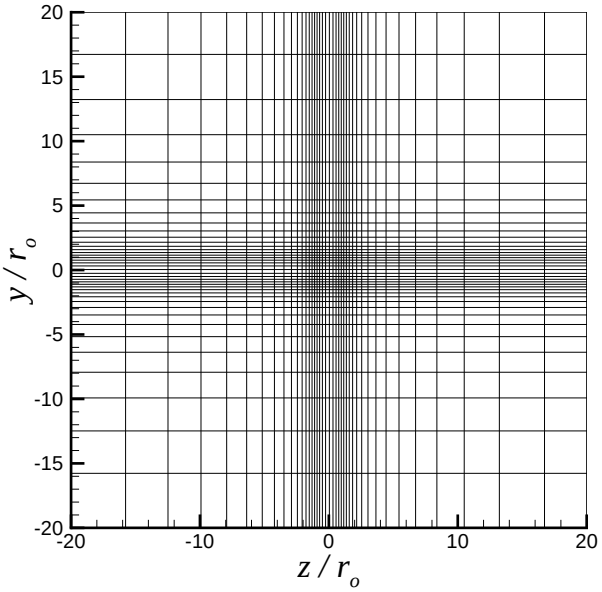

Figure 5.2. The $y - z$ cross-section of the grid on the $x = 5r_o$ plane. (Every 4^{th} grid node is shown.)

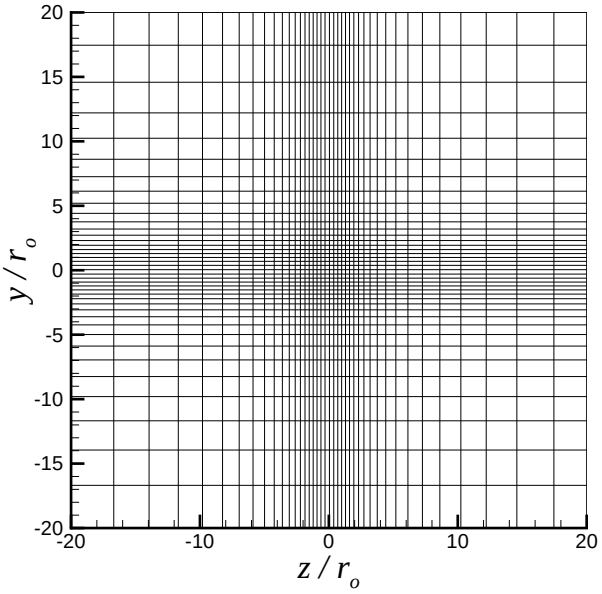

Figure 5.3. The $y-z$ cross-section of the grid on the $x = 15r_o$ plane. (Every 4^{th} grid node is shown.)

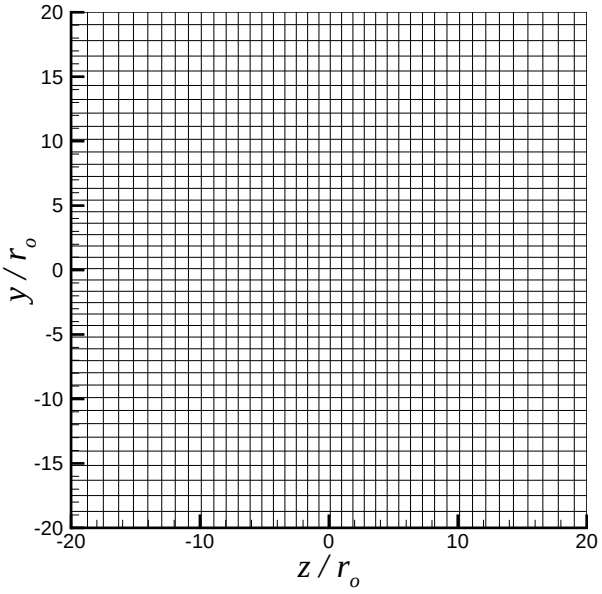

Figure 5.4. The $y-z$ cross-section of the grid on the $x = 35r_o$ plane. (Every 4^{th} grid node is shown.)

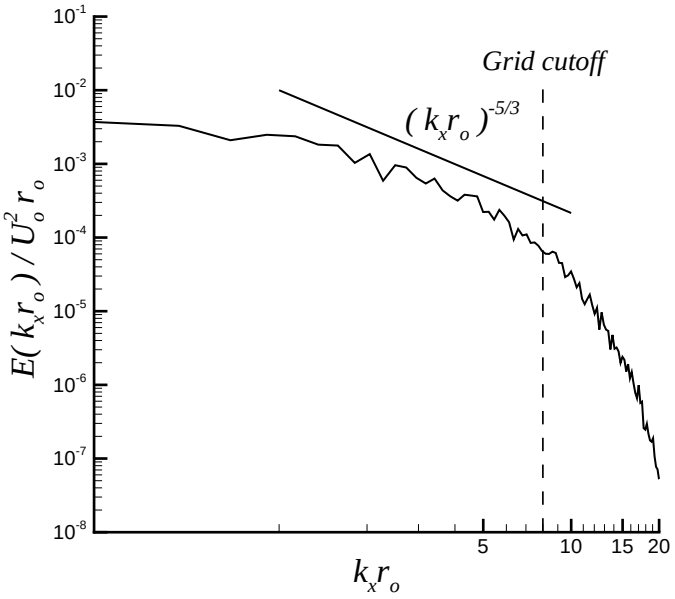

Figure 5.5. One-dimensional spectrum of the streamwise velocity fluctuations at the $x = 20r_o$ location on the jet centerline.

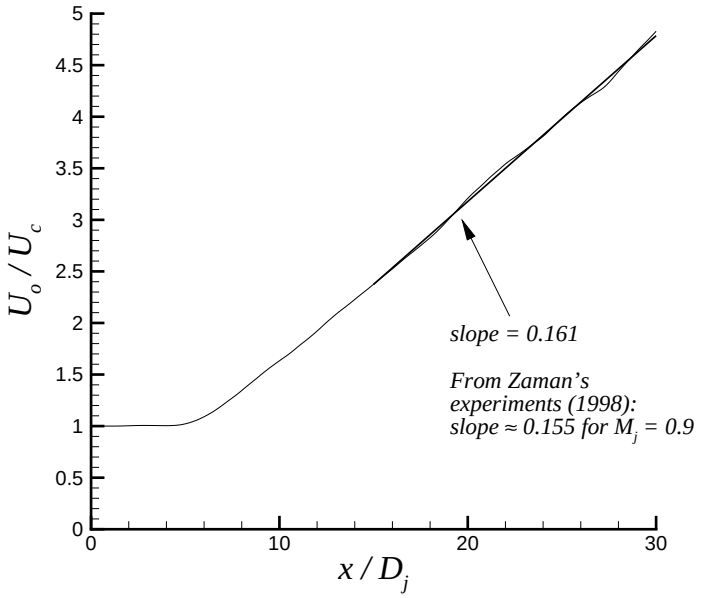

Figure 5.6. Streamwise variation of U_o/U_c.

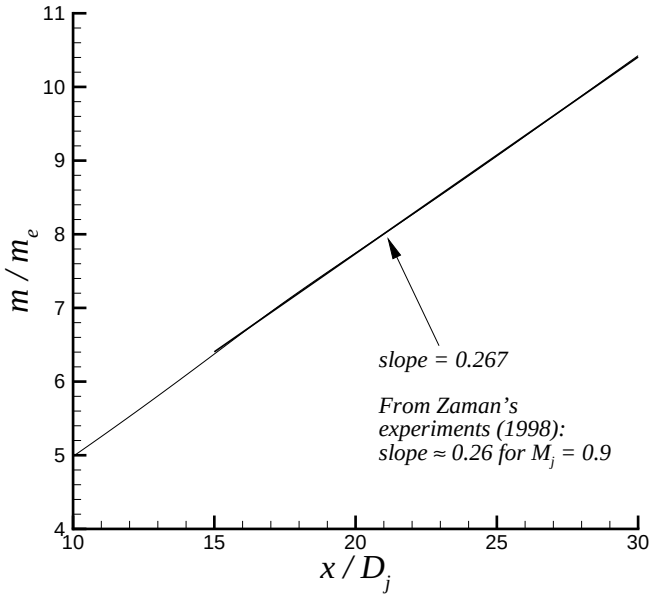

Figure 5.7. Streamwise variation of the mass flux normalized by the mass flux at the nozzle.

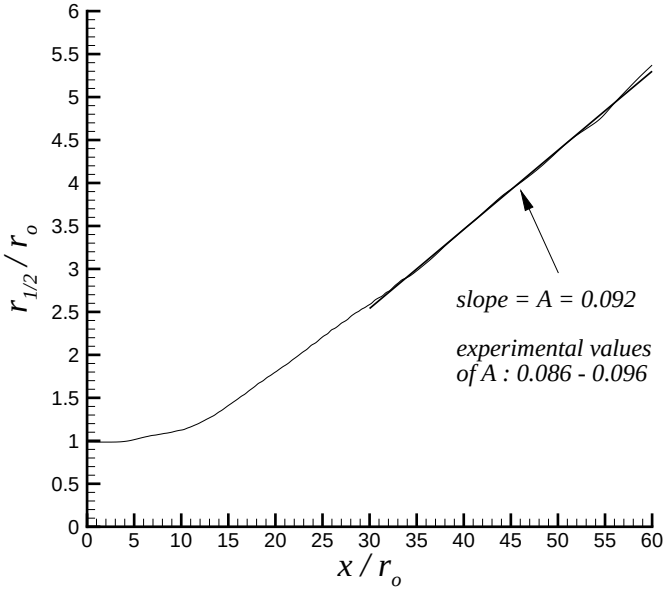

Figure 5.8. Streamwise variation of the half-velocity radius normalized by the jet radius.

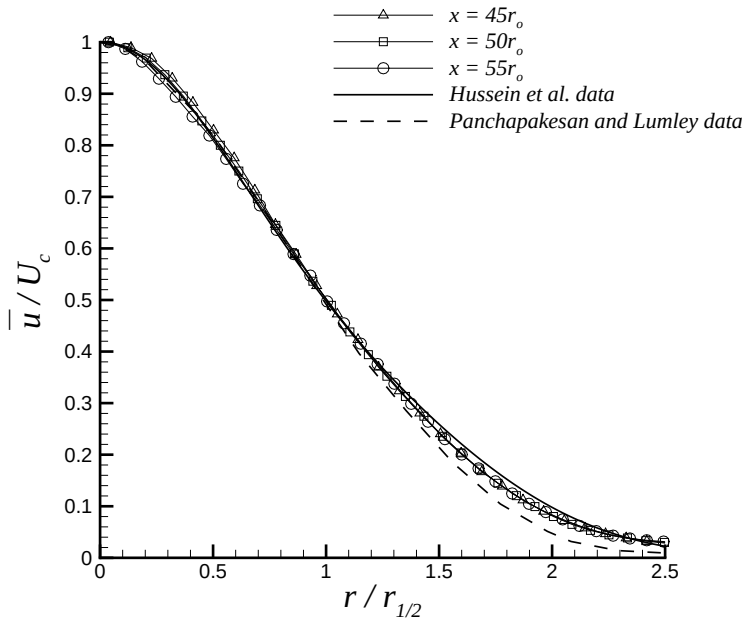

Figure 5.9. Normalized mean streamwise velocity profiles and comparison with experimental data.

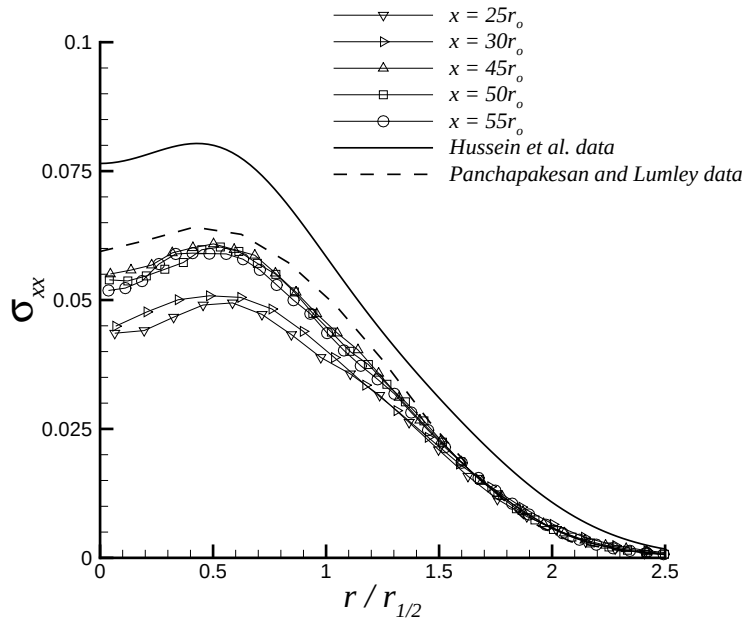

Figure 5.10. Normalized Reynolds normal stress σ_{xx} profiles and comparison with experimental data.

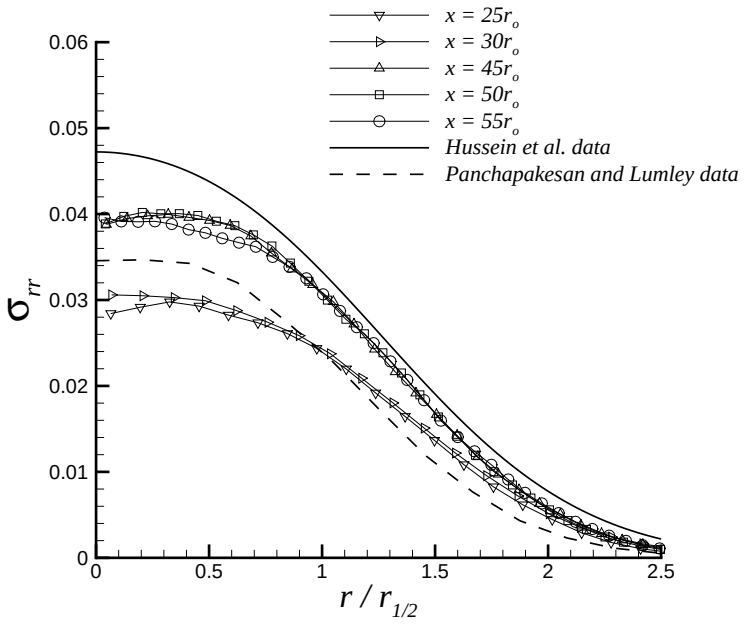

Figure 5.11. Normalized Reynolds normal stress σ_{rr} profiles and comparison with experimental data.

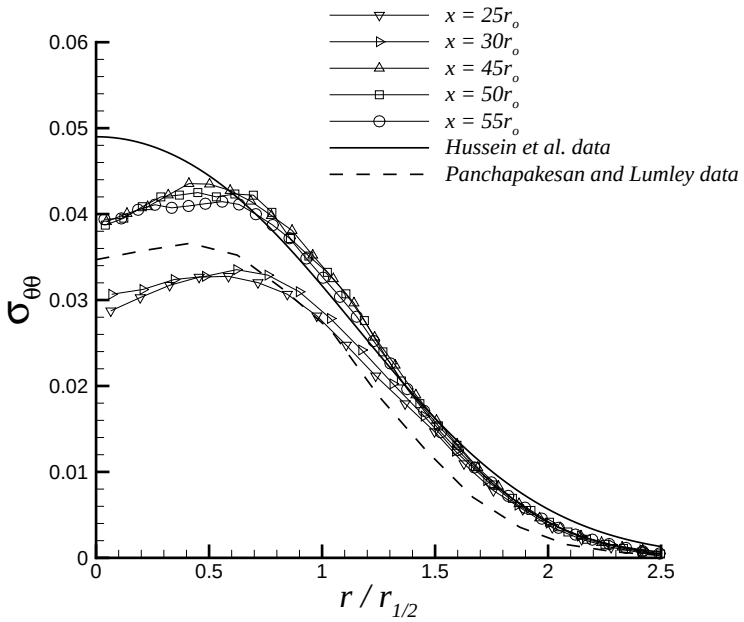

Figure 5.12. Normalized Reynolds normal stress $\sigma_{\theta\theta}$ profiles and comparison with experimental data.

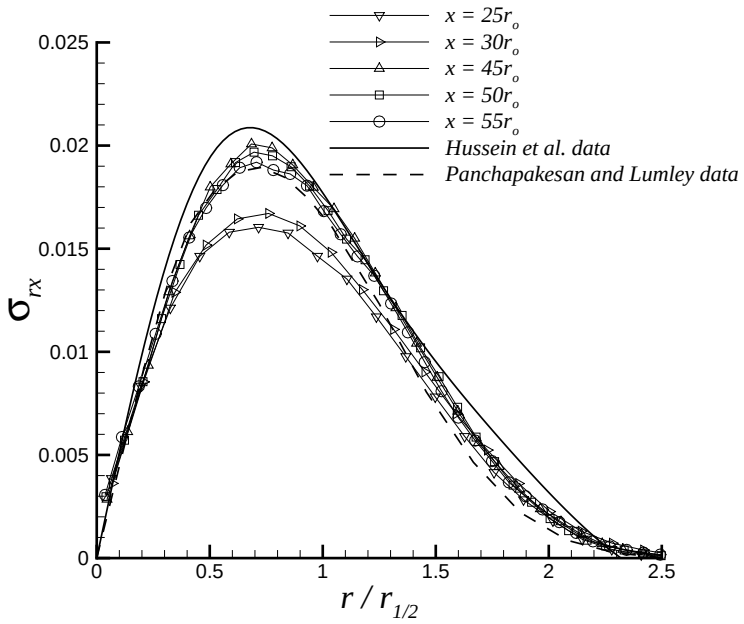

Figure 5.13. Normalized Reynolds shear stress σ_{rx} profiles and comparison with experimental data.

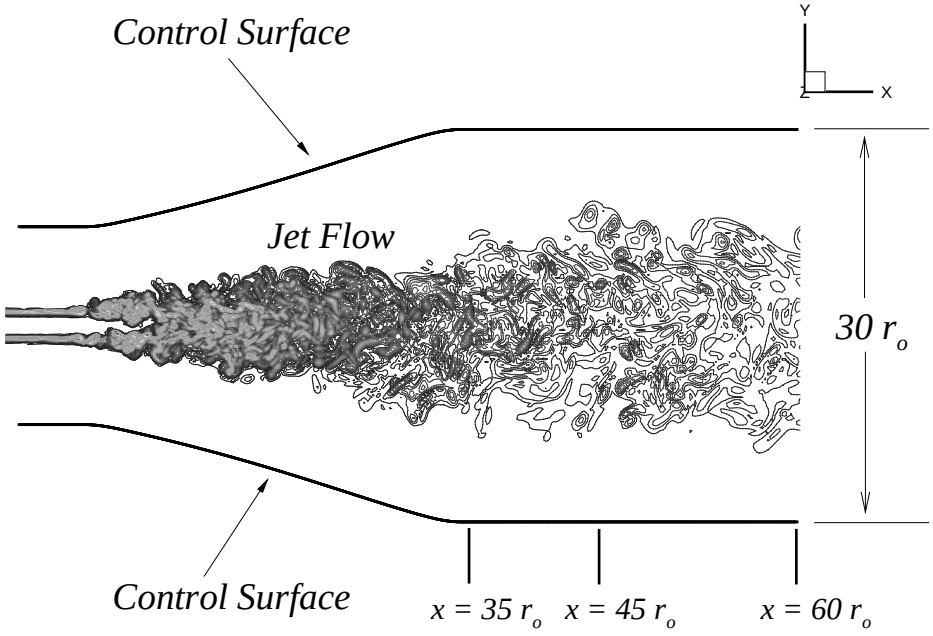

Figure 5.14. Schematic of the control surface surrounding the jet flow.

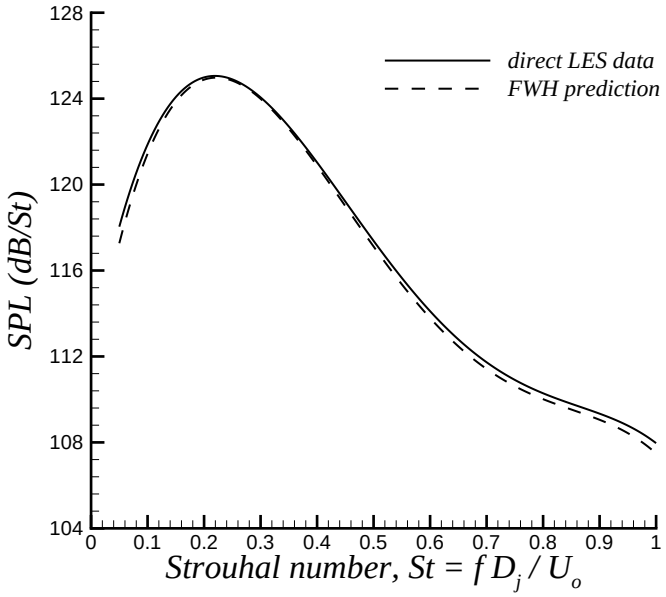

Figure 5.15. Acoustic pressure spectra at $x = 44.97r_o$, $y = 16.02r_o$, $z = 0.11r_o$.

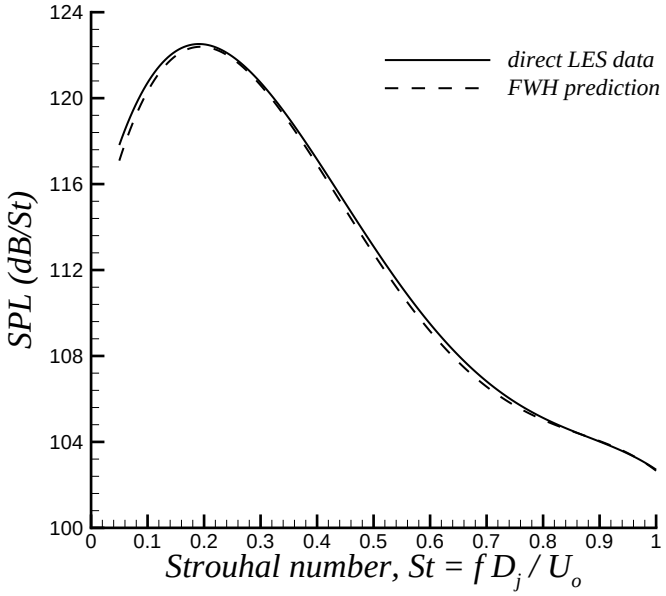

Figure 5.16. Acoustic pressure spectra at $x = 55.06r_o$, $y = 16.02r_o$, $z = 0.11r_o$.

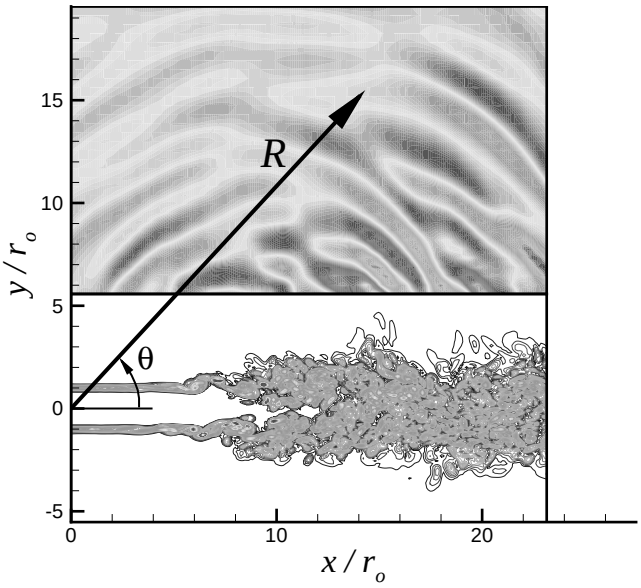

Figure 5.17. Schematic showing the center of the arc and how the angle θ is measured from the jet axis.

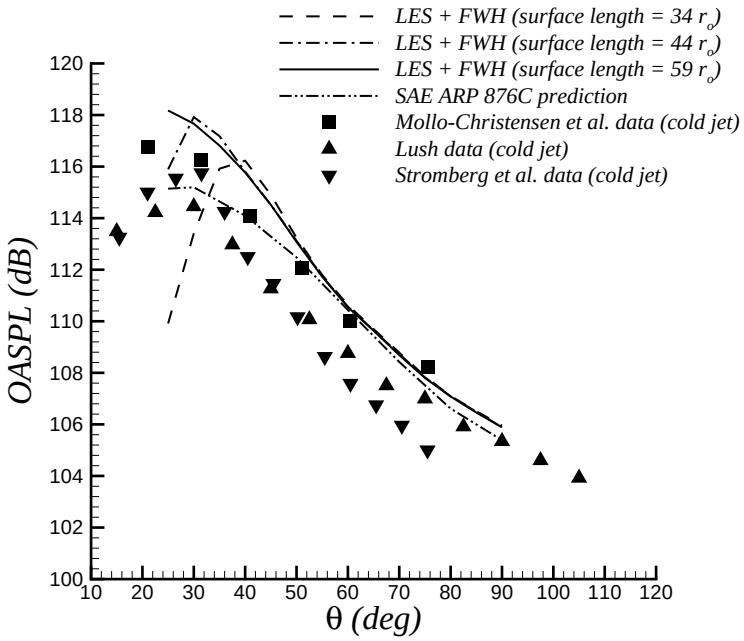

Figure 5.18. Overall sound pressure levels at $60r_o$ from the nozzle exit.

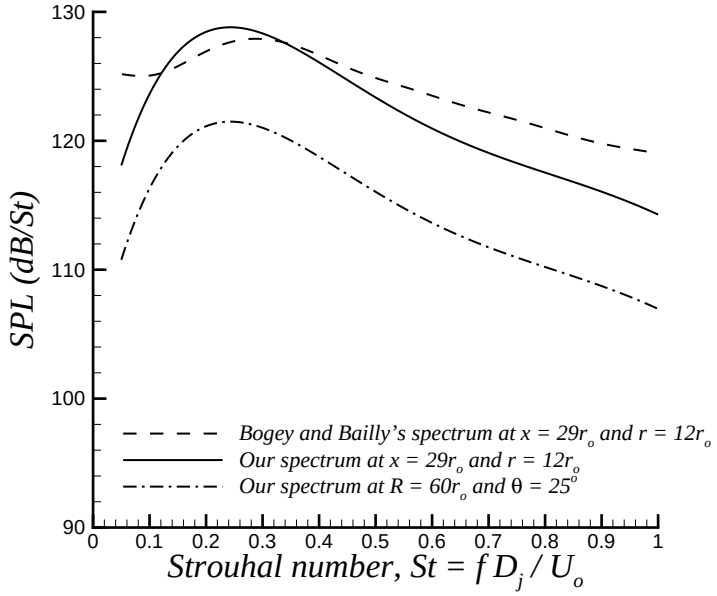

Figure 5.19. Acoustic pressure spectrum at $R = 60r_o$, $\theta = 25°$ in the far field and acoustic pressure spectra at $x = 29r_o$, $r = 12r_o$ in the near field.

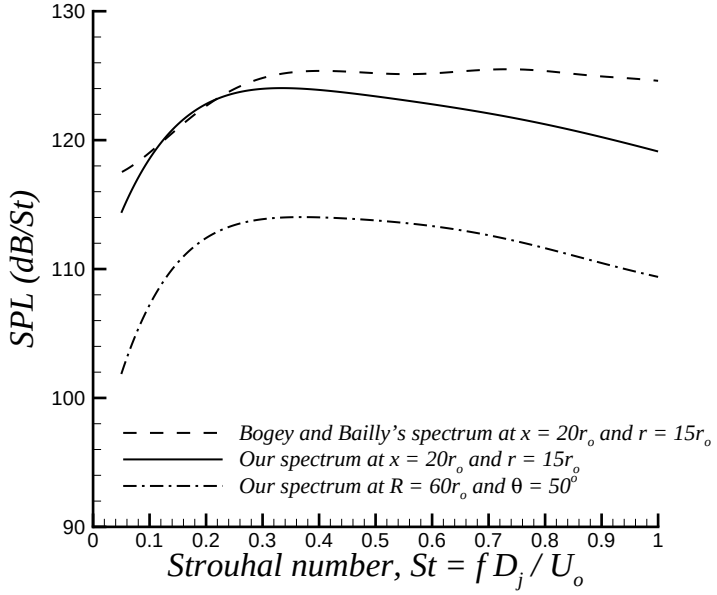

Figure 5.20. Acoustic pressure spectrum at $R = 60r_o$, $\theta = 50°$ in the far field and acoustic pressure spectra at $x = 20r_o$, $r = 15r_o$ in the near field.

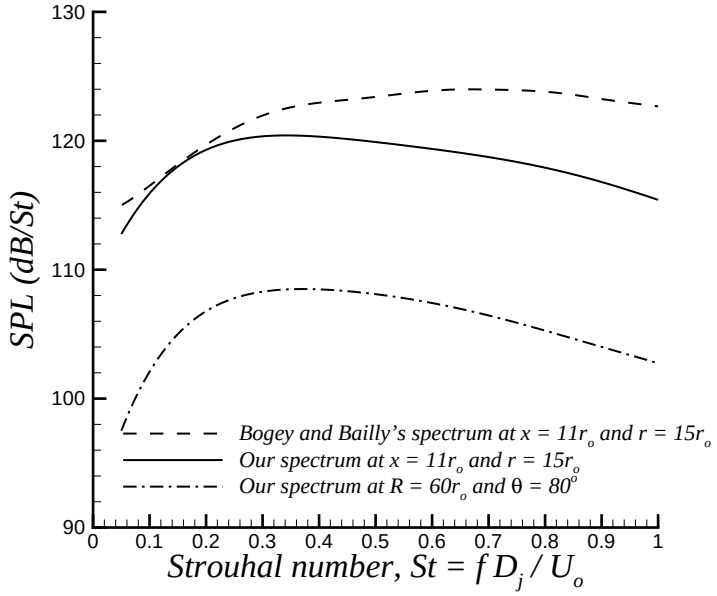

Figure 5.21. Acoustic pressure spectrum at $R = 60r_o$, $\theta = 80°$ in the far field and acoustic pressure spectra at $x = 11r_o$, $r = 15r_o$ in the near field.

6. LES AND AEROACOUSTICS OF HIGH REYNOLDS NUMBER JETS

Visbal and Rizzetta [87] and Visbal *et al.* [88] have recently performed some LES calculations of various turbulent flows without using any explicit SGS model. In those simulations, spatial filtering was treated as an implicit SGS model. They also showed that use of an SGS model in those simulations did not produce any results superior to those obtained without employing an SGS model. Bogey and Bailly [33], [34] also did some LES calculations for jet flows by using spatial filtering only. It is well understood in turbulent flows that the energy cascade is associated with a mean flux of energy that is directed from large scales towards small scales. The large scales contain the major part of the turbulent kinetic energy and they continuously feed the turbulent kinetic energy via the cascade to the smallest eddies where it is dissipated. Since the grid resolution is too coarse to resolve all the relevant length scales in an LES, the pile-up of energy at the high wavenumbers can be eliminated through the use of a spatial filter. Hence, the spatial filter can be thought of as an effective SGS model in an LES. In this chapter, we will perform some jet simulations with and without an SGS model and look at the quantitative differences between such simulations. In the first section, two simulations which were performed without an explicit SGS model will be presented. The first simulation in the first section exactly matches a previous test case studied by Bogey and Bailly [34]. Results of this simulation will compared with those of Bogey and Bailly [34]. The second simulation employs a slightly different inflow forcing than the one used in the first one, and all other parameters are kept the same as the ones used in the first simulation. Both the mean flow and the jet acoustic field obtained in the second simulation will be compared to those of the first simulation. Finally, the second

section in this chapter will present the results of a test case performed with the dynamic Smagorinsky SGS model and compare the results with those corresponding to the simulation done without an SGS model.

6.1 Simulations Performed without an Explicit SGS Model

6.1.1 Reynolds Number 400,000 Isothermal Round Jet Simulation

An LES was performed without any explicit SGS model for a turbulent isothermal round jet at a Mach number of 0.9 and Reynolds number of $400,000$. The tri-diagonal spatial filter was treated as an implicit SGS model. The filtering parameter was set to $\alpha_f = 0.47$. The jet centerline temperature was chosen the same as the ambient temperature and set to $286K$. A fully curvilinear grid consisting of approximately 16 million grid points was used in the simulation. The grid had 390 points along the streamwise x direction and 200 points along both y and z directions. The grid structure was very similar to the one used in the previous chapter. This test case corresponds to one of the test cases studied by Bogey and Bailly [34]. The physical portion of the domain in this simulation extended to 35 jet radii in the streamwise direction and 30 jet radii in the transverse directions. The following mean streamwise velocity profile was imposed on the inflow boundary

$$\bar{u}(r) = \frac{U_o}{2}\left[1 + \tanh\left[10\left(1 - \frac{r}{r_o}\right)\right]\right]. \tag{6.1}$$

This profile has a thinner jet shear layer than the one used in the previous Reynolds number 100,000 simulation. There are about 14 grid points in the initial jet shear layer. The following Crocco-Buseman relation for an isothermal jet is again specified for the density profile on the inflow boundary [33]

$$\bar{\rho}(r) = \rho_o\left(1 + \frac{\gamma - 1}{2}M_r^2\frac{\bar{u}(r)}{U_o}\left(1 - \frac{\bar{u}(r)}{U_o}\right)\right)^{-1}, \tag{6.2}$$

where $M_r = 0.9$.

In a recent study, Bogey and Bailly [34] took a close look at the effects of the inflow conditions on the jet flow and noise. They found out that reducing the amplitude

of the initial disturbances results in an increase in radiated noise. On the other hand, a thinner initial jet shear layer thickness was observed to cause increased noise levels in the sideline direction and reduced noise levels in the downstream direction. The most important changes were obtained when the first 4 azimuthal modes of forcing were removed. In this case, the noise levels were noticeably reduced. They concluded that further improvements are still needed to reduce the sideline noise levels which are overestimated with respect to experimental data. The reader is referred to Reference [34] for more detailed information. Based on their findings, we decided to use the inflow forcing which was found by Bogey and Bailly [34] to match the available experimental data best. There are 16 azimuthal modes total and the first 4 modes are not included in the forcing. The forcing parameter α is set to 0.007.

Computations were done on an IBM-SP3 machine using 200 processors in parallel. A total of about 5.5 days (132 hours) of computing time was needed. The initial transients exited the domain over the first 10,000 time steps. Time history of the unsteady flow data inside the jet was saved at every 10 time steps over period of 40,000 time steps. These data are used in the volume integrals in the next chapter where the far field noise of jet is computed using Lighthill's acoustic analogy. The sampling period corresponds to a time scale in which an ambient sound wave travels about 23 times the domain length in the streamwise direction.

Figures 6.1 through 6.6 show the one-dimensional spectra of the streamwise velocity fluctuations at various locations in the flowfield. Taylor's hypothesis of frozen turbulence was used together with the temporal spectra of the streamwise velocity fluctuations at the given locations to compute the one-dimensional spectra of the streamwise velocity fluctuations. As can be seen from the spectra, the one-dimensional spectra become almost flat as the axial wavenumber approaches zero. We also show the grid cutoff wavenumber corresponding to our grid resolution at the given locations. Before the grid cutoff wavenumber, all spectra exhibit a decay which is quite similar to Kolmogorov's $-5/3$ decay rate prediction in the inertial range of turbulence. Hence, a portion of the inertial range of turbulence is resolved at the

given locations. Mean flow and turbulence statistics results from this simulation will be shown later in this section when we compare our results with those of Bogey and Bailly [34].

Another task performed in this test case was to investigate the sensitivity of far field noise predictions to the position of the control surface on which aeroacoustic data are collected. For this purpose, we put 3 control surfaces around our jet as illustrated in figure 6.7. This figure plots the divergence of velocity contours on a plane that cuts the jet in half. By analyzing these contours, one can clearly identify the non-linear sound generation region inside the jet flow as well as the linear acoustic wave propagation outside the jet. The control surfaces start 1 jet radius downstream of the inflow boundary and extend to 35 jet radii along the streamwise direction. Hence the total streamwise length of the control surfaces is $34r_o$. Control surface 1, 2 and 3 are initially at a distance of 3.9, 5.9 and 8.1 jet radii from the jet centerline, respectively. They open up to a distance of 9.1, 10.8 and 12.2 jet radii from the jet centerline, respectively, at the far downstream location of $35r_o$. We gathered flow field data on the control surfaces at every 5 time steps over a period of $25,000$ time steps during our LES run. The total acoustic sampling period corresponds to a time scale in which an ambient sound wave travels about 14 times the domain length in the streamwise direction. Both the Ffowcs Williams - Hawkings and Kirchhoff's methods were employed in the far field noise predictions. It should be noted that the control surfaces employed here are open surfaces. The main assumption in the surface integral acoustics methods is that the control surface must be placed outside the non-linear flow region. It is known from the study conducted by Brentner and Farassat [65] that Kirchhoff's method will yield inaccurate predictions if one puts a control surface in the non-linear region and does not include any further corrections to account for the non-linearities. On the other hand, the Ffowcs Williams - Hawkings method can produce some reasonable predictions depending on how strong the non-linearities are in the region where the control surface is placed. In fact, one can take the non-linearities into account accurately by including the quadrupole sources

outside the control surface in the original Ffowcs Williams - Hawkings formulation. The disadvantage of including this term is that computationally expensive volume integrals are needed for its computation.

For simplicity, we decided to use open control surfaces in the first part of this study. Flow data needed by Kirchhoff's and the Ffowcs Williams - Hawkings methods were gathered on the lateral surfaces surrounding the jet only. No data were gathered on the inflow and outflow surfaces. Towards the end of this section, we will also show far field noise predictions obtained by including the contribution of the data gathered on an outflow surface. No refraction corrections [64] will be used when the outflow surface is included and only the Ffowcs Williams - Hawkings method will be employed in that case.

The far field acoustic pressure signals were calculated at 36 equally spaced azimuthal points on a full circle at a given θ location on a far field arc. The radius of the arc is equal to 60 jet radii and its center is chosen as the jet nozzle exit. θ values on the arc range from 25° to 90° with an increment of 5°. As explained in section 2.4.3, the run time of the Kirchhoff code is almost the same as that of the Ffowcs Williams - Hawkings code. For control surface 1, the computation of the 4096-point time history of acoustic pressure at a given far field location with both methods took about 6 minutes of computing time using 136 processors in parallel on an IBM-SP3. Hence, for control surface 1, both methods needed a total of 50 hours to compute the acoustic pressure history at a total of 504 far field points. Calculations on control surface 2 and 3 using 136 processors in parallel required 59 and 65 hours total, respectively.

Figures 6.8 through 6.13 plot the acoustic pressure spectra at various points located on the far field arc. The comparisons are done for 3 points on the arc which are located at 45°, 60° and 75°, respectively, from the jet axis. The time signals were broken into 4 1024-point signals which were then used in the Fast Fourier Transforms to get the acoustic pressure spectra. We then averaged the acoustic pressure spectra over the equally spaced 36 azimuthal points to obtain the final

averaged spectrum at the given observer location. It should be mentioned here that since the computed spectra are noisy, the spectra that are shown are polynomial fits to the actual computed spectra. As can be seen from the figures 6.8 through 6.13, for a given control surface, the Ffowcs Williams - Hawkings and Kirchhoff's methods give almost identical results. Although not shown here, comparisons at other locations along the arc yielded the same observations. This means that all of the control surfaces chosen in this study were indeed sufficiently far away from the jet (i.e., in the linear acoustic field) such that they did not encounter any non-linear sound generation regions. Also, the grid allows wave propagation without diffusion. Hence, the Kirchhoff's method prediction was just as good as the Ffowcs Williams - Hawkings method prediction for all control surfaces. The FWH code developed in this study was already validated in the previous chapter by comparing the near field noise spectra provided by the FWH method against the noise spectra computed using the data directly provided by LES. The conclusion that Kirchhoff and the FWH codes give almost identical predictions as long as the control surface does not encounter any non-linearities automatically provides validation of the Kirchhoff code developed in this study.

Assuming at least 6 points per wavelength are needed to accurately resolve an acoustic wave using compact difference schemes, we see that the maximum frequency resolved with our grid spacing around the control surfaces corresponds to a Strouhal number of approximately 3.0, 2.0 and 1.5 for control surface 1, 2 and 3, respectively. The Nyquist frequency, which is the maximum frequency that can be resolved with the time increment of our data sampling rate, corresponds to a Strouhal number of about 11.11. However, we choose the maximum frequency that is based on spatial resolution as our cutoff frequency. The time increment used in the LES corresponds to a Strouhal number of about 55.56. As will be evident shortly, 6 points per wavelength are indeed to sufficiently resolve an acoustic wave using compact difference schemes. When compared to the spectra predicted by control surface 1, the spectra predicted by control surface 2 will show a drop-off starting at around Strouhal num-

ber 2.0. Similarly, the spectra predicted by control surface 3 will show a drop-off at around Strouhal number 1.5. Based on the data sampling rate, the number of temporal points per period in these highest resolved frequencies are 8, 12, and 16, respectively. Hence, the temporal resolution is adequate. Since grid stretching was employed in the computational grid used in this simulation, the grid spacing gets coarser towards the outer domain boundaries. This means that grid spacing around control surface 1 is finer than that around control surface 2 and similarly the grid spacing around control surface 2 is finer than that around control surface 3. Hence, the maximum frequency that can be captured by a control surface decreases as one puts the control surface further away from the jet. The spectra comparison figures show solid vertical lines corresponding to the cutoff frequency for every control surface. Until Strouhal number 1.5, the spectra predicted by the three control surfaces are seen to be very similar. Then, the spectra predicted by control surface 3 starts to drop sharply due to the fact that the grid spacing around control surface 3 is too coarse to sufficiently resolve higher frequencies. Similarly, the spectra predicted by control surface 2 are very similar to those predicted by control surface 1 until Strouhal number 2.0 and then we observe a sharp drop in the spectra predicted by control surface 2 for the higher frequencies. From the findings in this study, we see that control surface 1 is the optimal surface to choose among the 3 control surfaces. Control surface 1 does not go through any flow non-linearities even though it has been placed quite close to the jet flow and at the same time it has a higher frequency resolution than the other two control surfaces since the grid spacing around it is finer than that around the other two surfaces.

It should be also mentioned at this point that although Bogey and Bailly [33], [34] used a computational grid that is comparable in size to our grid, their cut-off Strouhal number was 2.0 which is lower than our cut-off Strouhal number of 3.0 obtained with control surface 1. In their LES calculations, Bogey and Bailly [33], [34] use direct LES data in the immediate surroundings of the jet to evaluate the near field jet noise only. They do not employ integral acoustics methods to estimate the far field noise.

Since they directly compute the noise in the near field only, their computational grid is more mildly stretched compared to ours. However, since we are employing integral acoustics methods in our methodology to compute the far field noise, we choose to pack most of the grid points inside the jet flow and do rapid grid stretching outside. Then, placing a control surface such as control surface 1 quite close to the jet flow allows us to obtain higher cut-off frequencies in the subsequent noise calculations.

The acoustic pressure spectra predicted by the 3 control surfaces were integrated over their corresponding resolved frequency range to determine the overall sound pressure levels (OASPL). The overall sound pressure level predictions of the Ffowcs Williams - Hawkings and Kirchhoff's methods using the data gathered on the 3 control surfaces are respectively given in figures 6.14 and 6.15. Since control surface 3 has the lowest cutoff frequency, the OASPL values predicted by control surface 3 are slightly lower than those predicted by control surface 2. Similarly, the OASPL values predicted by control surface 2 are lower than those predicted by control surface 1 that has the highest cutoff frequency. It should also be noted here that since a relatively short domain length of $34r_o$ was used in this study, the streamwise length of the control surfaces is not sufficient to capture the acoustic waves travelling at the shallow angles, i.e., $\theta < 40^\circ$. Hence, the predicted OASPL values show a sharp drop-off at the shallow angles. At this point, the reader is reminded of the study done in the previous chapter in which the effect of the control surface streamwise length on the far field noise at shallow angles was shown (see figure 5.18). Figures 6.16 and 6.17 compare the OASPL predictions of the Ffowcs Williams - Hawkings and Kirchhoff's methods with the experimental data as well as with the SAE ARP 876C [84] database prediction and the previous Reynolds number 100,000 jet LES result. Although the numerical predictions are a few dB louder than the experiments, the overall agreement is encouraging. One reason for the overprediction of the numerical results relative to experimental measurements is believed to be the inflow forcing employed in the simulations. To see the impact of the inflow forcing on the noise, we will do a new simulation with a modified inflow forcing in the next section.

Next, we will do comparisons of our acoustic pressure spectra at 2 observation points with those of Bogey and Bailly [34]. Figures 6.18 and 6.19 do the comparisons at the observation points $x = 29r_0$, $r = 12r_o$ and $x = 11r_0$, $r = 15r_o$, respectively. Our spectra at these points were computed by coupling the data on control surface 1 with the Ffowcs Williams - Hawkings method, while those of Bogey and Bailly [34] are based on data directly provided by their LES. As can be seen from figure 6.18, the two spectra are quite similar at the observation point $x = 29r_0$, $r = 12r_o$. At this observation point, the cutoff frequency of Bogey and Bailly [34] corresponds to Strouhal number of 2.0 while our cutoff frequency is at Strouhal number 3.0 since that is the maximum frequency we can accurately resolve using the data gathered on control surface 1. These cutoff frequencies are also shown in the figure. It is seen that the spectrum of Bogey and Bailly is a few dB louder than ours. Figure 6.19 shows the spectra comparison at the observation point at $x = 11r_0$, $r = 15r_o$. This time, Bogey and Bailly's [34] cutoff frequency correspond to Strouhal number of about 1.1 due to their coarsened grid spacing at the given observation point. Our cutoff frequency at this location is still 3.0. The figure shows that Bogey and Bailly's [34] spectrum is similar to ours until Strouhal number 1.1, then their spectrum exhibits a sharp drop-off while ours continues until Strouhal number 3.0. Again, it is observed that their spectrum is a few dB louder than ours. At this stage, one might wonder as to why the far field noise predictions of Bogey and Bailly [34] are not identical to ours since exactly the same inflow forcing was used and all other flow parameters were kept the same in both simulations. The answer is to be found in the different numerical methods used in the two simulations. Bogey and Bailly [34] employed high-order accurate explicit finite differencing and explicit spatial filtering schemes in their calculations, whereas we have used implicit compact differencing and implicit spatial filtering schemes in our simulation. Since different numerical techniques have different characteristics, the differences observed are not surprising.

The differences between the two simulations can be further examined by comparing some mean flow quantities and turbulence statistics. The streamwise variation

of the mean jet centerline velocity profile and the half velocity radius are given in figures 6.20 and 6.21, respectively. Bogey and Bailly [34] have assumed the end of the jet potential core as the streamwise location where the jet mean centerline velocity is 0.95 times the value of the inflow boundary. Following this definition, we see that the potential core of the jet simulated by Bogey and Bailly [34] has a length of $12r_o$, whereas our jet's potential core length is about $13r_o$. Other than this difference, the streamwise variation of the mean jet centerline velocity in the two simulations is qualitatively similar. The half velocity radius variations are also quite similar. The almost linear growth of the half velocity radius starts a short distance downstream of the end of the jet potential core in both simulations. As mentioned in the previous chapter, Raman *et al.* [81] measured a potential core length of about $10r_o$ for jets with initially transient shear layers, while Arakeri *et al.* reported a value of about $14r_o$ for a Mach 0.9, Reynolds number 500,000 jet with initially transient shear layers. Potential core lengths of about $14r_o$ have been measured by Raman *et al.* [81] and Lau *et al.* [83] for high Reynolds number jets with initially turbulent shear layers. The potential core lengths obtained from the computations compare reasonably well with the experimental measurements.

The streamwise profiles of the root mean square of the fluctuating axial and radial velocities along $r = r_o$ are plotted in figures 6.22 and 6.23, respectively and comparisons are done with the corresponding profiles of Bogey and Bailly [34]. Although our profiles and theirs are qualitatively similar, their profiles have higher peak levels than ours. Furthermore, their peaks are located slightly downstream of ours. Bogey and Bailly [34] have observed that the sideline noise levels are directly linked to the radial velocity fluctuations in the shear layer. They showed that the lower the peak of the radial velocity fluctuations in the jet shear layer, the lower the sideline noise levels. This observation and the fact that the peak of our fluctuating radial velocity profile given in figure 6.22 is lower than that of Bogey and Bailly [34] explain why our acoustic pressure spectrum at the $x = 11r_0$, $r = 15r_o$ observation location is lower than theirs over the frequency range $0 < St < 1.1$ in figure 6.19. The reader

is once again reminded of the fact that the Bogey and Bailly's [34] spectrum has a cutoff frequency at $St = 1.1$ at this observation location. Figures 6.24 and 6.25 show the centerline variation of the root mean square of the fluctuating axial and radial velocities and compare them with those of Bogey and Bailly [34]. Our centerline profiles peak at a location downstream of their peaks. Our peaks are also seen to be lower than those of Bogey and Bailly [34]. Our peak values for $(v'_x)_{rms}/U_o$ and $(v'_r)_{rms}/U_o$ on the jet centerline are 0.117 and 0.100, respectively, while those of Bogey and Bailly [34] are 0.120 and 0.106, respectively. Arakeri *et al.* [82] obtained an experimental value of 0.12 for the peak $(v'_x)_{rms}/U_o$ on the centerline of a jet with initially transient shear layers. The experimental jet studied by Arakeri *et al.* [82] was a Mach 0.9 jet with Reynolds number 500,000. Lau *et al.* [83] measured a peak value of 0.14 for $(v'_x)_{rms}/U_o$ on the centerline of a Mach 0.9, Reynolds number 1 million jet with initially turbulent shear layers. Lau *et al.* [83] also reported a value of 0.11 for the peak $(v'_r)_{rms}/U_o$ on the jet centerline from the same experiment. The numerical predictions for the peak $(v'_x)_{rms}/U_o$ and $(v'_r)_{rms}/U_o$ on the jet centerline are seen to be in reasonable agreement with the experimental measurements. In their study, Bogey and Bailly [34] have also noted that the downstream noise levels are related to the centerline turbulence intensities. They showed that the lower the peak of the centerline turbulence intensities, the lower the downstream noise levels. Since our jet's centerline turbulence intensities are lower than those of Bogey and Bailly [34], we can now see why our spectrum at the $x = 29r_0$, $r = 12r_o$ location is lower than theirs.

The aeroacoustics results presented so far were obtained using an open control surface. Due to the relatively short streamwise control surface length, the acoustic pressure signals at observation angles less than 40° on the far field arc were not accurately captured. To see the effects of closing the control surface at the outflow, a new study was conducted. A new control surface that starts one jet radius downstream of the inflow boundary and extends to $31r_o$ in the downstream direction was generated. This control surface is the same as the open control surface 1 used in the

aeroacoustics studies presented earlier in this section. The current control surface is truncated at $x = 31r_o$ whereas the previous open control surface extended up to $x = 35r_o$. The outflow surface of the new control surface was placed at $x = 31r_o$. Since the physical portion of the domain ends at around $x = 35r_o$, placing the outflow surface a few radii away from the end of the physical domain ensures that the flow data gathered on the outflow surface are not affected by the presence of the sponge zone. The data gathered on the new control surface were coupled with the Ffowcs Williams - Hawkings method to compute the far field noise. No refraction corrections were included when the control surface was closed on the outflow surface. The Ffowcs Williams - Hawkings method required about 59 hours of computing time on 136 POWER3 processors of an IBM-SP3 to compute the 4096-point time history at a total of 504 far field points. Figure 6.26 plots the OASPL predictions on the far field arc which were obtained using the data gathered on the closed control surface and makes comparisons with other data. The OASPL values at all observation angles are shifted up by some amount when the control surface is closed at the outflow. The effect of the closed control surface appears to be minimal for the range of observation angles where $50^\circ < \theta < 65^\circ$, though. The increase of the OASPL at the shallow observation angles is expected, however, we clearly see a spurious effect for the range where $\theta > 80^\circ$. The OASPL profile in this range is very slowly decreasing with the observation angle. A similar observation was recently made by Rahier *et al.* [89] who conducted a study of surface integral acoustic methods and looked at the sensitivity of far field noise results to the placement of closed control surfaces in the non-linear flow field. The spurious effect observed here is attributed to the fact that we have placed a control surface inside the non-linear flow region ignoring the noise due to the quadrupole sources outside the control surface. Rahier *et al.* [89] also gave the same reason for the similar spurious effects they have observed. We also believe that an effective line of dipole sources is created as the quadrupoles exit the downstream surface. These dipole sources can also be partially responsible for the spurious effects observed here. It is believed that moving the outflow surface further

downstream will reduce the strength of the line of dipoles appearing on the outflow surface. Finally, we look at the acoustic pressure spectra predictions at the $\theta = 30°$, $\theta = 60°$, and $\theta = 90°$ locations on the far field arc. Figure 6.27 shows the two spectra at the $\theta = 30°$ observation point which were computed using the open and closed control surfaces. It is clear that at the $\theta = 30°$ location, the spectral energy is shifted up at all frequencies when the control surface is closed on the outflow surface. The spectra at $\theta = 60°$ computed using the open and closed control surfaces are shown in figure 6.28. The differences in the two spectra are minor at this observation point, hence the outflow surface does not have much influence on the noise spectrum at the $\theta = 60°$ observation location. The comparison at $\theta = 90°$ depicted in figure 6.29 once again shows that closing the outflow surface increases the spectral energy levels at all frequencies at this observation point.

6.1.2 Reynolds Number 400,000 Isothermal Round Jet Simulation with a Modified Inflow Forcing

To see the influence of the inflow forcing on the jet mean flow field and the far field noise, a new simulation was performed for the Reynolds number 400,000 jet using a modified inflow forcing. There are again 16 azimuthal forcing modes total and this time the first 6 modes are not included in the forcing. The forcing parameter α is set to 0.007, same as before. All other parameters are kept the same as those in the previous simulation in which only the first 4 modes were removed from the forcing.

The streamwise variation of the mean jet centerline velocity profile and the half velocity radius are given in figures 6.30 and 6.31, respectively. Comparisons are done with the previous simulation data as well as with the simulation of Bogey and Bailly [34]. The reader is once again reminded here that the simulation of Bogey and Bailly [34] employed an inflow forcing in which only the first 4 modes of a total of 16 azimuthal modes were removed. It is interesting to see our simulation in which the

first 6 modes modes were removed matches the results of Bogey and Bailly [34] better. Assuming that the end of the jet potential core is the streamwise location where the jet mean centerline velocity is 0.95 times the value of the inflow boundary, we see that our jet's potential core length in the current simulation is about $12.5r_o$, whereas it was $13r_o$ in the previous simulation. The streamwise profiles of the root mean square of the fluctuating axial and radial velocities along $r = r_o$ are plotted in figures 6.32 and 6.33, respectively and comparisons are again done with the previous simulation as well as with the profiles of Bogey and Bailly [34]. The peak of the fluctuating axial velocity profile in the shear layer with the modified inflow forcing is seen to be slightly lower than that in the previous simulation, whereas the peak of the fluctuating radial velocity profile in the present simulation is higher. The larger peak fluctuating radial velocity in the shear layer implies that the sideline noise levels will be higher in the current simulation. Figures 6.34 and 6.35 show the centerline variation of the root mean square of the fluctuating axial and radial velocities and make comparisons with the previous simulation as well with the profiles of Bogey and Bailly [34]. Relative to the original forcing, the modified inflow forcing results in the higher values of the centerline turbulence intensities. The larger peak turbulence intensities along the jet centerline mean that the noise levels in the downstream direction will be higher. Our peak values for $(v_x')_{rms}/U_o$ and $(v_r')_{rms}/U_o$ on the jet centerline are 0.129 and 0.106, respectively. In the previous simulation with the original forcing, they were 0.117 and 0.100, respectively. Once again, the experimental value obtained by Arakeri *et al.* [82] for the peak $(v_x')_{rms}/U_o$ on the centerline was 0.12 for a Mach 0.9, Reynolds number 500,000 jet with initially transient shear layers. The values measured by Lau *et al.* [83] for the peak $(v_x')_{rms}/U_o$ and $(v_r')_{rms}/U_o$ on the centerline of a Mach 0.9, Reynolds number 1 million jet with initially turbulent shear layers were 0.14 and 0.11, respectively.

An open control surface exactly the same as control surface 1 used in the previous section was placed around the jet flow in this test case and flow data were gathered on this surface during the LES run. The streamwise length of the control surface

is $34r_o$. This control surface has a maximum frequency resolution that corresponds to Strouhal number 3.0. The data on the control surface were coupled with the Ffowcs Williams - Hawkings method for the far field noise calculations. The acoustic pressure at $\theta = 45°, 60°, 75°$ locations on the far field arc are plotted in figures 6.36, 6.37 and 6.38, respectively. From these figures, it is clear that the modified inflow forcing modifies the acoustic pressure spectra at all observation points and moreover, causes more energetic far field pressure fluctuations. This is not surprising since the previous analysis of the turbulence intensities along the jet centerline and in the shear layer already implied higher noise levels. Finally, we plot the OASPL levels along the far field arc in figure 6.39 and do comparisons with the previous simulation. The OASPL values increase at all observation points on the on arc. The increase is on the order of 1 dB for large observation angles while it is less than 1 dB for smaller angles.

The findings in this section clearly demonstrate the impact of the inflow forcing on the jet mean flow, turbulence intensities as well as on the jet acoustic field. They also explain the discrepancies between numerical noise predictions and actual experimental measurements. It appears that one needs to match the actual nozzle exit conditions in an experiment as closely as possible in order to be able to get good agreement of the numerical noise predictions with the experimental data. Improved inflow boundary conditions need to be developed for this purpose. Another option could be to include the actual nozzle geometry in the computations so as the get away from the artificial inflow forcing although this seems to be a computationally more challenging task.

6.2 Reynolds Number 400,000 Isothermal Round Jet Simulation with the Dynamic Smagorinsky Model

To see the effects of an explicit SGS model on the flowfield and far field noise, a new simulation was performed by employing the dynamic Smagorinsky model (DSM) in the LES. All parameters in this simulation are kept the same as those used in the previous $Re_D = 400,000$ jet simulation in which the first 4 modes of the forcing were removed. Spatial filtering is also employed in this case so as to remove the very high frequency spurious oscillations not supported by the grid resolution. The tri-diagonal spatial filter with the filtering parameter set to $\alpha_f = 0.47$ is used in the current simulation for that purpose. The turbulent Prandtl number was set to a constant value of 0.7 while the compressibility correction constant in the SGS model was set to 0. With the DSM model turned on, the LES code required about 50% more computing time than the previous LES done with filtering only. Hence, a total of about 200 hours of run time was needed for this simulation using 200 POWER3 processors on an IBM-SP3.

The streamwise variation of the mean jet centerline velocity profile and the half velocity radius are plotted in figures 6.40 and 6.41, respectively and comparisons are done with the previous simulation done without an SGS model. From these figures, it is clear that both the decay of the mean jet centerline velocity and the growth of half velocity radius take place faster when an SGS model is employed. The streamwise profiles of the root mean square of the fluctuating axial and radial velocities along $r = r_o$ are plotted in figures 6.42 and 6.43, respectively and comparisons are again done with the simulation done without an SGS model. The peak intensities of the fluctuating axial and radial velocities in the shear layer of the current simulation are seen to be slightly lower than those in the simulation done without an SGS model. The lower peak fluctuating radial velocity in the shear layer means that the sideline noise levels will be lower in the current simulation. Figures 6.44 and 6.45 show the centerline variation of the root mean square of the fluctuating axial

and radial velocities and make comparisons with the simulation done without an SGS model. The centerline peak turbulence intensities in the current simulation are higher than those in the simulation done without an SGS model. The larger peak turbulence intensities along the centerline imply higher noise levels in the downstream direction. Figures 6.46 and 6.47 compare the temporal spectra of the streamwise velocity fluctuations at the $x = 17.5r_o$ and $x = 25r_o$ locations on the jet centerline, respectively. The $x = 17.5r_o$ location is where the peak of the streamwise velocity fluctuations are reached in both simulations. As can be seen from the spectra comparisons, the low frequencies which correspond to the large scales of turbulent motions are more energetic in the simulation done with the dynamic Smagorinsky model. The higher frequencies which correspond to the finer scales, however, are more energetic in the simulation done without an SGS model. The presence of more energetic finer scales in the simulation done without an SGS model will be more evident when the far field noise spectra are presented later in this section. The eddy viscosity of the DSM clearly causes a reduction of the turbulent kinetic energy in the finer scales. Because of this, the finer scales that the larger scales in the simulation done with the DSM have to feed are less "hungry" compared to the finer scales in the simulation done without an SGS model. Hence, the portion of the turbulent kinetic energy drained from the large scales towards the finer scales in the simulation done with the DSM must be smaller than that in the simulation done without an SGS model. Consequently, there is more turbulent kinetic energy residing in the large scales when the eddy viscosity based SGS model is employed in the LES. Comparison of some of the Reynolds stress profiles at two downstream locations are shown in figures 6.48 through 6.51. The Reynolds stress profiles from the previous Reynolds number 100,000 jet simulation are also included in the comparisons. From the comparison with experimental profiles, it is clear the self-similarity region is not reached at around $x = 30r_o$ in any of the simulations. To re-iterate, our analysis of the Reynolds number 100,000 jet in the previous chapter showed that a streamwise domain length of at least 60 jet radii is needed in order for the Reynolds stresses

to become truly self-similar in the Reynolds number 100,000 jet. As mentioned in the previous chapter, the Reynolds number of the jet is also believed to have an influence on how quickly the self-similarity region is reached. The experiments of Wygnanski and Fiedler [66] give a distance of about 100 jet radii downstream of the jet nozzle for the start of the self-similarity region in high Reynolds number jets, whereas Freund's DNS for a Reynolds number 3,600 jet [2] shows the start of the self-similarity region at around $x = 25r_o$ in a low Reynolds number jet. Going back to the Reynolds stress comparisons, we see that the profiles at $x = 25r_o$ and $x = 30r_o$ in the Reynolds number 400,000 simulations are lower than those in the Reynolds number 100,000 jet simulation. For the Reynolds number 400,000 jet, the Reynolds stress comparisons show that the Reynolds stress levels in the simulation done with the DSM are higher relative to those in the simulation without an SGS model. This observation can again be explained by using the above discussion of the distribution of the turbulent kinetic energy among the different length scales of motion in the two simulations. Due to the way the turbulent kinetic energy is distributed among the different length scales, integration of the spectra gives rise to higher levels of velocity fluctuations in the simulation done with the DSM and consequently higher Reynolds stresses. So it seems the more energetic finer scales in the simulation done without an SGS model drain more energy from the large scales. This observation can also be used to explain why the jet half velocity radius and the decay of the mean jet centerline velocity are slower in the simulation without an SGS model. It is believed that the large scale structures of the jet in that simulation lose more energy to finer scales via the energy cascade and hence the jet does not have as much energy left to spread out.

During this simulation, aeroacoustic data were gathered on a closed control surface that starts one jet radius downstream of the inflow boundary and extends to $31r_o$ in the downstream direction. This control surface is the same as the closed control surface used in the first section of this chapter. Far field noise computations were done by excluding the outflow surface (open closed surface) and also by

including the outflow surface (closed control surface). Comparison of the acoustic pressure spectra with the results from the simulation done without an SGS model at the observation angles of $\theta = 45°, 60°, 75°$ on the far field arc are presented in figures 6.52 through 6.54, respectively. These predictions were obtained using the open control surface. The spectral energy contained within the low frequencies are seen to be higher in the noise spectra computed from the simulation done with the DSM. This must be due to the presence of more energetic large turbulent scales in the simulation done with the DSM since it is the large scales that are responsible for low frequency noise generation. On the other hand, the spectra computed from the simulation with the DSM have significantly lower spectral energy at the higher frequencies. This is because the finer scales in the simulation done with the DSM have lower turbulent kinetic energy due to the well-known dissipative effect of eddy viscosity that acts on a wide range of well-resolved wavenumbers. Hence such scales in the simulation done with the DSM are far less effective in creating high frequency noise. Figure 6.55 plots the OASPL values along the far field arc obtained by using the data gathered on the open control surface. The figure shows that the OASPL values at the shallow angles are higher in the simulation done with the DSM. This is due to the fact that the lower frequencies are more dominant at the shallow observation angles and moreover, there is more spectral energy contained in the low frequencies at the shallow observation angles when the DSM is employed. Once again, the higher spectral energy in the lower frequencies is related to the more energetic large scales of motion when the DSM is employed. Consequently, the spectra obtained from the simulation with the DSM give higher OASPL values at the shallow observation angles. On the other hand, the OASPL values at the higher observation angles are lower in the simulation done with the DSM. This is obviously due to the fact that higher frequencies are more dominant at the larger observation angles and there is much less energy contained in the high frequencies of the spectra obtained from the simulation with the DSM. Figure 6.56 shows the OASPL values along the far field arc computed by using the data gathered on the closed control

surface. As it has been observed earlier, the use of a closed control surface tends to shift the OASPL values by some amount at all observation angles. The figure also shows higher OASPL values at the shallow angles and lower OASPL values at the larger observation angles when the DSM is employed. The discrepancy previously observed for $\theta > 80^\circ$ (see section 6.1.1) is also observed here and the reason for this discrepancy was explained earlier. Finally, the comparison of the acoustic pressure spectra at the $\theta = 30^\circ$ location is shown in figure 6.57. These spectra were computed using the data gathered on the closed control surface. Both spectra have their peak at the same frequency at this observation location. Once again, the spectral energy contained within the lowest frequencies is higher while the spectral energy within the higher frequencies is lower for the noise spectrum computed from the simulation done with the DSM.

The effects of the SGS model on noise predictions have been shown. The main conclusion from this study is that the jet noise is sensitive to the SGS model. When the dynamic Smagorinsky model is employed in an LES, the spectral energy in the high-frequency part of the noise spectra is significantly reduced due to the eddy viscosity. LES with filtering only, on the other hand, predicts increased spectral energy levels at the higher frequencies. At this point, it is not possible to reach a definitive conclusion about which LES approach is the best. From a computational standpoint, an LES done using the dynamic Smagorinsky model is 50% more time consuming than an LES done with filtering only.

It is also of interest to look at the effects of the jet Reynolds number on the noise. For this purpose, we will compare the present LES done with the dynamic Smagorinsky model for the Reynolds number 400,000 jet with the previous LES done with the dynamic Smagorinsky model for the Reynolds number 100,000 jet. The spectra comparisons at the observation angles of $\theta = 45^\circ, 60^\circ, 75^\circ$ on the far field arc are presented in figures 6.58 through 6.60, respectively. Since the cut-off Strouhal number in the Reynolds number 100,000 jet LES was 1.0, the spectra of the two jets are plotted until Strouhal number 1.0. The spectra comparisons show that

the low frequency part of the noise spectra is more energetic for the lower Reynolds number jet. We should also note that the larger domain size used in the Reynolds number 100,000 jet LES might result in a better resolution of the low frequencies. The peaks of the lower Reynolds number jet noise spectra are slightly lower than those of the higher Reynolds number jet noise spectra. On the other hand, the spectrum decay after the peak happens faster for the lower Reynolds number jet. It is well known that the range of turbulent length scales gets wider with increasing Reynolds number. Because of the wider range of turbulent eddies in the higher Reynolds number jet, the drain of the turbulent kinetic energy from the very large scales towards the finer scales is greater in a higher Reynolds number jet than in a lower Reynolds number jet. Hence, the lower Reynolds number jet apparently creates more energetic low frequency noise while the higher Reynolds number jet creates more energetic higher frequency noise. From the comparisons, it is evident that the spectra of the higher Reynolds number jet decay more slowly.

The Reynolds stresses from the present LES done with the dynamic Smagorinsky were previously compared with those from the LES done with the dynamic Smagorinsky model for the Reynolds number 100,000 jet in figures 6.48 through 6.51. These comparisons show that at a given downstream location, the Reynolds stress profiles of the lower Reynolds number jet are higher than those of the Reynolds number 400,000 jet. This suggests that the lower Reynolds number jet will reach the self-similarity region quicker than the higher Reynolds number jet. Hence, a higher jet Reynolds number delays the start of the self-similarity region. To re-iterate, this observation is supported by the experiments of Wygnanski and Fiedler [66] which give a distance of about 100 jet radii downstream of the jet nozzle for the start of the self-similarity region in high Reynolds number jets, and also by Freund's DNS [2] that shows the start of the self-similarity region at around $x = 25r_o$ in a low Reynolds number jet.

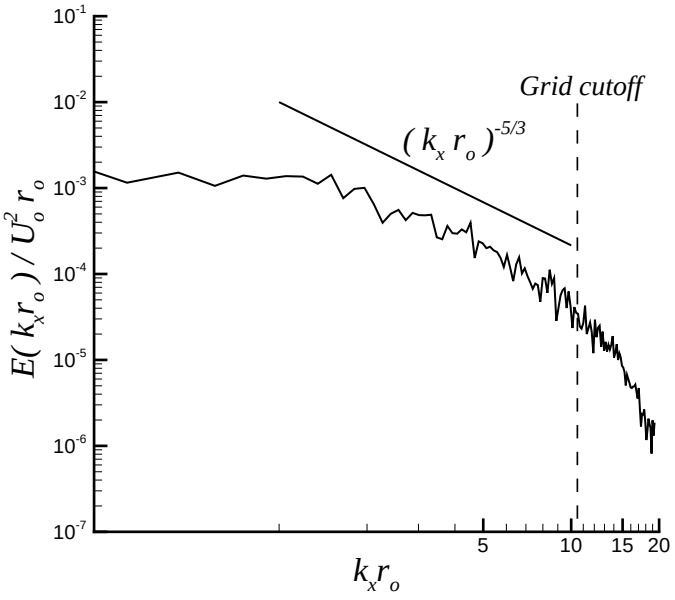

Figure 6.1. One-dimensional spectrum of the streamwise velocity fluctuations at the $x = 15r_o$ location on the jet centerline.

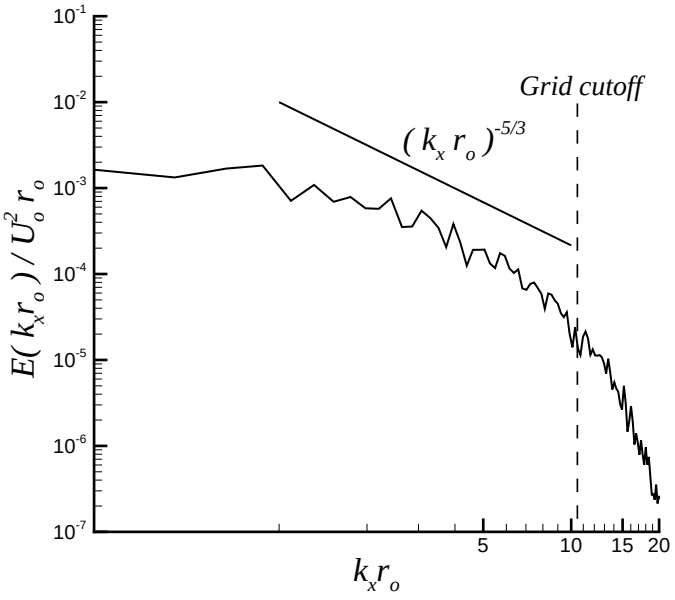

Figure 6.2. One-dimensional spectrum of the streamwise velocity fluctuations at the $x = 25r_o$ location on the jet centerline.

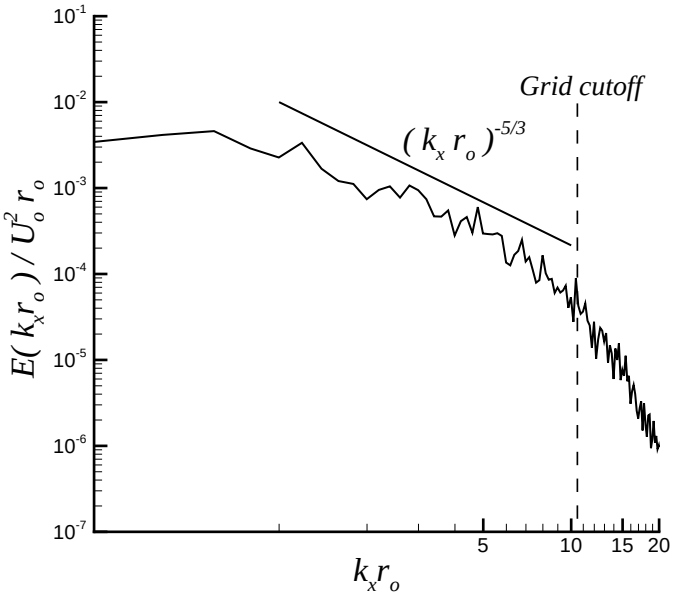

Figure 6.3. One-dimensional spectrum of the streamwise velocity fluctuations at the $x = 15r_o$, $y = r_o$, $z = 0$ location.

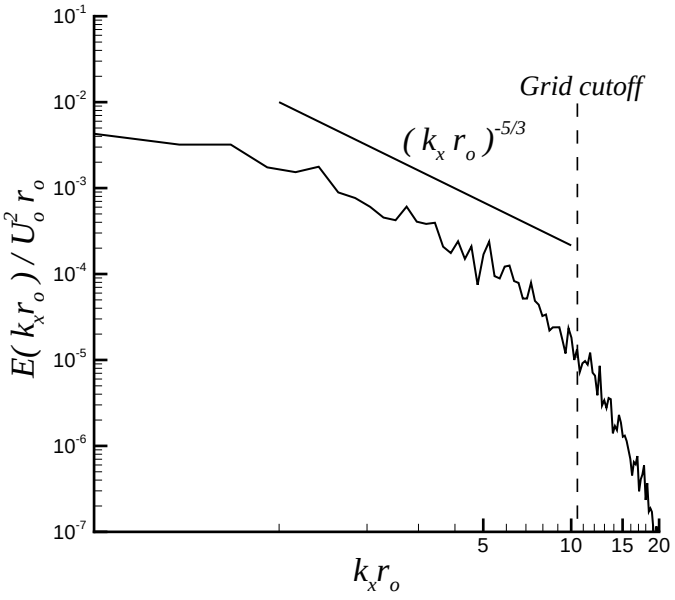

Figure 6.4. One-dimensional spectrum of the streamwise velocity fluctuations at the $x = 25r_o$, $y = r_o$, $z = 0$ location.

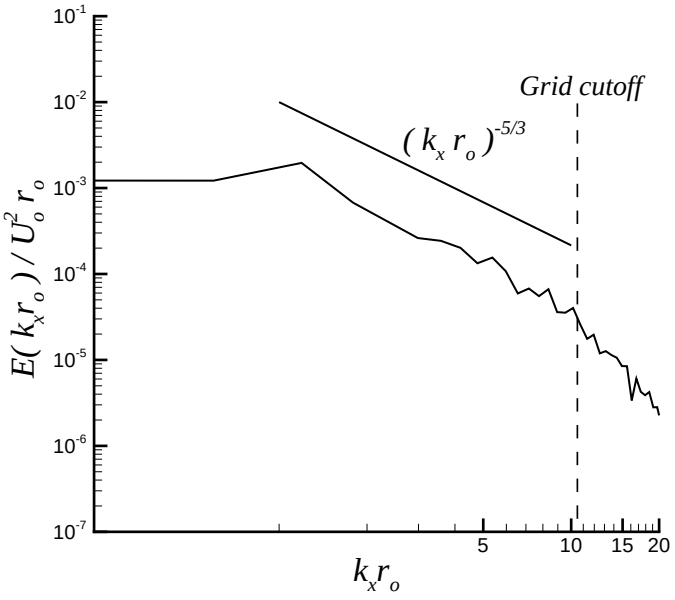

Figure 6.5. One-dimensional spectrum of the streamwise velocity fluctuations at the $x = 15r_o$, $y = 2r_o$, $z = 0$ location.

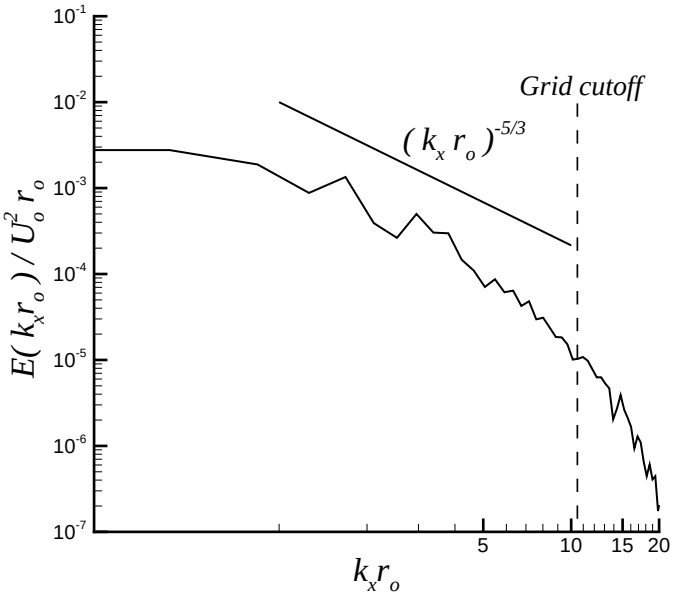

Figure 6.6. One-dimensional spectrum of the streamwise velocity fluctuations at the $x = 25r_o$, $y = 2r_o$, $z = 0$ location.

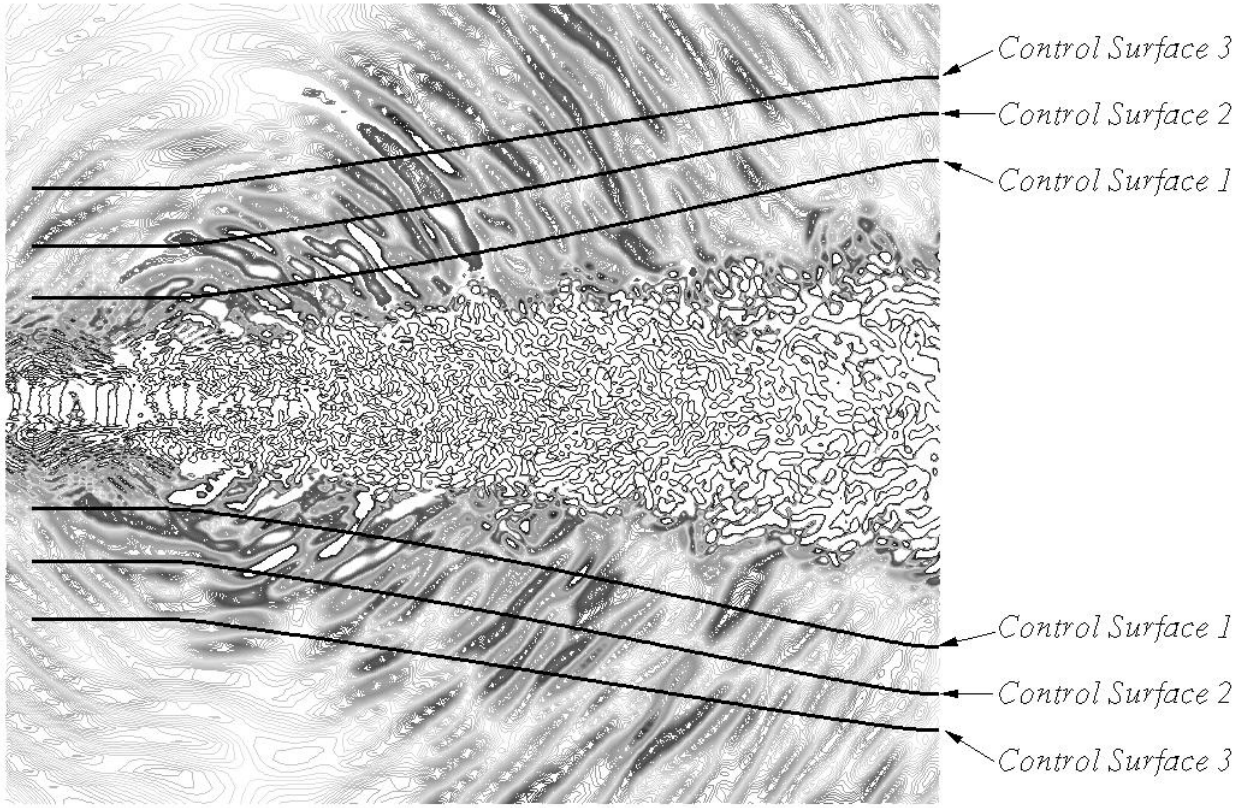

Figure 6.7. Schematic showing the 3 open control surfaces surrounding the jet flow. (Divergence of velocity contours are shown.)

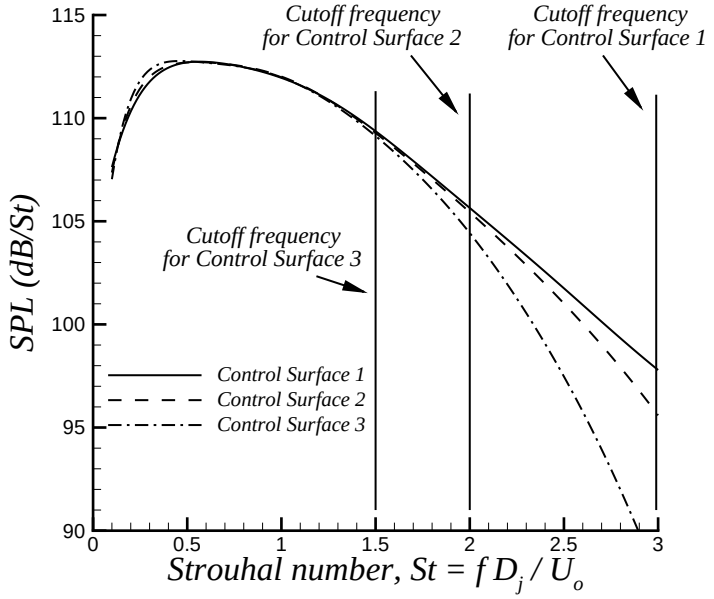

Figure 6.8. The Ffowcs Williams - Hawkings method prediction for the acoustic pressure spectra at $R = 60r_o$, $\theta = 45°$ location on the far field arc.

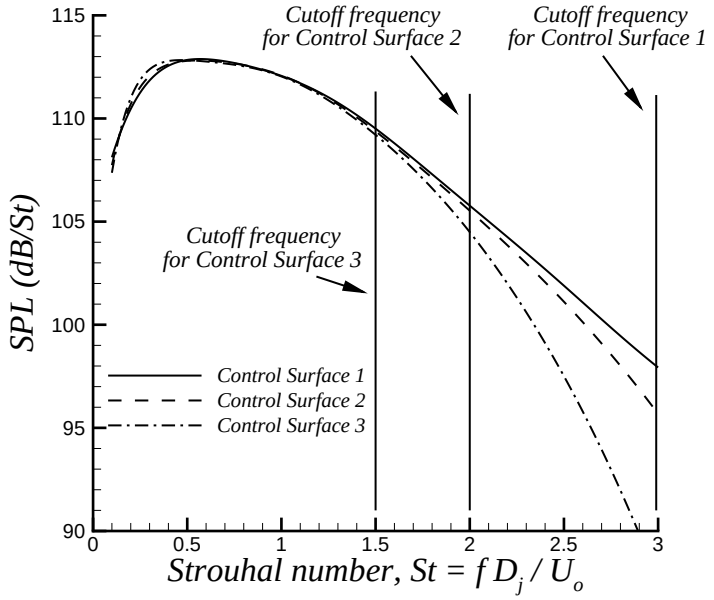

Figure 6.9. Kirchhoff's method prediction for the acoustic pressure spectra at $R = 60r_o$, $\theta = 45°$ location on the far field arc.

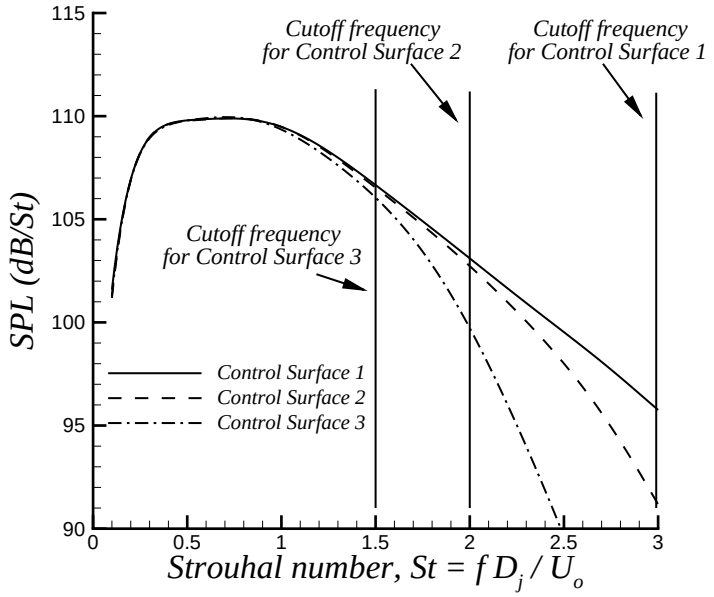

Figure 6.10. The Ffowcs Williams - Hawkings method prediction for the acoustic pressure spectra at $R = 60r_o$, $\theta = 60°$ location on the far field arc.

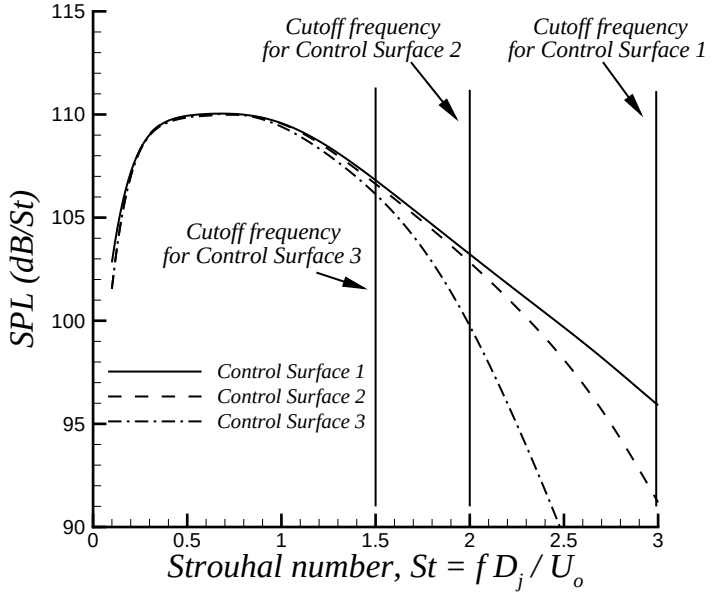

Figure 6.11. Kirchhoff's method prediction for the acoustic pressure spectra at $R = 60r_o$, $\theta = 60°$ location on the far field arc.

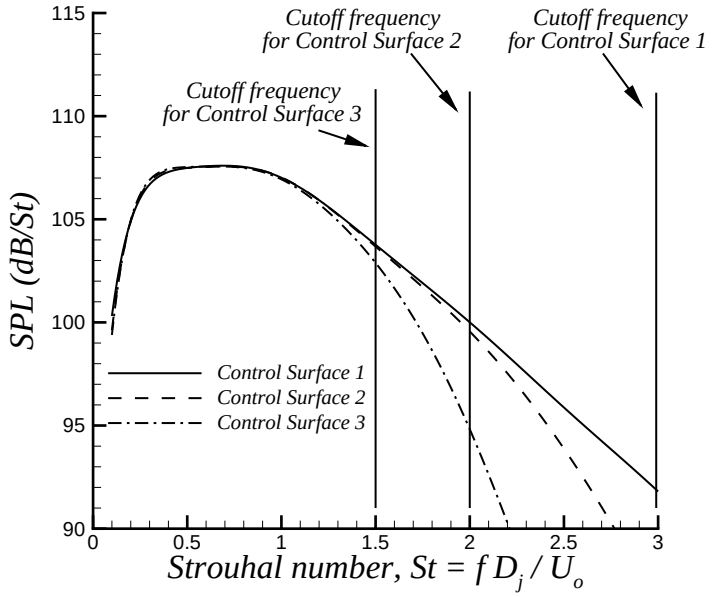

Figure 6.12. The Ffowcs Williams - Hawkings method prediction for the acoustic pressure spectra at $R = 60r_o$, $\theta = 75°$ location on the far field arc.

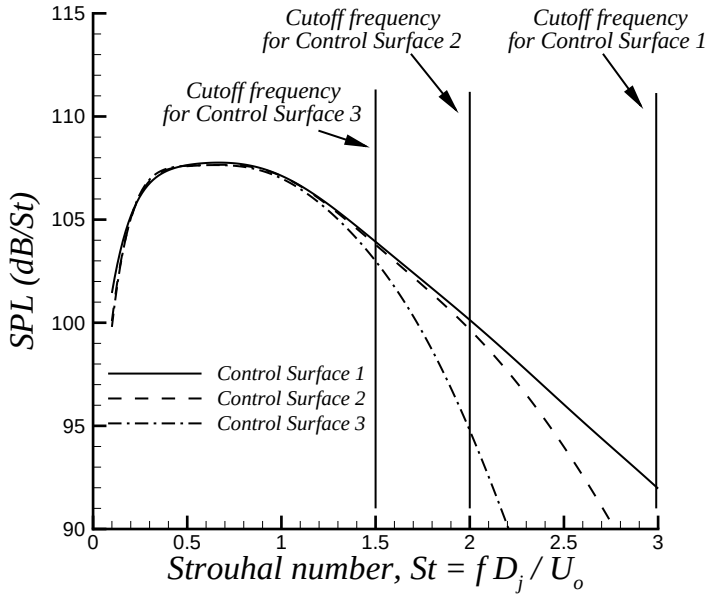

Figure 6.13. Kirchhoff's method prediction for the acoustic pressure spectra at $R = 60r_o$, $\theta = 75°$ location on the far field arc.

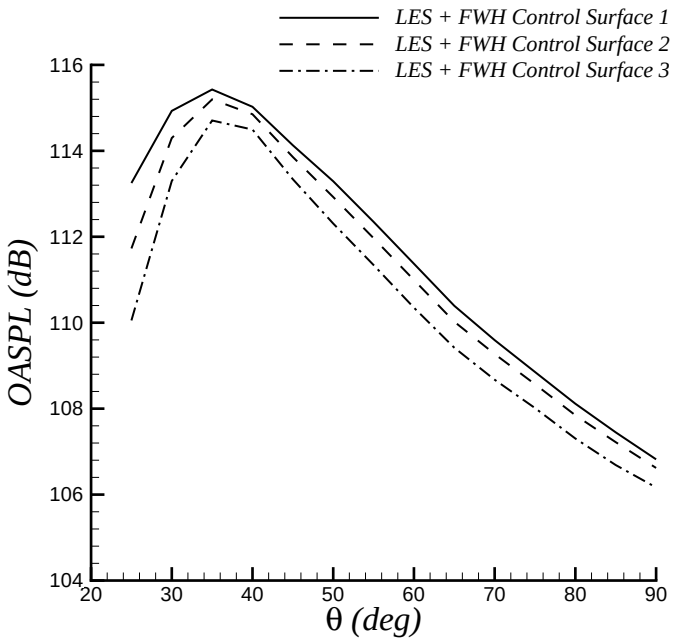

Figure 6.14. Overall sound pressure levels along the far field arc obtained with the data gathered on the 3 control surfaces and the Ffowcs Williams - Hawkings method.

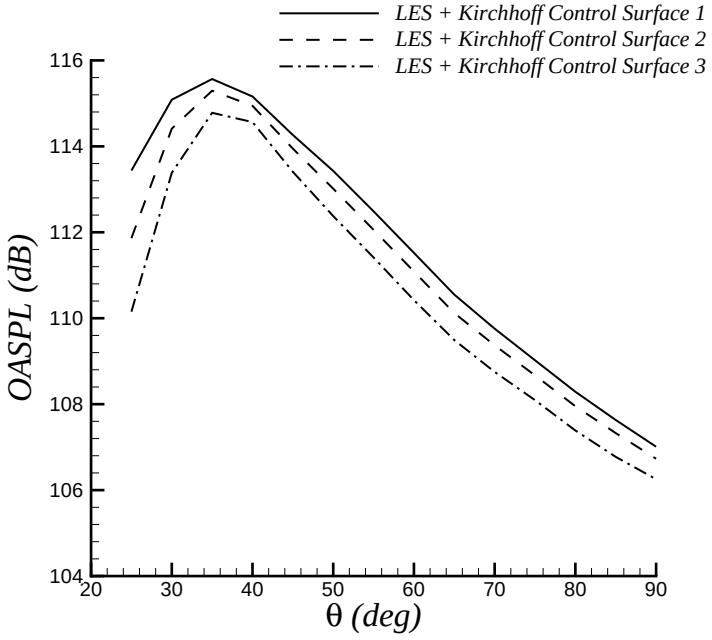

Figure 6.15. Overall sound pressure levels along the far field arc obtained with the data gathered on the 3 control surfaces and Kirchhoff's method.

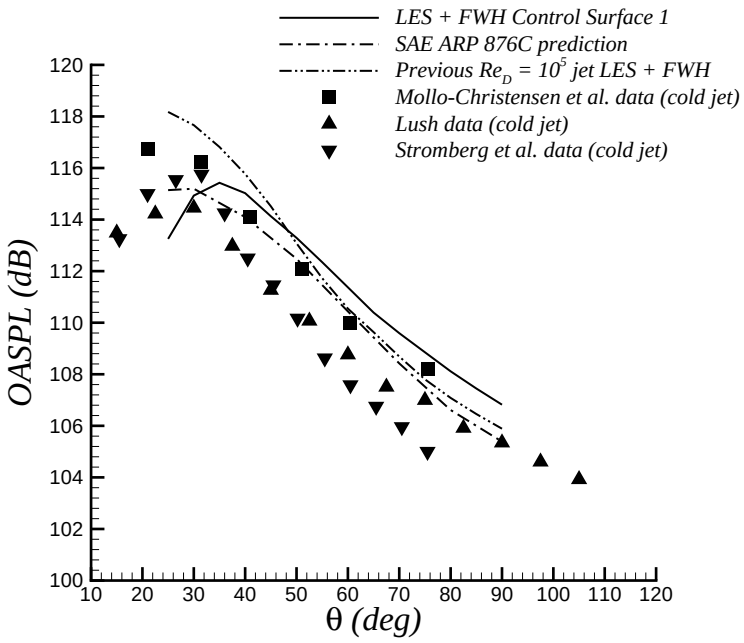

Figure 6.16. The Ffowcs Williams - Hawkings method prediction for the overall sound pressure levels along the far field arc and comparison with other data.

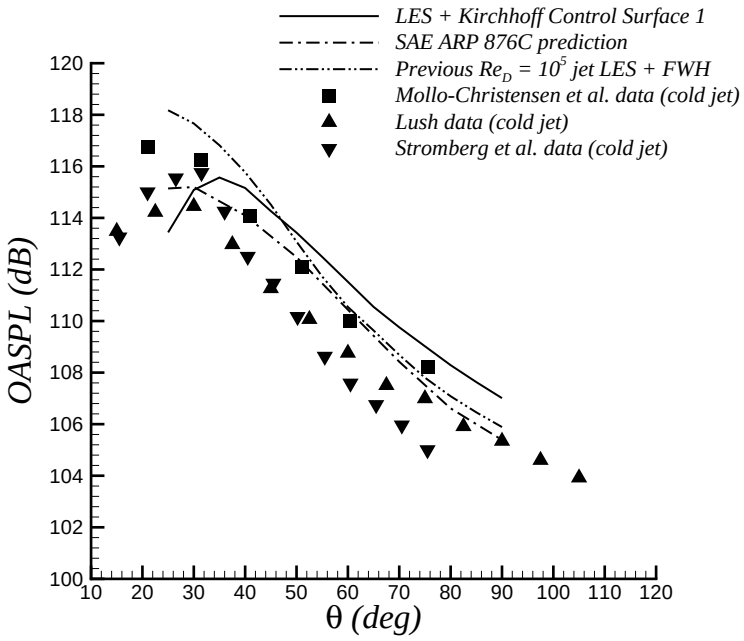

Figure 6.17. Kirchhoff's method prediction for the overall sound pressure levels along the far field arc and comparison with other data.

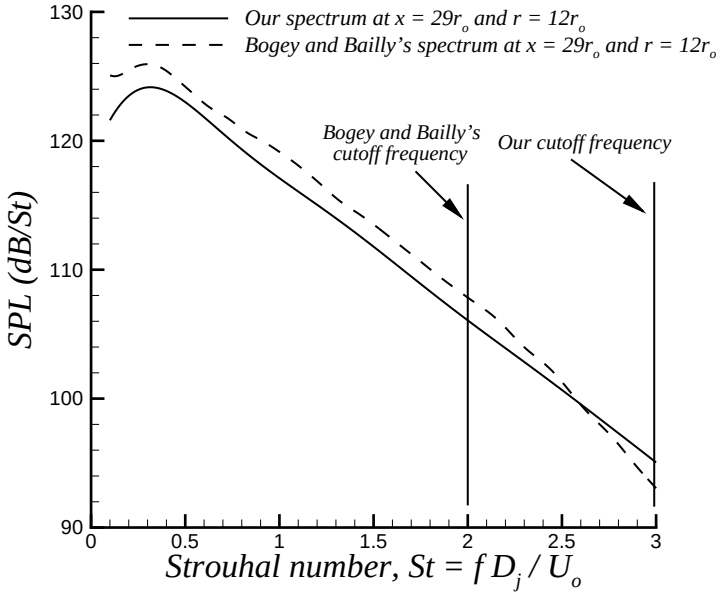

Figure 6.18. The Ffowcs Williams - Hawkings method prediction for the acoustic pressure spectrum at $x = 29r_0$, $r = 12r_o$ and comparison with the spectrum of Bogey and Bailly [34].

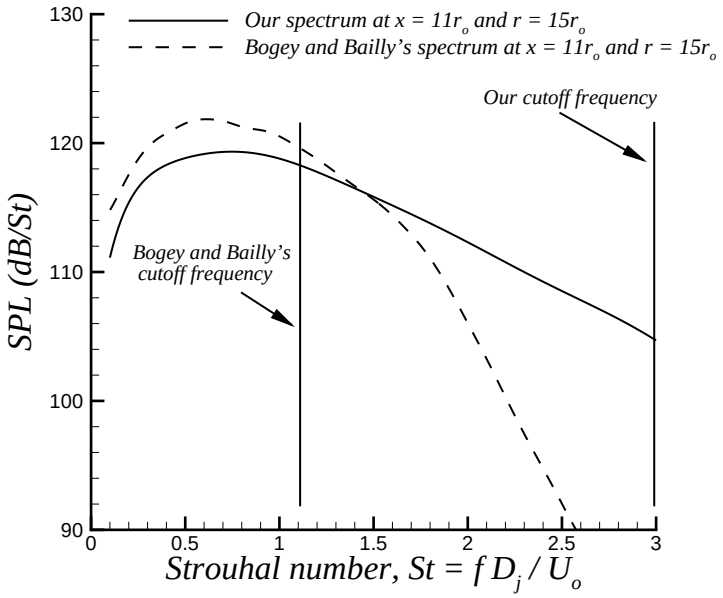

Figure 6.19. The Ffowcs Williams - Hawkings method prediction for the acoustic pressure spectrum at $x = 11r_0$, $r = 15r_o$ and comparison with the spectrum of Bogey and Bailly [34].

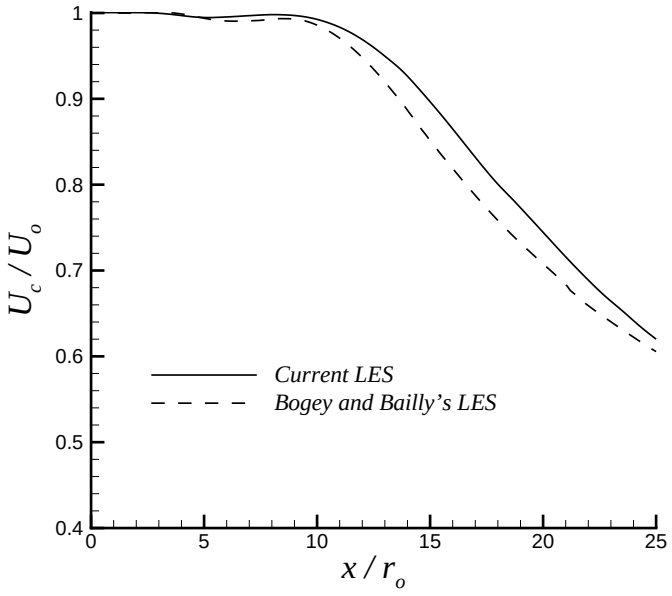

Figure 6.20. Axial profile of the mean jet centerline velocity and comparison with the profile of Bogey and Bailly [34].

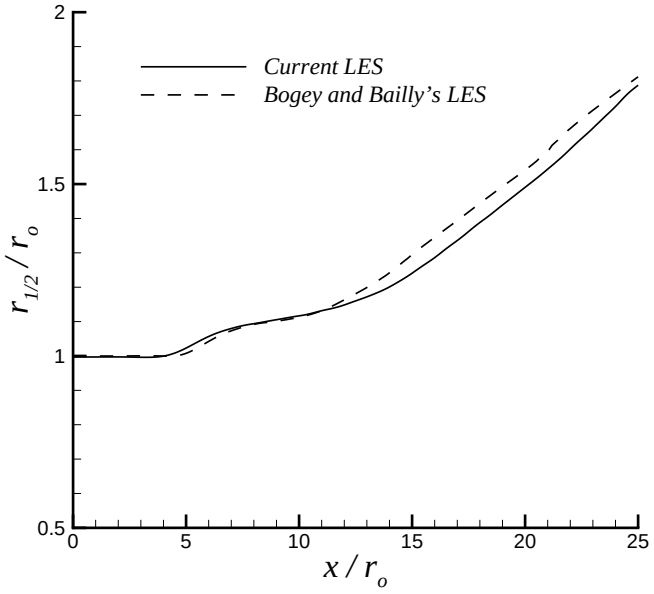

Figure 6.21. Axial profile of the jet half velocity radius and comparison with the profile of Bogey and Bailly [34].

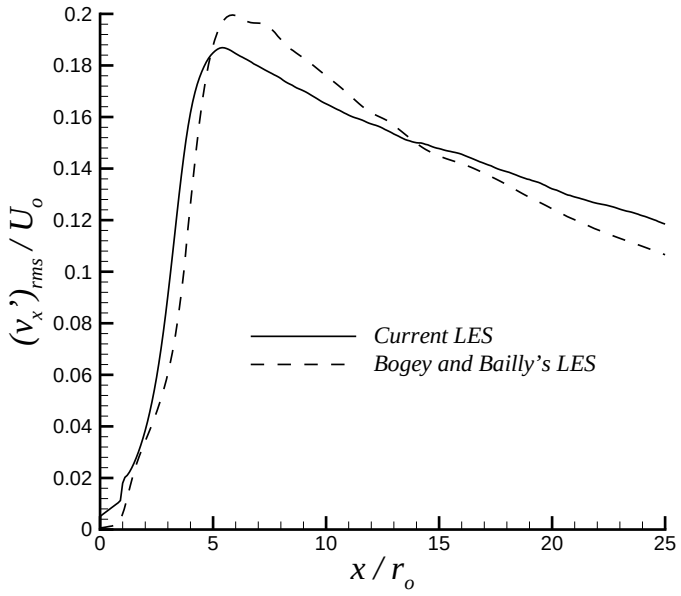

Figure 6.22. Axial profile of the root mean square of axial fluctuating velocity along $r = r_o$ and comparison with the profile of Bogey and Bailly [34].

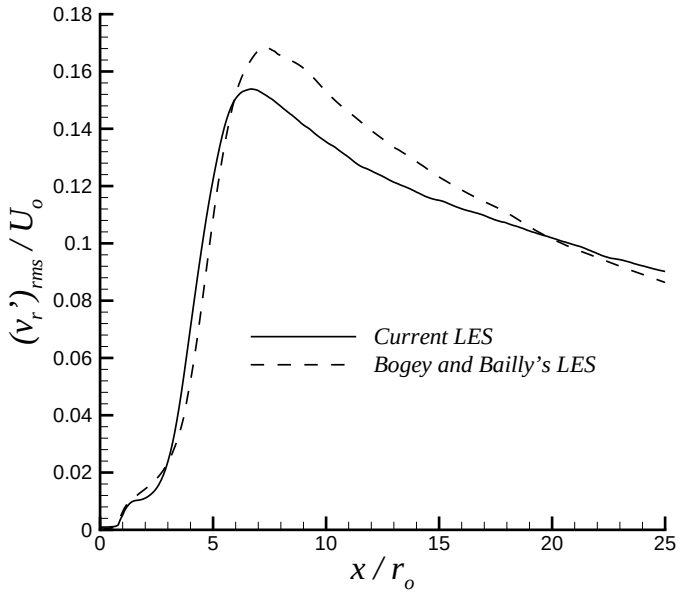

Figure 6.23. Axial profile of the root mean square of radial fluctuating velocity along $r = r_o$ and comparison with the profile of Bogey and Bailly [34].

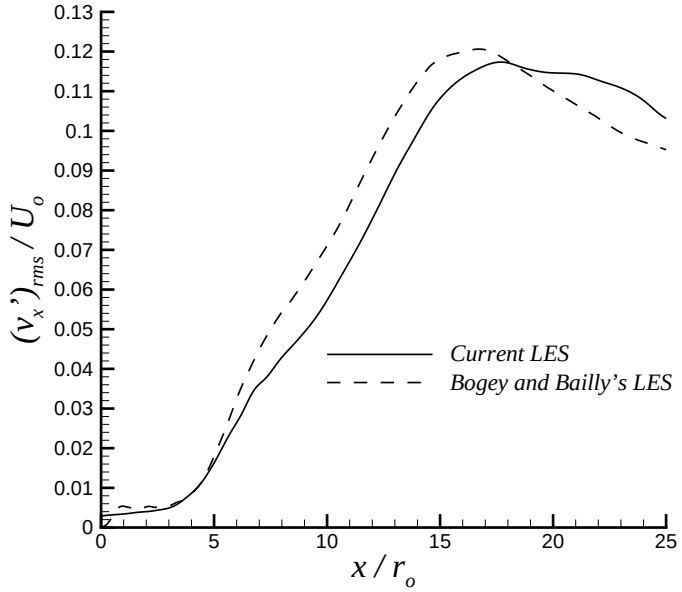

Figure 6.24. Centerline profile of the root mean square of axial fluctuating velocity and comparison with the profile of Bogey and Bailly [34].

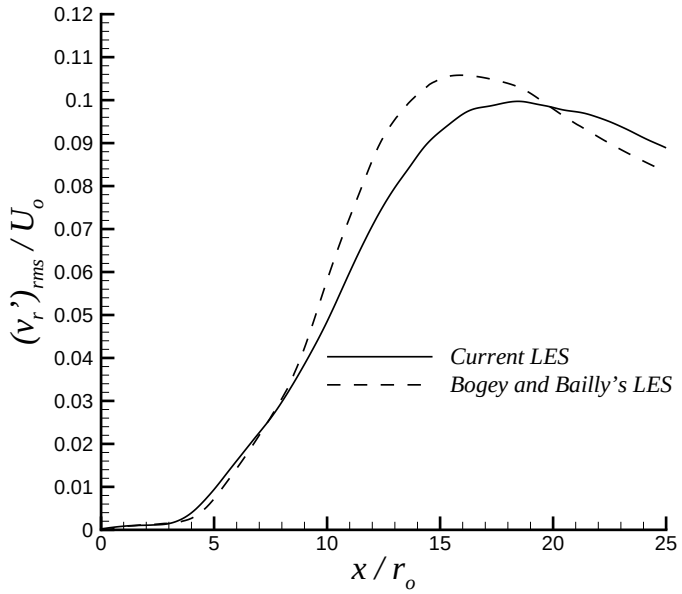

Figure 6.25. Centerline profile of the root mean square of radial fluctuating velocity and comparison with the profile of Bogey and Bailly [34].

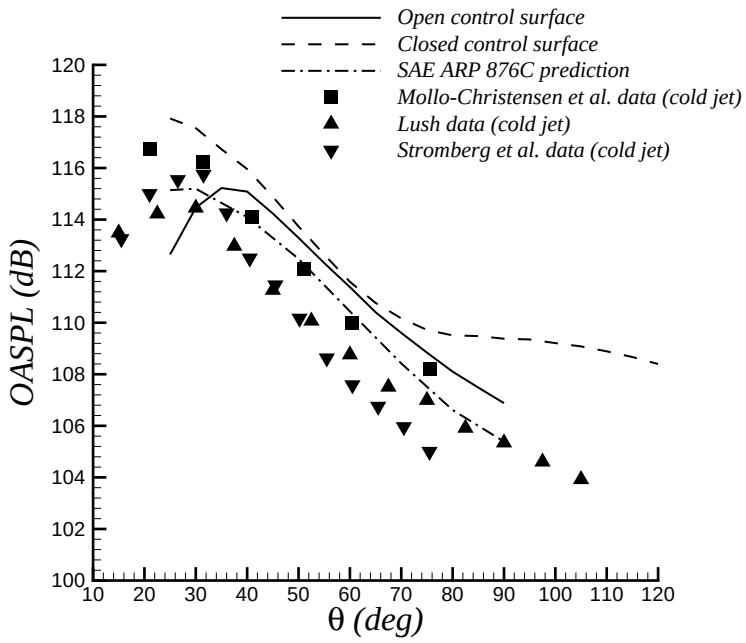

Figure 6.26. Overall sound pressure levels along the far field arc obtained using the open and closed control surfaces of streamwise length $30r_o$.

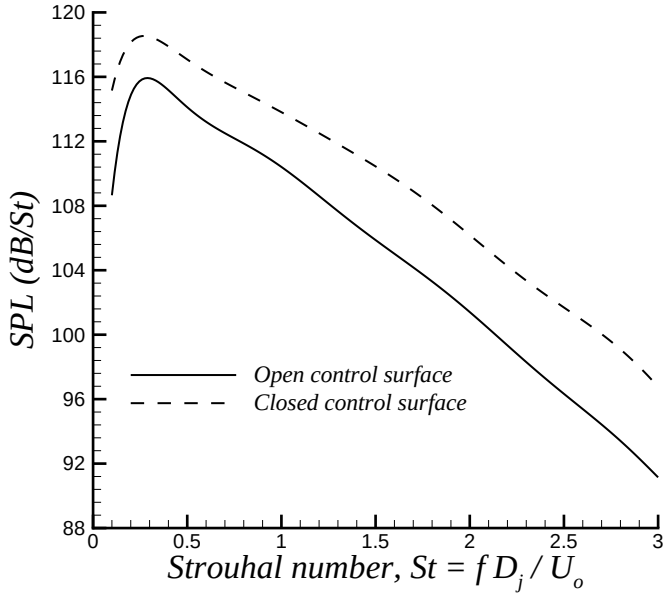

Figure 6.27. Acoustic pressure spectra at $R = 60r_o$, $\theta = 30^\circ$ location on the far field arc. (Obtained using the open and closed control surfaces of streamwise length $30r_o$.)

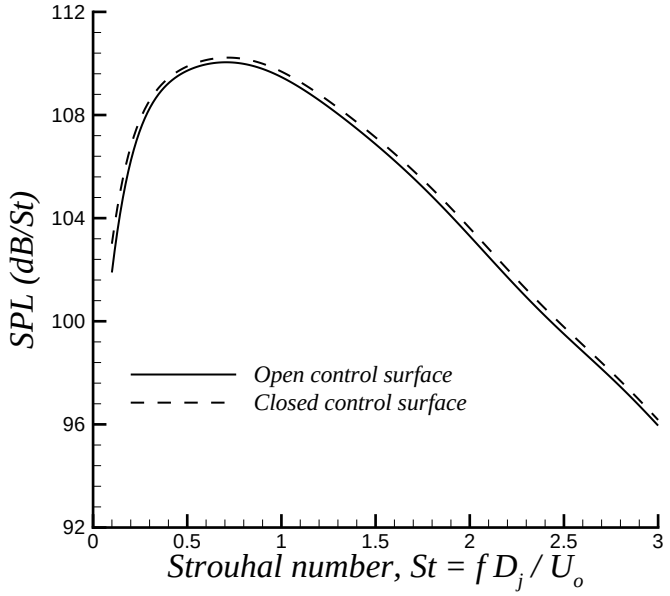

Figure 6.28. Acoustic pressure spectra at $R = 60r_o$, $\theta = 60^\circ$ location on the far field arc. (Obtained using the open and closed control surfaces of streamwise length $30r_o$.)

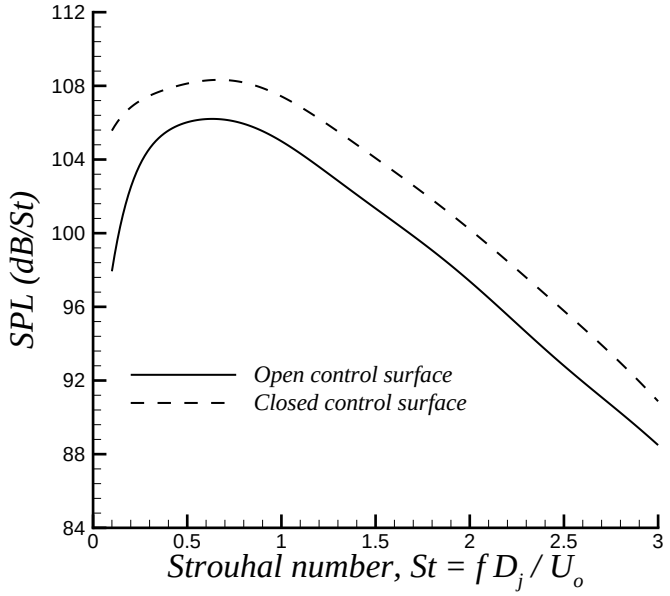

Figure 6.29. Acoustic pressure spectra at $R = 60r_o$, $\theta = 90^\circ$ location on the far field arc. (Obtained using the open and closed control surfaces of streamwise length $30r_o$.)

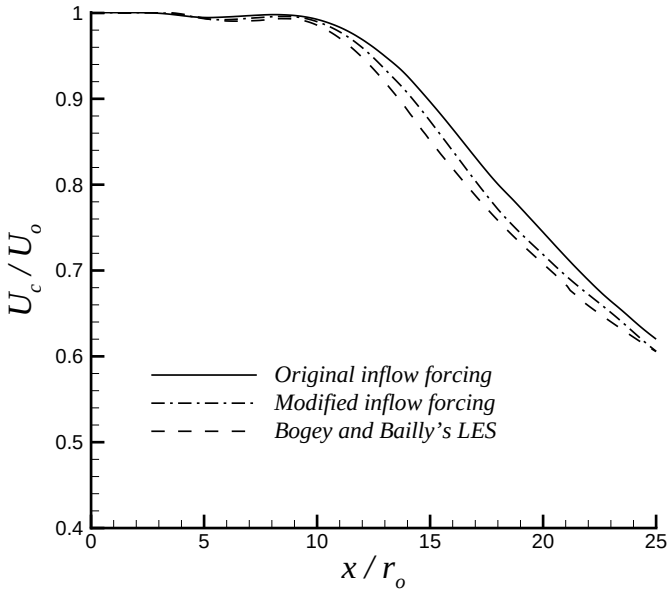

Figure 6.30. Axial profiles of the mean jet centerline velocity and comparison with the profile of Bogey and Bailly [34].

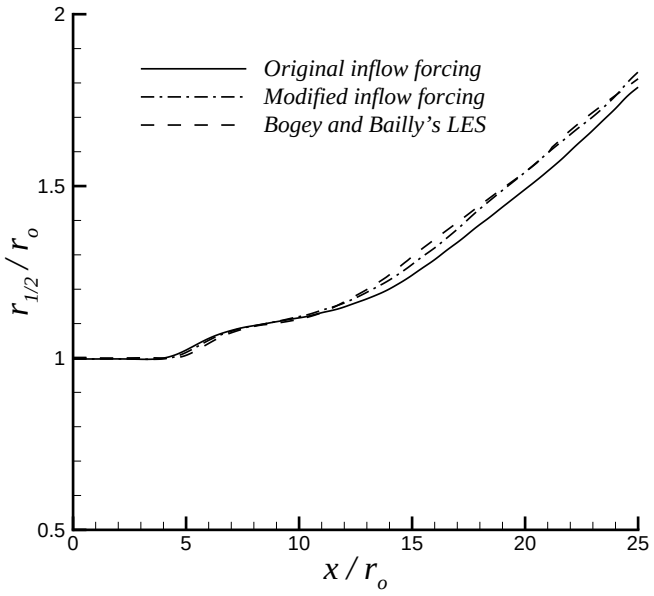

Figure 6.31. Axial profiles of the jet half velocity radius and comparison with the profile of Bogey and Bailly [34].

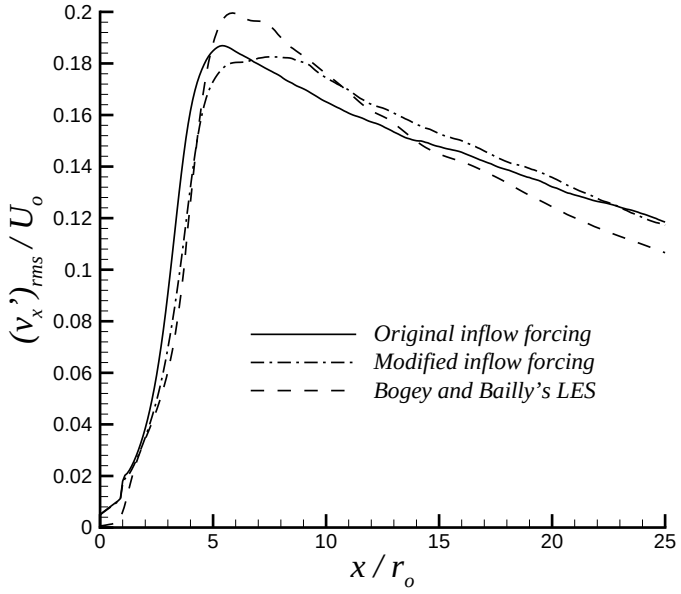

Figure 6.32. Axial profiles of the root mean square of axial fluctuating velocity along $r = r_o$ and comparison with the profile of Bogey and Bailly [34].

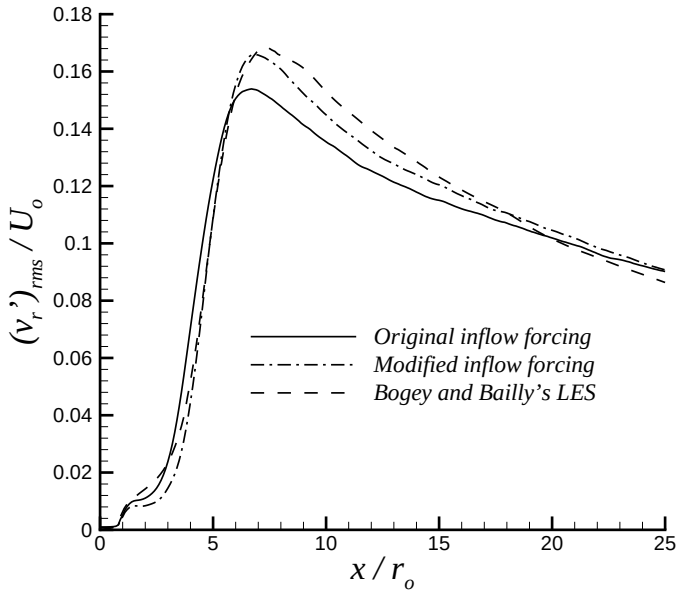

Figure 6.33. Axial profiles of the root mean square of radial fluctuating velocity along $r = r_o$ and comparison with the corresponding profile of Bogey and Bailly [34].

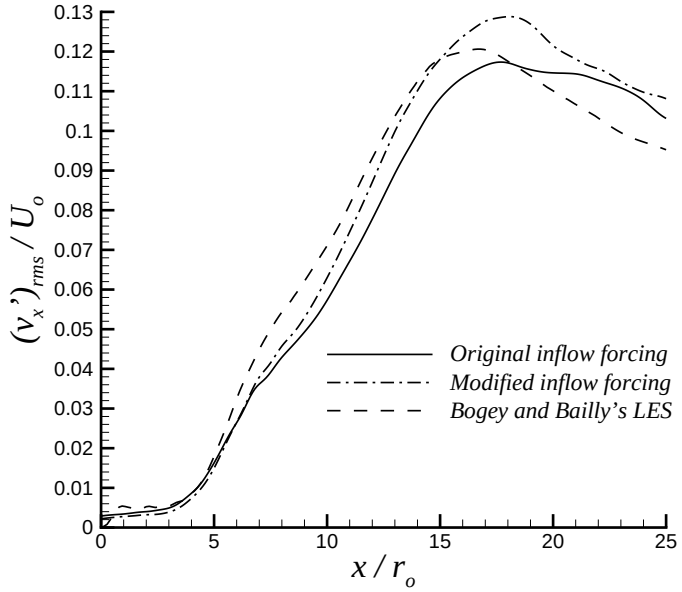

Figure 6.34. Centerline profiles of the root mean square of axial fluctuating velocity and comparison with the profile of Bogey and Bailly [34].

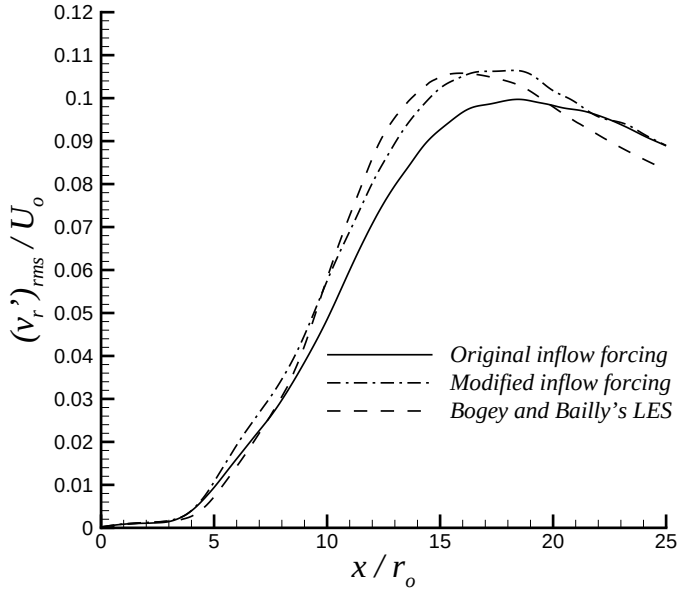

Figure 6.35. Centerline profiles of the root mean square of radial fluctuating velocity and comparison with the corresponding profile of Bogey and Bailly [34].

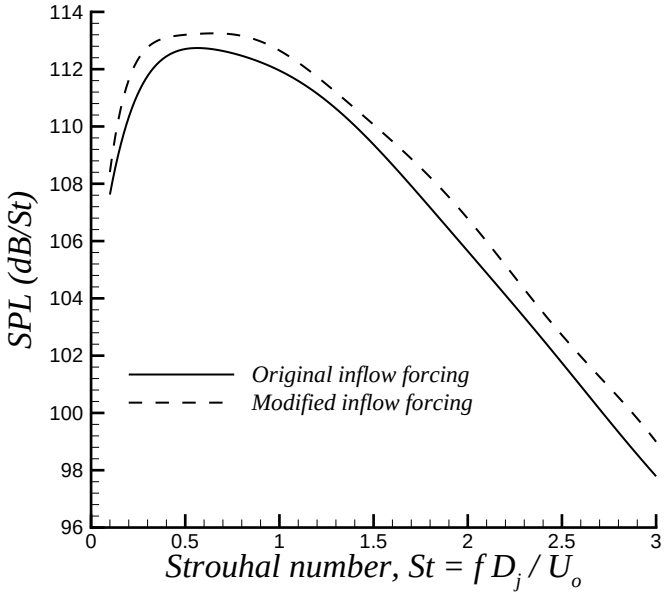

Figure 6.36. Acoustic pressure spectra at $R = 60r_o$, $\theta = 45°$ location on the far field arc. (Obtained using the open control surface of streamwise length $34r_o$.)

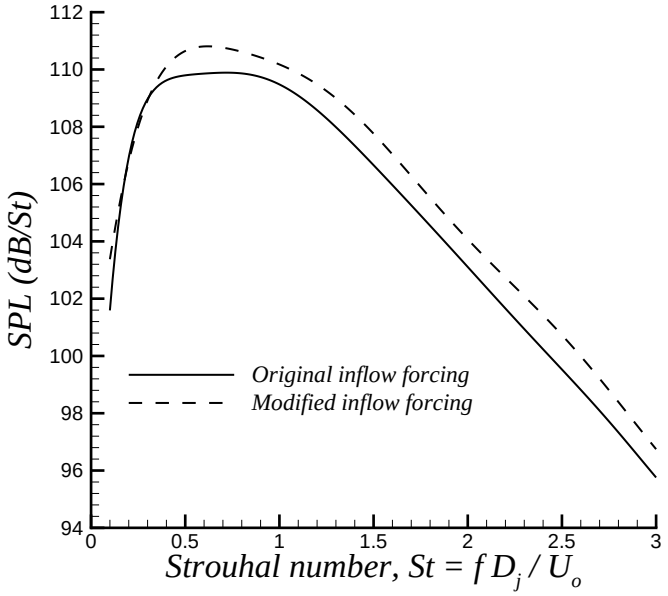

Figure 6.37. Acoustic pressure spectra at $R = 60r_o$, $\theta = 60°$ location on the far field arc. (Obtained using the open control surface of streamwise length $34r_o$.)

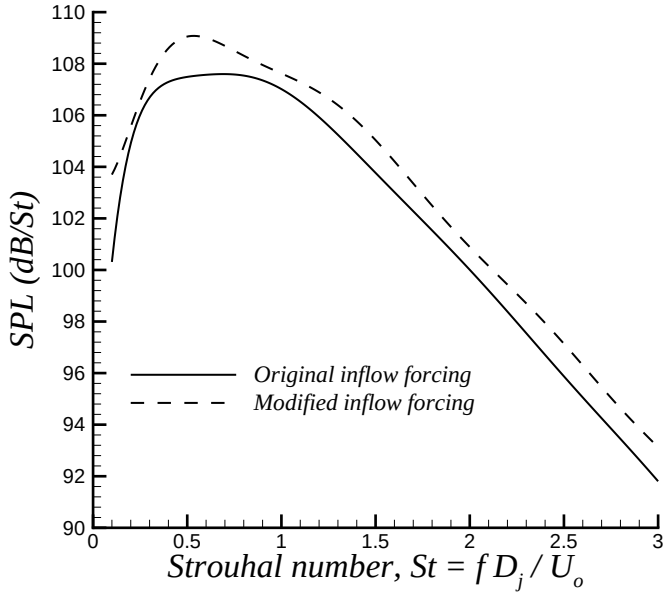

Figure 6.38. Acoustic pressure spectra at $R = 60r_o$, $\theta = 75^\circ$ location on the far field arc. (Obtained using the open control surface of streamwise length $34r_o$.)

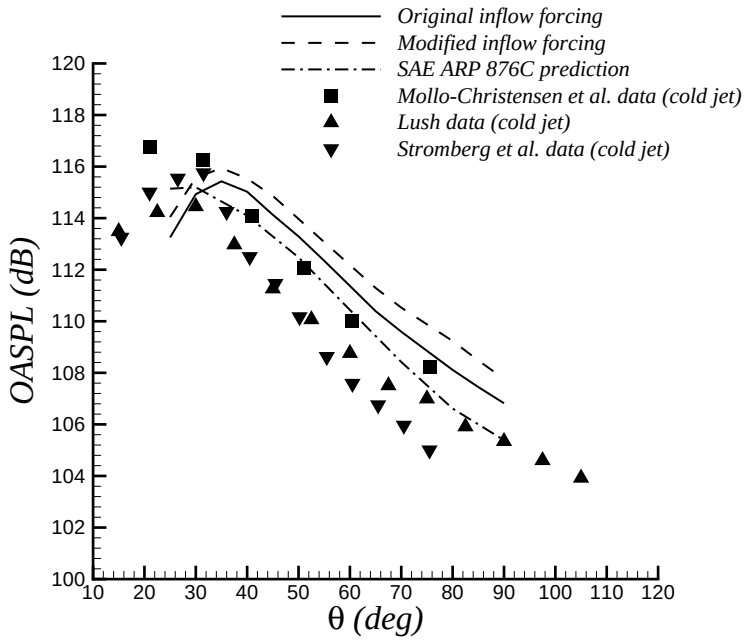

Figure 6.39. Overall sound pressure levels along the far field arc. (Obtained using the open control surface of streamwise length $34r_o$.)

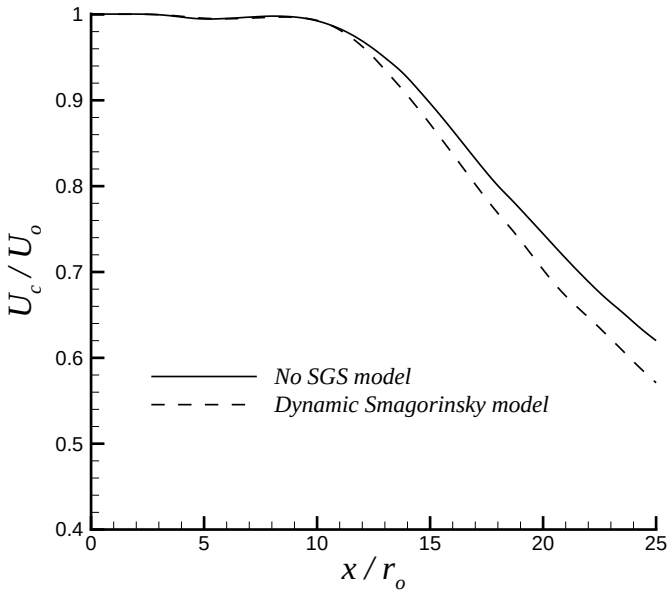

Figure 6.40. Axial profiles of the mean jet centerline velocity.

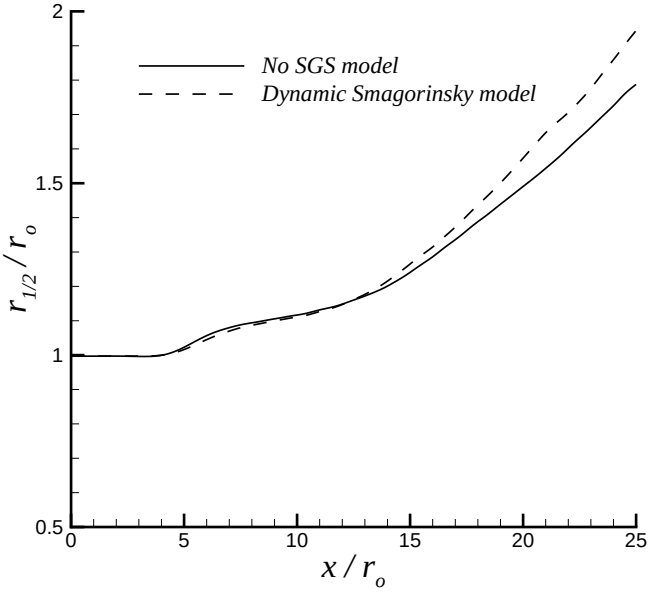

Figure 6.41. Axial profiles of the jet half velocity radius.

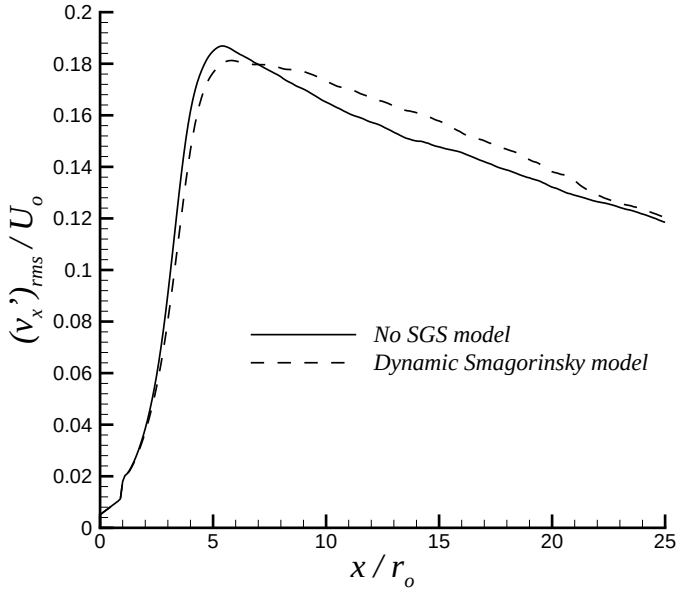

Figure 6.42. Axial profiles of the root mean square of axial fluctuating velocity along $r = r_o$.

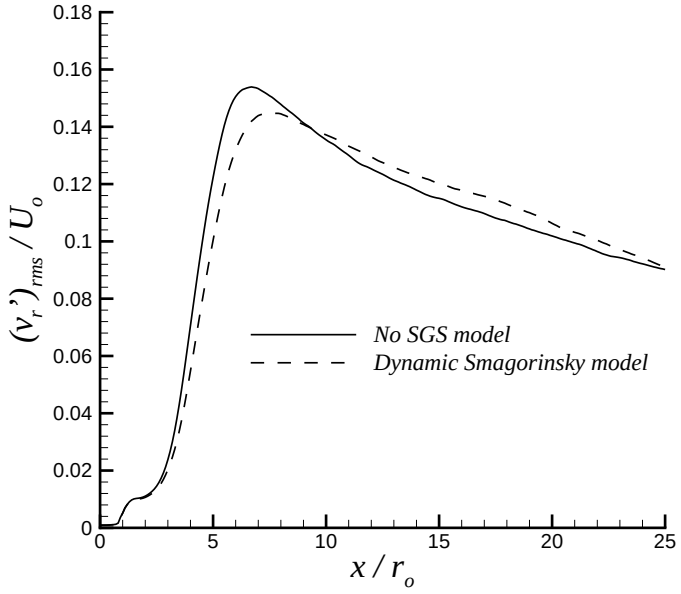

Figure 6.43. Axial profiles of the root mean square of radial fluctuating velocity along $r = r_o$.

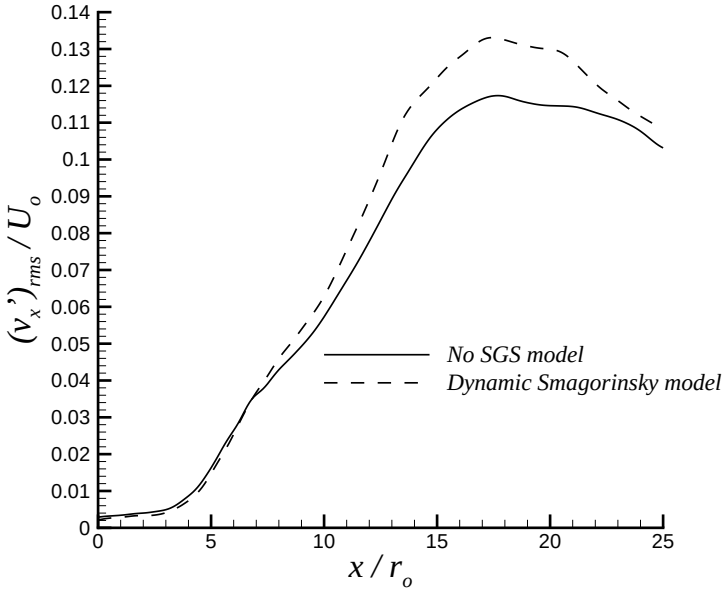

Figure 6.44. Centerline profiles of the root mean square of axial fluctuating velocity.

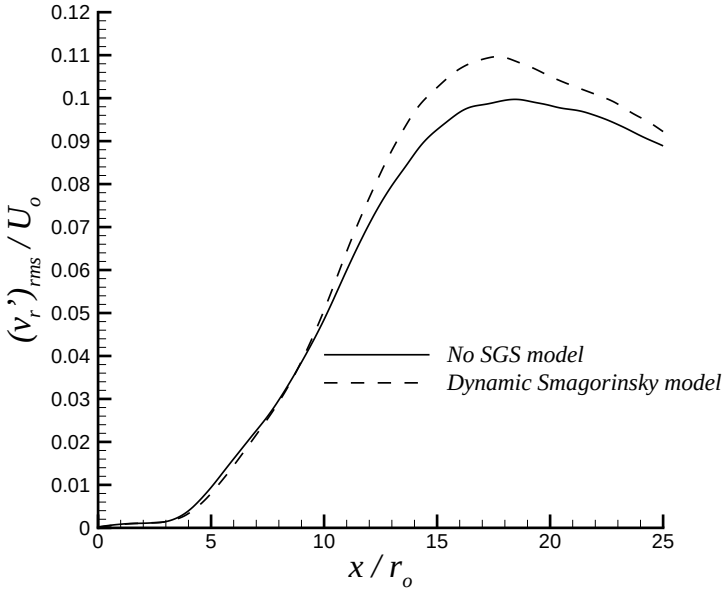

Figure 6.45. Centerline profiles of the root mean square of radial fluctuating velocity.

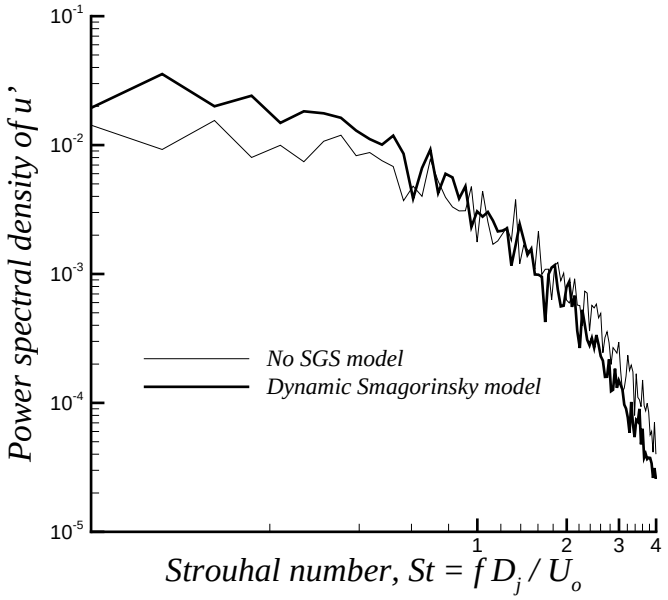

Figure 6.46. Temporal spectrum of the streamwise velocity fluctuations at the $x = 17.5r_o$ location on the jet centerline.

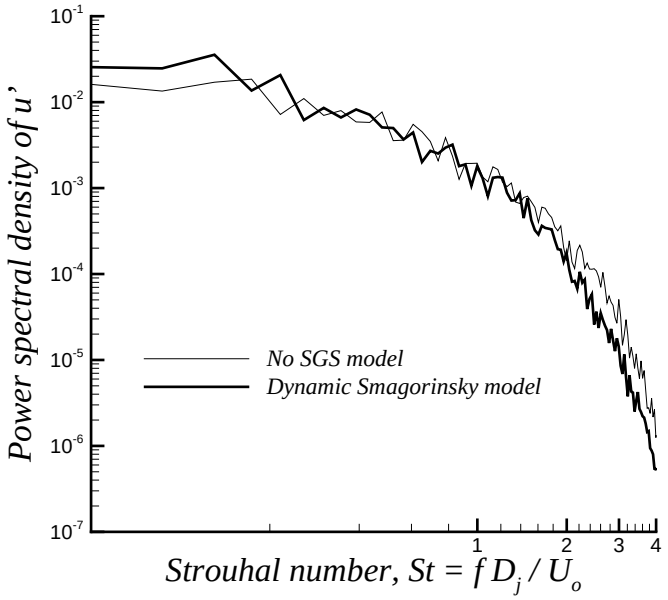

Figure 6.47. Temporal spectrum of the streamwise velocity fluctuations at the $x = 25r_o$ location on the jet centerline.

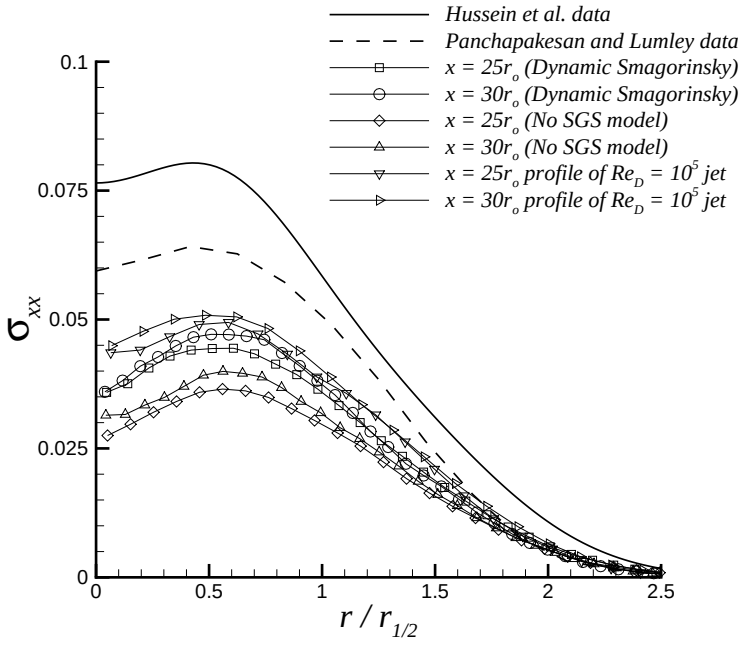

Figure 6.48. Normalized Reynolds normal stress σ_{xx} profiles.

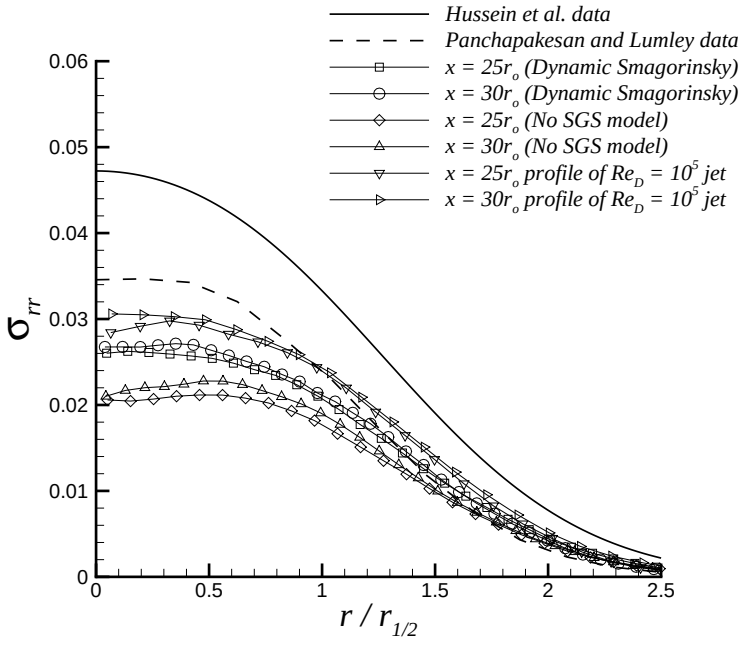

Figure 6.49. Normalized Reynolds normal stress σ_{rr} profiles.

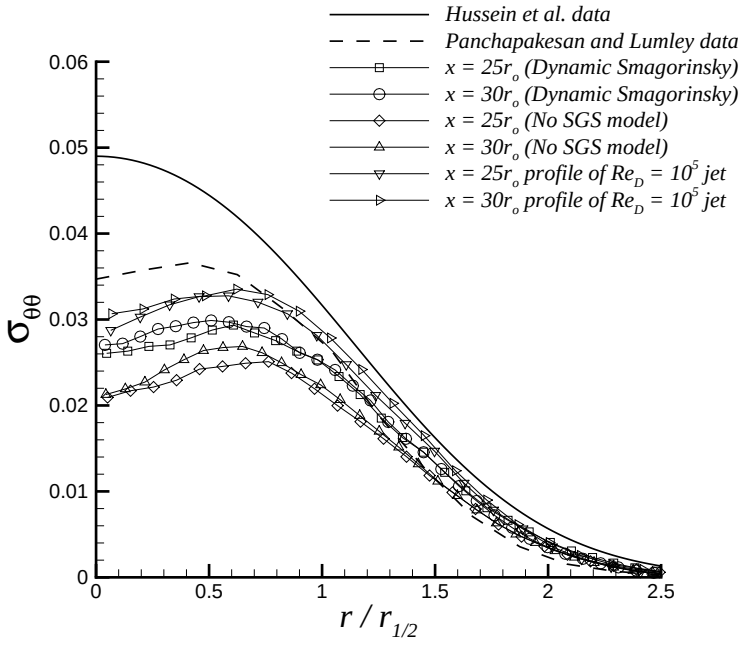

Figure 6.50. Normalized Reynolds normal stress $\sigma_{\theta\theta}$ profiles.

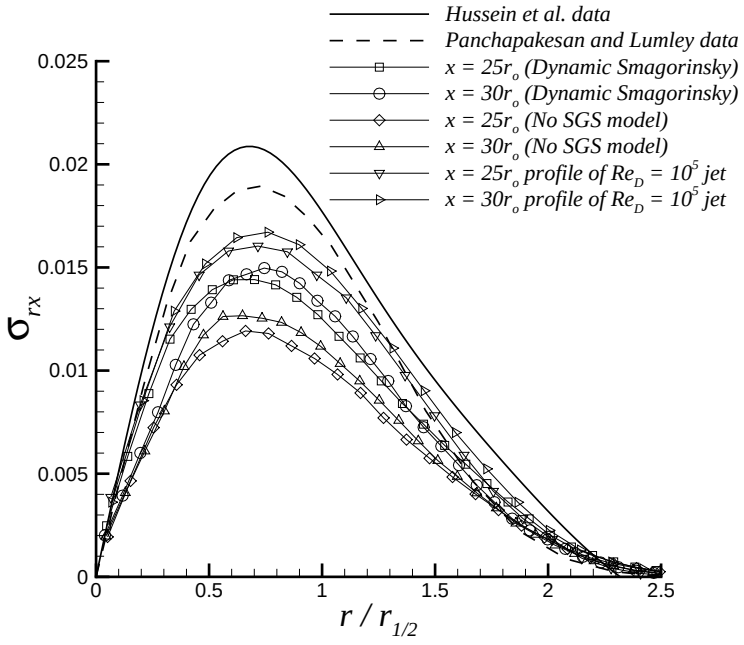

Figure 6.51. Normalized Reynolds shear stress σ_{rx} profiles.

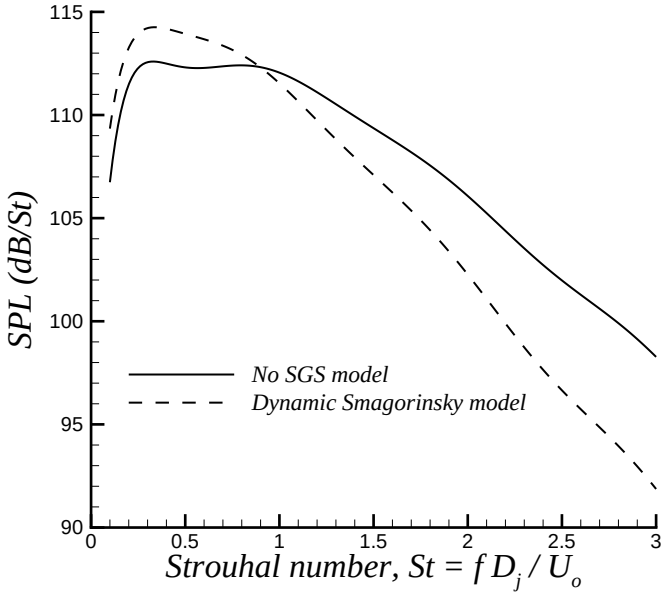

Figure 6.52. Acoustic pressure spectra at $R = 60r_o$, $\theta = 45°$ location on the far field arc. (Obtained using the open control surface of streamwise length $30r_o$.)

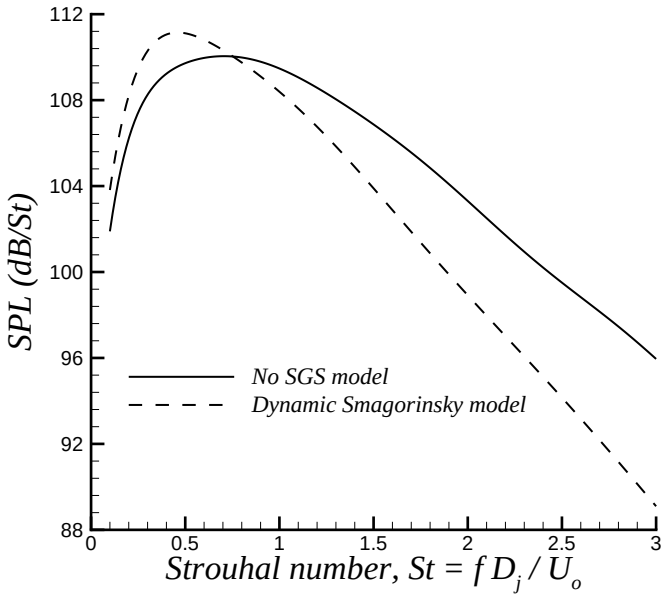

Figure 6.53. Acoustic pressure spectra at $R = 60r_o$, $\theta = 60°$ location on the far field arc. (Obtained using the open control surface of streamwise length $30r_o$.)

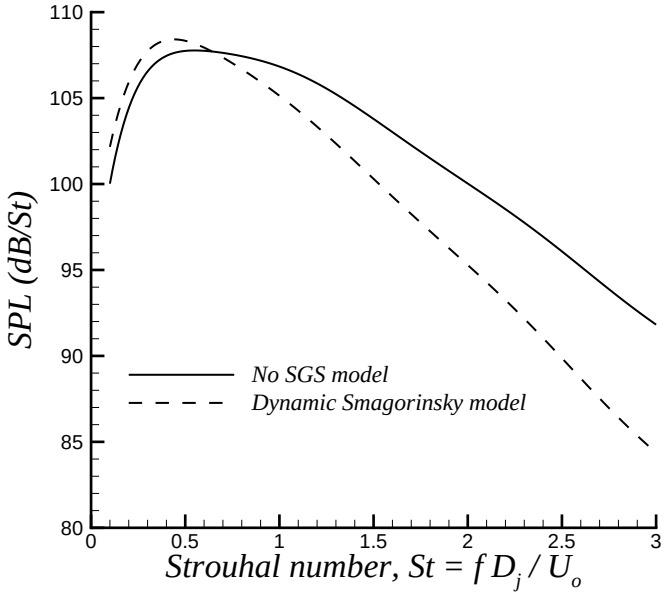

Figure 6.54. Acoustic pressure spectra at $R = 60r_o$, $\theta = 75^\circ$ location on the far field arc. (Obtained using the open control surface of streamwise length $30r_o$.)

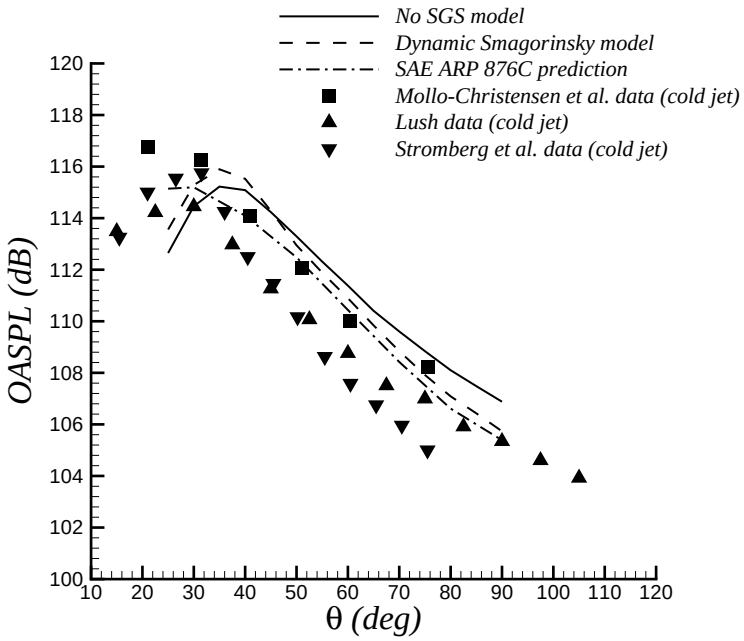

Figure 6.55. Overall sound pressure levels along the far field arc. (Obtained using the open control surface of streamwise length $30r_o$.)

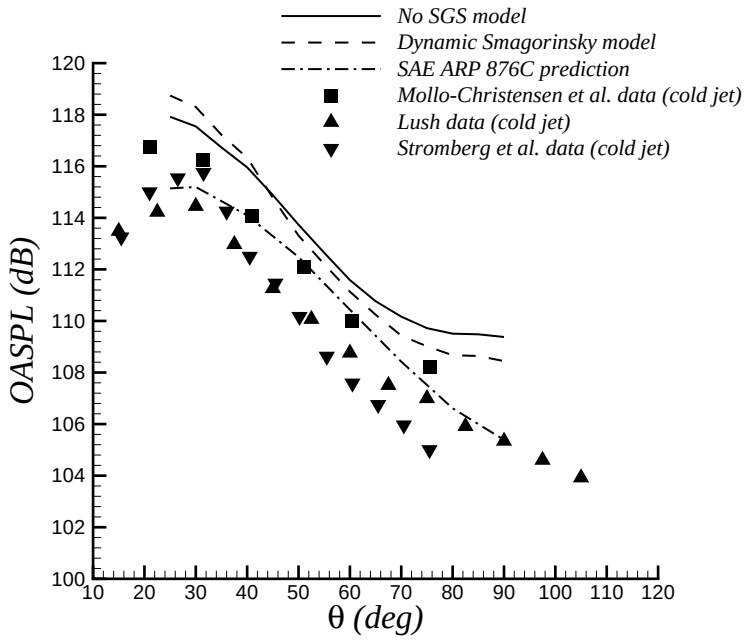

Figure 6.56. Overall sound pressure levels along the far field arc. (Obtained using the closed control surface of streamwise length $30r_o$.)

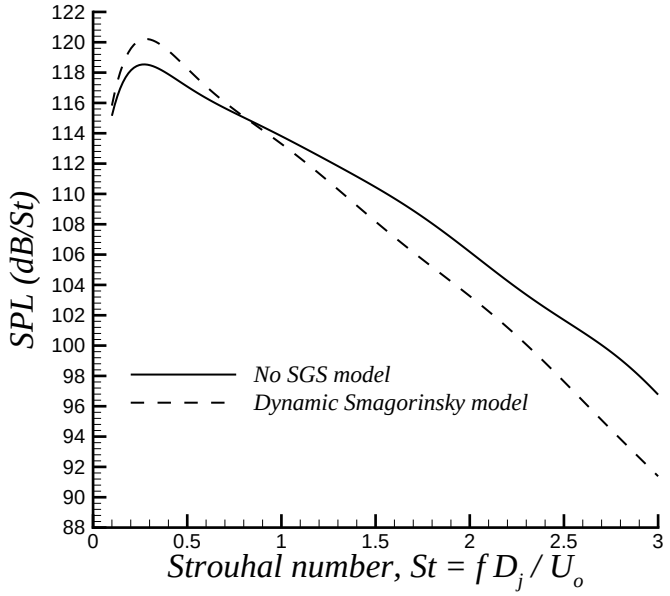

Figure 6.57. Acoustic pressure spectra at $R = 60r_o$, $\theta = 30^\circ$ location on the far field arc. (Obtained using the closed control surface of streamwise length $30r_o$.)

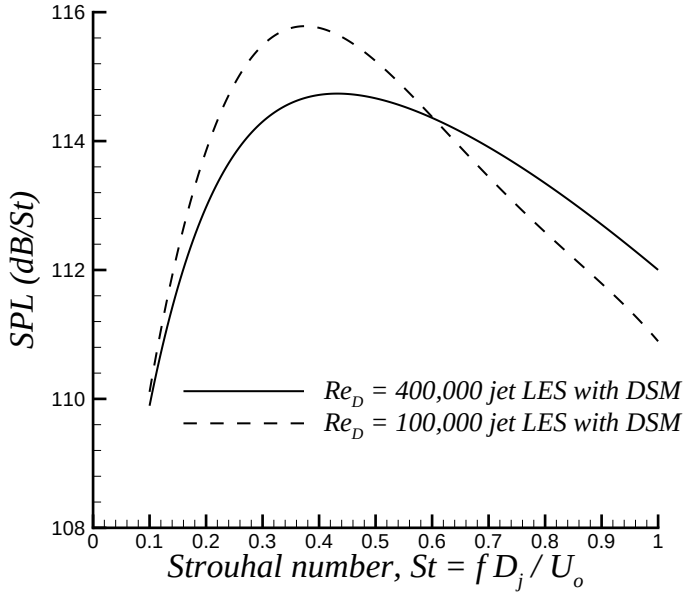

Figure 6.58. Effect of jet Reynolds number on the noise spectra at $R = 60r_o$, $\theta = 45°$ location on the far field arc.

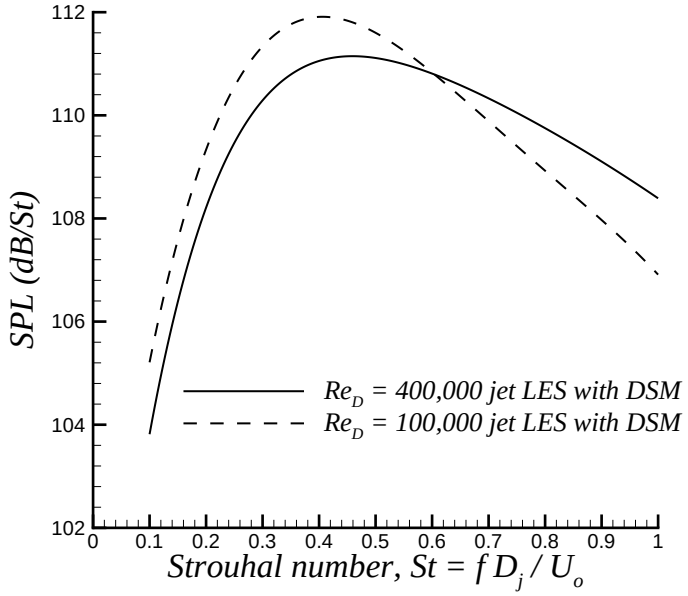

Figure 6.59. Effect of jet Reynolds number on the noise spectra at $R = 60r_o$, $\theta = 60°$ location on the far field arc.

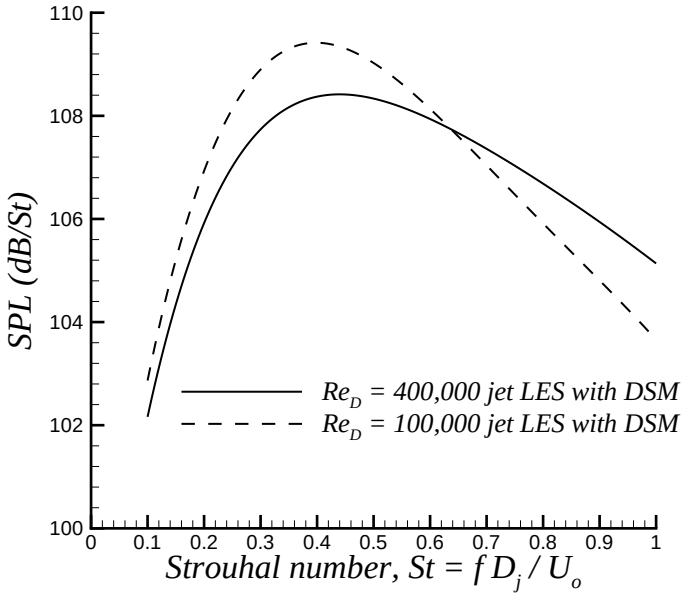

Figure 6.60. Effect of jet Reynolds number on the noise spectra at $R = 60r_o$, $\theta = 75^\circ$ location on the far field arc.

7. COMPUTATION OF THE FAR FIELD NOISE USING LIGHTHILL'S ACOUSTIC ANALOGY

In this chapter, we will compute the far field noise of the Reynolds number 400,000 jet using Lighthill's acoustic analogy. As mentioned in the previous chapter, data from the simulation which was performed without any explicit SGS model will be used for this purpose. The spatial filter was treated as the effective SGS model in the LES. Estimation of the far field noise of this jet using Kirchhoff's and the Ffowcs Williams - Hawkings methods was presented in the previous chapter. Far field noise computations done using Lighthill's acoustic analogy will be compared with the Ffowcs Williams - Hawkings method results as well as with some experimental noise spectra in this chapter.

Lighthill's equation [15] can be written as

$$\frac{\partial^2 \rho'}{\partial t^2} - c_\infty^2 \frac{\partial^2 \rho'}{\partial x_i \partial x_j} = \frac{\partial^2 T_{ij}}{\partial x_i \partial x_j}, \tag{7.1}$$

where the Lighthill stress tensor, T_{ij} is given as

$$T_{ij} = \rho u_i u_j + (p - c_\infty^2 \rho)\delta_{ij}, \tag{7.2}$$

with the viscous stress term neglected. In Lighthill's equation, all effects other than propagation, such as refraction, are lumped into the right hand side. It should be stated here that the right hand side of the above equation is by no means a true or unique representation of the acoustic sources in the turbulent flow. The double divergence of T_{ij} only serves as a nominal acoustic source and what it provides is an exact connection between the near field turbulence and the far field noise.

Lighthill's equation is exact and has the following solution for the far field pressure fluctuations generated by an unbounded flow [15],

$$p - p_\infty = (\rho - \rho_\infty)c_\infty^2 = \frac{1}{4\pi} \int_V \frac{\partial^2}{\partial y_i \partial y_j} T_{ij} \left(\mathbf{y}, t - \frac{|\mathbf{x} - \mathbf{y}|}{c_\infty} \right) \frac{d\mathbf{y}}{|\mathbf{x} - \mathbf{y}|}, \tag{7.3}$$

where $\mathbf{x}$, $\mathbf{y}$ are the observer and source coordinates, respectively, and the integration is carried over the entire turbulent volume containing the acoustic sources. In Lighthill's acoustic analogy, the sound generated by a turbulent flow is equivalent to what the quadrupole distribution T_{ij} per unit volume would emit if placed in a uniform acoustic medium at rest. In other words, in this analogy the quadrupole source distribution replaces the actual fluid flow and moreover, the sources may move, but the fluid in which they are embedded may not. The sources are embedded in a medium at rest that has the constant properties ρ_∞, p_∞ and c_∞, the same as those in the ambient fluid external to the flow.

The above integral is the formulation in which the double divergence of T_{ij} is used. At points far enough from the flow region, Lighthill shows that the following equation can be alternatively used to get an approximation to the far field pressure fluctuations [15],

$$p - p_\infty = (\rho - \rho_\infty)c_\infty^2 \approx \frac{1}{4\pi}\int_V \frac{(x_i - y_i)(x_j - y_j)}{|\mathbf{x}-\mathbf{y}|^3}\frac{1}{c_\infty^2}\frac{\partial^2}{\partial t^2}T_{ij}\left(\mathbf{y}, t - \frac{|\mathbf{x}-\mathbf{y}|}{c_\infty}\right)d\mathbf{y}. \quad (7.4)$$

This equation is the time derivative formulation of Lighthill's volume integral. It may be preferable to use the time derivative formulation over the spatial derivative formulation since the spatial derivative formulation seems to be more computationally expensive.

The time derivative formulation of Lighthill's volume integral will be used in this chapter for computing the far field noise. Following Freund [90], we can split the Lighthill stress tensor, T_{ij} into a mean component, T_{ij}^m, a component that is linear in velocity fluctuations, T_{ij}^l, a component that is quadratic in velocity fluctuations, T_{ij}^n and the so-called entropy component, T_{ij}^s, as follows

$$T_{ij} = T_{ij}^m + T_{ij}^l + T_{ij}^n + T_{ij}^s, \quad (7.5)$$

where

$$T_{ij}^m = \rho\bar{u}_i\bar{u}_j + (\bar{p} - c_\infty^2\bar{\rho})\delta_{ij}, \quad (7.6)$$

$$T_{ij}^l = \rho\bar{u}_i u_j' + \rho\bar{u}_j u_i', \quad (7.7)$$

$$T_{ij}^{n} = \rho u_i' u_j', \tag{7.8}$$

$$T_{ij}^{s} = (p' - c_\infty^2 \rho')\delta_{ij}. \tag{7.9}$$

By definition, the mean component T_{ij}^{m} does not make noise. In the above equations, density in the $\rho u_i u_j$ terms has not been decomposed into a mean and fluctuating part. Freund [90] shows that the noise from T_{ij} is nearly the same as that from

$$T_{ij}^{\bar{\rho}} = \bar{\rho} u_i u_j + (p' - c_\infty^2 \rho')\delta_{ij}. \tag{7.10}$$

Hence, the effect of the density fluctuations in the $\rho u_i u_j$ terms is not considered in this study. The noise from T_{ij}^{l} is called the shear noise since this component consists of turbulent fluctuations interacting with the sheared mean flow. On the other hand, the noise from T_{ij}^{n} is called the self noise since this component consists of turbulent fluctuations interacting with themselves, whereas the noise from T_{ij}^{s} is called the entropy noise since it is composed of the density and pressure fluctuations in the turbulent flow.

The 5 primitive flow variables were saved in nearly 7.5 million cell volumes inside the jet flow at every 10 time steps over a period of 40,000 time steps during the LES run. The sampling period corresponds to a time scale in which an ambient sound wave travels about 23 times the domain length in the streamwise direction. The flow data were saved in double precision format and the entire flow field database consisted of almost 1.2 Terabytes (TB) of data. Figures 7.1 through 7.3 depict the distribution of the Lighthill sources that radiate noise in the direction of the observers located at 30°, 60°, and 90° on an arc of radius $60r_o$ from the jet nozzle. The solid dark lines in these figures correspond to the boundaries of the volume in which time accurate LES data were saved. The volume starts at the inflow boundary and extends to 32 jet radii in the streamwise direction. The initial width and height of the volume are $10r_o$ at the inflow boundary. At $x = 32r_o$, the width and height of the volume are $20r_o$. As can be seen from the figures, the lateral boundaries are sufficiently far away from the sources that radiate noise. After a careful analysis of the spatial extent of the sources that radiate noise and based on the grid resolution in

the region where the sources are located, the cut-off frequency in the subsequent noise calculations was found to be located at around Strouhal number 4. Based on the data sampling rate, there are about 4 temporal points per period in this highest resolved frequency. An 8^{th}-order accurate explicit scheme will be employed for computing the time derivatives while computing the noise and 4 points per period is sufficient for this numerical scheme [48] whose details will be presented shortly. It should also be noted here that this cut-off frequency is higher than the Strouhal number 3 cut-off frequency of the previous aeroacoustics computations that employed surface integral acoustics methods. This is because the grid spacing is finest inside the jet and gets coarser outside the jet flow. Hence, the maximum frequency that can be accurately captured by the control surfaces placed around the jet flow is lower than that can be captured in the volume integrals. Using the 5 primitive variables and the mean flow data, one can easily compute T_{ij} and all of its components. To compute the noise of T_{ij} or one of its components, the following procedure was used. A retarded time based on the distance between the observer location and the source point inside the jet was computed first. Then, a 24-point time stencil was constructed around the retarded time point such that 12 points fell to the left and 12 points fell to the right of the retarded time point. These 24 points correspond to the time history points at which LES flow data were saved. Using the following 8^{th}-order accurate, 9-point explicit finite difference scheme developed by Bogey and Bailly [48], the second time derivative of the source term was computed at the 4 points to the left and 4 points to the right of the retarded time point.

$$f_i' = \frac{1}{\Delta t} \sum_{n=0}^{4} d_n (f_{i+n} - f_{i-n}), \tag{7.11}$$

where $f_i^{'}$ is the approximation of the first time derivative of f at time history point i and f_i denotes the value of f at time point i. The coefficients d_n are given as follows,

$$d_0 = 0 \quad d_1 = 0.841570125482 \quad d_2 = -0.244678631765,$$

$$d_3 = 0.059463584768 \quad d_4 = -0.007650904064. \tag{7.12}$$

It should be noted here that the above explicit finite difference was originally derived to compute the first derivative of a given variable, hence we applied it twice successively to get the second time derivative. Furthermore, to reduce the number of quantities whose second time derivative need to be computed, we first take the product of T_{ij} (or one of its components) with $(x_i - y_i)(x_j - y_j)$ (see the time derivative formulation of the volume integral) and compute the time derivative of the resulting quantity instead. This operation reduces the number of quantities to be time differentiated from 24 to 4. The source time derivatives at the 8 time history points were then used in a cubic spline interpolation subroutine of the NAG software library to get the second time derivative of the source term at the retarded time point. This value was then used in the integrand appearing in the volume integral. The turbulent flow region is divided into many cell volumes and the volume integrals are performed in a discrete sense by adding up the contributions from all cell volumes. Lighthill's volume integral was computed using 1160 processors in parallel on the *Lemieux* cluster at the Pittsburgh Supercomputing Center. Computation of the 3072-point time history of the noise from T_{ij}, T_{ij}^l, T_{ij}^n, and T_{ij}^s took about 8 minutes of computing time per observer point.

As we had done previously, we computed the overall sound pressure levels and acoustic pressure spectra along a far field arc of radius $60r_o$ from the jet nozzle in this study. There are 14 observer points on the far field arc. Even though acoustic pressure spectra were averaged over 36 equally spaced azimuthal points on a full circle at a given observer location in the previous chapters, we determined through numerical experimentation that averaging the spectra over 8 equally spaced azimuthal points gives almost the same averaged spectrum as that obtained by averaging the spectra over 36 equally spaced azimuthal points. Hence, in order to save computing time, the acoustic pressure signals were computed at only 8 equally spaced azimuthal points on a full circle at a given θ location on the arc. The 3072-point time signal at a given observer location was then broken up into 3 1024-point signals and the 1024-point signals were used in the spectral analysis. Hence, there were a total of 24 1024-point

signals available for a given observer point on the arc. The 24 acoustic pressure spectra were used to obtain the averaged spectrum which was integrated later to compute the overall sound pressure level at the given θ location on the arc. For 112 far field points, the total run time needed was about 15 hours on 1160 processors.

The distribution of the Lighthill sources that radiate noise in the direction of the observers located at 30°, 60°, and 90° on the far field arc was previously shown in figures 7.1 through 7.3. As can be seen from these figures, although the sources near the outflow boundary at $x = 32r_o$ seem to be relatively weak for the observers located at 30° and 60° on the arc, the sources that radiate noise in the direction of the observer at 90° are still strong near the outflow boundary. So it seems like a longer streamwise domain length is necessary in order for the convecting acoustics sources to sufficiently decay. The implications of truncating the domain at $x = 32r_o$ will be discussed in more detail shortly.

We first looked at the effect of the integration domain size on the far field noise estimations. For this purpose, Lighthill's volume integral was carried out for 3 different streamwise domain lengths. The domain lengths considered were $24r_o$, $28r_o$ and $32r_o$, respectively. Figure 7.4 shows the Lighthill's volume integral predictions for the 3 different streamwise domain lengths and makes comparisons with experimental data as well as with the open and closed control surface predictions of the Ffowcs Williams - Hawkings method from the previous chapter. From this figure, it is clear that as the integration domain size is increased from $24r_o$ to $32r_o$, the overall sound pressure levels at all observation angles other than those in the range $60° < \theta < 80°$, decrease as much as 2 dB. The changes in OASPL for observation angles greater than 90°, on the other hand, are on the order of 2 to 3 dB. This observation implies that there are significant noise cancellations taking place as one includes a longer streamwise length in the volume integration and such cancellations cause a reduction in the overall sound pressure levels for certain observation angles in the far field. The difference in the OASPL predictions when the integration domain size is increased from $28r_o$ to $32r_o$ is within 1 dB for the observation angles $\theta < 80°$. The OASPL curve

that is obtained when the integration domain length is $32r_o$ has an almost flat portion in the range where $80^\circ < \theta < 120^\circ$. On the other hand, the experimental data show a continuous drop at those observation angles. The spurious effects observed here are quite similar to those observed in the previous chapter when the Ffowcs Williams - Hawkings method was applied on a closed control surface. It is also interesting to note that the MGB method [91] shows that the sources beyond $32r_o$ in a jet are not significant. This is evident in figure 7.5 which plots the OASPL predicted by MGB versus θ for various streamwise lengths. It can also be argued at this point that the sudden truncation of the domain in the current computations creates spurious dipole sources on the outflow surface as the quadrupole sources pass through downstream surface. Such spurious dipole sources could also be partially responsible for the behavior seen in the OASPL plot for the range where $\theta > 80^\circ$. Since all acoustic sources decay as we move downstream, a longer streamwise domain will improve the predictions for $\theta > 80^\circ$. In his study, Freund [90] also observed substantial noise cancellations happening among the noise generated in different streamwise sections of the jet, however he did not get the spurious effects we observe here. His streamwise domain size was $31r_o$. So it appears that although the acoustic sources decay by $x = 31r_o$ for a low Reynolds number jet, they have a larger streamwise extent in the present high Reynolds number jet.

Figures 7.6 through 7.8 depict the overall sound pressure levels from the individual components T^l_{ij}, T^n_{ij} and T^s_{ij}, respectively for the 3 different streamwise domain sizes over which volume integrations are done. The OASPL values of the shear noise from T^l_{ij} show less than 2 dB difference for some observation angles in the range $\theta < 80^\circ$ while we see 2 to 3 dB difference in the OASPL values for observation angles in the range $\theta > 80^\circ$ as the integration domain is increased from $24r_o$ to $32r_o$. On the other hand, the OASPL values of the self noise from T^n_{ij} show very small differences for observation angles $\theta < 80^\circ$ and less than 1 dB difference for $\theta > 80^\circ$, while there are only minor changes in the OASPL values of the entropy noise from T^s_{ij} at all observation angles as the integration domain size is increased from $24r_o$ to $32r_o$.

Although not shown here, analysis of the shear noise spectra for observer angles $\theta > 80°$ revealed decreasing spectral energy at the higher frequencies with increasing integration domain size. It is evident from these observations that the acoustic sources located in the region $x > 32r_o$ which were not captured in the current LES are most likely to alter the shear noise from T_{ij}^l for observer angles $\theta > 80°$.

Figure 7.9 shows the OASPL values of the noise from T_{ij} and its individual components T_{ij}^l, T_{ij}^n and T_{ij}^s when the streamwise integration domain extends up to $32r_o$. Even though the current jet is an isothermal jet ($T_o/T_\infty = 1$), the entropy noise from T_{ij}^s is significant near the jet axis where the observation angle is small, but becomes insignificant at large angles. It is also observed from the figure that the shear noise from T_{ij}^l and the self noise from T_{ij}^n are louder than the total noise due to T_{ij} for observation angles $\theta < 40°$ while the entropy noise from T_{ij}^s is louder than the total noise for $\theta < 15°$. The shear noise reaches its minimum OASPL value at around $\theta = 80°$ and starts to increase for larger angles, whereas the self noise exhibits a continuous drop. The fact that the shear noise, self noise and entropy noise components are more intense that the total noise for some observation angles near the jet axis means that the noise from the different components must be correlated as suggested by Freund [90] so that significant cancellations are happening among the noise generated by the individual components. To see the correlation between the noise components, we can define the following correlation coefficients [90],

$$C_{ln} = \frac{\langle p^l p^n \rangle}{p^l_{rms} p^n_{rms}}, \quad C_{ls} = \frac{\langle p^l p^s \rangle}{p^l_{rms} p^s_{rms}}, \quad C_{ns} = \frac{\langle p^n p^s \rangle}{p^n_{rms} p^s_{rms}}, \tag{7.13}$$

where the superscripts l, n, and s indicate the shear noise from T_{ij}^l, the self noise from T_{ij}^n and the entropy noise from T_{ij}^s, respectively. The correlation coefficients C_{ln}, C_{ls} and C_{ns} are plotted in figure 7.10. For observation angles in the range $\theta < 40°$, the shear noise from T_{ij}^l cancels the self noise from T_{ij}^n with a correlation coefficient on the order of -0.6. There is also some correlation between the self noise from T_{ij}^n and the entropy noise from T_{ij}^s at the small observation angles where the correlation coefficient has a value around -0.3. The shear noise from T_{ij}^l and the entropy noise from T_{ij}^s also cancel each other at very small angles near the

jet axis with a correlation coefficient of almost -0.3. The correlation coefficient between these two noise components starts to rapidly move towards zero as the observation angle increases and reaches a positive value in between 0.1 and 0.2 at the $\theta = 40^\circ$ observation point. It then starts to approach towards the zero line for larger observation angles. All correlations reach a value close to zero at around $\theta = 80^\circ$ and $\theta = 90^\circ$ locations. Since it was concluded from figure 7.6 that the acoustic sources located in the region $x > 32r_o$ are expected to alter the shear noise for the observation angles $\theta > 80^\circ$, the correlation coefficients that involve the shear noise are probably not very accurate for observation angles in the range $\theta > 80^\circ$.

Figures 7.11 through 7.14 depict the acoustic pressure spectra at the observation angles of 30°, 60°, 90° and 120° on the far field arc. Comparisons are shown for 3 streamwise domain lengths over which Lighthill's volume integral is carried out. As mentioned earlier, the cut-off noise frequency in the current computations is located around Strouhal number 4, hence the portion of the spectra for frequencies greater than Strouhal number 4 are missing. The spectra at the $\theta = 60^\circ$ location show minor changes as the integration domain is increased from $24r_o$ to $32r_o$, whereas there are more significant changes at the other 3 observation angles. At the 30° and 90° observation angles, the high frequency part of the spectra shifts down as the integration domain increases along the streamwise direction. At the 120° location, we observe a secondary high frequency peak in the spectra which is located in between Strouhal number 3.5 and 4. It is interesting to see the spectral energy at the second peak decreases slightly, whereas the spectral energy contained in the frequencies in between the primary and the secondary peaks decreases significantly as the integration domain size increases. Once again, the decrease in the spectral energy at certain frequencies is due to the significant cancellations taking place among the noise generated by the sources in different regions of the jet.

Next, we look at the noise spectra of the individual components of T_{ij} at the observation locations of 30°, 60°, 90° and 120° on the far field arc. Figures 7.15 through 7.18 plot the total noise from T_{ij}, shear noise from T_{ij}^l, self noise from T_{ij}^n

and entropy noise from T_{ij}^{s} for these observation angles. As can be see in figure 7.15, at 30°, the peak of the shear noise spectrum coincides with that of the total noise at around Strouhal number 0.3. The peak of the experimental noise spectra at the 30° observation location has also been observed at around Strouhal number 0.25 - 0.3. We see the high frequency part of both the shear noise and the self noise spectra is more energetic than that of the total noise. The entropy noise is relatively weak over most of the frequency range when compared with the shear noise and the self noise. Figure 7.10 shows that at the observation angle of 30°, the shear noise and the self noise cancel each other with a correlation coefficient of about -0.6, whereas the self noise and the entropy noise cancel each other with a correlation coefficient of about -0.3. Hence, the interaction of the shear noise, self noise and entropy noise at the 30° location results in a total noise spectrum that that has reduced spectral energy levels in the high frequency range.

From figure 7.16, it is seen that the total noise spectrum is very similar to the self noise spectrum at the 60° location. The portion of the shear noise spectrum for Strouhal number greater than 2 has the same spectral energy levels as the self noise spectrum. Except for the low frequency region, the entropy noise is very weak over the entire frequency range. From figure 7.10, we now see that at the observation angle of 60°, the shear noise and the self noise cancel each other with a correlation coefficient of about -0.4, whereas the self noise and the entropy noise cancel each other with a correlation coefficient of about -0.15. Such an interaction among the noise components at the given observation point causes the total noise spectrum to be essentially the same as the self noise spectrum.

Figure 7.17 shows the noise spectrum of T_{ij} and its components at the $\theta = 90°$ location. Although the shear noise spectrum appears to be slightly more energetic than the self noise spectrum at this observation angle, the reader is reminded of our earlier analysis which revealed that noise sources located in the region $x > 32r_o$ which were not captured in the current LES are expected to further reduce the shear noise for observation angles $\theta > 80°$. Hence, the actual shear noise spectrum at the

90° observation angle should have reduced spectral energy levels. Nevertheless, the current spectra comparison shows that the total noise is louder than both the shear noise and the self noise until about Strouhal number 2. For higher frequencies, the spectral energy level of the total noise spectrum comes in between the the shear noise and self noise spectral energy levels. This must be due to the slight cancellations taking place since figure 7.10 gives a correlation coefficient of about -0.05 between the shear and self noise components at the 90° observation angle. Once again, the entropy noise is very weak over the entire frequency range except in the low frequency region.

Finally, we look at the noise spectra at the 120° location which are given in figure 7.18. A very interesting observation is that the although the entropy noise is relatively weak in the frequency range where the Strouhal number is less than 2.5, it jumps up to a significant peak value at a frequency close to Strouhal number 4. The total noise spectrum also forms a secondary peak at a frequency in between Strouhal number 3.5 and 4. The self noise spectrum has lower spectral energy levels than the total noise spectrum at all frequencies and it also forms a secondary peak in between Strouhal number 3.5 and 4. The shear noise spectrum, on the other hand, has greater spectral energy levels than the total noise spectrum over some of the frequency range. It exhibits a drop in the spectral energy from the primary peak until Strouhal number 3.5, and then it seems to be leveling off. It is perhaps moving towards a secondary peak that is located at a frequency greater than Strouhal number 4. The shear noise and the self noise cancel each other at the 120° location with a correlation coefficient of about -0.3 that can be seen from figure 7.10. The reader is again reminded here that the actual shear noise spectrum at this observation location should have reduced spectral energy levels due to the sound sources located in the region $x > 32r_o$.

It seems appropriate at this point to compare the current far field noise spectra predictions with the results previously obtained by using the Ffowcs Williams - Hawkings method and also with some experimental noise spectra obtained from the NASA Glenn Research Center [92]. Experimental noise data from a Mach 0.85

cold jet will be shown in the comparisons. The Mach number of this jet is close enough to that of our simulated jet. The estimated Reynolds numbers of the experimental jet is approximately 1.2 million, while the ratio of the jet temperature to the ambient temperature is 0.88. The far field noise spectra of the experimental jet were obtained at 40 jet diameters away from the nozzle. In order to facilitate the comparison with numerical results, the experimental noise spectra were shifted to 30 jet diameters away from the nozzle using the $1/r$ decay assumption of the acoustic waves. In this adjustment, the experimental SPL values were shifted upwards by approximately 2.5 dB/St. Moreover, since the Mach number of the experimental jet was not exactly 0.9, the experimental noise spectra were also adjusted for Mach 0.9 following the SAE ARP 876C guidelines [84]. The spectra obtained from the previous Reynolds number 100,000 jet simulation presented in Chapter 5 will also be included in the comparisons. Figures 7.19 through 7.21 make comparisons at the observation locations of 30°, 60° and 90°, respectively. All spectra shown in these figures are curve fits to the actual data. The Ffowcs Williams - Hawkings method results for the Reynolds number 400,000 jet are shown both for the open and closed control surfaces. The reader is reminded here that the open control surface extends until $x = 31r_o$ and the outflow surface which closes the control surface is placed at the $x = 31r_o$ location, whereas the Lighthill volume integral was performed until the $x = 32r_o$ downstream location. The slight difference in the streamwise extent of the surface and volume integrals is not expected to cause a significant difference in the comparisons. The Ffowcs Williams - Hawkings method results for the Reynolds number 100,000 jet were obtained using an open surface that extended $59r_o$ in the streamwise direction. At the 30° location, we see that the closed surface FWH method prediction for the Reynolds number 400,000 jet is in fairly good agreement with Lighthill's acoustic analogy until Strouhal number 2 or so. Then, we observe higher spectral energy levels in Lighthill's acoustic analogy prediction for higher frequencies. The open surface FWH method prediction for the Reynolds number 400,000 jet, on the other hand, shows lower spectral energy levels at all frequencies.

This is due to the fact that the relatively short open control surface cannot effectively capture the acoustic waves travelling at the shallow angles. It is interesting to note that the agreement of the shape of the Reynolds number 100,000 jet noise spectrum with the experimental spectrum until Strouhal number 1 is better than that between the Reynolds number 400,000 jet noise spectra and the experiment. The reason for this is believed to be the fact that the larger domain in the Reynolds number 100,000 LES allows a better evaluation of the lower frequencies. For the Reynolds number 400,000 jet, the Lighthill prediction seems to be showing the best qualitative agreement with the experimental noise spectrum at this observation location. The peaks of all noise spectra in the figure are seen to be in the Strouhal number 0.25 - 0.3 range. However, the experimental spectrum exhibits a much stronger decay right after the peak. The decay rate of the spectrum obtained from Lighthill's acoustic analogy seems to be similar to the experimental spectrum decay rate in the frequency range where $1.5 < St < 3.0$. Then, the Lighthill spectrum decays with a faster rate for the higher frequencies. At the 60° location, for the Reynolds number 400,000 jet, the FWH method yields almost identical results for the open and the closed control surfaces. The Lighthill prediction is also in acceptable agreement with the FWH prediction, considering the fact that the two methods are based on completely different formulations. The comparison with the experimental noise spectrum at this observation location reveals that the experimental peak is located at a lower frequency than that of the numerical predictions. Furthermore, the numerical results for the Reynolds number 400,000 jet show a faster spectrum decay rate at the higher frequencies. The decay of the Reynolds number 100,000 jet spectrum after the peak takes place at a faster rate than that observed in the Reynolds number 400,000 jet spectra as well as in the experiment. Finally, the comparison at the 90° location shows that the closed surface FWH prediction gives increased spectral energy levels relative to those given by the open surface FWH prediction. The Lighthill prediction is seen to be in between the two predictions given by the FWH method. It should be reminded here once again that from our previous analysis, the spectra of

the Reynolds number 400,000 jet for observation angles in the range $\theta > 80^\circ$ are expected to be affected by the noise sources located in the far downstream region where $x > 32r_o$ which were not captured in the current LES due to the short domain size. The numerical predictions at this observation location once again reveal a spectrum decay rate that is larger than that of the experimental noise spectra. The decay of the the Reynolds number 100,000 jet spectrum takes place at a faster rate than that of the Reynolds number 400,000 jet spectra. The experimental peak is again located at a lower frequency than that of the numerical predictions. The comparison of the numerical OASPL predictions against the OASPL values of the NASA Mach 0.85 cold jet along the far field arc is plotted in figure 7.22. We see OASPL differences as high as 6 dB between the numerical predictions and the experimental measurements.

The differences observed between the numerical and experimental noise spectra might be due to various reasons. One reason could be the mismatch of the inflow conditions in the numerical simulations with those in the actual experiment. The experiment was performed at a high enough Reynolds number so that the jet shear layers at the nozzle exit were fully turbulent. In the numerical simulations, since it was deemed computationally too expensive to include the nozzle geometry, laminar shear layers were fed into the domain and randomized velocity fluctuations in the form of a vortex ring were imposed into the jet shear layers. Moreover, it has been observed experimentally [93], [94] that high-frequency sources are located a small distance downstream of the jet nozzle and a significant portion of the noise spectrum originates from this near field of the jet. Hence, the high-frequency noise generated in the near-nozzle jet shear layer within a few diameters downstream of the nozzle exit is missing in the current simulations. The absence of the noise generated just downstream of the nozzle could be responsible for the faster decay rates in the high frequency range of the spectra in the current computations. The present findings once again emphasize the importance of correctly modelling the inflow conditions in jet noise simulations. It is also believed that the limited domain size in the simulations might influence the low frequencies.

The Ffowcs Williams - Hawkings code was validated in earlier studies by comparing the FWH predictions with the direct LES data. The good agreement between the Lighthill and the Ffowcs Williams - Hawkings predictions shown in this section provides validation of the Lighthill code.

Finally, we will make a comparison of the computing times needed for Lighthill's acoustic analogy and for the Ffowcs Williams - Hawkings method. Lighthill's acoustic analogy required about 15 hours of run time on 1160 processors of the *Lemieux* cluster at the Pittsburgh Supercomputing Center to compute the 3072-point time history of acoustic pressure at a total of 112 far field points. In comparison, for the closed control surface computations, the Ffowcs Williams - Hawkings method required about 59 hours of run time on 136 POWER3 processors of an IBM-SP3 to compute the 4096-point time history of acoustic pressure at a total of 504 far field points. The Ffowcs Williams - Hawkings method would require 44 hours to compute the 3072-point time history of acoustic pressure at 504 far field points. The total number of CPU hours needed by Lighthill's acoustic analogy to compute the 3072-point history at 112 far field points is 17,400. On the other hand, the total number of CPU hours needed by the Ffowcs Williams - Hawkings method to compute the 3072-point history at 504 far field points is close to 6,000. The total number of CPU hours needed by the Ffowcs Williams - Hawkings method for 112 far field points would be about 1,333. Considering the fact that the Ffowcs Williams - Hawkings code was run on an IBM-SP3 platform that is about 3 times slower than *Lemieux*, we see that the Ffowcs Williams - Hawkings code would require about 444 CPU hours total for 112 far field points if it was run on *Lemieux*. Based on these timings on *Lemieux*, the ratio of the CPU hours needed for Lighthill's acoustic analogy to that need for the Ffowcs Williams - Hawkings method turns out to be almost 40/1. This means that Lighthill's acoustic analogy is 40 times more computationally expensive than the Ffowcs Williams - Hawkings method.

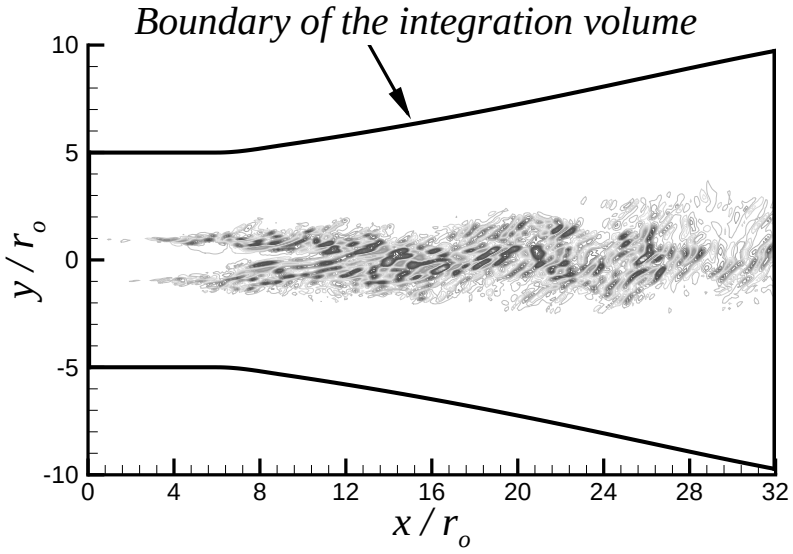

Figure 7.1. Instantaneous distribution of the Lighthill sources that radiate noise in the direction of the observer at $R = 60r_o$, $\theta = 30°$ on the far field arc.

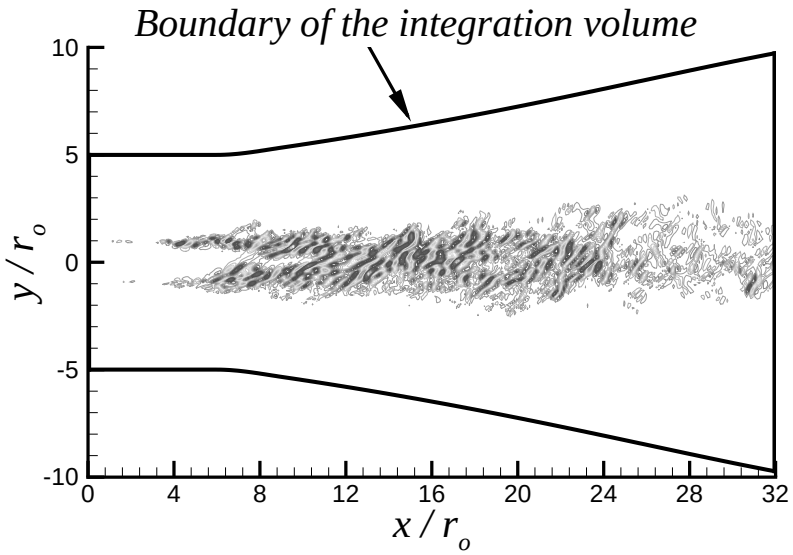

Figure 7.2. Instantaneous distribution of the Lighthill sources that radiate noise in the direction of the observer at $R = 60r_o$, $\theta = 60°$ on the far field arc.

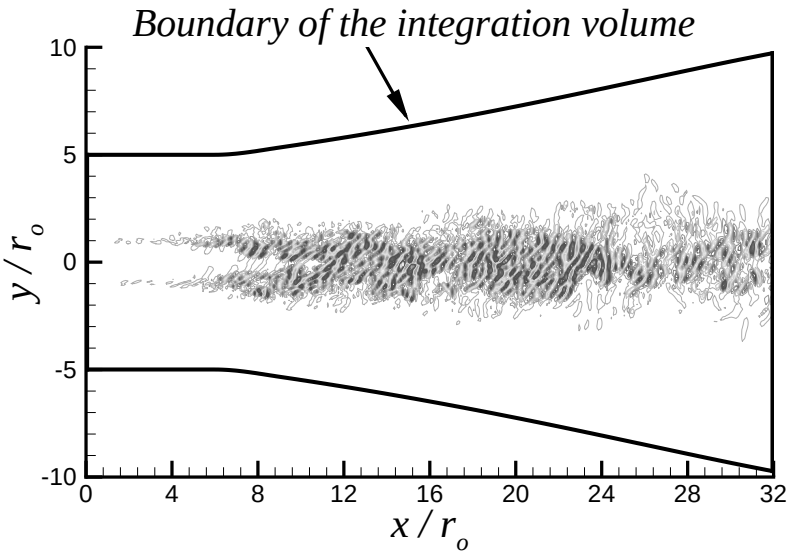

Figure 7.3. Instantaneous distribution of the Lighthill sources that radiate noise in the direction of the observer at $R = 60r_o$, $\theta = 90°$ on the far field arc.

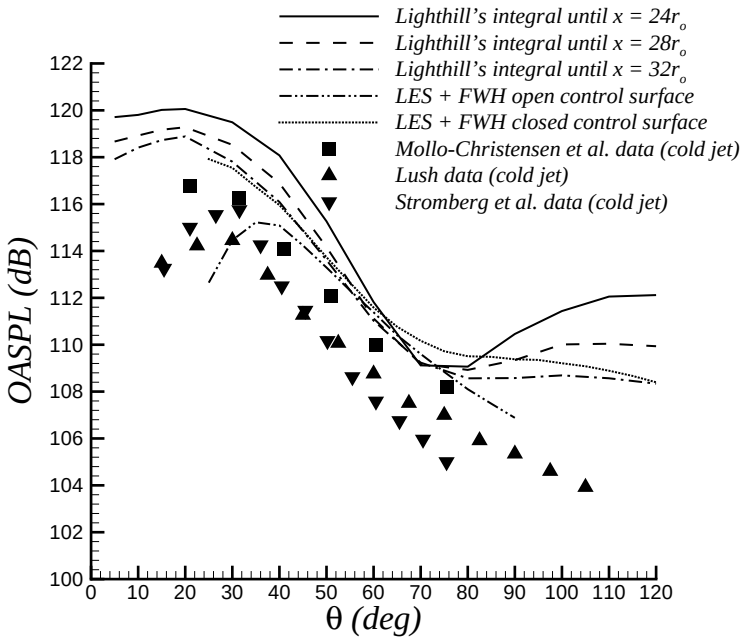

Figure 7.4. Overall sound pressure levels of the noise from T_{ij} along the far field arc.

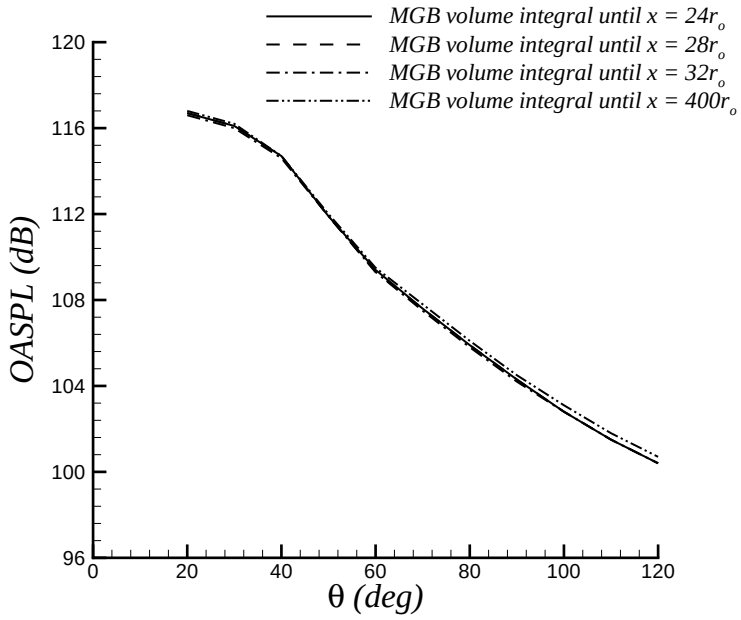

Figure 7.5. MGB method [91] prediction of the overall sound pressure levels along the far field arc.

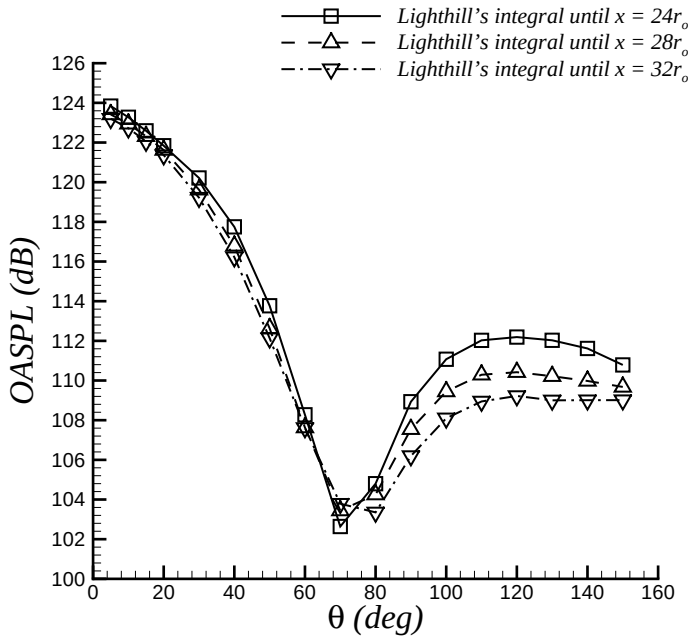

Figure 7.6. Overall sound pressure levels of the shear noise from T_{ij}^{l} along the far field arc.

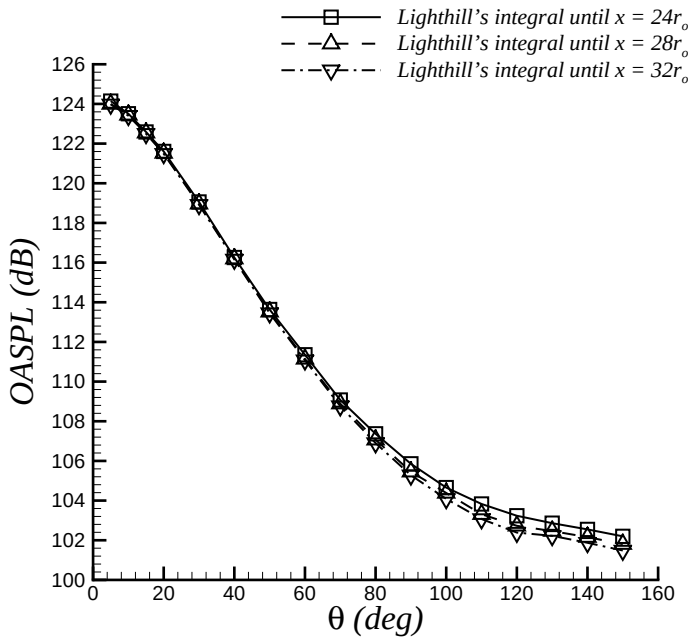

Figure 7.7. Overall sound pressure levels of the self noise from T_{ij}^{n} along the far field arc.

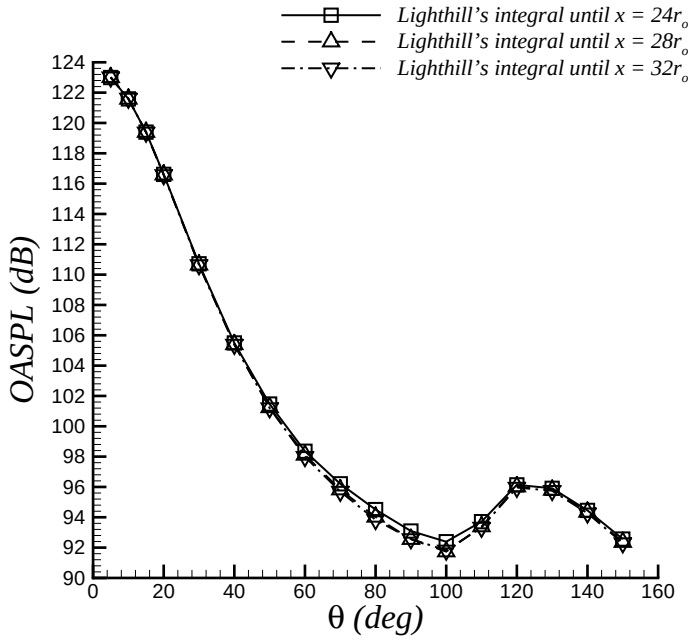

Figure 7.8. Overall sound pressure levels of the entropy noise from T_{ij}^{s} along the far field arc.

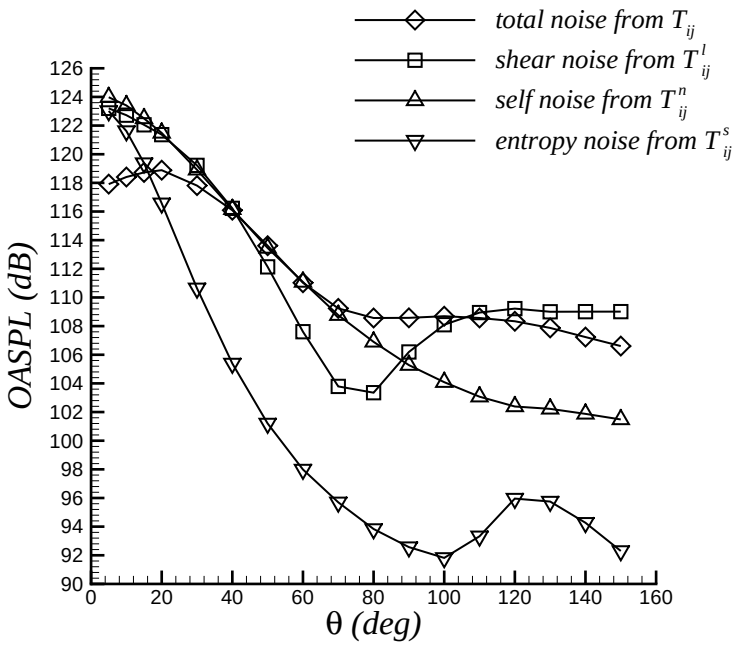

Figure 7.9. Overall sound pressure levels of the noise from T_{ij} and its components along the far field arc. (Volume integrals are performed until $x = 32r_o$.)

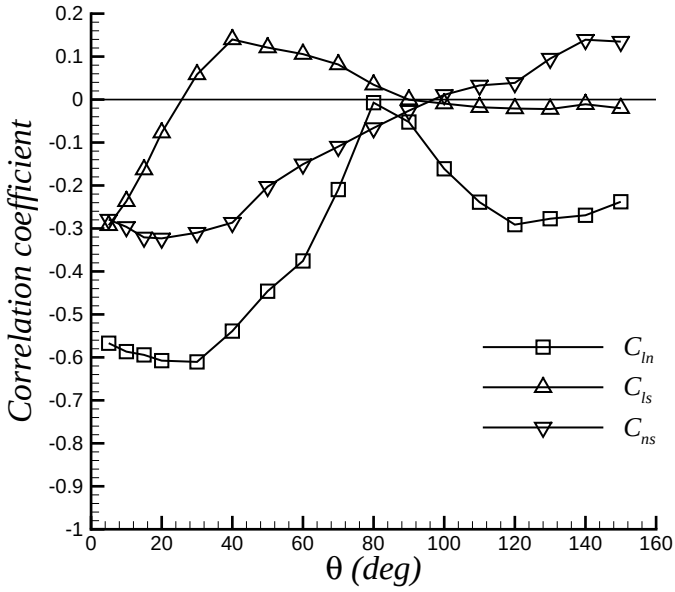

Figure 7.10. Variation of the correlation coefficients along the far field arc.

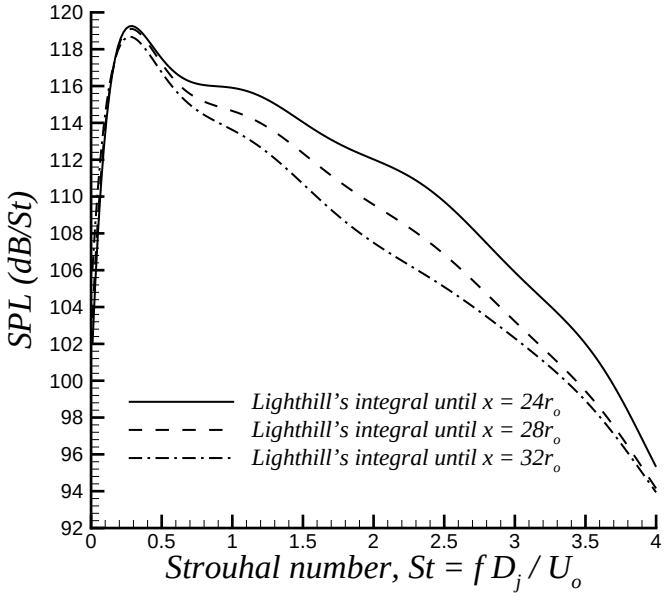

Figure 7.11. Spectra of the noise from T_{ij} at the $R = 60r_o$, $\theta = 30°$ location on the far field arc.

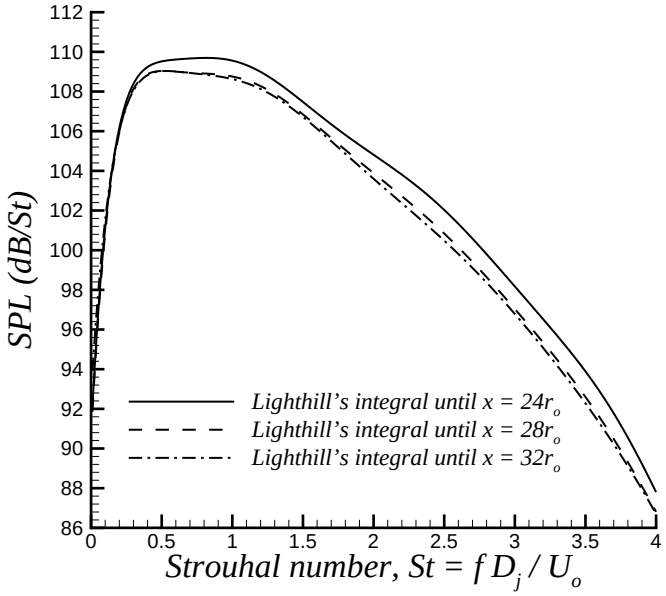

Figure 7.12. Spectra of the noise from T_{ij} at the $R = 60r_o$, $\theta = 60°$ location on the far field arc.

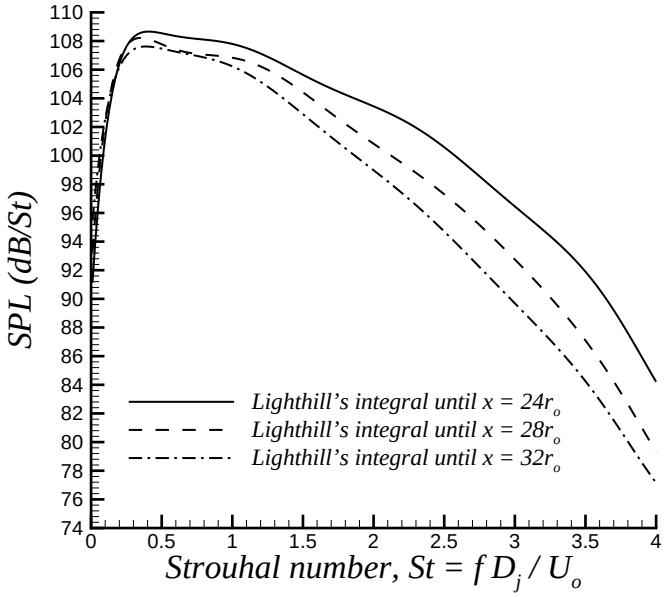

Figure 7.13. Spectra of the noise from T_{ij} at the $R = 60r_o$, $\theta = 90°$ location on the far field arc.

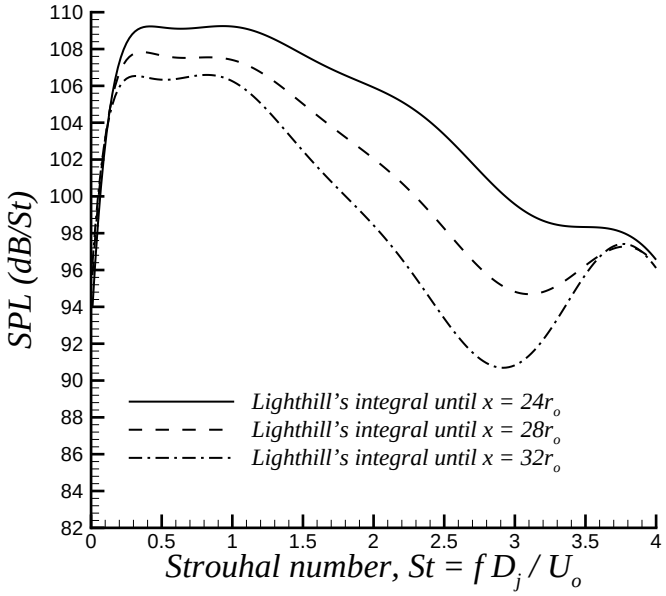

Figure 7.14. Spectra of the noise from T_{ij} at the $R = 60r_o$, $\theta = 120°$ location on the far field arc.

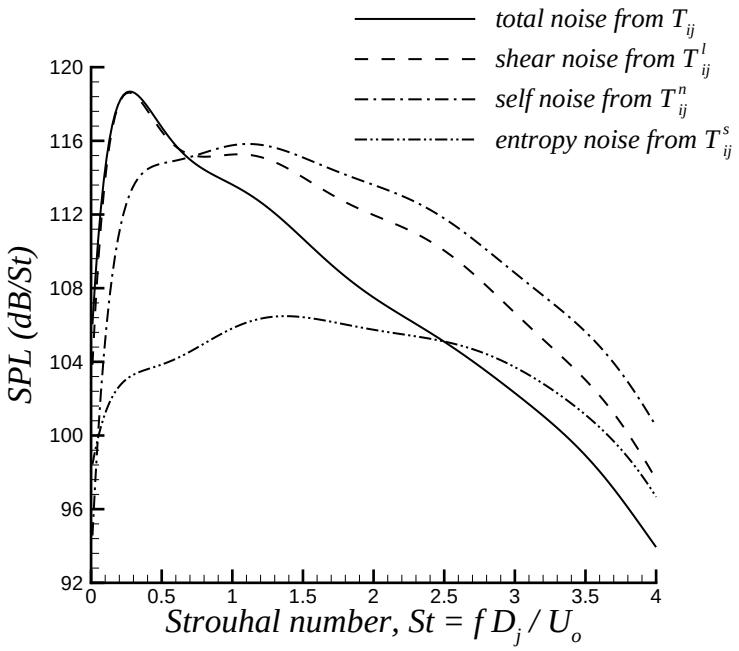

Figure 7.15. Spectra of the noise from T_{ij} and its components at the $R = 60r_o$, $\theta = 30^\circ$ location on the far field arc.

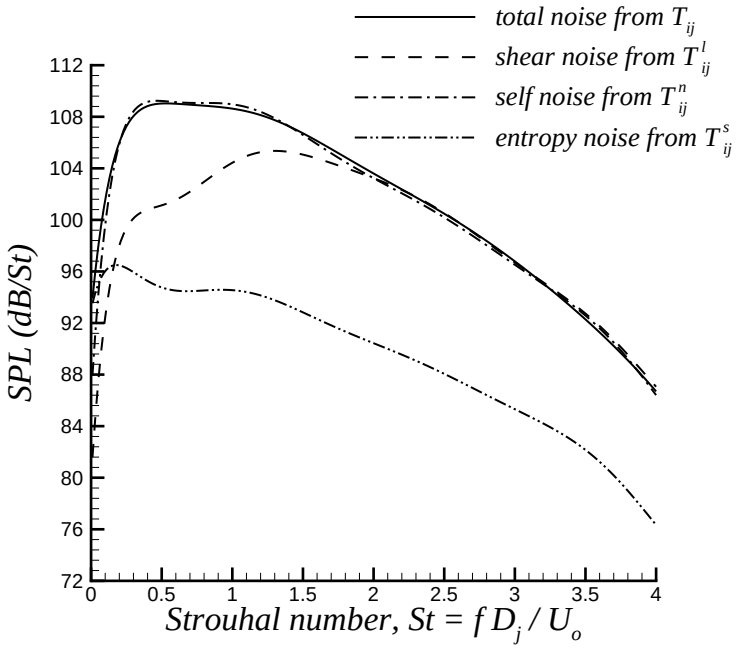

Figure 7.16. Spectra of the noise from T_{ij} and its components at the $R = 60r_o$, $\theta = 60^\circ$ location on the far field arc.

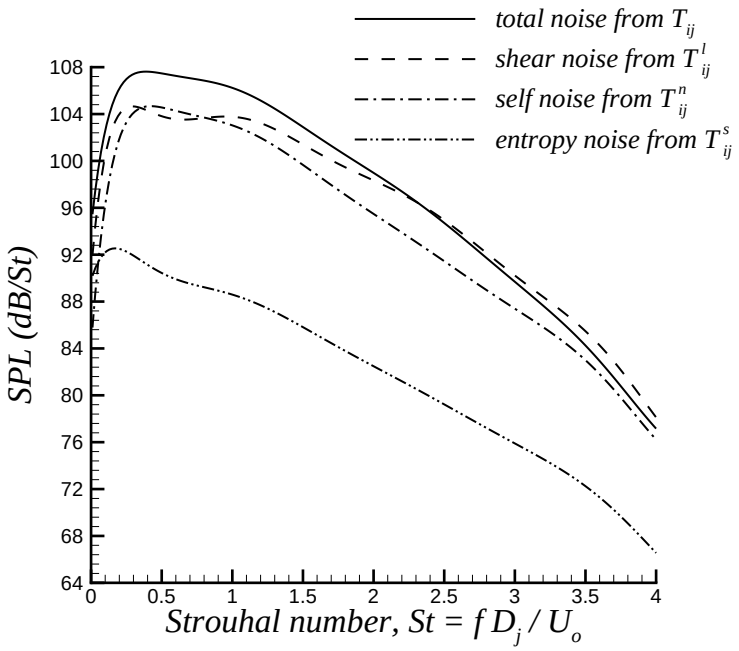

Figure 7.17. Spectra of the noise from T_{ij} and its components at the $R = 60r_o$, $\theta = 90°$ location on the far field arc.

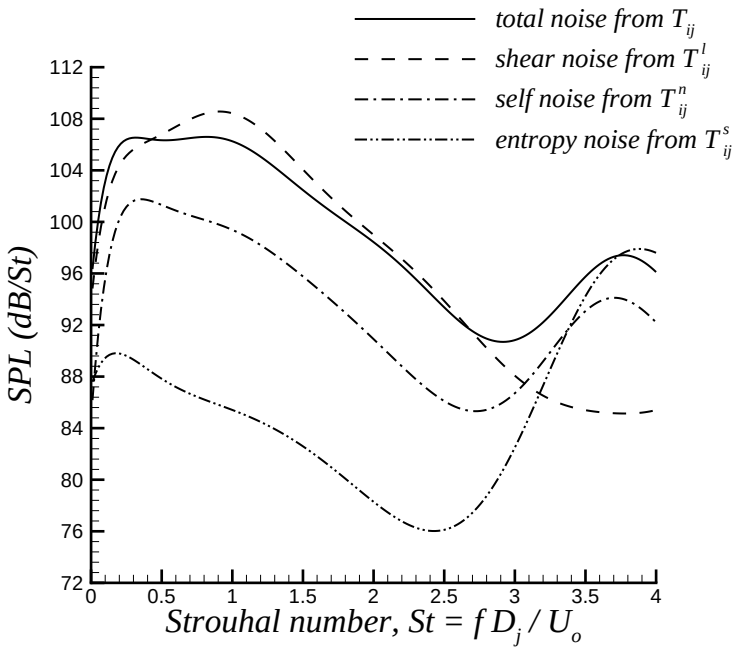

Figure 7.18. Spectra of the noise from T_{ij} and its components at the $R = 60r_o$, $\theta = 120°$ location on the far field arc.

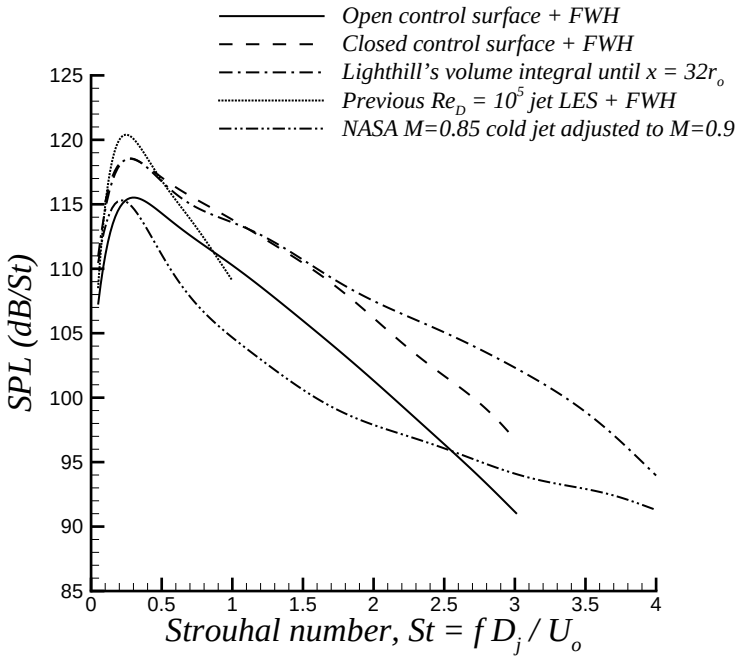

Figure 7.19. Acoustic pressure spectra comparisons at the $R = 60r_o$, $\theta = 30°$ location on the far field arc.

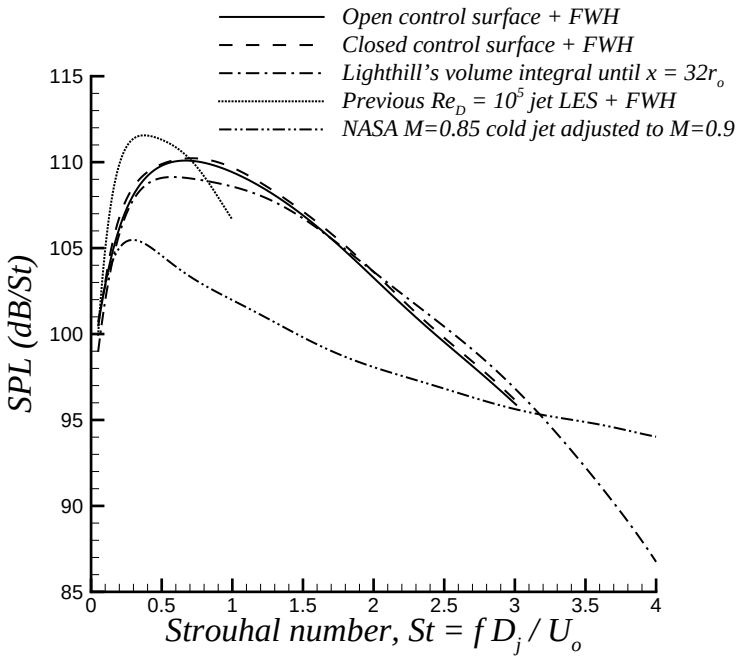

Figure 7.20. Acoustic pressure spectra comparisons at the $R = 60r_o$, $\theta = 60°$ location on the far field arc.

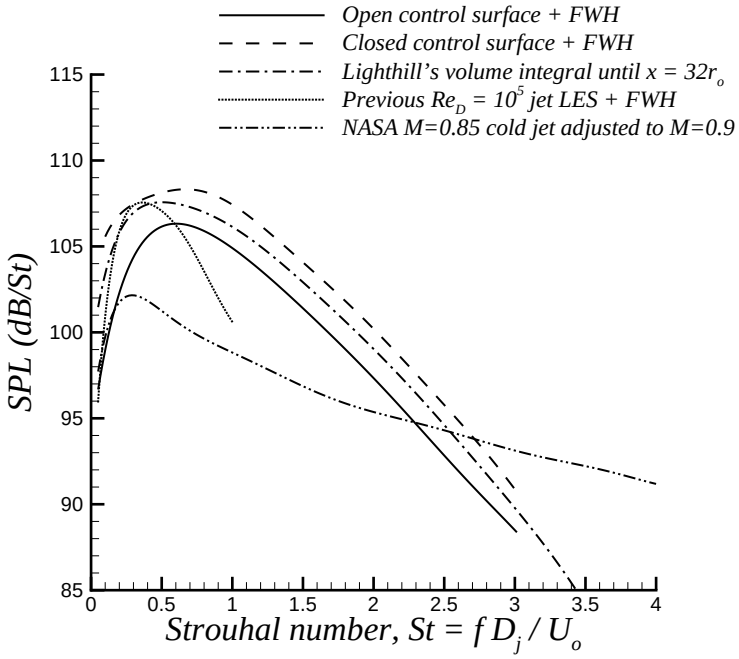

Figure 7.21. Acoustic pressure spectra comparisons at the $R = 60r_o$, $\theta = 90°$ location on the far field arc.

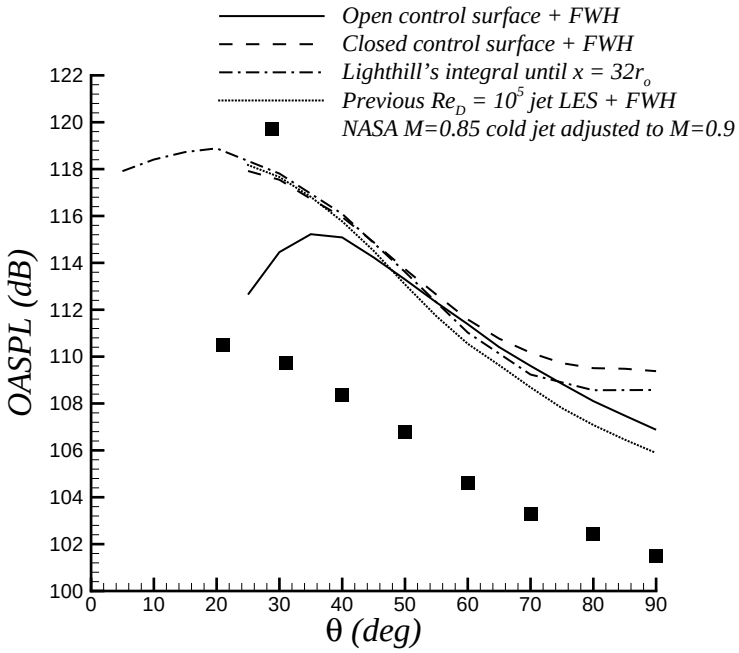

Figure 7.22. Overall sound pressure levels along the far field arc.

8. CONCLUSIONS AND RECOMMENDATIONS FOR FUTURE WORK

8.1 Conclusions

Using state-of-the-art numerical techniques, we have developed and tested a Computational Aeroacoustics (CAA) methodology for jet noise prediction. The CAA methodology has two main components. The first one is a 3-D Large Eddy Simulation (LES) code. The latest version of the LES code employs high-order accurate compact finite differencing as well as implicit spatial filtering schemes together with Tam and Dong's boundary conditions on the LES domain boundaries. Explicit time integration is accomplished by means of the standard 4^{th}-order, 4-stage Runge-Kutta method. The localized dynamic Smagorinsky subgrid-scale model is utilized to model the effect of the unresolved scales on the resolved scales. The code also has the capability to turn off the dynamic SGS model and perform simulations by treating the spatial filter as an implicit SGS model. The second component of the CAA methodology consists of integral acoustics methods. We have developed acoustics codes that employ Kirchhoff's and Ffowcs Williams - Hawkings methods as well as Lighthill's acoustic analogy.

We performed turbulence simulations of various jet flows on grids consisting up to 16 million grid points. Jet mean flow, turbulence statistics and jet aeroacoustics results were presented. The Reynolds numbers of the jets simulated in this study ranged from as low as 3,600 up to as high as 400,000. The initial simulations performed with the constant-coefficient SGS model showed the strong sensitivity of the mean flow results to the choice of the model constant. To overcome the limitations of the constant-coefficient SGS model, we implemented a localized dynamic SGS model into the LES code. The mean flow and various turbulence statistics results

compared reasonably well with the available experimental data of jets at similar flow conditions. The time accurate LES data were coupled with integral acoustics methods for far field noise calculations. Far field aeroacoustics results also compared favorably with existing experimental measurements. However, it was shown that the inflow forcing had a significant impact on the far field noise estimations. The effect of the Smagorinsky SGS model on the far field noise is also important. It appears that the eddy viscosity of the SGS model reduces the amplitude of the resolved scale high-frequency acoustic waves. So it seems like the issues of inflow forcing and SGS model effects on the jet noise need to resolved first through further studies before jet LES calculations can be used with full confidence to obtain reliable noise predictions. Comparison of the noise spectra of the Reynolds number 100,000 and 400,000 jets shows that the noise spectra of the higher Reynolds number jet decay slower. The growth of the Reynolds stresses with increasing downstream distance also seems to be dependent on the jet Reynolds number. This suggests that the start of the self-similarity region also depends on the jet Reynolds number. In our Reynolds number 400,000 jet simulations, the highest noise frequency resolved in the surface integral acoustics calculations corresponded to Strouhal number 3, while the highest frequency resolved when Lighthill's acoustic analogy was employed corresponded to Strouhal number 4. Both of these frequencies are larger than Bogey and Bailly's cut-off frequency of Strouhal number 2 in their recent Reynolds number 400,000 jet LES [33], [34], [35]. Hence, to our best knowledge, the LES and the noise computations done for the Reynolds number 400,000 jet in this study are certainly some of the biggest calculations ever done in jet noise research. Moreover, our noise computations for the Reynolds number 400,000 jet have cut-off frequencies which are greater than the cut-off frequencies of all other jet noise LES results in the literature to date. Use of integral acoustics methods allows clustering of the majority of the grid points inside the jet flow where non-linear noise generation takes place and rapid grid stretching outside the jet. Consequently, the maximum frequency resolved in noise computations using integral acoustics methods is higher compared

to that captured in the simulations (with similar number of grid points) in which only the near field jet noise is computed using direct LES data. Finally, to the best of our knowledge, computation of the Lighthill volume integral over the turbulent near field of a turbulent jet at a reasonably high Reynolds number has been carried out for the first time in this study. The Lighthill stress tensor was decomposed into several components and the noise generated by the individual components was analyzed in detail. It appears that a streamwise domain longer than $32r_o$ is needed to enclose the most significant acoustic sources. Far field noise predictions using the FWH method on the closed control surface were found be comparable to those given by Lighthill's volume integral. Hence, it is preferable to use the relatively cheaper FWH method over the very expensive Lighthill volume integral if one's sole purpose is to predict the far field noise. However, if a connection between the near field jet turbulence and the far field noise is sought, then an analysis of the Lighthill source term inside the jet would be very useful. Both Ffowcs Williams - Hawkings (applied on a closed control surface) and Lighthill's methods show increased OASPL levels for observation angles greater than 80° on the far field arc. Such spurious effects are believed to be due to the spurious line of dipoles appearing on the outflow surface and the relatively short domain size in the streamwise direction.

8.2 Recommendations for Future Work

8.2.1 Improved Inflow Forcing and Near Nozzle Simulations

As mentioned in the Conclusions section, the simulations revealed the importance of correctly modelling the inflow conditions. To get better agreement with experimental measurements, an improved modelling of the inflow forcing is needed. More rigorous mathematical models of the inflow conditions may be developed for this purpose. However, this may be a challenging task. Recently, Glaze and Frankel [95] studied the behaviors of two different stochastic inlet conditions which are intended to simulate a turbulent inflow for a round jet. They tested a Gaussian random forcing

technique as the baseline case, and a version of the weighted amplitude wave superposition spectral representation method as an improved technique. They found that the Gaussian random inlet fluctuations model turbulent inflow poorly and dissipate almost immediately, whereas the spectral inlet fluctuations reproduce the jet near field much more accurately and allow the flow to transition rapidly to self-sustaining turbulence. The spectral inlet fluctuations studied by Glaze and Frankel [95] can be implemented into the present LES code and new simulations can be performed with this new inflow forcing technique. Another alternative could be to include the actual nozzle geometry in the computations so as to get away from the artificial inflow forcing. In this way, the turbulent shear layers at the nozzle lip could be directly computed as part of the LES. Including the actual nozzle in the computations, on the other hand, will definitely make the LES calculations more challenging and more expensive. However, with the technological advances rapidly taking place in the computer industry, the computing power needed for these kind of computations may be available to researchers in less than a decade.

Another interesting aspect of jet noise research is the high-frequency noise generated in the near-nozzle jet shear layer within a few diameters downstream of the nozzle exit [96]. It has been observed experimentally [93], [94] that a significant portion of the noise spectrum originates from this near field of the jet (before the end of the jet potential core) where high-frequency sources are located. Experimental observations [94], [97] suggest the possibility of a dipole type noise source associated with the vortex-solid body interaction due to the presence of the nozzle. The connection between the flow dynamics and the noise generation in this region is poorly understood and needs to be investigated further. The conclusions drawn from the experimental studies of Narayanan *et al.* [94] indeed justify the need for computations of the near jet flowfield where high-frequency noise sources are known to dominate. However, the usual practice in LES calculations to date has been to neglect the nozzle geometry and hence the acoustically significant region just downstream of the nozzle. This is due to the obvious reason that it is computationally too

expensive to include the actual nozzle in the computations. Laminar shear layers are usually fed into the simulations and randomized perturbations are introduced into the jet shear layers to mimic the actual jet shear layer conditions. Freund and Lele [96], on the other hand, estimate that 150 - 200 million grid points are needed in a high Reynolds number jet flow LES to accurately resolve the acoustically significant region near the nozzle. The existing single-block LES/DNS code could be to extended to a multi-block version which can be used for performing such simulations. In the multi-block implementation, a complex domain can be broken up into several relatively simple domains and the already existing high-order accurate single-block code could be easily used in each of the simpler domains simultaneously. Grid point overlaps will be required to exchange data between adjacent sub-domains during the course of the computations. A similar multi-block approach was followed by Yao *et al.* [98] to do a DNS for a turbulent flow over a rectangular trailing edge. Multi-domain implementation strategies similar to those studied by Gaitonde and Visbal [99] as well as Zhang *et al.* [100] can be utilized while developing the multi-block version of the code. The main goal in these simulations should be to analyze the acoustically significant near-nozzle jet shear layer in great detail. For example, the vortex-solid body interaction process which is suspected to be one of the primary sources of the near-nozzle high-frequency noise generation can be investigated through numerical simulations. Although an LES on a grid of 200 million points may seem too expensive on present day supercomputers, LES computations on grids consisting of 300 million grid points are already being performed for wind turbine noise predictions on the Japanese Earth Simulator machine at the time of this writing [101]. Hence, high fidelity jet noise computations are very likely to take place in the near future once supercomputers as powerful as the Japanese Earth Simulator become available to the research community within the US. As an intermediate step, perhaps a calculation with a smaller domain, but including the nozzle lips using 50 - 80 million grid points should be attempted first.

8.2.2 Acoustically Aware SGS Model

Improved SGS models need to be developed and implemented into LES calculations so as to get away from the undesired effects of the eddy viscosity on the noise predictions. In other words, acoustically aware SGS models that do not affect the already well-resolved portions of the noise spectra and that do not create spurious noise need to be implemented into LES calculations. Filtering only without employing an explicit SGS model already seems to be a promising acoustically aware implicit SGS model. The filtering operation only removes the energy pile-up at the very high wavenumbers without affecting the well-resolved scales. However, more studies in this area need to be done and comparisons with well documented experimental jet noise spectra need to be performed to ensure the validity of the noise predictions from LES that do filtering only without an SGS model. Good agreement with experimental noise spectra, as mentioned earlier, will also demand inflow conditions for LES that are as close as possible to the actual experimental nozzle exit conditions.

8.2.3 Noise Model for Predicting High Frequency Noise of Unresolved Scales

We were able to compute only a portion of the noise spectra in our LES calculations. The cutoff frequency was determined by the grid resolution. A model for predicting the high frequency noise of the unresolved scales would be very attractive. As mentioned in the Introduction section of this report, even though there has been some efforts on the investigation of the contribution of small-scales to the noise spectrum [9], [10], [11], [12], [13], none of the LES studies in the literature so far have predicted the high-frequency noise associated with the unresolved scales. More research in this area that will lead to the development of subgrid-scale acoustic models is needed.

8.2.4 Spectral Makeup of the Lighthill Stress Tensor

It may be interesting to look into the wavenumber-frequency makeup of the Lighthill stress tensor in order to gain some insight into the physics of jet noise generation. Furthermore, the radiating and the non-radiating components of the Lighthill stress tensor can be analyzed in detail. Due to time constraints, we were unable to perform such analyses in this study. Data needed for such an analysis are already available from our Reynolds number 400,000 jet LES. However, since the current LES data were saved on a curvilinear grid and since the cylindrical coordinate system is more suitable to analyze a round jet, it will be necessary to interpolate the current data onto a cylindrical grid first. Such an interpolation could be computationally expensive since our current data set is 1.2 Terabytes in size. However, the interpolation should be feasible on a modern parallel computing platform. Once the interpolation process is complete, Fourier transform techniques similar to those used by Freund [2] could be used to analyze the spectral makeup of the Lighthill stress tensor and to identify components capable of radiating to the far field.

LIST OF REFERENCES

LIST OF REFERENCES

[1] J. B. Freund, S. K. Lele, and P. Moin. Direct numerical simulation of a Mach 1.92 turbulent jet and its sound field. *AIAA Journal*, 38(11):2023–2031, November 2000.

[2] J. B. Freund. Noise sources in a low-Reynolds-number turbulent jet at Mach 0.9. *Journal of Fluid Mechanics*, 438:277–305, 2001.

[3] J. L. Stromberg, D. K. McLaughlin, and T. R. Troutt. Flow field and acoustic properties of a Mach number 0.9 jet at a low Reynolds number. *Journal of Sound and Vibration*, 72(2):159–176, 1980.

[4] A. Khavaran, E. A. Krejsa, and C. M. Kim. Computation of supersonic jet mixing noise for an axisymmetric convergent-divergent nozzle. *Journal of Aircraft*, 31(3):603–609, May-June 1994.

[5] A. Khavaran. Role of anisotropy in turbulent mixing noise. *AIAA Journal*, 37(7):832–841, July 1999.

[6] L. D. Koch, J. Bridges, and A. Khavaran. Flow field comparisons from three Navier-Stokes solvers for an axisymmetric separate flow jet. AIAA Paper 2002-0672, January 2002.

[7] R. H. Self and A. Bassetti. A RANS based jet noise prediction scheme. AIAA Paper 2003-3325, May 2003.

[8] C. A. Hunter and R. H. Thomas. Development of a jet noise prediction method for installed jet configurations. AIAA Paper 2003-3169, May 2003.

[9] U. Piomelli, C. L. Streett, and S. Sarkar. On the computation of sound by large-eddy simulations. *Journal of Engineering Mathematics*, 32:217–236, 1997.

[10] R. Rubinstein and Y. Zhou. Characterization of sound radiation by unresolved scales of motion in computational aeroacoustics. Technical Report NASA/CR-1999-209688, ICASE Report No. 99-39, ICASE, NASA Langley Research Center, October 1999.

[11] C. Seror, P. Sagaut, C. Bailly, and D. Juvé. On the radiated noise computed by large-eddy simulation. *Physics of Fluids*, 13(2):476–487, February 2001.

[12] W. Zhao, S. H. Frankel, and L. Mongeau. Effects of spatial filtering on sound radiation from a subsonic axisymmetric jet. *AIAA Journal*, 38(11):2032–2039, November 2000.

[13] D. J. Bodony and S. K. Lele. A statistical subgrid scale noise model: Formulation. AIAA Paper 2003-3252, May 2003.

[14] R. R. Mankbadi, M. E. Hayder, and L. A. Povinelli. Structure of supersonic jet flow and its radiated sound. *AIAA Journal*, 32(5):897–906, May 1994.

[15] M. J. Lighthill. On sound generated aerodynamically: I. General theory. *Proceedings of the Royal Society of London, Series A: Mathematical and Physical Sciences*, 211(1107):564–587, 1952.

[16] A. S. Lyrintzis and R. R. Mankbadi. Prediction of the far-field jet noise using Kirchhoff's formulation. *AIAA Journal*, 1(2):1–4, 1996.

[17] G. R. Kirchhoff. Zur theorie der lichtstrahlen. *Annalen der Physik und Chemie*, 18:663–695, 1883.

[18] L. Gamet and J. L. Estivalezes. Application of large-eddy simulations and Kirchhoff method to jet noise prediction. *AIAA Journal*, 36(12):2170–2178, December 1998.

[19] D. Choi, T. J. Barber, L. M. Chiappetta, and M. Nishimura. Large eddy simulation of high-Reynolds number jet flows. AIAA Paper 99-0230, January 1999.

[20] W. Zhao, S. H. Frankel, and L. Mongeau. Large eddy simulations of sound radiation from subsonic turbulent jets. *AIAA Journal*, 39(8):1469–1477, August 2001.

[21] P. J. Morris, Q. Wang, L. N. Long, and D. P. Lockhard. Numerical predictions of high speed jet noise. AIAA Paper 97-1598, May 1997.

[22] P. J. Morris, L. N. Long, A. Bangalore, and Q. Wang. A parallel three-dimensional computational aeroacoustics method using nonlinear disturbance equations. *Journal of Computational Physics*, 133:56–74, 1997.

[23] P. J. Morris, L. N. Long, T. E. Scheidegger, Q. Wang, and A. R. Pilon. High speed jet noise simulations. AIAA Paper 98-2290, 1998.

[24] P. J. Morris, L. N. Long, and T. Scheidegger. Parallel computations of high speed jet noise. AIAA Paper 99-1873, 1999.

[25] P. J. Morris, T. E. Scheidegger, and L. N. Long. Jet noise simulations for circular nozzles. AIAA Paper 2000-2080, June 2000.

[26] S. Boluriaan, P. J. Morris, L. N. Long, and T. Scheidegger. High speed jet noise simulations for noncircular nozzles. AIAA Paper 2001-2272, May 2001.

[27] T. S. Chyczewski and L. N. Long. Numerical prediction of the noise produced by a perfectly expanded rectangular jet. AIAA Paper 96-1730, May 1996.

[28] B. J. Boersma and S. K. Lele. Large eddy simulation of a Mach 0.9 turbulent jet. AIAA Paper 99-1874, May 1999.

[29] C. Bogey, C. Bailly, and D. Juvé. Computation of the sound radiated by a 3-D jet using large eddy simulation. AIAA Paper 2000-2009, June 2000.

[30] G. S. Constantinescu and S. K. Lele. Large eddy simulation of a near sonic turbulent jet and its radiated noise. AIAA Paper 2001-0376, January 2001.

[31] J. R. DeBonis and J. N. Scott. Large-eddy simulation of a turbulent compressible round jet. *AIAA Journal*, 40(7):1346–1354, 2002.

[32] D. J. Bodony and S. K. Lele. Influence of inlet conditions on the radiated noise of high speed turbulent jets. International workshop on "LES for Acoustics", DLR Göttingen, Germany, October 2002.

[33] C. Bogey and C. Bailly. Direct computation of the sound radiated by a high-Reynolds-number, subsonic round jet. CEAS Workshop *From CFD to CAA*, Athens, Greece, November 2002.

[34] C. Bogey and C. Bailly. LES of a high Reynolds, high subsonic jet : Effects of the inflow conditions on flow and noise. AIAA Paper 2003-3170, May 2003.

[35] C. Bogey and C. Bailly. LES of a high Reynolds, high subsonic jet : Effects of the subgrid modellings on flow and noise. AIAA Paper 2003-3557, June 2003.

[36] J. E. Ffowcs Williams and D. L. Hawkings. Sound generation by turbulence and surfaces in arbitrary motion. *Proceedings of the Royal Society of London, Series A: Mathematical and Physical Sciences*, 264(1151):321–342, 1969.

[37] D. G. Crighton, A. P. Dowling, J. E. Ffowcs Williams, M. Heckl, and F. G. Leppington. *Modern Methods in Analytical Acoustics: Lecture Notes*. Springer–Verlag, London, 1992.

[38] N. Curle. The influence of solid boundaries upon aerodynamical sound. *Proceedings of the Royal Society of London, Series A: Mathematical and Physical Sciences*, 231(1187):505–514, 1955.

[39] A. Uzun, G. A. Blaisdell, and A. S. Lyrintzis. Recent progress towards a large eddy simulation code for jet aeroacoustics. AIAA Paper 2002-2598, June 2002.

[40] A. Uzun, G. A. Blaisdell, and A. S. Lyrintzis. 3-D large eddy simulation for jet aeroacoustics. AIAA Paper 2003-3322, May 2003.

[41] A. Uzun, G. A. Blaisdell, and A. S. Lyrintzis. Sensitivity to the Smagorinsky constant in turbulent jet simulations. *AIAA Journal*, 41(10):2077–2079, October 2003.

[42] A. Uzun, G. A. Blaisdell, and A. S. Lyrintzis. Application of compact schemes to large eddy simulation of turbulent jets. Submitted to the *Journal of Scientific Computing*, 2003.

[43] A. Uzun, A. S. Lyrintzis, and G. A. Blaisdell. Coupling of integral acoustics methods with LES for jet noise prediction. AIAA Paper 2004-0517, to be presented at the 42^{nd} AIAA Aerospace Sciences Meeting and Exhibit, Reno, NV, January 2004.

[44] J. S. Smagorinsky. General circulation experiments with the primitive equations. *Monthly Weather Review*, 91(3):99–165, March 1963.

[45] M. Germano, U. Piomelli, P. Moin, and W. Cabot. A dynamic subgrid-scale eddy viscosity model. *Physics of Fluids A*, 3(7):1760–1765, July 1991.

[46] P. Moin, K. Squires, W. Cabot, and S. Lee. A dynamic subgrid-scale model for compressible turbulence and scalar transport. *Physics of Fluids A*, 3(11):2746–2757, November 1991.

[47] A. Yoshizawa. Statistical theory for compressible turbulent shear flows, with application to subgrid modeling. *Physics of Fluids*, 29(7):2152–2164, July 1986.

[48] C. Bogey and C. Bailly. A family of low dispersive and low dissipative explicit schemes for computing aerodynamic noise. AIAA Paper 2002-2509, June 2002.

[49] M. R. Visbal and D. V. Gaitonde. Very high-order spatially implicit schemes for computational acoustics on curvilinear meshes. *Journal of Computational Acoustics*, 9(4):1259–1286, 2001.

[50] S. K. Lele. Compact finite difference schemes with spectral-like resolution. *Journal of Computational Physics*, 103(1):16–42, November 1992.

[51] W. Zhao. *A Numerical Investigation of Sound Radiated from Subsonic Jets with Application to Human Phonation*. PhD thesis, School of Mechanical Engineering, Purdue University, West Lafayette, IN, June 2000.

[52] B. E. Mitchell, S. K. Lele, and P. Moin. Direct computation of the sound generated by subsonic and supersonic axisymmetric jets. Technical Report TF-66, Thermosciences Division, Department of Mechanical Engineering, Stanford University, Stanford, CA, November 1995.

[53] W. K. Thompson. Time-dependent boundary conditions for hyperbolic systems. *Journal of Computational Physics*, 68:1–24, January 1987.

[54] W. K. Thompson. Time-dependent boundary conditions for hyperbolic systems, II. *Journal of Computational Physics*, 89(1):439–461, August 1990.

[55] L. Jiang, H. Shan, C. Liu, and M. R. Visbal. Non-reflecting boundary conditions for DNS in curvilinear coordinates. In *Proceedings of the* 2^{nd} *AFOSR International Conference on DNS/LES*, pages 219–233, June 1999.

[56] C. K. W. Tam and Z. Dong. Radiation and outflow boundary conditions for direct computation of acoustic and flow disturbances in a nonuniform mean flow. *Journal of Computational Acoustics*, 4(2):175–201, 1996.

[57] C. Bogey and C. Bailly. Three-dimensional non-reflective boundary conditions for acoustic simulations: Far field formulation and validation test cases. *Acta Acustica*, 88(4):463–471, 2002.

[58] C. Bogey, C. Bailly, and D. Juvé. Noise investigation of a high subsonic, moderate Reynolds number jet using a compressible LES. *Theoretical and Computational Fluid Dynamics*, 16(4):273–297, 2003.

[59] T. Colonius, S. K. Lele, and P. Moin. Boundary conditions for direct computation of aerodynamic sound generation. *AIAA Journal*, 31(9):1574–1582, September 1993.

[60] A. S. Lyrintzis. From the near-field to the far-field: Integral acoustics methods. CEAS Workshop *From CFD to CAA*, Athens, Greece, November 2002.

[61] A. S. Lyrintzis and A. Uzun. Integral techniques for aeroacoustics calculations. AIAA Paper 2001-2253, May 2001.

[62] A. R. Pilon and A. S. Lyrintzis. Development of an improved Kirchhoff method for jet aeroacoustics. *AIAA Journal*, 36(5):783–790, May 1998.

[63] J. B. Freund, S. K. Lele, and P. Moin. Calculation of the radiated sound field using an open Kirchhoff surface. *AIAA Journal*, 34(5):909–916, May 1996.

[64] A. R. Pilon and A. S. Lyrintzis. Mean flow refraction corrections for the modified Kirchhoff method. *Journal of Aircraft*, 35(4):661–664, July-August 1998.

[65] K. S. Brentner and F. Farassat. Analytical comparison of the acoustic analogy and Kirchhoff formulation for moving surfaces. *AIAA Journal*, 36(8):1379–1386, August 1998.

[66] I. Wygnanski and H. Fiedler. The two-dimensional mixing region. *Journal of Fluid Mechanics*, 41(2):327–361, 1970.

[67] B. W. Spencer and B. G. Jones. Statistical investigation of pressure and velocity fields in the turbulent two-stream mixing layer. AIAA Paper 71-613, 1971.

[68] J. H. Bell and R. D. Mehta. Development of a two-stream mixing layer from tripped and untripped boundary layers. *AIAA Journal*, 28(12):2034–2042, December 1990.

[69] M. M. Rogers and R. D. Moser. Direct simulation of a self-similar turbulent mixing layer. *Physics of Fluids*, 6(2):903–923, February 1994.

[70] S. Stanley and S. Sarkar. Simulations of spatially developing two-dimensional shear layers and jets. *Theoretical and Computational Fluid Dynamics*, 9:121–147, 1997.

[71] C. Bogey. *Calcul Direct du Bruit Aérodynamique et Validation de Modèles Acoustiques Hybrides*. PhD thesis, Laboratoire de Mécanique des Fluides et d'Acoustique, École Centrale de Lyon, France, April 2000.

[72] S. B. Pope. *Turbulent Flows*. Cambridge University Press, 2000.

[73] F. H. Champagne, Y. H. Pao, and I. J. Wygnanski. On the two-dimensional mixing region. *Journal of Fluid Mechanics*, 74:209–250, 1976.

[74] H. J. Hussein, S. C. Capp, and W. K. George. Velocity measurements in a high-Reynolds-number, momentum-conserving, axisymmetric, turbulent jet. *Journal of Fluid Mechanics*, 258:31–75, 1994.

[75] J. B. Freund. Direct numerical simulation of the noise from a Mach 0.9 jet. FEDSM Paper No. 99-7251, July 1999.

[76] J. B. Freund. Private Communication, April 2002.

[77] N. R. Panchapakesan and J. L. Lumley. Turbulence measurements in axisymmetric jets of air and helium. Part 1. Air jets. *Journal of Fluid Mechanics*, 246:197–223, 1993.

[78] U. Piomelli, A. Scotti, and E. Balaras. Large eddy simulations of turbulent flows, from desktop to supercomputer (invited talk). Vector and Parallel Processing - VECPAR 2000, 4th International Conference, Porto, Portugal, Selected Papers and Invited Talks, June 2000.

[79] K. B. M. Q. Zaman. Asymptotic spreading rate of initially compressible jets - experiment and analysis. *Physics of Fluids*, 10(10):2652–2660, 1998.

[80] I. Wygnanski and H. Fiedler. Some measurements in the self-preserving jet. *Journal of Fluid Mechanics*, 38(3):577–612, 1969.

[81] G. Raman, E. J. Rice, and E. Reshotko. Mode spectra of natural disturbances in a circular jet and the effect of acoustic forcing. *Experiments in Fluids*, 17:415–426, 1994.

[82] V. H. Arakeri, A. Krothapalli, V. Siddavaram, M. B. Alkislar, and L. Lourenco. Turbulence suppression in the noise producing region of a Mach 0.9 jet. AIAA Paper 2002-2523, June 2002.

[83] J. C. Lau, P. J. Morris, and M. J. Fisher. Measurements in subsonic and supersonic free jets using a laser velocimeter. *Journal of Fluid Mechanics*, 93(1):1–27, 1979.

[84] Society of Automotive Engineers. *SAE ARP 876C : Gas Turbine Jet Exhaust Noise Prediction*. November 1985.

[85] E. Mollo-Christensen, M. A. Kolpin, and J. R. Martucelli. Experiments on jet flows and jet noise far-field spectra and directivity patterns. *Journal of Fluid Mechanics*, 18:285–301, 1964.

[86] P. A. Lush. Measurements of subsonic jet noise and comparison with theory. *Journal of Fluid Mechanics*, 46(3):477–500, 1971.

[87] M. R. Visbal and D. P. Rizzetta. Large-eddy simulation on curvilinear grids using compact differencing and filtering schemes. *Journal of Fluids Engineering*, 124:836–847, December 2002.

[88] M. R. Visbal, P. E. Morgan, and D. P. Rizzetta. An implicit LES approach based on high-order compact differencing and filtering schemes (invited). AIAA Paper 2003-4098, June 2003.

[89] G. Rahier, J. Prieur, F. Vuillot, N. Lupoglazoff, and A. Biancherin. Investigation of integral surface formulations for acoustic predictions of hot jets starting from unsteady aerodynamic simulations. AIAA Paper 2003-3164, May 2003.

[90] J. B. Freund. Noise-source turbulence statistics and the noise from a Mach 0.9 jet. *Physics of Fluids*, 15(6):1788–1799, June 2003.

[91] R. Mani, P. R. Gliebe, and T. F. Balsa. High velocity jet noise source location and reduction. Federal Aviation Administration, Task 2, FAA-RD-76-79-II, May 1978.

[92] J. Bridges, NASA Glenn Research Center, AeroAcoustics Propulsion Lab. Private Communication, November 2003.

[93] J. Simonich, S. Narayanan, T. J. Barber, and M. Nishimura. High subsonic jet experiments part 1: Aeroacoustic characterization, noise reduction and dimensional scaling effects. AIAA Paper 2000-2022, 2000.

[94] S. Narayanan, T. J. Barber, and D. R. Polak. High subsonic jet experiments: Turbulence and noise generation studies. *AIAA Journal*, 40(3):430–437, 2002.

[95] D. J. Glaze and S. H. Frankel. Stochastic inlet conditions for large-eddy simulation of a fully turbulent jet. *AIAA Journal*, 41(6):1064–1073, June 2003.

[96] J. B. Freund and S. K. Lele. Computer simulation of high speed jets and their noise. In *High Speed Jet Flows: Fundamentals and Applications*, edited by G. Raman, D. K. McLaughlin, and P. J. Morris, Taylor & Francis, New York, 2002.

[97] J. Bridges and F. Hussain. Effects of nozzle body on jet noise. *Journal of Sound and Vibration*, 188(3):407–418, 1995.

[98] Y. F. Yao, T. G. Thomas, and N. D. Sandham. Direct numerical simulation of turbulent flow over a rectangular trailing edge. *Theoretical and Computational Fluid Dynamics*, 14:337–358, 2001.

[99] D. V. Gaitonde and M. R. Visbal. Further development of a Navier-Stokes solution procedure based on higher-order formulas. AIAA Paper 99-0557, 1999.

[100] X. Zhang, G. A. Blaisdell, and A. S. Lyrintzis. High-order compact schemes with filters on multi-block domains. Second MIT Conference on Computational Fluid and Solid Mechanics, June 2003.

[101] O. Fleig and C. Arakawa. Numerical simulation of wind turbine tip noise. AIAA Paper 2004-1190, January 2004.

VITA

VITA

Ali Uzun was born in Nicosia, Cyprus in 1975. After graduating from high school in 1993, he studied Aeronautical Engineering at the Middle East Technical University in Turkey, graduating with a bachelors degree in 1997. He then moved to the United States to attend graduate school. He received his masters degree in Mechanical Engineering from Indiana University Purdue University Indianapolis (IUPUI) in August 1999. He developed parallel computing algorithms to solve unsteady aerodynamics and moving boundary problems using deforming unstructured grids in his master's thesis work. He started his doctoral level studies in the School of Aeronautics and Astronautics at Purdue University in Fall 1999 and he focused on developing a Computational Aeroacoustics methodology for jet noise prediction during his Ph.D. research. His research interests are Computational Fluid Dynamics (CFD), Large Eddy Simulation (LES), Direct Numerical Simulation (DNS), Computational Aeroacoustics (CAA), Parallel Computing and Applied Aerodynamics. After completing his Ph.D. degree in December 2003, he will be joining the Florida State University in Tallahassee, Florida as a post-doctoral research associate.